Carbon dots for synthetic applications

Inaugural-Dissertation

to obtain the academic degree

Doctor rerum naturalium (Dr. rer. nat.)

submitted to the Department of Biology, Chemistry, Pharmacy

of Freie Universität Berlin

by

Zhouxiang Zhao

from Zhejiang, China

2022

This work was performed between November 2018 and September 2022 under the supervision of Dr. Martina Delbianco and Prof. Dr. Peter H. Seeberger in the Department of Biomolecular Systems, Max Planck Institute of Colloids and Interfaces, Potsdam, and the Institute of Chemistry and Biochemistry, Freie Universität Berlin.

I hereby declare that this dissertation was written and prepared by me independently. Furthermore, no sources and aids other than those indicated have been used. Intellectual property of other authors has been marked accordingly. I also declare that I have not submitted the dissertation in this or any other form to any other institution as a dissertation.

1st Reviewer: Prof. Dr. Peter H. Seeberger

2nd Reviewer: Prof. Dr. Rainer Haag

Date of oral defense: 4th of January 2023

Acknowledgement

First and foremost, I would like to express my deepest gratitude to Dr. Martina Delbianco for her supervision throughout my PhD study and continuous support on this thesis. Thank you so much for your constant encouragement and patience in providing me with suggestions on my research.

I would like to thank Prof. Dr. Peter H. Seeberger for offering me the opportunity to work in the Department of Biomolecular Systems, Max Planck Institute of Colloids and Interfaces. Thank you for providing me the excellent research environment and for reviewing this thesis.

I thank to Prof. Dr. Rainer Haag for kindly agreeing to review this thesis.

I would like to thank all the previous and current members of Carbohydrate Materials group, Dr. Yang Yu, Dr. Yuntao Zhu, Dr. Vittorio Bordoni, Dr. Manishkumar Chaube, Dr. Denisa Vargová, Dr. Soeun Gim, Dr. Theodore Tyrikos-Ergas, Dr. Nives Hribernik, Dr. Kaimeng Liu, Dr. Giulio Fittolani, Jhih-Yi Huang, Surusch Djalali, Marlene Dal Colle, Nishu Yadav for their help in the lab work, warm atmosphere they created in the lab, and proofreading of my papers and this thesis. Thank Surusch Djalali for the German translation of the summary in this thesis.

I am particularly grateful to my collaborators, Dr. Susanne Reischauer, Dr. Bartholomäus Pieber, for giving me many beneficial suggestions about photocatalytic cross coupling reactions. I am thankful to Lewis Mcghie, Dr. John James Molloy for providing valuable isomerization materials.

My thanks also go to other colleagues of Department of Biomolecular Systems. Special thanks to Eva Settels, Olaf Niemeyer, Dorothee Böhme for their technical and organizational support. I am thankful to Heike Runge, Bolortuya Badamdorj, Daniel Werner, Dr. Oleksandr Savatieiev for the training and sample measurement.

My deep gratitude also goes to my family for continuous support and constant encouragement all the time. Their unconditional love keeps me motivated to finish my doctoral studies.

Table of Contents

Summary

Carbon dots (CDs), nanoscale quasi-spherical carbon materials, have attracted considerable attention in recent years, owing to their unique properties such as superior photoluminescence (PL) properties as well as excellent chemical- and photo-stability. CDs could act as metal-free, green nano-catalysts and their tailorable surface groups such as hydroxyl, carboxylic acid and amino groups have been exploited for organic synthesis. Meanwhile, CDs have shown great potential as visible-light-absorbing photocatalysts due to their light-harvesting ability and electron-transfer efficiency. Still, their photcatalytic applications are limited to simple organic transformations.

In this thesis, CDs were synthesized from abundant carbohydrate sources, following a microwave-based carbonization method. The use of different doping agents was explored to adjust the functional groups on the CD surface and tune the photophysical properties. The obtained CDs were implemented as nano-photocatalysts for complex organic transformations such as cross-coupling and isomerization reactions.

In Chapter 2, CDs were immobilized on the surface of TiO_2 to generate heterogeneous photocatalytic systems. The applicability of **CD1**/TiO_2 nanocomposites as photocatalysts for nickel-catalyzed cross-couplings was demonstrated for a C-O arylation using visible-light. **CD1**/TiO_2 nanocomposites also served as an active photocatalyst for the coupling of aryl halides with an alcohol, a thiol, a sodium sulfonate, and a sulfonamide. Next, the photostability and recyclability of the **CD1**/TiO_2 nanocomposite were explored, showing superior performances in comparison to organic dyes. Having demonstrated the potential of **CD1** as photosensitizer for dual photoredox/Ni catalysis, I assessed the effect of different carbon sources and doping agents on the photocatalytic reaction.

In Chapter 3, CDs were used to construct a quasi-homogenous colloidal catalytic system in combination with a Ni complex. This approach bypassed the need of CD immobilization onto a semiconductor (TiO_2) and expanded the scope of suitable Ni ligands. This quasi-homogeneous system was applied to catalyze a broad range of carbon–heteroatom cross-couplings. I further investigated the mechanism of a C-S cross-coupling, optimized the reaction conditions, and expanded the substrate scope. New CDs were synthesized and a series of characterizations were performed to explore their influence on the photocatalytic performance.

In Chapter 4, CDs were tested as cheap and green visible-light-absorbing photocatalyst for *E*-to-*Z* isomerization, a reaction that follows an energy-transfer-based

catalytic mechanism. The isomerization results of *trans*-stilbene proved the catalytic capabilities of CDs in energy-transfer reaction. Next, I showcased the potential of CDs for the photo-isomerization of ethyl (*E*)-3-(*p*-tolyl)but-2-enoate (**4-3**), an alkene exhibiting larger separation of the excited state energy with its *Z*-isomers. I further expanded the substrate scope of *E*-to-*Z* isomerization reactions and screened a collection of CDs as photocatalysts to shine light on the process of *E*-to-*Z* isomerization.

Overall, I demonstrated that CDs could serve as valuable photocatalysts for complex organic transformations, enriching their applications in the field of photocatalytic organic synthesis. Their ease of preparation from abundant precursor, tunable PL properties, and superior photostability make CDs valuable alternatives for expensive metal-based photocatalysts.

Zusammenfassung

Carbon Dots (CDs) sind nanoskalige, quasi-sphärische Kohlenstoffmaterialien und haben in den letzten Jahren aufgrund ihrer einzigartigen Eigenschaften, wie der überragenden Photolumineszenz (PL), sowie der ausgezeichneten chemischen und photochemischen Stabilität, große Aufmerksamkeit auf sich gezogen. CDs können als metallfreie, grüne Nanokatalysatoren verwendet werden, da ihre modifizierbare Oberfläche eine Vielzahl an Funktionalitäten erlaubt. Hydroxyl-, Carboxyl- und Aminogruppen ermöglichen den Einsatz in der organischen Synthese, während ihre Lichtsammelfähigkeit und Elektronentransfereffizienz ein großes Potenzial im Bereich der Photokatalyse mit sichtbaren Licht birgt. Dennoch beschränkt sich zum jetzigen Zeitpunkt ihre photokatalytischen Anwendungen auf einfache organische Transformationen.

Auf Basis von allgegenwertigen Kohlenhydratquellen und einer mikrowellenbasierten Karbonisierungsmethode, wurden in dieser Arbeit CDs synthetisiert. Die Verwendung verschiedener Dotierstoffe erlaubte es die funktionellen Gruppen auf der CD-Oberfläche anzupassen und die resultierenden photophysikalischen Eigenschaften ihrer entsprechenden Anwendung zu optimieren. Die erhaltenen CDs wurden im Folgenden als Nano-Photokatalysatoren für komplexe organische Umwandlungen wie Kreuzkupplungs- und Isomerisierungsreaktionen verwendet.

Im zweiten Kapitel dieser Arbeit wurden CDs auf der Oberfläche von TiO_2 immobilisiert, um heterogene photokatalytische Systeme zu erzeugen. Die Anwendbarkeit des **CD1**/TiO_2-Nanokompositen als Photokatalysator für Nickel-katalysierte Kreuzkupplungen konnte im Falle einer C-O-Arylierung unter Verwendung von sichtbarem Licht nachgewiesen werden. Des Weiteren konnte das **CD1**/TiO_2-Nanokomposite auch als aktiver Photokatalysator für Kopplungsreaktionen von Arylhalogeniden mit Alkoholen, Thiolen, Natriumsulfonaten und Sulfonamiden genutzt werden. Anschließend wurden die Photostabilität und die Recycelbarkeit des **CD1**/TiO_2-Nanokomposits untersucht, wobei sich überlegene Eigenschaften im Vergleich zu organischen Farbstoffen zeigten. Nachdem das Potenzial von **CD1** als Photosensibilisator für die duale Photoredox/Ni-Katalyse nachgewiesen wurde, untersuchte ich die Auswirkungen verschiedener Kohlenstoffquellen und Dotierstoffe auf die photokatalytische Reaktion.

Im dritten Kapitel wurde ein quasi-homogenes, kolloidales, katalytisches System aus CDs in Kombination mit einem Ni-Komplex konstruiert. Mit diesem Ansatz wurde die Notwendigkeit der CD-Immobilisierung auf einem Halbleiter (TiO_2) umgangen und die

Bandbreite der geeigneten Ni-Liganden erweitert. Das homogene System wurde zur Katalyse einer breiten Palette von Kohlenstoff-Heteroatom-Kreuzkupplungen eingesetzt. Des Weiteren untersuchte ich den Mechanismus einer C-S-Kreuzkupplung, optimierte die Reaktionsbedingungen und erweiterte das Spektrum der tolerierten Substrate. Es wurden neue CDs synthetisiert und im Anschluss auf ihren Einfluss auf die photokatalytische Leistung charakterisiert.

Im vierten Kapitel wurde das Potenzial von CDs als billige, grüne Photokatalysatoren für *E*-*Z*-Isomerisierungen getestet − eine Reaktion, die einem energietransfer-basierenden, katalytischen Mechanismus folgt. Die Ergebnisse der Isomerisierung von *trans*-Stilben bewiesen die katalytischen Fähigkeiten von CDs bei der Energietransferreaktion. Als Nächstes habe ich das Potenzial von CDs für die Photoisomerisierung von Ethyl-(*E*)-3-(*p*-tolyl)but-2-enoat vorgestellt, einem Alken, das eine größere Differenz der Energien des angeregten Zustands mit seinen *Z*-Isomeren aufweist. Ich habe den Substratbereich der *E*-*Z*-Isomerisierungsreaktionen erweitert und dabei eine Reihe von CDs als Photokatalysatoren untersucht.

Insgesamt konnte ich zeigen, dass CDs als wertvolle Photokatalysatoren für komplexe organische Umwandlungen dienen können, was ihre Anwendungsmöglichkeiten auf dem Gebiet der photokatalytischen organischen Synthese erweitert. Ihre einfache Herstellung aus zugänglichen Präkursoren, ihre abstimmbaren PL-Eigenschaften und ihre hervorragende Photostabilität machen CDs zu einer wertvollen Alternative gegenüber herkömmlichen, metallbasierten Photokatalysatoren.

List of Publications

Scientific Publications:

1. *Carbon dot/TiO_2 nanocomposites as photocatalysts for metallaphotocatalytic carbon–heteroatom cross-couplings*
   Z. Zhao, S. Reischauer, B. Pieber, M. Delbianco. *Green Chem.*, **2021**, 23, 4524-4530.
   https://doi.org/10.1039/D1GC01284C
2. *Modulating the surface and photophysical properties of carbon dots to access colloidal photocatalysts for cross-couplings*
   Z. Zhao, B. Pieber, M. Delbianco. *ACS Catal.*, **2022**, 12, 13831-13837.
   https://doi.org/10.1021/acscatal.2c04025

Scientific Conferences and Symposia Presentations:

August 2021, ACS Fall 2021 webinar, Atlanta (USA), Poster presentation

List of Abbreviations

AFM	atomic force microscopy
β-Ala	β-alanine
BIPA	*N*-*tert*-butylisopropylamine
Boc-Pro-OH	*N*-(*tert*-butoxycarbonyl)-L-proline
BSA	bovine serum albumin
CB	conduction band
CD	carbon dot
DBU	1,8-diazabicyclo[5.4.0]undec-7-en
dcbpy	2,2’-bipyridine-4,4’-dicarboxylic acid
DCM	dichloromethane
DLS	dynamic light scattering
DMAc	dimethylacetamide
DMSO	dimethyl sulfoxide
DOX	doxorubicin
dtbbpy	4,4’-di-*tert*-butyl-2,2’-dipyridyl
EDA	ethylenediamine
EDX	energy dispersive X-ray
EnT	energy transfer
EtOAc	ethyl acetate
FA	folic acid
Fluo	fluorescein
Gal	galactose
Glc	glucose
GlcNAc	*N*-acetyl-glucosamine
GlcN·HCl	glucosamine hydrochloride
Gly	glycine
HRTEM	high-resolution transmission electron microscopy
ICP-OES	inductively coupled plasma-optical emission spectrometry
IR	infrared
ISC	intersystem crossing
Lac	D-lactose
l-Cys	l-cysteine
LED	light-emitting diode
mcbpy	4’-methyl-2,2’-bipyridine-4-carboxylic acid
MeCN	acetonitrile
MeOH	methanol
NIR	near-infrared
NMR	nuclear magnetic resonance
PC	photocatalyst
PDT	photodynamic therapy

PEG	poly(ethylene glycol)
PL	photoluminescence
py	pyridine
pyHI	pyridinium iodide
SEM	scanning electron microscopy
SET	single electron transfer
TCSPC	time-correlated single photon counting
TEM	transmission electron microscopy
TLC	thin layer chromatography
UV	ultraviolett
VB	valence band
Vis	visible
XRD	X-ray diffraction

1. Introduction

1.1. Carbon dots

Carbon nanomaterials have attracted extensive attention over the past few decades. Nowadays, several types of nanocarbon families exist and have been systematically studied, including graphene, graphene oxide, carbon dots, carbon nanotubes, fullerenes and nano-diamonds.[1-3] Among them, carbon dots (CDs) have shown great potential due to their superior photoluminescence (PL) properties, chemical inertness, excellent photostability, and low toxicity. Fluorescent CDs are a nanoscale quasi-spherical carbon materials with a size of typically less than 10 nm. They were accidentally discovered in 2004 during the purification process of single-walled carbon nanotube fragments through preparative electrophoresis.[4]

1.1.1. Synthesis and properties

CDs can be easily obtained on a multi-gram scale from low-cost starting materials by a variety of simple synthetic routes. Two synthetic strategies are generally employed to access CDs: *top-down* and *bottom-up* (**Figure 1-1**).[5, 6]

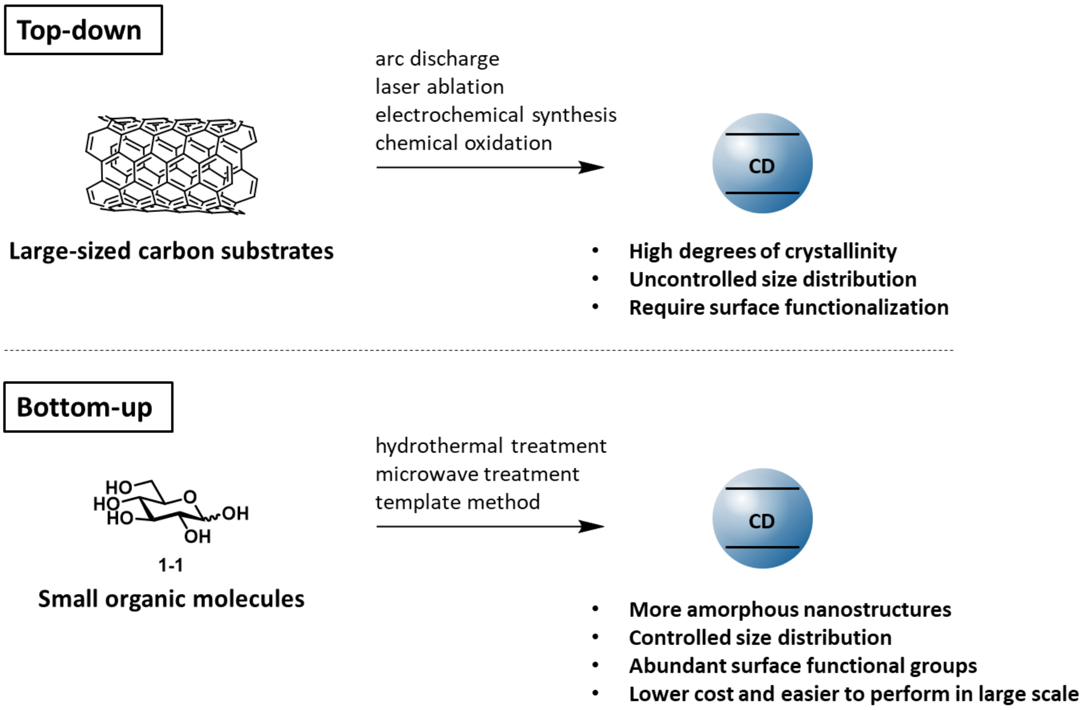

Figure 1-1. Top-down and bottom-up synthetic strategies for CD synthesis.

1.1.1.1. *Top-down* synthesis

In *top-down* synthetic strategies, nano-sized CDs are generated from relatively large-sized carbon substrates *via* physical or chemical exfoliation. Carbon nanotubes or fibers, graphite, graphite oxide, or carbon soot are commonly used as starting materials and decomposed by means of arc discharge, laser ablation, electrochemical synthesis and chemical oxidation.[4, 7-10] Arc discharge is producing CDs with excellent fluorescence performance. However, during the preparation process many impurities that are difficult to be removed are also generated, decreasing the yields significantly. Laser ablation is rapid and effective method to generate CDs with tunable surface states from carbon precursors such as graphite, upon laser irradiation. The CDs obtained with this method have low quantum yield and uncontrollable size. Compared to the previous two methods, electrochemical synthesis is easier to operate and enables the preparation of CDs in high-yield with precisely control on their sizes. Lastly, chemical treatment of carbon sources with strong oxidants (e.g., HNO_3, H_2SO_4) could produce CDs with abundant surface oxygen-containing functional groups. This method is simple and scalable, but the size distribution of the resulting CDs is not controllable.

Top-down-synthesized CDs usually have high degrees of crystallinity, which is preserved from the sp^2-hybridized carbon nanostructure in the starting materials. In most cases, these physical or chemical cutting processes lack precise control over the size distribution and shape of the resulting CDs.[7] Additionally, the *top-down* approach often requires an extra surface functionalization step to tune the CDs' PL properties.

1.1.1.2. *Bottom-up* synthesis

Compared to *top-down* approach, *bottom-up* procedures for CD synthesis have lower costs and are easier to perform. CDs can be synthesized in large scale and controlled size distribution from molecular precursors through processing methods such as hydrothermal treatment, microwave treatment and template method.[11-14] Hydrothermal treatment is a low-cost and eco-friendly route for CD synthesis. The CDs have high quantum yields and dispersibility in water. However, this method requires high temperature and high pressure. In comparison, microwave treatment is facile and convenient, generating CDs within a few minutes. The template method can precisely control the CD size and deliver CDs with high purity. Still, the separation of CDs and template (e.g. mesoporous silica) is difficult, limiting large-scale applications.

Unlike top-down-synthesized CDs, bottom-up-synthesized CDs tend to have amorphous nanostructures. A variety of organic molecules, natural materials, and even waste products can be used as carbon precursors. Moreover, the introduction of doping agents is important to generate CDs exposing different functional groups on their surfaces (e.g. carboxylic acid and amino groups) or to tune their elemental compositions, by addition of heteroatoms.[15, 16] This process is useful to enhance the CDs fluorescence properties, their solubility in aqueous solution, and allows for further surface functionalization.

1.1.1.3. CDs from carbohydrates

Carbohydrates are inexpensive and biocompatible starting materials that became very attractive carbon sources for CD synthesis.[17] Other advantages are high abundance, ease of carbonization at low temperatures, and excellent water solubility. Monosaccharides, such as glucose and glucosamine, as well as polysaccharides such as cellulose and chitosan, have been employed to prepare a variety of CDs.[18-22]

Water-soluble CDs were prepared from glucose (**1-1**) following the microwave method (**Figure 1-2**).[23] Meanwhile, doping with poly(ethylene glycol) (PEG-200, **1-2**) could enhance surface passivation and improve the PL properties (e.g. stronger PL). Sucrose (**1-3**), an abundant disaccharide, can also be used as an alternative starting material to glucose (**1-1**) for CD synthesis. For example, the orange-red emitting CDs with a size of less than 5 nm were successfully synthesized from sucrose (**1-3**) employing a simple hydrothermal treatment (**Figure 1-3**).[24] Many more dots have been prepared using mono- and disaccharides as carbon sources, generating a wide portfolio of CDs with different size and emission properties. A comprehensive review has been recently published by Galan.[17]

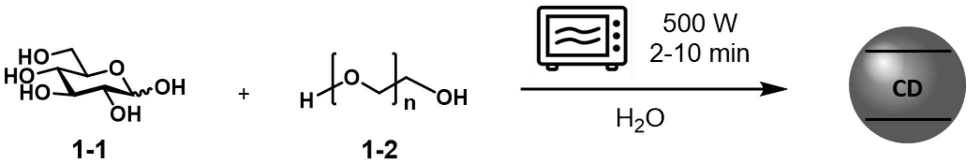

Figure 1-2. Preparation of CDs from glucose and PEG-200 following microwave treatment.

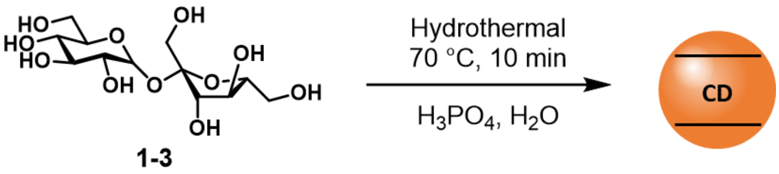

Figure 1-3. Preparation of CDs from sucrose following hydrothermal treatment.

Polysaccharides are also important carbon sources for the preparation of CDs. Due to their size, and in some cases high crystallinity, the carbonization process often requires harsher conditions than smaller oligomers. Particular interest has been devoted to nitrogen-containing polysaccharide. Chitosan (**1-4**), the *N*-deacetylated derivative of chitin, has been extensively used for numerous biomedical applications, due to its excellent biocompatible and biodegradable properties. Pramanik and co-workers selected chitosan (**1-4**) doping with PEG-200 (**1-2**) to yield CDs following a microwave carbonization protocol (**Figure 1-4**).[25] The synthesized CDs with a diameter of about 2-10 nm have high amount of surface amino groups, and could emit a blue luminescence.

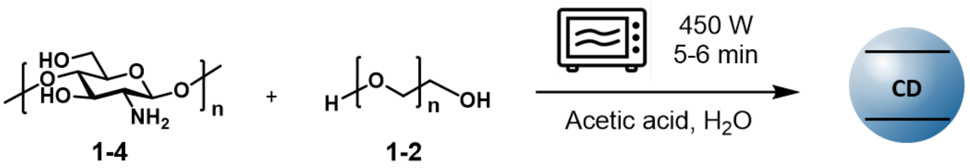

Figure 1-4. Preparation of CDs from chitosan and PEG-200 following microwave treatment.

Other heteroatom-containing polysaccharides such as heparin (**1-5**) have also been used to prepare water-soluble nitrogen and sulfur co-doped CDs employing a facile hydrothermal treatment (**Figure 1-5**).[26]

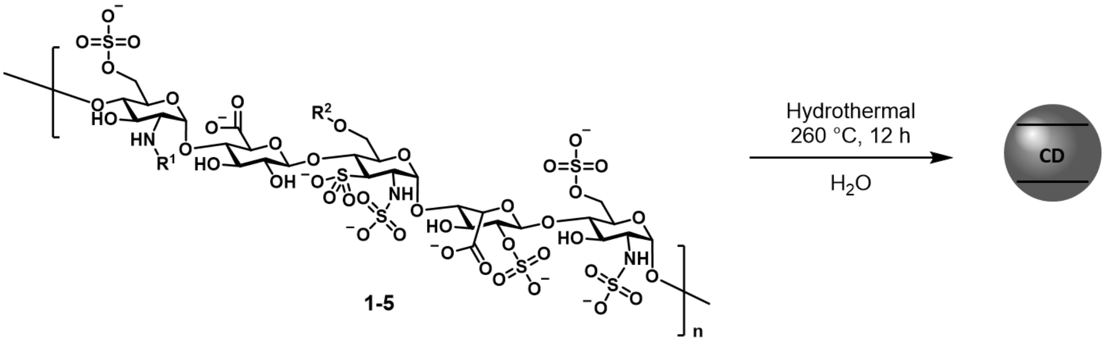

Figure 1-5. Preparation of CDs from heparin following hydrothermal treatment.

1.1.1.4. Physical and optical properties of CDs

The elemental composition and structure of CDs are very much connected to the preparation methods. These parameters have a great influence on the physical and optical properties of the CD. In general, CDs show a quasi-spherical morphology with the sizes of typically less than 10 nm in diameter, although larger sizes of about 60 nm have also been reported.[27, 28] The shapes and sizes of CDs can be measured using transmission electron microscopy (TEM) and their height can be characterized using atomic force microscopy (AFM). The CD nanostructure can be investigated using X-ray diffraction (XRD) and the lattice spacing of crystalline CDs can be measured by high-resolution TEM (HRTEM). Generally, CDs synthesized from *bottom-up* methods are amorphous, whereas high degrees of crystallinity is obtained following *top-down* methods. The elemental composition can be measured with energy dispersive X-ray spectroscopy (EDX). CDs consist of a core with abundant C, H and O elements. Functional groups on the surface such as alcohols, carboxylic acids, or amines can be detected with nuclear magnetic resonance (NMR) spectroscopy, infrared (IR) spectroscopy, and zeta potential.

The optical properties of CDs have received increasing attention in recent years, even though the origin of these properties is still debated. Light absorption originates from π–π* transitions of C=C bonds in the core and n–π* edge transitions of C=O bonds on the surface (**Figure 1-6A**).[11, 29, 30] Compared to amorphous CDs, CDs with high degrees of crystallinity exhibit higher extinction coefficients (i.e. stronger absorbance) due to the larger number of C=C bonds. Three main possible causes of CDs PL have been proposed: i) PL emission arises from sp^2 conjugated domains of the polyaromatic structures in the core; ii) PL emission is the results of defect states caused by *O*-related functional groups on the CD surface; iii) PL emission is due to various molecular fluorophores generated during the synthesis.[6, 31] Often, CDs show excitation wavelength-dependent and pH-dependent PL emission, which is useful for sensing applications (**Figure 1-6B**).[32-34] The latter may be due to the variation of charge on the CD surface with the change of pH, owing to the many surface functional groups such as amino and carboxylic acid groups. In contrast, no clear explanation exists for the excitation wavelength-dependent emission. Still, the tunable PL emission of CDs provides tremendous advantages for a wide variety of imaging applications. Moreover, the introduction of heteroatoms such as N, S and P from the starting materials into CDs during the synthesis process is a common procedure to adjust their energy bandgap and tune their PL properties even further.[35] Compared to conventional organic or inorganic fluorophores, CDs show superior chemical- and photo- stability in aqueous as well as in organic media, even under prolonged irradiation with powerful Xe lamps.[7] Surface passivation with organic or polymeric materials is a common method for achieving brighter PL, as passivation can stabilize the surface defects of CDs.[13, 36]

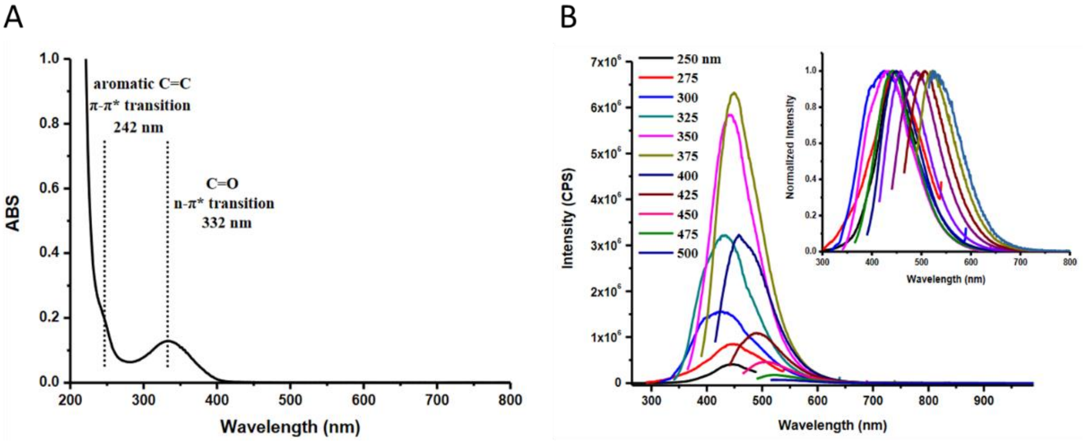

Figure 1-6. Absorption spectrum (A) and excitation wavelength-dependent PL emission spectra (B) of CD. Adapted with permission from *ChemPhysChem* **2018**, 19, 2589-2597 Copyright (2018).

1.1.2. Applications of CDs

The unique properties of CDs such as low cost, low toxicity, excellent chemical- and photo- stability, tunable PL emission, promoted a wide range of applications in sensing, bioimaging, and nanomedicine.

Heavy metal pollution is a major global concern because of the non-biodegradation and high toxicity on the environment and biological organisms. Fluorescent CDs can be used for the rapid and efficient detection of toxic heavy metals such as mercury(II) (Hg^{2+}) in industrial wastewater and living cells.[37, 38] The fluorescence of CDs is selectively quenched by Hg^{2+}, upon coordination to the surface oxygen-containing functional groups of CDs such as hydroxyl and carboxylic acid groups. These interactions destroy defect states on the CD surface and result in fluorescent quenching. The same principles have been applied to detect other heavy metal ions such as iron(III) (Fe^{3+}) and lead(II) (Pb^{2+}).[39, 40] CDs have been proven useful sensors also for pH, organic/biological molecules, and gases with high sensitivity and selectivity.[5]

Another highly attractive application of CDs is bioimaging.[41] Compared to most organic fluorophores that suffer from photobleaching and semiconductor Cd/S quantum dots with high toxicity, photostable and low-toxic CDs are suitable alternatives for cellular imaging. Moreover, CDs can be efficiently internalized into live cells owing to their nano-size. In recent years, many functionalized CD complexes have been developed for target-specific cell imaging. Despite the majority of CDs emit strong blue or green fluorescence under UV light irradiation, CDs or CD-based complexes emitting in the red or near-infrared (NIR) regions have been developed, overcoming the problem of tissue-penetration depth for *in vivo* imaging. For example, a water-soluble nanocomposite was prepared by encapsulating CDs and Rhodamine B into the silica layer.[42] Owing to their high stability, high biocompatibility and long lifetime, this nanocomposite was used as imaging agent for deep-tissue time-gated afterglow imaging.

Recently, CDs have also been exploited as multifunctional tools in nanomedicine. For example, CDs have been employed as nano-carriers for the controlled release of drugs or genes in the targeted cells.[43] Green fluorescent CDs prepared from sorbitol were further modified with bovine serum albumin (BSA) or folic acid (FA) to enhance their biocompatibility and selectively target cancer cells.[44] The modified CDs could act as drug delivery vehicles for doxorubicin (DOX) for cancer therapy. In addition, CDs were employed as photosensitizers in photodynamic therapy (PDT) strategy that uses photosensitizing agents to produce free radicals and singlet oxygen in the tumor tissue when irradiated with light, eventually leading to the death of cancer cells.[45]

1.1.3. Carbon dots in organic synthesis

In the last few years, CDs have been suggested as metal-free, green nano-catalysts for organic synthesis. CDs possess the core-shell structures with a carbon core that is surrounded by various functional groups such as hydroxyl, carboxylic acid and amino groups (**Figure 1-7**).[46, 47] These tailorable surface groups have been exploited to generate nano-organocatalysts.

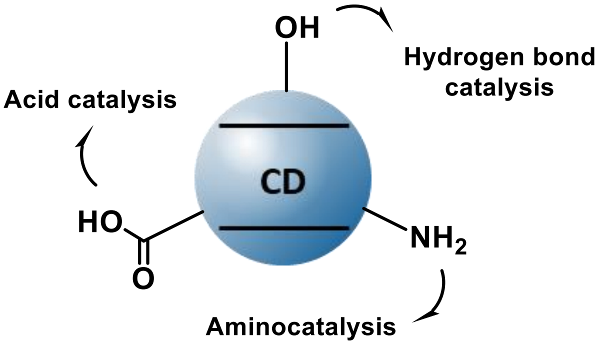

Figure 1-7. Functional groups on CD surface as nano-organocatalysts.

CDs are easy-to-prepare and environmentally friendly alternatives for traditional acid catalysts (mineral acids, organic acids),[48, 49] overcoming issues of high corrosion and toxicity. The carboxylic acid groups on CD surface could serve as catalytic sites for acid-catalyzed organic reactions. Moreover, the surface functional groups can be easily tuned by changing the starting materials during CD synthesis. Owing to its abundant surface carboxylic acid groups, CD synthesized from β-carotene could effectively catalyze condensation reactions and aza-Michael reactions (**Figure 1-8**).[50] Even low amounts of catalysts (0.5 mg/mL) were sufficient to achieve selective transformations in good yields.

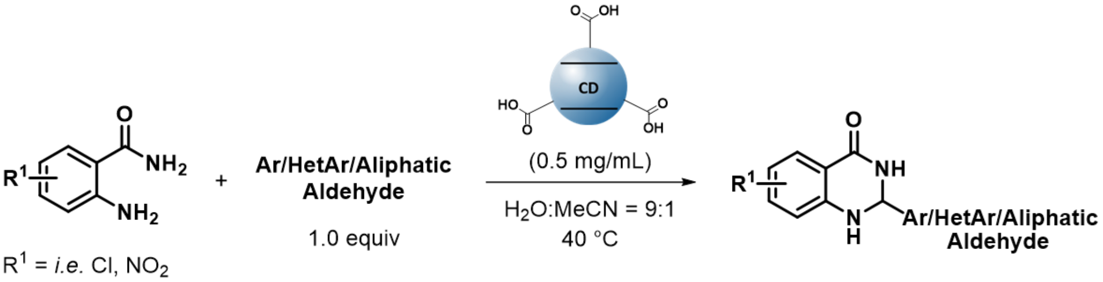

Figure 1-8. Application of CDs with surface carboxylic acid groups as nano-organocatalysts for condensation reactions.

Inspired by enzyme-catalyzed reactions in nature, hydrogen bond catalysis using organic molecules with hydroxyl groups was developed.[51-53] Hydrogen bonds between the substrate and the catalyst orient the substrate molecules, while lowering activation barriers. Thus, CDs bearing many surface hydroxyl groups are excellent hydrogen bond organocatalysts. For instance, a uniformly dispersed CDs prepared from citric acid was encapsulated in a micelle system formed by ionic liquids, which could trap organic reactants and promote multi-component condensation reactions in the interior cavity (**Figure 1-9**).[54] The high density of surface hydroxyl groups resulted in excellent catalytic performances, even after ten reaction cycles.

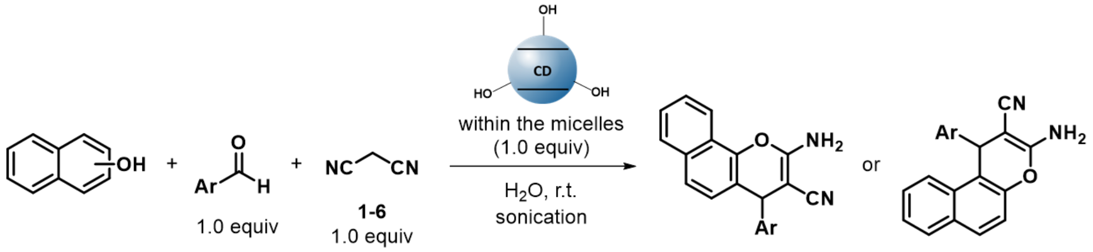

Figure 1-9. Application of CDs with surface hydroxyl groups as nano-organocatalysts for multi-component condensation reactions.

Aminocatalysis is another convenient and effective strategy for numerous transformations, such as proline-catalyzed intermolecular aldol reaction, using primary and secondary amines as organocatalysts.[55, 56] CDs with surface amino functional groups have shown promising results for the functionalization of carbonyl substrates. CDs were synthesized *via* pyrolysis of citric acid using amines as doping agents to ensure a high amount of primary, secondary and tertiary amines on the CD surface.[57] These nanocatalysts efficiently promoted Knoevenagel condensation reactions

(**Figure 1-10**). Moreover, the CDs could be easily separated from the reaction mixture, showing great reusability even after six reaction cycles.

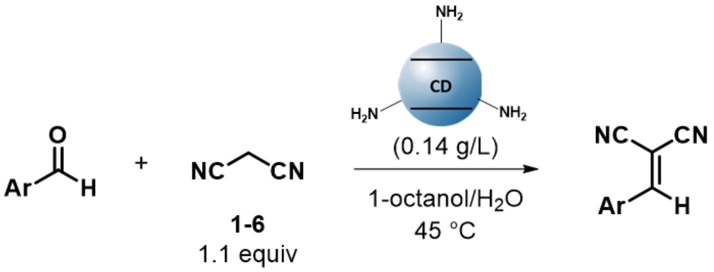

Figure 1-10. Application of CDs with surface amino groups as nano-organocatalysts for Knoevenagel condensation reactions.

1.2. Photocatalytic reactions

Solar energy, a clean and renewable energy, has been extensively considered as one of the most promising natural energy sources for solving the problem of global energy crisis. In nature, the most common example of utilization of solar energy is photosynthesis. In this process, the sunlight is harvested to initiate a chemical cascade of reactions, using chlorophylls as the photocatalyst. Inspired by this natural process, many chemical reactions driven by light have been studied and many photocatalysts have been designed.[58, 59] To date, photochemistry represents a promising strategy to obtain organic products in academia and chemical industry.[60]

The Jablonski diagram (**Figure 1-11**) describes the energy levels and the transitions between them upon absorption of a photon.[61, 62] After absorbing a photon with adequate energy, a molecule is excited from the ground state (S_0) to its singlet excited state (S_1). The singlet excited state (S_1) has a short lifetime (~10^{-9} s) and can rapidly relax back to the ground state (S_0) following different pathways: non-radiative relaxation or emission of fluorescence. In addition, intersystem crossing (ISC) to its triplet excited state (T_1) can happen. The transitions from the triplet excited state (T_1) to the ground state (S_0) are spin-forbidden, making T_1 a long-lived excited state. Owing to its long lifetime (>>10^{-7} s), T_1 can engage in bimolecular processes.

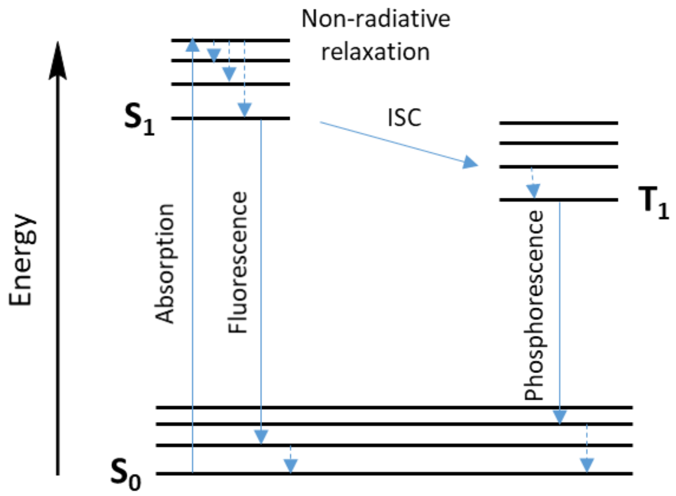

Figure 1-11. A simplified Jablonski diagram illustrating the transitions between the different energy levels of a molecule.

In a photocatalytic reaction, the photocatalyst absorbs light to generate a long-lived excited state. Subsequently, the excited state energy of the photocatalyst is used to access an excited-state substrate, finally launching and completing the photochemical reaction. There are two modes of interaction between the excited photocatalyst and the substrate: single electron transfer (SET) in photoredox catalysis and energy transfer (EnT) in photosensitization (**Figure 1-12**).[61, 63] In photoredox catalysis, quenching of the excited photocatalyst can happen either by accepting or donating a single electron to the substrate (reductive or oxidative quenching respectively). In EnT catalysis, the excited state energy is transferred from the photocatalyst to a substrate without a redox process.

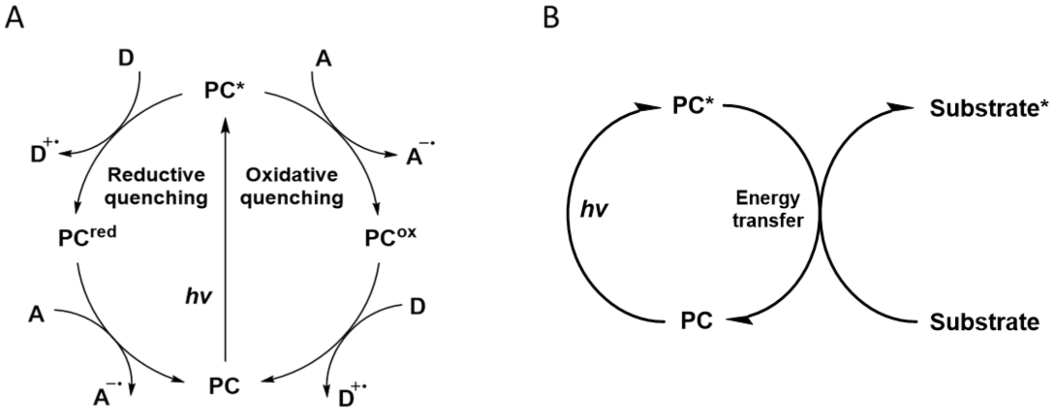

Figure 1-12. Schematic diagrams of photoredox catalysis (A) and energy-transfer catalysis (B). PC = photocatalyst, D = electron donor, A = electron acceptor.

1.2.1. Photocatalysts for organic transformations

A photocatalyst requires several key properties for achieving excellent photocatalytic performances. First, the photocatalyst should be chemical- and photo-stable, because most reactions are performed under strong light irradiation that could generate highly reactive undesired intermediates. Second, a good absorption in the visible-light range is highly beneficial. Ultraviolet (UV) light may decompose the organic substrates due to the high energy, promoting numerous undesired side reactions; in contrast, visible light is a milder and safer light source.[64] Then, a long excited state lifetime of the photocatalyst is key to ensure SET or EnT to the target molecules before relaxation to the ground state. Finally, ideal photocatalysts should be prepared easily in large scale from the cheap starting materials. Currently, the photocatalysts used in photochemical reactions are mainly divided into two categories according to their physical-state appearance: homogeneous photocatalysts, such as organometallic complexes and organic dyes, and heterogeneous photocatalysts, such as semiconductors (**Figure 1-13**).

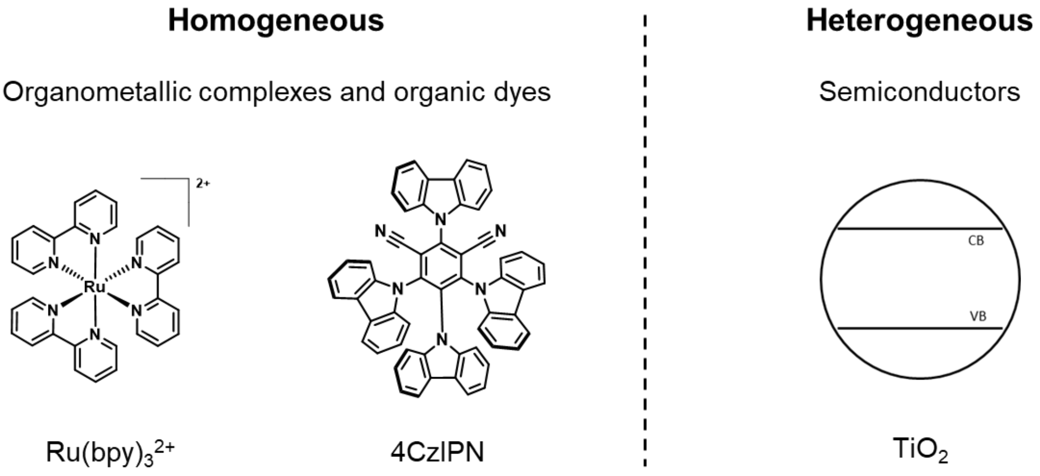

Figure 1-13. Representative examples of photocatalysts commonly employed in photocatalysis.

1.2.1.1. Homogeneous photocatalysts

The most commonly used photocatalysts are metal complexes, such as ruthenium (Ru) and iridium (Ir) polypyridyl complexes.[65] They are the major players in photocatalysis due to their long excited-state lifetimes and high catalytic activity. They have been employed in numerous organic transformations, such as cross coupling reactions and isomerization. However, the high economic cost and toxicity of these noble-metal photocatalysts have limited their large-scale applications. Metal-free organic dyes, such as the long-lived excited-state 4CzIPN and Eosin Y, can act as “low-cost” alternative homogeneous photocatalysts and are capable of efficiently catalyzing a wide variety of reactions.[66-69] However, only a small fraction of organic dyes can be employed in photocatalysis, while the vast majority of dyes, such as fluorescein, are not useful due to their short excited state lifetimes.[70] Photobleaching and lack of recyclability pose additional issues for all homogeneous photocatalysts.

1.2.1.2. Heterogeneous photocatalysts

Heterogeneous photocatalysts, such as semiconductors, are generally recyclable and photostable, capable of achieving numerous organic transformations.[71] An ideal semiconductor possesses a narrow band gap and is capable of absorbing visible-light. Upon irradiation with sufficiently high-energetic photons, the electrons in the semiconductor are excited from the valence band (VB) to the conduction band (CB), forming a long-lived changed separated state, which could reduce electron acceptors and oxidize electron donors.

Titanium dioxide (TiO_2) is one of the most promising semiconductors in photocatalysis owing to its numerous advantages such as abundance, low cost, low toxicity, long-term photostability and superior photoactivity.[72, 73] However, the poor absorption of TiO_2 in the visible-light region restricts its applications for a wide range of photochemical reactions. To overcome this problem, Opatz and co-workers designed a TiO_2 nanocomposites with 6,7-dihydroxy-2-methylisoquinolinium (DHMIQ) as catalysts for oxidative cyanation of amines (**Figure 1-14**).[74] Enhanced photocatalytic performances were observed under visible and even NIR light irradiation.

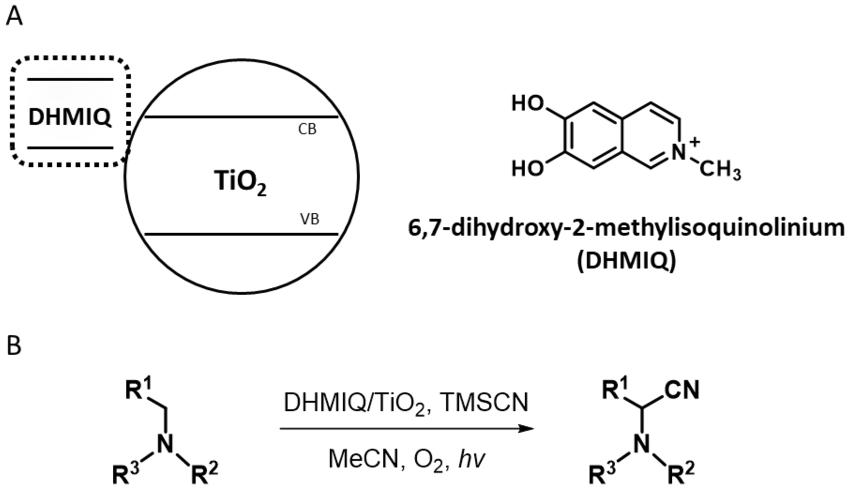

Figure 1-14. Schematic representation of DHMIQ/TiO_2 nanocomposite (A) and its application as photocatalyst in the oxidative cyanation of amines (B).

Carbon nitrides, metal-free polymeric semiconductors, have emerged as excellent photocatalysts for various organic transformations, offering low cost, ease of preparation, and visible-light absorption ability.[75, 76] For example, mesoporous carbon nitride (mpg-C_3N_4) could selectively oxide the alcohols to the corresponding aldehydes/ketones under O_2 atmosphere and visible light irradiation (**Figure 1-15**).[77]

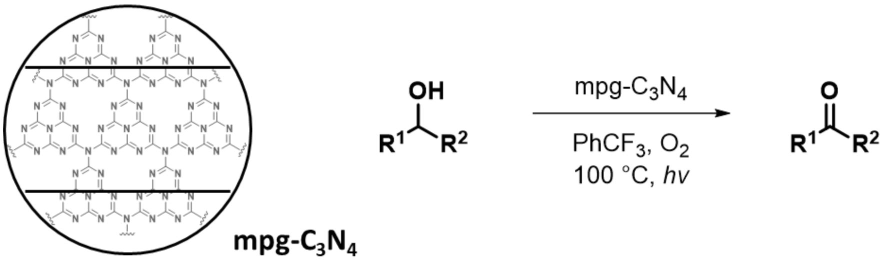

Figure 1-15. Application of mpg-C_3N_4 as photocatalyst for the oxidation of alcohols.

A major limitation of heterogeneous photocatalysts is the poor compatibility with continuous flow systems, limiting the scalability of some photochemical reactions. Recently, Gilmore and co-workers developed an effective strategy based on a serial micro-batch reactor (SMBR) approach allowing for selective and efficient fluorination reactions using a modified graphitic carbon nitride heterogeneous catalyst.[78]

1.2.2. Carbon dots in photocatalysis

CDs have proven interesting metal-free visible-light-absorbing photocatalysts. Owing to their photostability, light-harvesting ability, and electron-transfer efficiency, they were successfully employed for water splitting and pollutant degradation.[6, 79, 80] In addition, the high solubility in water of CDs offers a great opportunity for their use in aqueous reaction media as suitable alternative to hydrophobic organic materials, such as carbon nitride and graphite.[81]

The combination of CDs photophysical properties and tailorable surface groups is particularly important to access powerful nano-organocatalysts. CDs with dual catalytic properties have been explored in various photoenhanced organic transformations, including condensation, ring-opening, and cross coupling reactions.[46, 82] Sulfonated CDs have been used as the metal-free photocatalysts in C–C coupling reactions.[83] These CDs were synthesized from glucose following a microwave-based carbonization procedure and a subsequent treatment with fuming sulfuric acid to form surface acid functional groups. These dots were showcased in the cross-coupling of benzylic hydrocarbons with nucleophiles under blue light irradiation. During the reaction process, the photocatalytic activity of CDs ensures photoactivation of benzylic position in benzylic hydrocarbons to form hydroperoxide intermediates; the surface sulfate groups subsequently catalyze the coupling of nucleophiles (**Figure 1-16**).

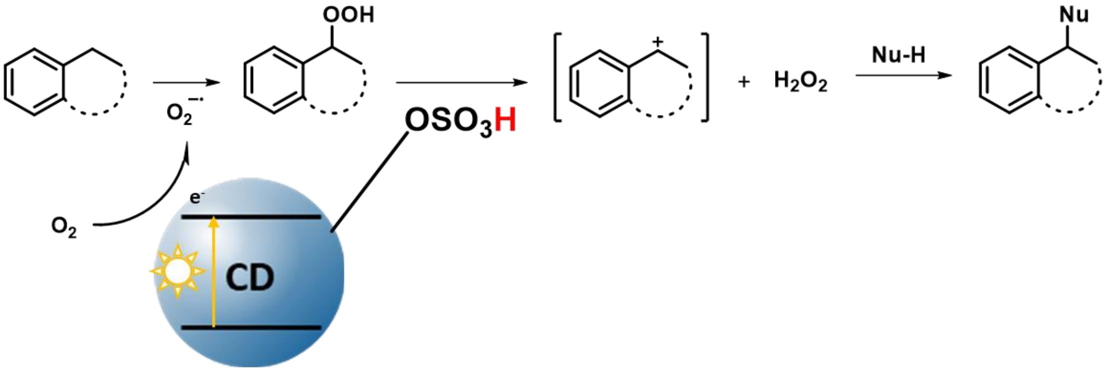

Figure 1-16. Proposed reaction mechanism for cross coupling reactions using sulfonated CDs as catalysts.

CD-based nanocomposites, in combination with other semiconductors or metallic and synthetic molecular catalysts, have been prepared to expand the applications of CDs in photocatalysis.[84-86] These nanocomposites have been developed to improve the electron-transfer efficiency, tune the light absorption ability to a wide range of wavelengths, and enhance the photocatalytic efficiency. Still, the short PL lifetime, comparable to most organic dyes, is a limitation to the implementation of CDs in more complex photocatalytic processes.[46, 87, 88]

1.2.3. Photocatalytic Ni-mediated cross-couplings

Cross coupling reactions are powerful tools to form numerous challenging carbon–carbon and carbon–heteroatom bonds, generally catalyzed by transition metals.[89, 90] In particular, palladium (Pd) complexes have been widely used in cross-couplings due to their high efficiency, high reactivity and controllable selectivity. The discovery of Pd-catalyzed Buchwald-Hartwig cross coupling reactions opened up new prospects to generate carbon–heteroatom bonds. Since its first discovery for amination reactions, its scope was expanded to alcohols and thiols to form C-O and C-S bonds, respectively.[91, 92]

In recent years, there has been significant interest in replacing the high-cost Pd catalysts with nickel (Ni) alternatives. Ni is attractive owing to its abundance and low cost compared to Pd.[93] However, to develop Ni-catalyzed cross coupling reactions, some challenges have to be overcome. The obtained Ni^{II} intermediates after oxidative addition of the electrophile (aryl halides) to the Ni^0 complexes and transmetalation of the nucleophile (amines, alcohols and thiols) are thermodynamically stable. High temperature, strong bases, or tailored ligands can facilitate effective reductive elimination permitting the formation of the desired product. [94-96] Among those strategies, the combination with photocatalysis has stood out as a very promising and mild option.

In 2014, the MacMillan group developed a dual catalytic approach merging visible-light photoredox and Ni catalysis (**Figure 1-17**).[97] In these seminal works, direct decarboxylative arylation of α-carboxyl sp^3-carbons with aryl halides was successfully achieved under visible-light irradiation using heteroleptic Ir(III) photocatalyst. Since then, photoredox mediated Ni-catalyzed cross-couplings have become powerful synthetic organic transformations, forging numerous carbon-heteroatoms and carbon-carbon bonds.[97, 98] Their attractive advantages are high chemoselectivity, excellent functional group tolerance, and mild reaction conditions. In the photoredox catalytic cycle, Ru and Ir polypyridyl complexes are the major players due to their long excited-state lifetimes.

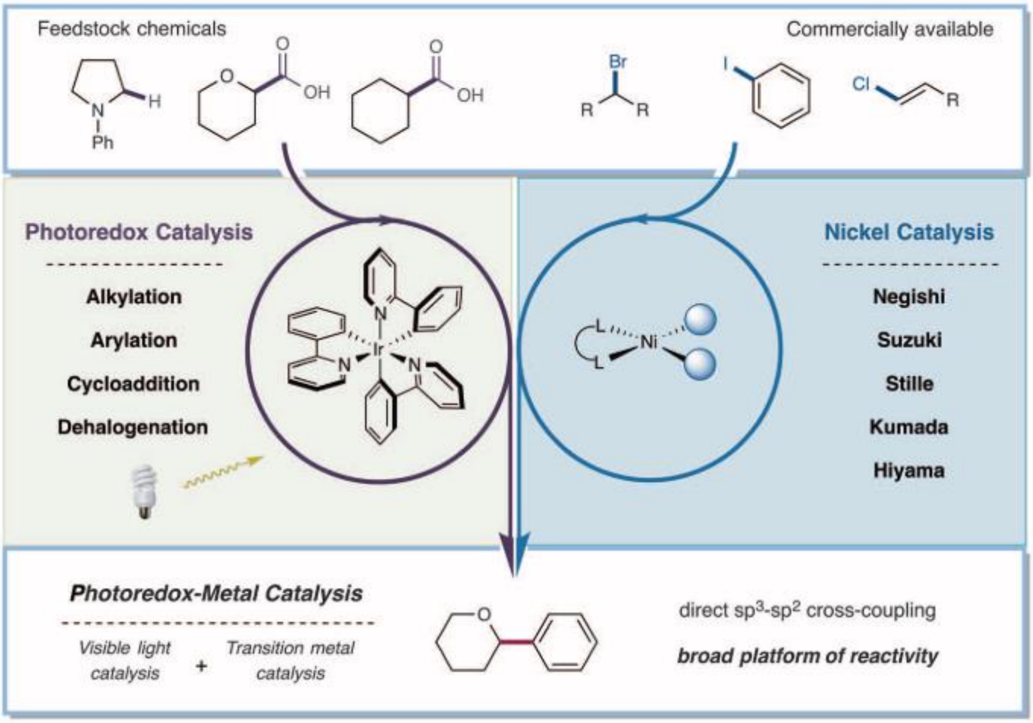

Figure 1-17. Schematic representation of a dual catalytic system. Adapted with permission from *Science* **2014**, 345, 437-440 Copyright (2014).

Later on, Pieber and co-workers introduced a metal-free heterogeneous semiconductor carbon nitrides, as alternative for the high-cost Ir(III) photocatalysts (**Figure 1-18**).[99] Esterification of carboxylic acids with aryl halides was efficiently achieved using the dual photoredox/Ni catalysis system under visible-light irradiation, affording the desired products with high yield and selectivity. The recyclable and inexpensive heterogeneous photocatalysts were easily separated and used in C-O cross-couplings multiple times, without significantly affecting the catalytic efficiency. In a follow up work by Antonietti and König, carbon nitrides were employed as photo- and chemically stable semiconductor photocatalysts exhibiting excellent catalytic activities in C-H functionalizations of arenes and heteroarenes.[100]

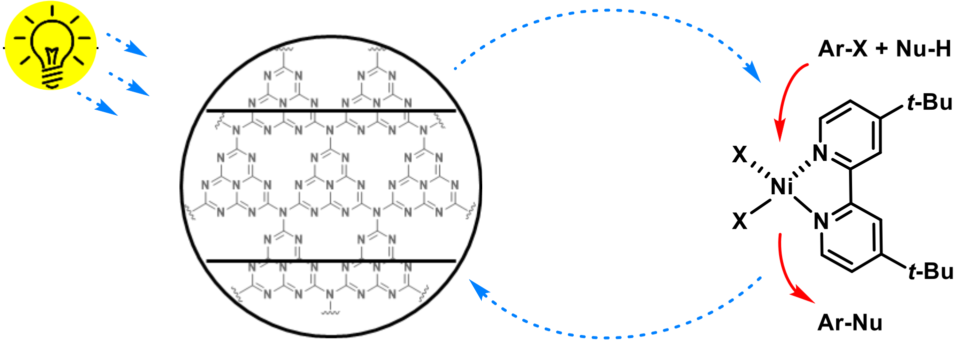

Figure 1-18. Schematic representation of semi-heterogeneous dual photoredox/Ni catalysis system.

Many more examples of the dual photoredox/Ni catalysis have been reported, permitting access to a wide variety of scaffolds. Among those, the C-S cross-coupling of various unprotected biological thiols with aryl halides was performed using a dual Ru/Ni catalytic system under visible-light irradiation.[101] Ir/Ni dual-catalyzed amination reactions with a wide scope of primary aryl amine and aryl halide coupling partners have been developed to forge C-N bonds.[102] The formation of C-C bond could also be effectively achieved under dual photoredox/Ni-catalyzed cross-coupling procedure using donor-acceptor fluorophores as metal-free photocatalysts.[103]

1.2.4. Photocatalytic isomerizations

Alkenes exist in numerous advanced functional materials, industrial dyes, and bioactive small drug molecules. Moreover, alkenes are versatile precursors in organic synthesis, allowing for many types of chemical transformations. The stereochemistry of alkenes (*E*/*Z* isomers) dramatically affects the physical, chemical, and biological properties of these compounds. Several methods to access thermodynamically stable *E*-alkenes have been reported, while the synthesis of the thermodynamically unfavoured *Z*-alkenes is still a challenge.

Diverse approaches for the stereoselective synthesis of *Z*-alkenes have been developed, including the Wittig reactions and its modification, cross coupling reactions, *Z*-selective partial hydrogenation of alkynes, and *Z*-selective metathesis reactions.[104, 105] However, these strategies typically depend on kinetic control of the reaction and need severe reaction conditions such as very low temperature (-78 ^oC), an expensive transition-metal catalyst (Pd) and a strong base (*n*-BuLi).[106]

A green, mild, and highly selective route to access *Z*-alkenes is visible-light photocatalytic *E*-to-*Z* isomerization *via* energy transfer (**Figure 1-19A**). The reaction is efficient, easy to perform, and does not require stringent reaction conditions. Photocatalytic energy transfer can overcome the normal thermodynamic constraints and favor the higher in energy *Z*-isomers efficiently as a result. Additionally, visible light is a milder and safer external light source for the isomerization of double bonds when compared to UV light with higher energy, which may decompose the molecules and result in numerous undesired side reactions.

This approach relies on photocatalysts with a suitably high triplet energy. These are generally transition-metal complexes, such as Ir-based polypyridyl complex ($Ir(ppy)_3$ and $[Ir(ppy)_2(bpy)]PF_6$). The triplet energy transfer pathway in *E*-to-*Z* isomerizations of alkenes is described in **Figure 1-19B**.[105, 107] The photocatalyst is excited to its triplet excited state, upon absorption of visible light followed by ISC (**Figure 1-20**).[108, 109] Subsequently, energy transfer from the catalyst to the *E*-alkenes occurs, to generate a biradical intermediates (triplet state). This intermediate lacks the π-bond, thus it is free to rotate and may relax back to either *E*- or *Z*-alkenes. The inaccessible triplet state of *Z*-alkenes owing to nonbonding interactions and reduced conjugation and the higher sensitization efficiency of *E*-alkenes by photocatalysts, leads to the accumulation of the *Z*-alkenes over time. Weaver and co-workers reported such photocatalytic approach for the *E*-to-*Z* isomerization of styrenyl substrates using the commercially available photocatalyst *fac*-$[Ir(ppy)_3]$.[104] Broad reaction scope, high yield, and selectivity were obtained under blue-light irradiation.

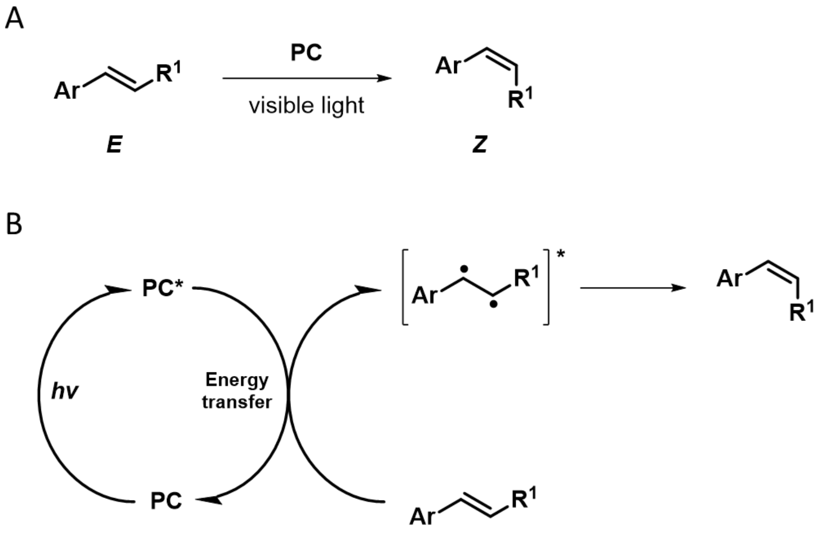

Figure 1-19. Visible-light photocatalytic *E*-to-*Z* isomerization (A) and the proposed mechanism (B).

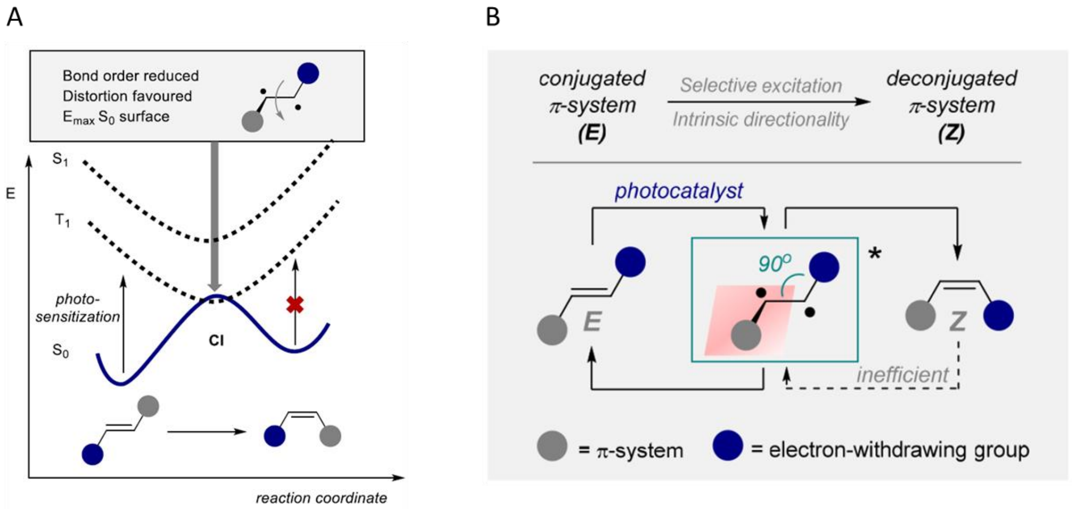

Figure 1-20. Potential energy surfaces for the ground state, first triplet state and first singlet state of a generic alkene (A). Adapted with permission from *Chem. Rev.* **2022**, 122, 2650-2694 Copyright (2022). Conceptual framework for photocatalytic isomerization of polarized alkenes (B). Adapted with permission from *J. Org. Chem.* **2017**, 82, 9955-9977 Copyright (2017).

1.3. Aims of this thesis

The general aim of this thesis was to develop low-cost and efficient photocatalytic systems for different types of organic transformations. CDs are promising metal-free photocatalysts owing to their excellent light absorption, electron-transfer ability, and photostability. However, due to their short PL lifetimes, examples of CDs as photocatalysts for selective organic synthesis are scarce.

The aim of my first project was to overcome the problem of short-lived excited states of CDs by immobilizing CDs on heterogeneous semiconductors, such as TiO_2, to generate a composite material that absorbs visible-light and generates a long-lived charge-separated species. To this end:

1. CDs need to be synthesized and characterized
2. CD/TiO_2 nanocomposites need to be prepared and characterized
3. The applicability of CD/TiO_2 as photocatalyst for metallaphotocatalytic cross-couplings has to be tested
4. The photostability and recyclability studies of CD/TiO_2 nanocomposites have to be evaluated
5. A library of CD photosensitizers has to be prepared from different carbon sources and doping agents

The aim of my second project was to explore whether CDs can be designed to generate colloidal nano-photocatalysts for Ni-mediated cross-couplings. Compared to previous CD/TiO_2 nanocomposite, no requirement for immobilization on TiO_2 will expand the portfolio of CDs to analogues with different surface functionalities and photophysical properties (i.e. not strictly matching the TiO_2 energy levels). Similarly, more efficient Ni ligands could be implemented. To this end:

1. New CDs have to be designed and synthesized
2. The applicability of CD as colloidal photocatalysts for metallaphotocatalytic cross-couplings has to be tested
3. Mechanistic studies have to be performed
4. The new protocol has to be compared to existing literature procedures

The aim of my third project was to explore whether CDs can be applied as photocatalysts in the *E*-to-*Z* isomerization reactions under visible light irradiation. Compared to photocatalytic cross-couplings, the *E*-to-*Z* isomerization is based on an energy-transfer mechanism. To this end:

1. The applicability of CD as visible-light-absorbing photocatalyst for *E*-to-*Z* isomerization has to be tested
2. Different alkenes have to be tested and the reaction conditions have to be optimized
3. A collection of CDs has to be synthesized and their applicability has to be tested

2. Carbon dot/TiO_2 nanocomposites as photocatalysts for metallaphotocatalytic carbon–heteroatom cross-couplings

This chapter has been modified in part from the following article:

Z. Zhao, S. Reischauer, B. Pieber, M. Delbianco. *Green Chem.*, **2021**, 23, 4524-4530.

2.1. Introduction

CDs are quasi-spherical fluorescent carbon-based materials with a size of typically less than 10 nm,[4, 6, 7, 110, 111] easily prepared through top-down or bottom-up approaches from a variety of carbon sources.[5, 41] Their chemical inertness and biocompatibility has prompted applications in sensing, bioimaging, and nanomedicine. [41, 112-115] Moreover, the surface functional groups enabled applications as sustainable nano-organocatalysts for synthetic transformations.

CDs are also promising metal-free photocatalysts for pollutant degradation, H_2 evolution and CO_2 conversion, owing to their photostability, light-harvesting ability and electron-transfer efficiency.[80, 116-118] The high solubility of CDs in water makes them a suitable alternative to hydrophobic organic materials, such as carbon nitride and graphite.[81] This feature permitted to use CDs in combination with Ni catalysis for H_2 evolution in aqueous solution.[119, 120]

However, due to their short PL lifetimes,[121, 122] examples of CDs as photocatalysts for selective organic synthesis are scarce[82, 123] when compared to common photocatalysts, such as Ru and Ir polypyridyl complexes that have long-lived triplet excited states.[82, 123] To overcome the problems associated with the short-lived excited states, CDs can be immobilized on heterogeneous semiconductors such as TiO_2 to generate a composite material that absorbs visible-light and generates a long-lived charge-separated species.[124-126] Still, the applications of such composites remained limited to water splitting, CO_2 reduction, and pollutant degradation (**Figure 2-1**).[85, 127, 128]

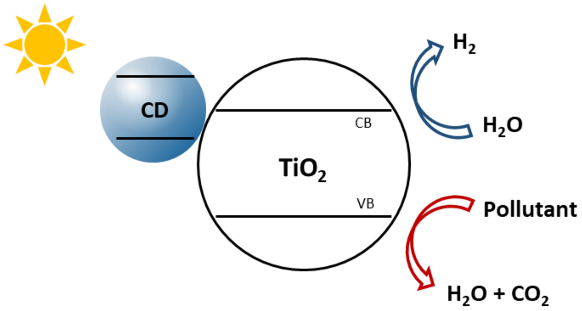

Figure 2-1. Schematic representation of CD/TiO_2 nanocomposites as photocatalysts for water splitting and pollutant degradation.

The combination of a photo- and a Ni catalyst (termed metallaphotocatalysis) triggers many important carbon−heteroatom and carbon−carbon cross-couplings using light as sustainable energy source.[129] Suitable photocatalysts for these reactions range from Ru and Ir polypyridyl complexes and organic dyes to heterogeneous semiconductors.[129] Moreover, Ni complexes and photocatalysts were combined in bifunctional heterogeneous materials, such as metal-organic frameworks,[130, 131] or organic polymers.[132]

TiO_2 can be sensitized with organic dyes to serve as a visible light photocatalyst for selective organic transformations.[71, 133] Recently, it was shown that the immobilization of a Ni(II) catalyst and an organic dye on the surface of metal oxides provides a heterogeneous catalytic system for metallaphotocatalytic carbon–carbon and carbon–heteroatom cross-couplings that overcomes the problems associated with short-lived singlet excited states of organic dyes (**Figure 2-2**).[70] Following this seminal work, I showed that CDs are a valuable alternative to organic dyes in such catalytic systems due to i) their low economic cost and toxicity, ii) their facile immobilization on semiconductors, iii) their broad absorption across the visible-light spectrum, and iv) their superior photo- and chemical stability (**Figure 2-3**).[119, 126]

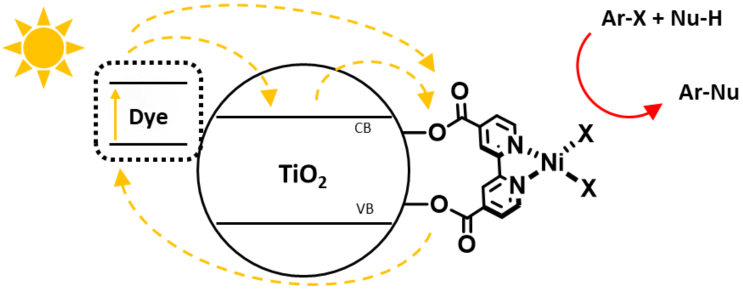

Figure 2-2. Schematic representation of dye/TiO_2 nanocomposites as photocatalysts for metallaphotocatalytic carbon–heteroatom cross-couplings.

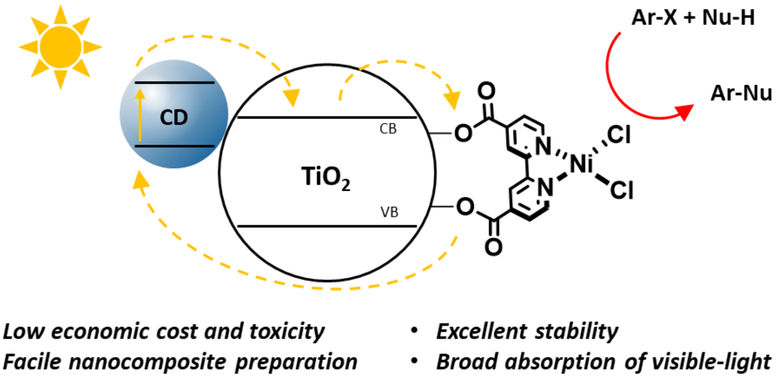

Figure 2-3. Schematic representation of CD/TiO_2 nanocomposites as photocatalysts for metallaphotocatalytic carbon–heteroatom cross-couplings.

2.2. Results and discussion

2.2.1. Preparation of CD1/TiO_2 nanocomposite

Carbohydrates are an attractive carbon source for CD synthesis owing to their low cost, high solubility in water, easy carbonization at relatively low temperatures, and presence of heteroatoms.[17] I therefore began my investigations by preparing **CD1** from glucosamine hydrochloride (GlcN·HCl, **2-1**), following a microwave-based carbonization method (**Figure 2-4A**).[15] Doping with β-alanine (β-Ala, **2-2**) ensured a high amount of surface carboxylic acid groups (**Figure 6-7** and **Figure 6-8**).[15] The zeta potential in the range of -11.1 to +18.7 mV suggested the presence of several functional groups (carboxylic acids, alcohols, and amino groups) on the surface of **CD1** (**Figure 6-6**).[15, 134]

TEM confirmed a spherical shape of the CD nanoparticles with a diameter of about 4 nm (**Figure 2-4B** and **Figure 6-4**). XRD profile showed a single broad peak ($2\theta = 23^o$), indicating the amorphous structure of **CD1** (**Figure 6-9**). A colloidal solution of **CD1** in H_2O emitted blue light under UV light irradiation (λ_{ex} = 366 nm) (**Figure 6-12**). Spectroscopic analysis showed an absorption peak at 276 nm (**Figure 2-4B** and **Figure 6-10**) and a PL emission maximum at ~460 nm (λ_{ex} = 360 nm, **Figure 2-4B** and **Figure 6-11**). A PL lifetime of 4.45 ns was measured by fitting the PL decay curve of **CD1** (**Figure 6-13**).

CD1 was immobilized on the surface of TiO_2 P25 by stirring a mixture of the two components in water (mass ratio 1:1; **Figure 2-4A**). The resulting brown powder (**CD1**/TiO_2) was analysed by scanning electron microscopy (SEM) and energy dispersive X-ray spectroscopy (EDX) (**Figure 6-21**). The morphology and size of the nanocomposites remained similar to unfunctionalized TiO_2. The increased carbon content confirmed the immobilization of **CD1** (**Figure 2-4C** and **Figure 6-21**). UV-Vis spectroscopy of the resulting material confirmed its extended absorption in the visible-light region (**Figure 2-4C**).

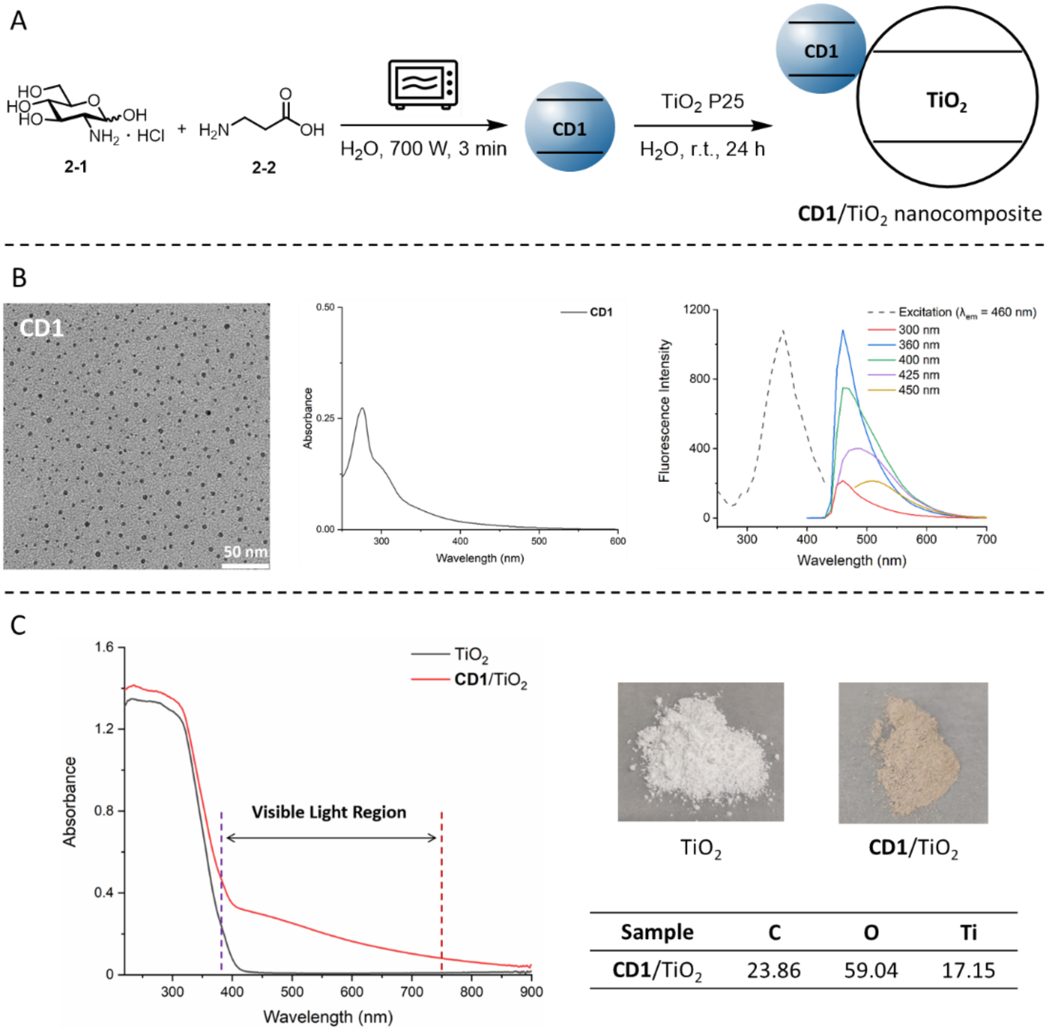

Sample	C	O	Ti
CD1/TiO$_2$	23.86	59.04	17.15

Figure 2-4. Schematic representation of the preparation of **CD1** and **CD1**/TiO$_2$ nanocomposite (A). Characterization of **CD1** (B). Characterization of **CD1**/TiO$_2$ nanocomposite (C).

2.2.2. Applicability of CD1/TiO$_2$ as photocatalyst

The applicability of **CD1**/TiO$_2$ as photocatalyst for metallaphotocatalytic cross-couplings was tested for the C–O arylation of *N*-(*tert*-butoxycarbonyl)-L-proline (Boc-Pro-OH, **2-3**) with methyl 4-iodobenzoate (**2-4**) using visible-light (**Table 2-1**).[70, 99] A Ni(II) complex that contains carboxylic acid groups was employed to bind to the nanocomposite. The selective formation of 83% of the desired ester product (**2-5**) was observed when the reaction was irradiated with blue (440 nm) light for 24 h (**Table 2-1**, entry 1). Control experiments confirmed the necessity of TiO$_2$, **CD1**, and the carboxylic acid functionalized ligand 2,2'-bipyridine-4,4'-dicarboxylic acid (dcbpy) (**Table 2-1**, entries 2-5).

A previous report that used molecular dyes with short excited state lifetimes instead of **CD1** showed that insulating materials, such as SiO_2, can be used instead of TiO_2 for the same reaction.[70] In this case, it was proposed that the close proximity between dye molecules and the nickel complex is responsible for productive catalysis (**Figure 2-5**). Using a **CD1**/SiO_2 nanocomposite, I only observed a modest yield of 7% of the desired product (**Table 2-1**, entry 6), suggesting that an electronic communication between the excited CD and the immobilized Ni complex "through" a semiconducting material is crucial.

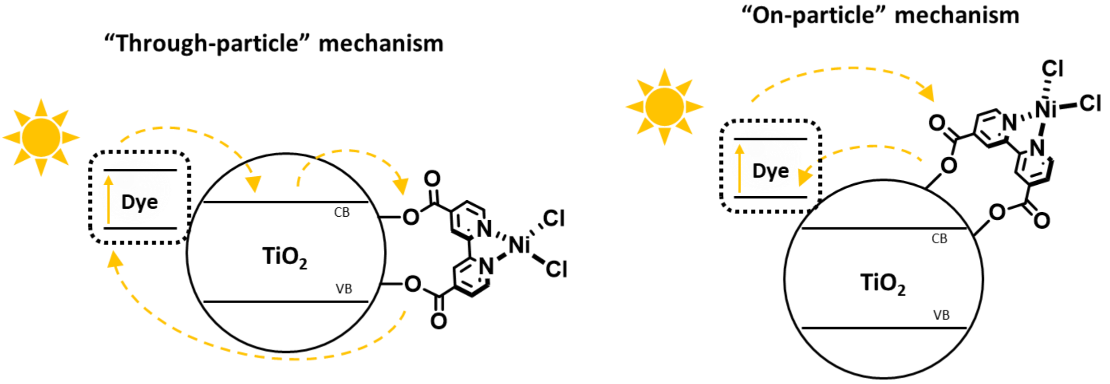

Figure 2-5. Two possible mechanisms of electronic communication between the dye molecule and the Ni complex.

Using **CD1**/TiO_2 an almost quantitative formation of **2-5** required 40 h (**Table 2-1**, entry 7). The broad absorption of the nanocomposite also enabled cross-coupling at longer wavelengths (525 nm), albeit with longer reaction times (**Table 2-1**, entry 8). It is worth noting that **CD1**/TiO_2 is also highly active using very low loadings (**Table 6-8**), and that the nanocomposite is bench-stable and does not lose its catalytic activity upon storage at room temperature for 26 weeks (**Table 6-7**).

Table 2-1. Optimized conditions and control experiments for the cross-coupling of Boc-Pro-OH with methyl 4-iodobenzoate using **CD1**/TiO_2 nanocomposite.

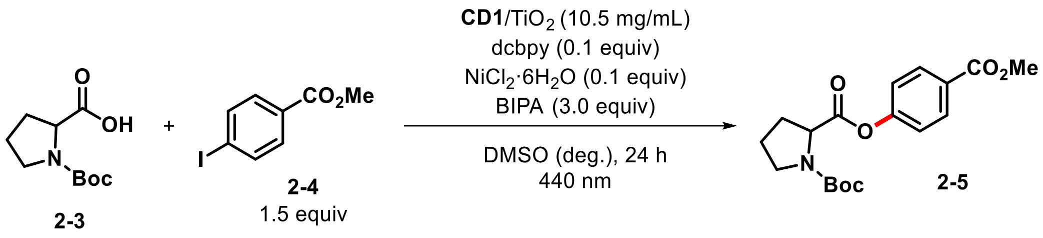

Entry	Conditions	2-5 [%]
1	As shown	83
2	No TiO_2	n.d.
3	No TiO_2, dtbbpy instead of dcbpy	n.d.
4	No **CD1**	15
5	No dcbpy	4
6	SiO_2 instead of TiO_2	7
7	40 h instead of 24 h	96 (84)[a]
8	525 nm[b], 96 h	63

Reaction conditions: methyl 4-iodobenzoate (285.4 µmol), Boc-Pro-OH (190.3 µmol), $NiCl_2 \cdot 6H_2O$ (19.0 µmol) and dcbpy (19.0 µmol) in DMSO (anhydrous, 3 mL), BIPA (570.8 µmol), **CD1**/TiO_2 (31.6 mg), 440 nm LED lamp (50% power), 24 h. NMR yields were determined by ^1H-NMR using 1,3,5-trimethoxybenzene as internal standard. [a] Isolated yield in parentheses. [b] 525 nm LED lamp (200% power). $NiCl_2 \cdot 6H_2O$ = nickel(II) chloride hexahydrate. BIPA = *N*-*tert*-butylisopropylamine. SiO_2 = silicon dioxide. n.d. = not detected. deg. = degassed.

To my delight, **CD1**/TiO_2 served as an active photocatalyst for a range of metallaphotocatalytic carbon−heteroatom cross-couplings.[129] Moderate to excellent yields were obtained for the coupling of aryl halides with an alcohol, a thiol, a sodium sulfonate, and a sulfonamide using slightly adapted conditions (**Figure 2-6**).

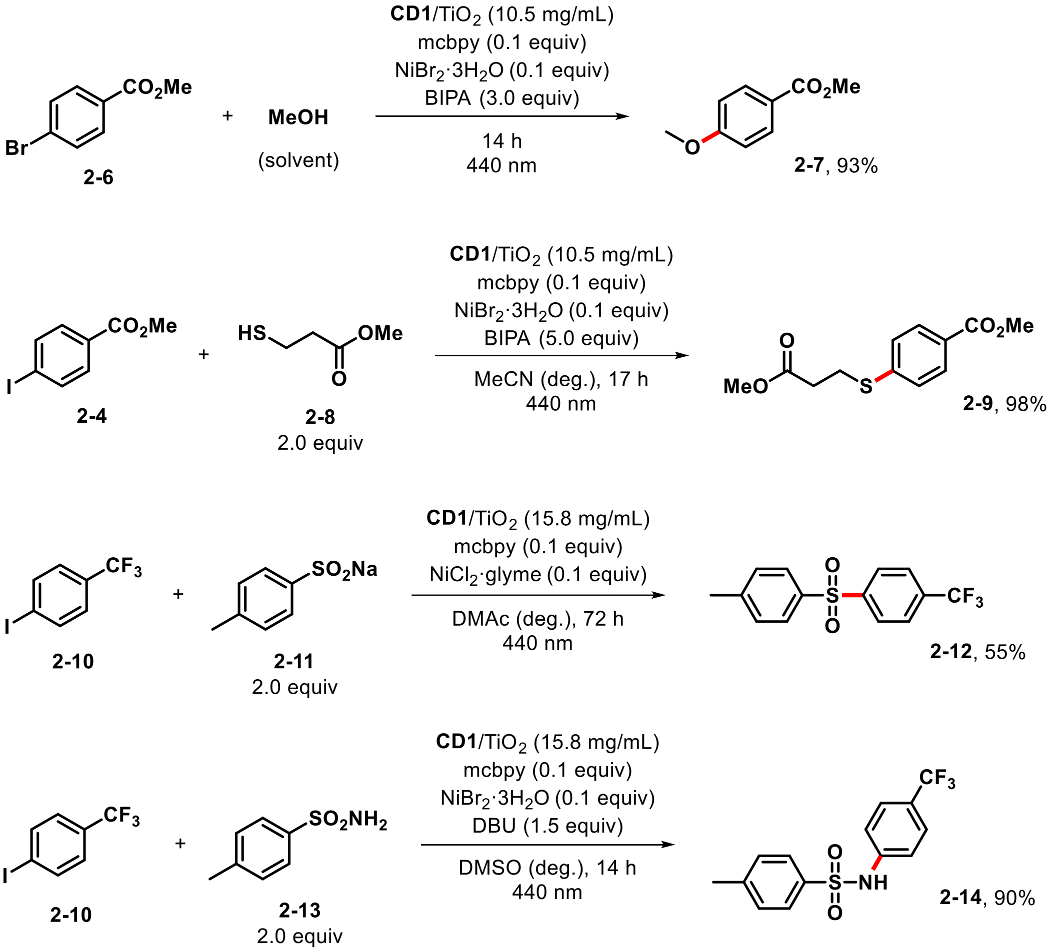

Figure 2-6. Application of **CD1**/TiO$_2$ as photocatalyst for C–O, C–S, and C–N cross-couplings.

2.2.3. Photostability and recyclability studies

Next, I sought to compare the photostability of the **CD1**/TiO$_2$ nanocomposite with TiO$_2$ that was functionalized with the organic dye fluorescein (Fluo/TiO$_2$) (**Figure 2-7**). The functionalized semiconductors were pre-irradiated with blue light for a defined amount of time and subsequently used as photocatalysts in the metallaphotocatalytic C–O arylation of Boc-Pro-OH (**2-3**). The photocatalytic performance of **CD1**/TiO$_2$ remained unchanged even after 72 h exposure to light. In contrast, Fluo/TiO$_2$ suffered from significantly lower yields after 6 h irradiation. The yield obtained with the Fluo/TiO$_2$ photocatalyst did not decrease linearly with the irradiation time, but seemed to reach a plateau after 6-12 h pre-irradiation. I assume that the prolonged irradiation could promote the formation of fluorescein degradation products that still serve as a sensitizer.[135, 136]

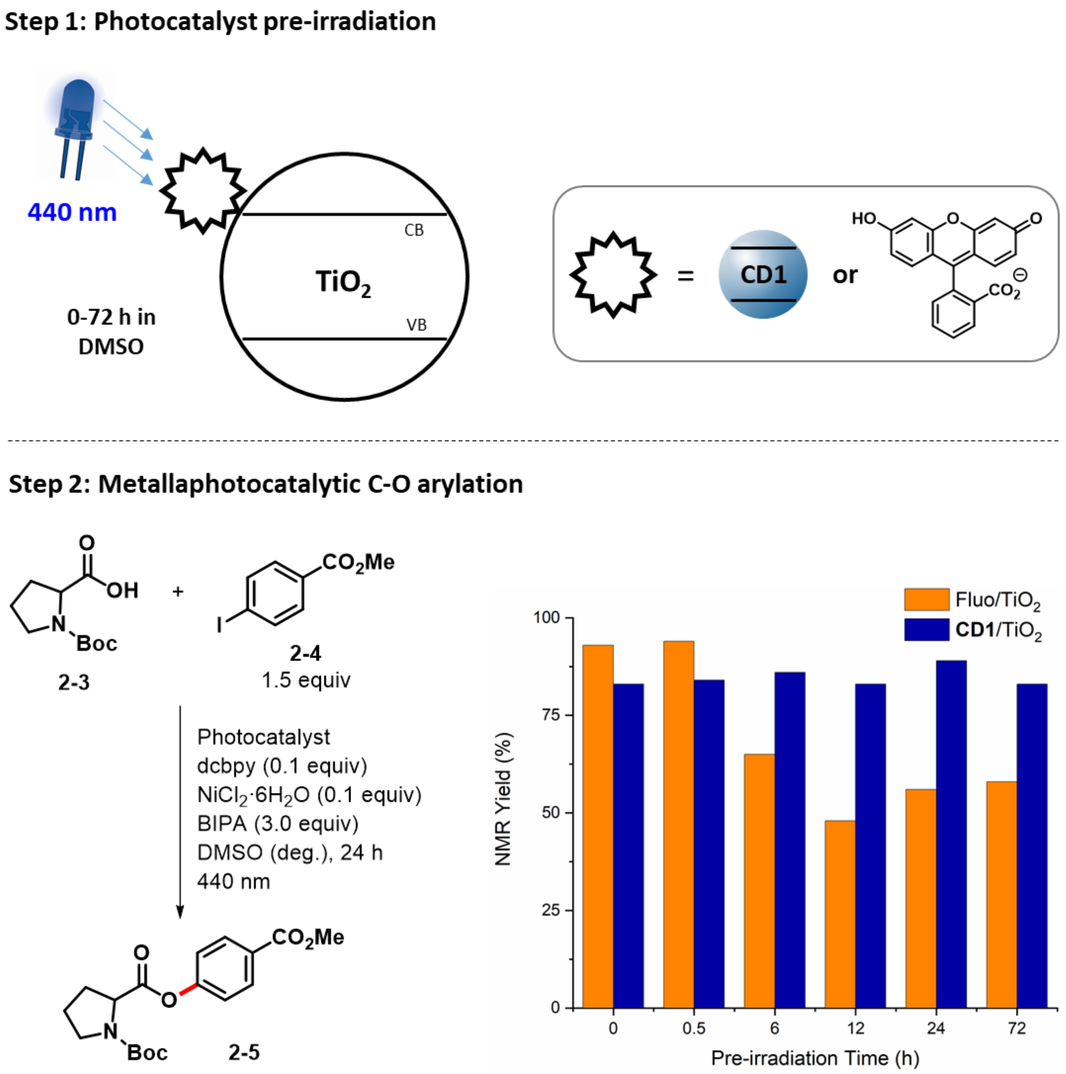

Figure 2-7. Photobleaching experiments to compare the photostability of **CD1**/TiO_2 and Fluo/TiO_2. The two photocatalysts were pre-irradiated with blue light and then used in the metallaphotocatalytic C–O arylation. Yields were determined *via* ^{1}H-NMR using 1,3,5-trimethoxybenzene as internal standard. Fluo = fluorescein.

The nanocomposite was characterized before and after the catalytic reaction (**Table 6-5**). Inductively coupled plasma - optical emission spectrometry (ICP-OES) revealed the presence of Ni in the **CD1**/TiO_2 nanocomposite after the C–O cross-coupling (**Table 2-1**, entry 7). This indicated that the Ni complex remained immobilized on **CD1**/TiO_2, prompting us to explore the recyclability of the bifunctional heterogeneous catalyst (**Figure 2-8**). Recyclability experiments were performed using the reaction conditions reported in **Table 2-1** (Entry 1). After each cycle, the heterogeneous material was separated, washed and reused in the next C–O cross-coupling. Excellent catalytic performances were observed even after four recycling cycles. Importantly, the addition of Ni salt or Ni complex after each cross-coupling cycle, which was previously required in a related approach,[70] was not only unnecessary, but significantly decreased the catalytic activity. This may be ascribed to Ni accumulation and formation of Ni-black upon irradiation by high-energy light (**Figure 6-32**).[137]

Overall, these results underscore the potential of **CD1**/TiO_2 nanocomposites as a robust, cheap, and green photocatalyst for applications in organic chemistry.

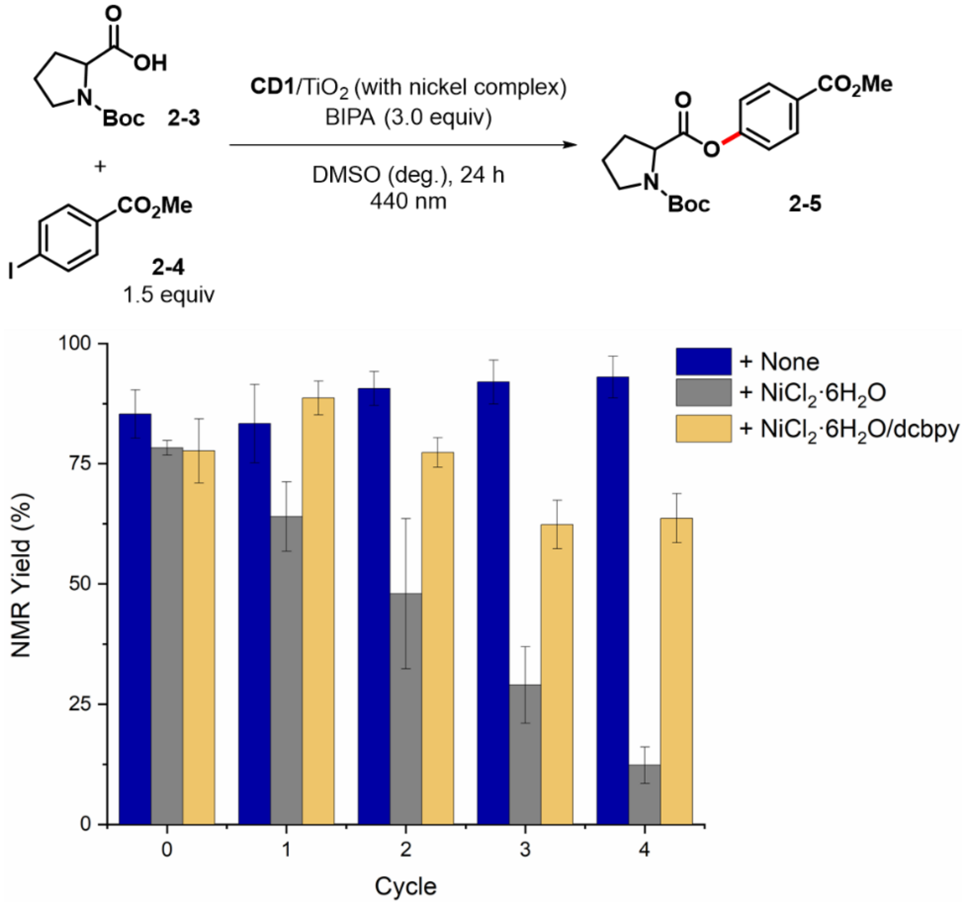

Figure 2-8. Reusability of **CD1**/TiO_2 nanocomposite decorated with a Ni complex in the metallaphotocatalytic C–O arylation.

2.2.4. Screening of different CD photosensitizers

Having demonstrated the potential of **CD1** as photosensitizer for dual photoredox/Ni catalysis, I assessed the effect of different carbon sources and doping agents on the photocatalytic reaction (**Figure 2-9**). A first set of CDs was synthesized maintaining GlcN·HCl (**2-1**) as the carbon source and screening different doping agents. 1,3-Diaminobenzene (**2-15**), l-cysteine (l-Cys, **2-16**), PEG (average M_n 400, **2-17**), and glycine (Gly, **2-18**) were tested. Each compound was selected to introduce respectively aromatic groups,[138] sulphur atoms, polymers to enhance surface passivation,[35] or aminoacid analogues of β-Ala (**2-2**). A second set of CDs was based on β-Ala (**2-2**) as doping agent and different carbon sources. Three monosaccharides (glucose (Glc, **1-1**), *N*-acetyl-glucosamine (GlcNAc, **2-19**), galactose (Gal, **2-20**)), a disaccharide (D-lactose (Lac, **2-21**)) and a polysaccharide (pullulan, **2-22**) were tested to explore the influence of chain length and sugar structure on the photocatalytic performance. All CD precursors resulted in spherical nanoparticles with diameters smaller than 10 nm (**Figure 6-4** and **Figure 6-17**). Most CDs showed similar photophysical properties, with the exception of **CD2** that emitted bright green light under UV light irradiation (λ_{ex} = 366 nm) (**Figure 6-11**, **Figure 6-12**, **Figure 6-18** and **Figure 6-19**) and had an absorption maximum at 363 nm (**Figure 6-10** and **Figure 6-20**). All CDs were immobilized on TiO_2 P25 to prepare nine CD/TiO_2 nanocomposites able to absorb light in the visible region (**Figure 2-10** and **Figure 6-24**). While most UV-Vis spectra share a similar profile, **CD2**/TiO_2 nanocomposites exhibit a strong absorption band with a maximum at 466 nm. The photocatalytic performances of all nanocomposites were compared (**Figure 2-11**). Despite the broad and intense absorption in the visible range, **CD2**/TiO_2 resulted in low yields, whereas all other nanocomposites showed good to excellent results. For a fair comparison it should be noted that, even though all nanocomposites were prepared starting with an initial 1:1 mass ratio of CD:TiO_2, differences in immobilization might play a role in the photocatalytic results.

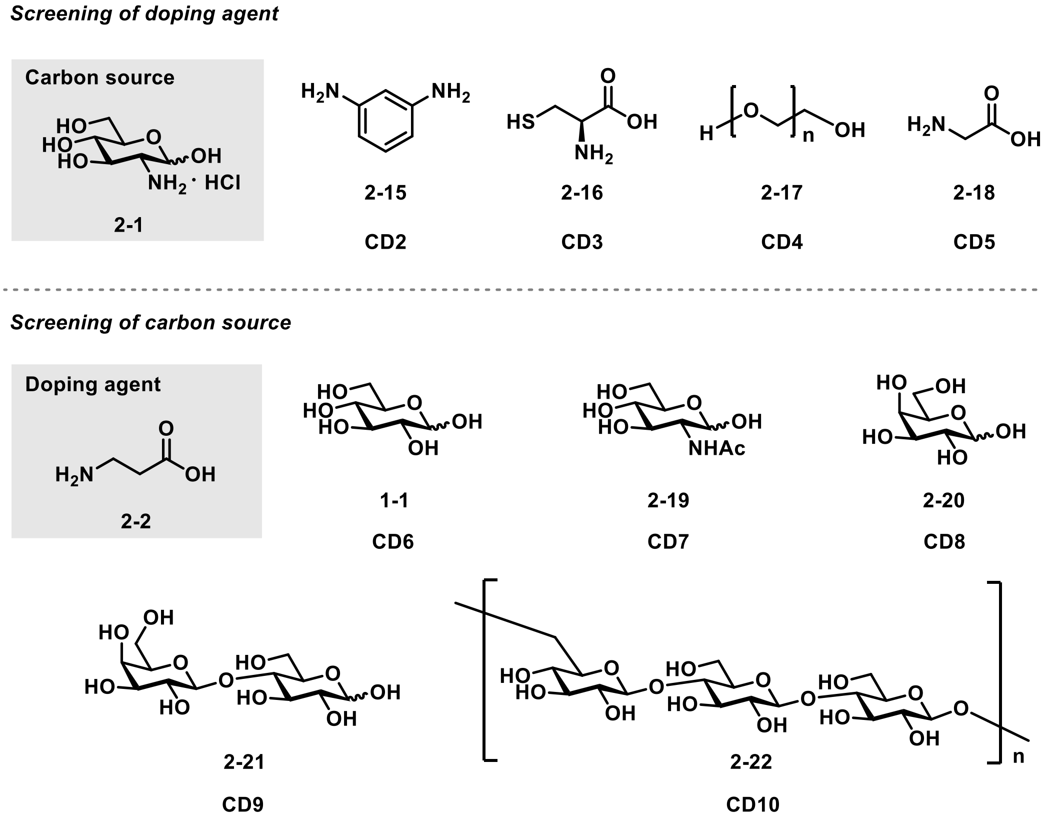

Figure 2-9. Chemical structures of carbon sources and doping agents used for CD synthesis.

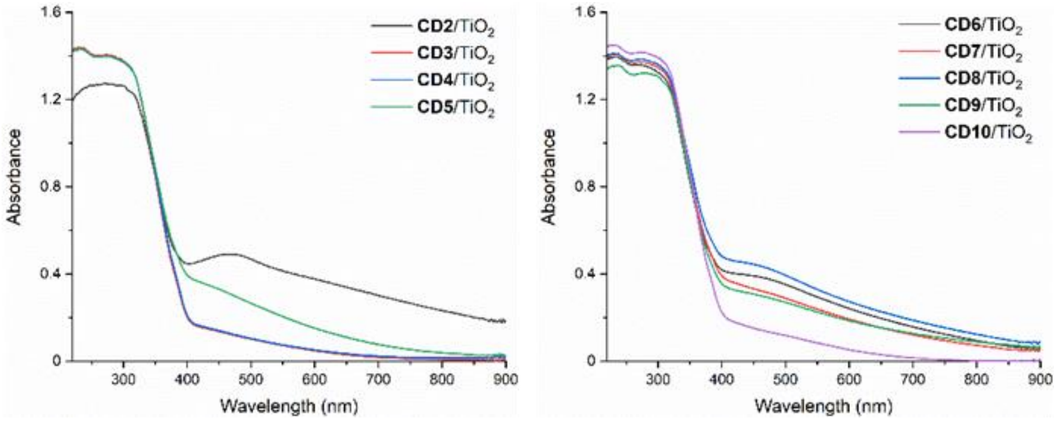

Figure 2-10. UV-Vis absorption spectra (solid state) of CD/TiO_2 nanocomposites.

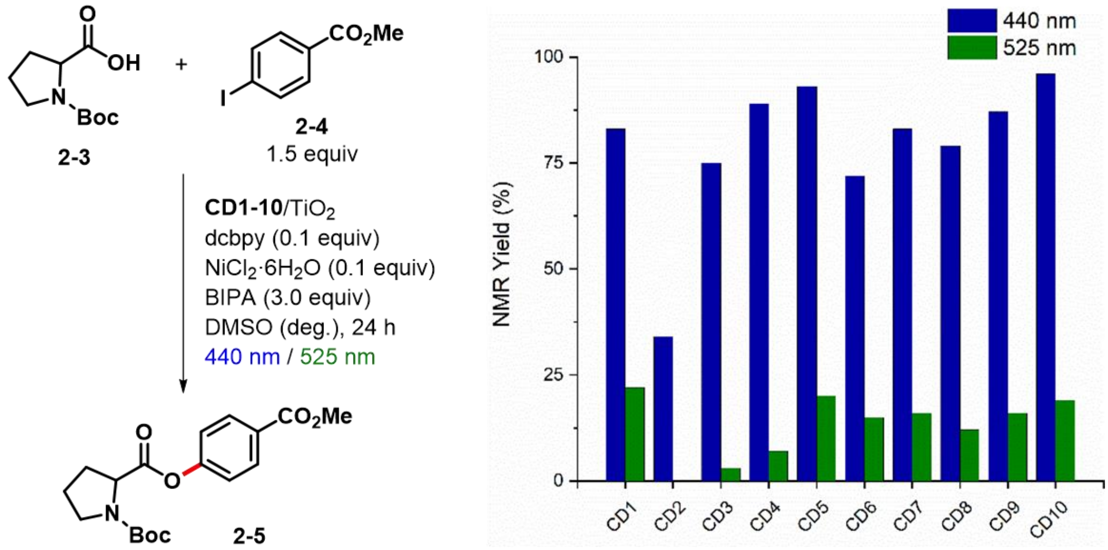

Figure 2-11. Evaluation of different CD/TiO_2 nanocomposites as photocatalyst for the metallaphotocatalytic C–O arylation of Boc-Pro-OH with methyl 4-iodobenzoate.

These results show that the system is highly flexible and that CD photosensitizers can be prepared from several starting materials, without affecting the catalytic performances. For example, excellent results were obtained for **CD9** and **CD10** prepared using lactose (**2-21**) and pullulan (**2-22**) as carbon source, respectively. These materials are highly abundant and cheap (lactose (**2-21**) is a waste product of the dairy industry that is produced at >6 million ton scale every year) suggesting the possibility of turning naturally sourced polysaccharides from waste materials into valuable catalysts. Fine-tuning of the elemental composition and its effect on the photocatalytic reaction will be explored in follow up studies.

2.3. Conclusion

In summary, I have prepared nanocomposites by immobilizing carbohydrate-based CDs on TiO_2, offering a cheap and robust alternative to organic dyes. This approach can overcome the issues associated with the short excited state lifetime of CDs. I demonstrated that CDs are valuable photocatalysts for metallaphotocatalytic carbon–heteroatom cross-couplings. High conversions were observed under irradiation by either blue or green light. Photobleaching experiments confirmed that the catalytic performances of the CD/TiO_2 nanocomposites are not affected by long-time light irradiation prior to their use in catalytic reactions. Recycling experiments showed the excellent reusability of this catalytic system in C–O cross-coupling reactions. CDs could be prepared from different carbohydrate sources and doping agents, without significant difference in the catalytic performance. This is particularly important in the perspective of using polysaccharide waste materials to generate valuable photocatalysts.

3. Modulating the surface and photophysical properties of carbon dots to access colloidal photocatalysts for cross-couplings

This chapter has been modified in part from the following article:

Z. Zhao, B. Pieber, M. Delbianco. *ACS Catal.*, **2022**, 12, 13831-13837.

3.1. Introduction

In Chapter 2, I overcame the short PL lifetime of CD by immobilizing CDs on TiO_2 to create a heterogeneous system that absorbs visible-light and generates long-lived charge-separated species.[139] By combining these recyclable and photostable composite materials with an acid-functionalized Ni bipyridine complex, I could perform several visible-light mediated carbon-heteroatom cross-couplings (**Figure 3-1B**). Efficient electronic communication between the Ni catalyst and our CD/TiO_2 nanocomposite required: i) pre-immobilization of the CDs on TiO_2 aided by carboxylic acid groups on the CD surface and, ii) Ni ligands containing carboxylic acid functionalities that, in return, decreased the electron density on the catalytic metal center, which limits its applicability to certain cross-couplings.[140, 141]

The possibility of using CDs as quasi-homogenous colloidal nanocatalysts is attractive,[46, 142] allowing for a much more flexible catalytic system. No requirement for immobilization on TiO_2 would expand the portfolio of CDs to analogues with different surface functionalities and photophysical properties (i.e. not strictly matching the TiO_2 energy levels).[57, 123, 143] Similarly, more efficient Ni complexes could be implemented. In this scenario, the CDs act as visible-light-absorbing nano-catalysts, offering a higher surface area for catalysis and better light penetration.[46, 142]

Here, I demonstrate that CDs can be designed to generate colloidal nano-photocatalysts for visible-light-mediated Ni-catalyzed cross-couplings. By tuning the surface and PL properties of CDs, I have discovered that a CD decorated with amino-groups photocatalyzes a broad range of carbon–heteroatom cross-couplings between aryl halides and nucleophiles in the presence of a molecular Ni complex (**Figure 3-1C**). Moreover, this CD permitted the development of a base-free protocol that allowed expanding the scope of C–S cross-couplings to aryl bromides. Mechanistic studies shined light on the process of sensitization and identified that pyridinium iodide (pyHI), which was previously used as additive in metallaphotocatalyzed cross-couplings,[144] also can act as photocatalyst in such transformations.

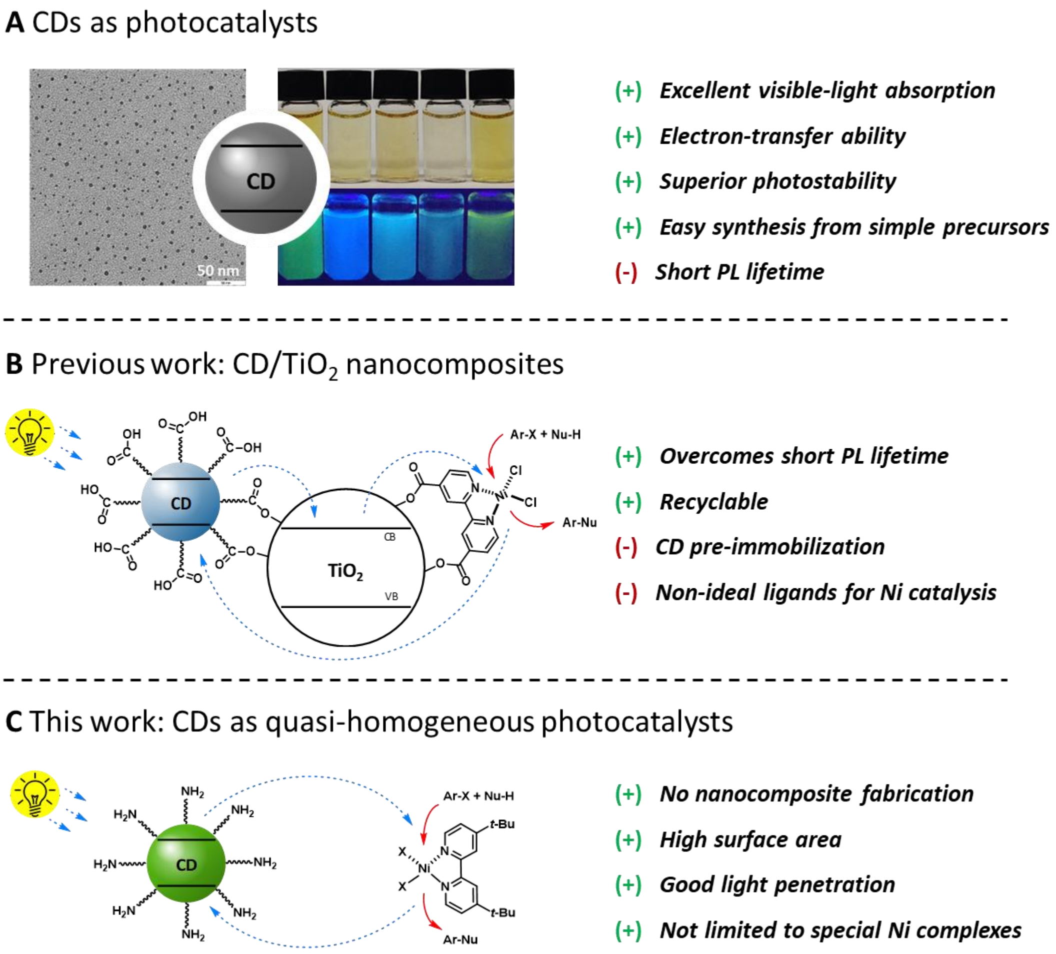

Figure 3-1. Schematic representation of CDs as metal-free photocatalysts (A). CD/TiO_2 nanocomposites as photocatalysts for dual Ni-mediated cross-couplings (B). Colloidal CDs as photocatalysts for dual Ni-mediated cross-couplings (C, this work).

3.2. Results and discussion

3.2.1. Applicability of CDs as photocatalysts

Two CDs (**CD1** and **CD2**) were prepared from GlcN·HCl (**2-1**) using β-Ala (**2-2**) and 1,3-diaminobenzene (**2-15**) as doping agents, following established procedures (**Figure 3-2**).[15, 138] Both dots present a spherical shape and an amorphous core (**Figure 6-4** and **Figure 6-9**). Due to the different dopants, the surface of **CD1** mainly consisted of carboxylic acid groups,[15] whereas **CD2** was predominately stabilized by amino functionalities and deoxyfructosazine derivatives,[138] as indicated by NMR analysis (**Figure 6-7**) and the zeta potentials (**Figure 6-6**). Spectroscopic analysis of the colloidal carbon nanodots revealed that the aromatic doping agent lead to significantly improved absorption in the visible part of the electromagnetic spectrum. Excitation of **CD1** resulted in a blue luminescence, whereas **CD2** emitted green light.

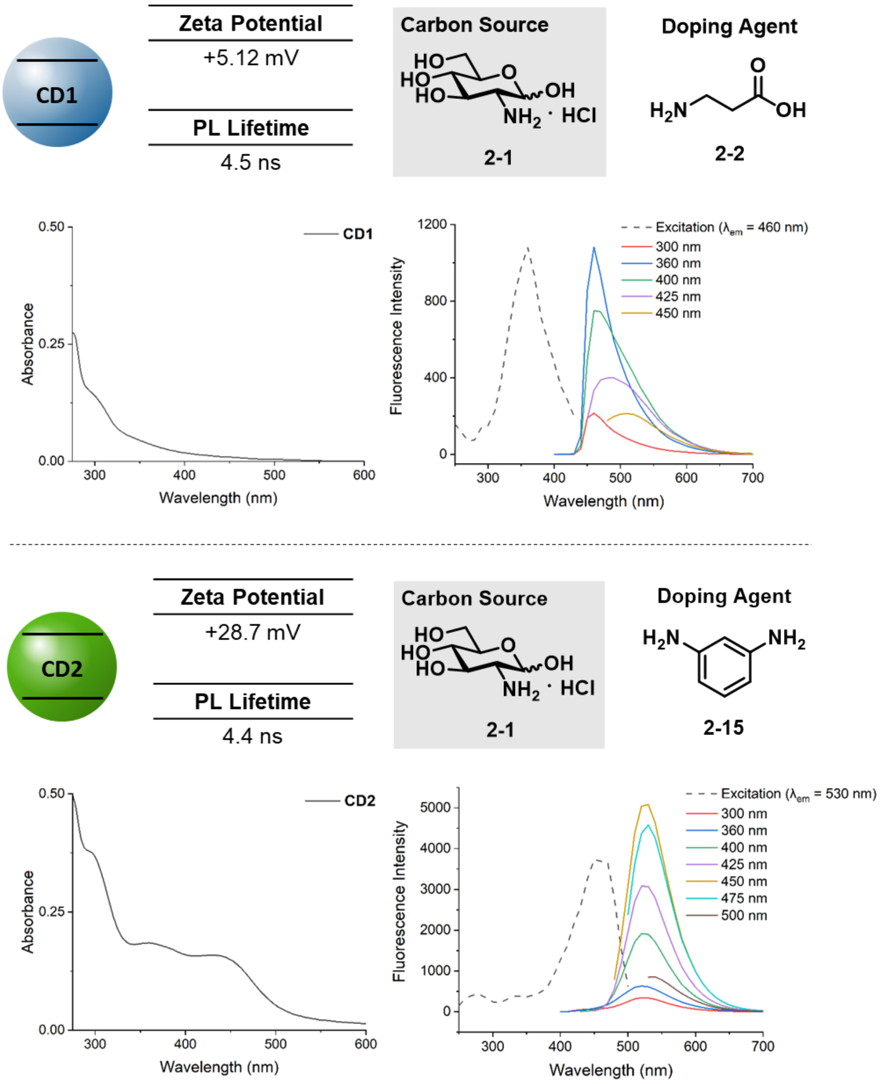

Figure 3-2. Characterization of **CD1** and **CD2** (H_2O, 298 K).

The surface carboxylic acid groups of **CD1** enabled immobilization on TiO_2, which was essential for the use of these CDs in heterogeneous metallaphotocatalytic C–O arylations of carboxylic acids (**Table 3-1**, entry 1).[139] No product was formed using **CD1** in the absence of TiO_2 (**Table 3-1**, entry 2). Lower yields were obtained with the **CD2**/TiO_2 nanocomposite (**Table 3-1**, entry 3), but the reaction could be performed even in the absence of the semiconducting materials. **CD2** enabled homogeneously catalyzed metallaphotocatalysis, providing 23% of the target molecule under similar conditions (**Table 3-1**, entry 4). I assumed that the photocatalytic activity of **CD2** is a result of the stronger absorption at 440 nm in combination with the amino surface groups that lead to coordination to the Ni complex, thereby overcoming the short PL lifetime.[145-147] Optimization studies showed that 4,4'-di-*tert*-butyl-2,2'-dipyridyl (dtbbpy), which is commonly used as Ni ligand in homogeneous metallaphotocatalysis, gave improved results (**Table 3-1**, entry 5). Further screenings of all reaction parameters resulted in conditions that afforded the desired product in 80% yield within 24 h (**Table 3-1**, entry 6 and **Table 6-15**). Control studies confirmed the necessity of all ingredients of the catalytic cocktail, as well as blue light irradiation (**Table 6-15**).

Table 3-1. Optimization of the cross-coupling of Boc-Pro-OH with methyl 4-iodobenzoate.

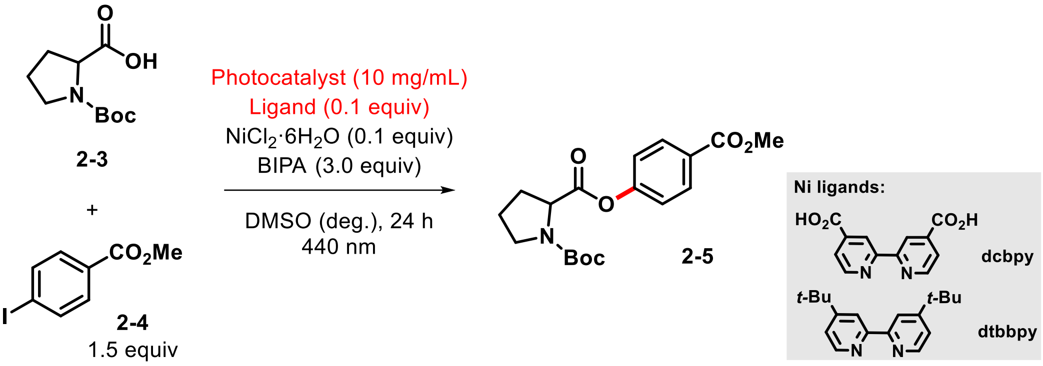

Entry	Conditions	2-5 [%]
1	**CD1**/TiO_2, dcbpy	83
2	**CD1**, dcbpy	0
3	**CD2**/TiO_2, dcbpy	34
4	**CD2**, dcbpy	23
5	**CD2,** dtbbpy	35
6	**CD2** (0.67mg/mL)[a], dtbbpy	80

[a] 440 nm LED lamp (100% power). Reaction conditions: Boc-Pro-OH (190.3 µmol), methyl 4-iodobenzoate (285.4 µmol), photocatalyst (30 mg), $NiCl_2 \cdot 6H_2O$ (19.0 µmol) and ligand (19.0 µmol) in DMSO (3 mL), BIPA (570.8 µmol), 440 nm LED lamp (50% power), 24 h. NMR yields determined by ^{1}H-NMR using 1,3,5-trimethoxybenzene as internal standard. deg. = degassed.

Next, I studied if the combination of **CD2**, a Ni(II) salt, and dtbbpy could be used for other metallaphotocatalytic carbon–heteroatom cross-couplings (**Figure 3-3**). To my delight, I found that **CD2** was a suitable photocatalyst for the metallaphotocatalytic coupling of aryl halides with carboxylic acids, thiols, sodium sulfonates, sulfonamides, and amines. The optimized conditions also resulted in product formation using **CD1**, but yields were generally lower.

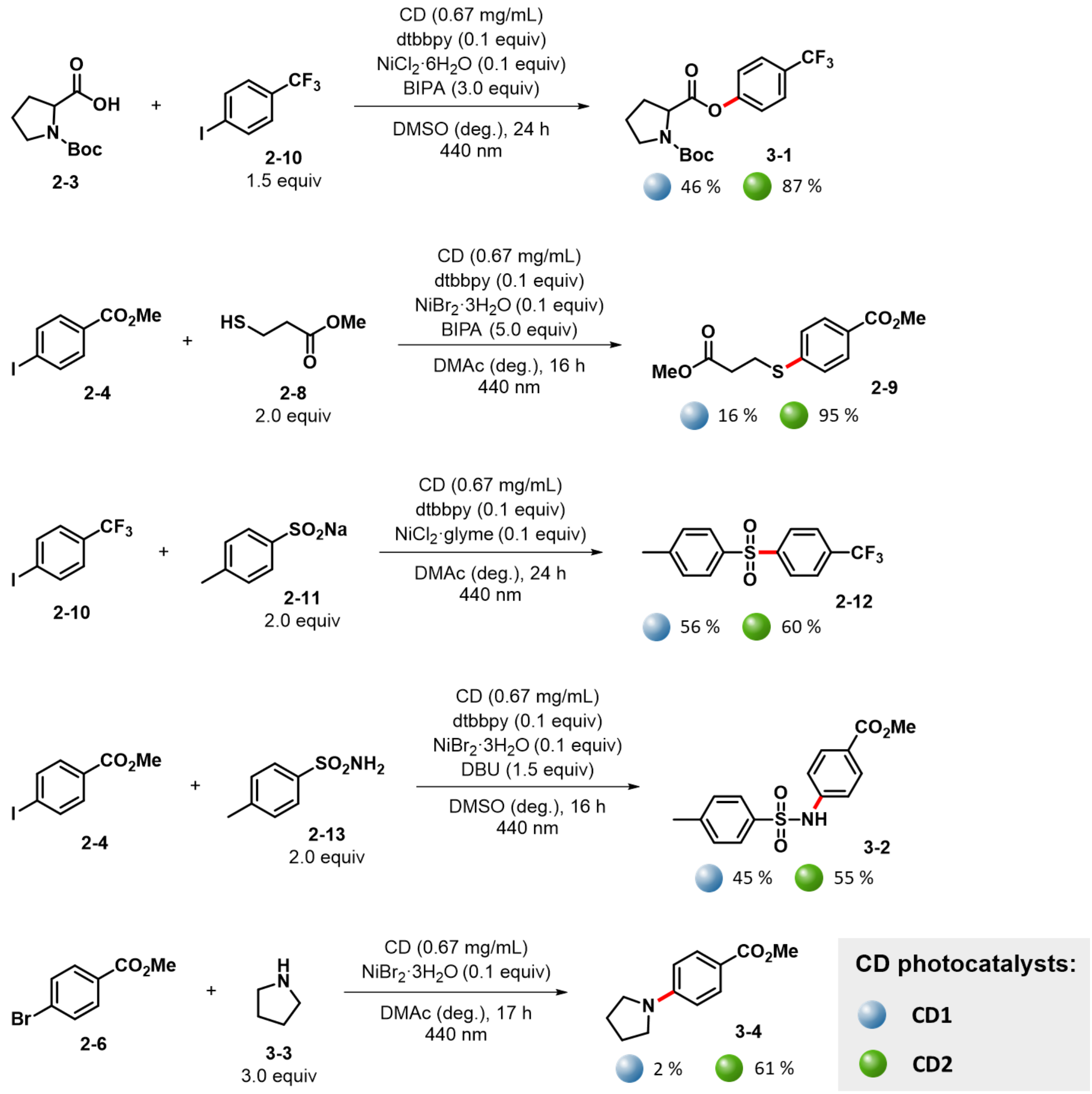

Figure 3-3. Application of **CD1** and **CD2** as photocatalysts for C–O, C–S, and C–N cross-couplings.

3.2.2. C-S cross-coupling catalyzed by CDs

In particular, the use of **CD2** in combination with $NiBr_2·3H_2O$, dtbbpy and BIPA in dimethylacetamide (DMAc) resulted in excellent yield for the C–S cross-coupling of methyl 3-mercaptopropionate (**2-8**) with methyl 4-iodobenzoate (**2-4**) (**Table 3-2**, entry 1). No product formation was observed when the reaction was carried out using the corresponding aryl bromide under identical conditions (**Table 3-2**, entry 2).

Table 3-2. Comparison of the applicability of aryl bromides and aryl iodides in the C–S cross-coupling in the presence of BIPA.

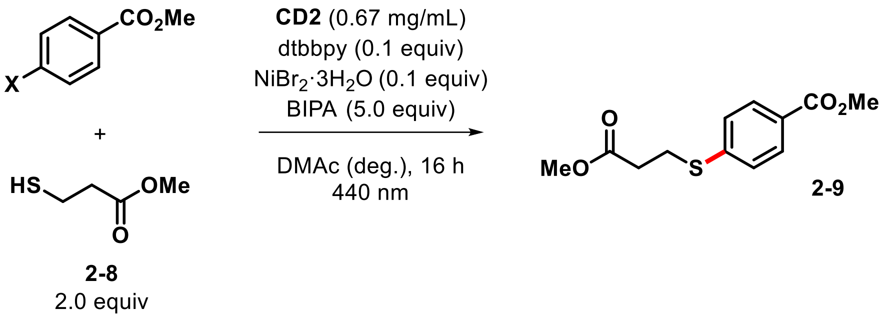

Entry	X	Conditions	2-9 [%]
1	I	As shown	95
2	Br	As shown	0

Reaction conditions: methyl 4-iodobenzoate or methyl 4-bromobenzoate (190.3 µmol), methyl 3-mercaptopropionate (380.5 µmol), **CD2** (2 mg), $NiBr_2 \cdot 3H_2O$ (19.0 µmol), dtbbpy (19.0 µmol) and BIPA (951.5 µmol) in DMAc (3 mL), 440 nm LED lamp (100% power), 16 h. NMR yields determined by ^1H-NMR using 1,3,5-trimethoxybenzene as internal standard. deg. = degassed.

A literature survey revealed conflicting outcomes for this type of reaction. Aryl bromides were successfully coupled with thiols using metallaphotocatalysis when 3,7-(4-biphenyl)-1-naphthalene-10-phenoxazine was applied as photocatalyst (**Figure 3-4**).[148] On the contrary, carbon nitride and dye-sensitized TiO_2 photocatalysts, were limited to aryl iodides.[70, 149] $Ir[dF(CF_3)ppy]_2(dtbbpy)PF_6$ in combination a Ni(II) salt and dtbbpy was originally reported to only couple aryl iodides,[150] but a more recent report showed that the scope of this reaction could be extended to aryl bromides following addition of pyHI to the reaction mixture (**Figure 3-5**).[144] This additive and its downstream products were proposed to serve as a quencher for the photocatalyst, as an electron shuttle between the photocatalyst and the Ni complex, and to prevent the formation of Ni-thiolate complexes that act as inner filters.

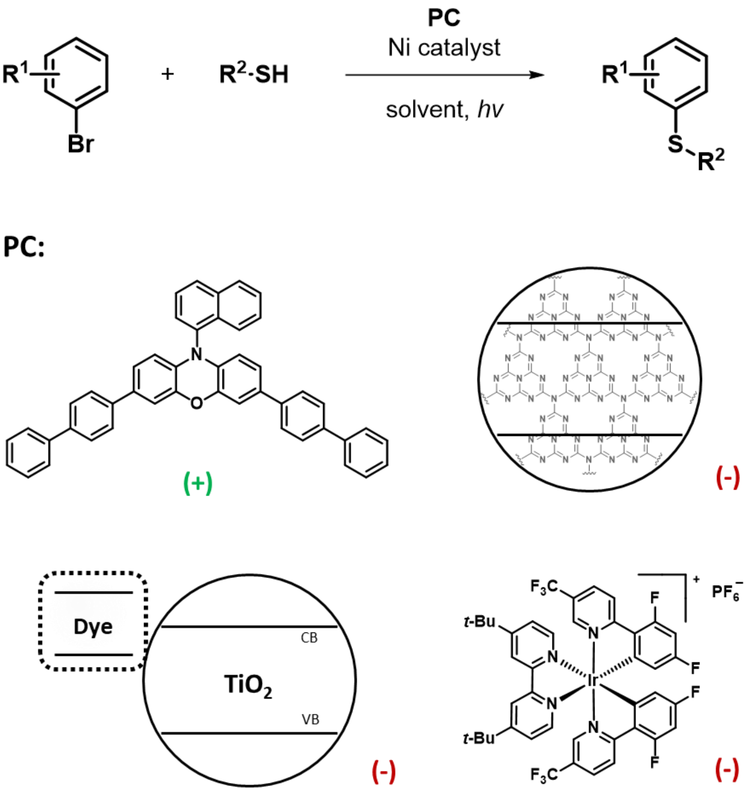

Figure 3-4. A literature survey revealed conflicting outcomes for the C-S cross-coupling using aryl bromides and different PC.

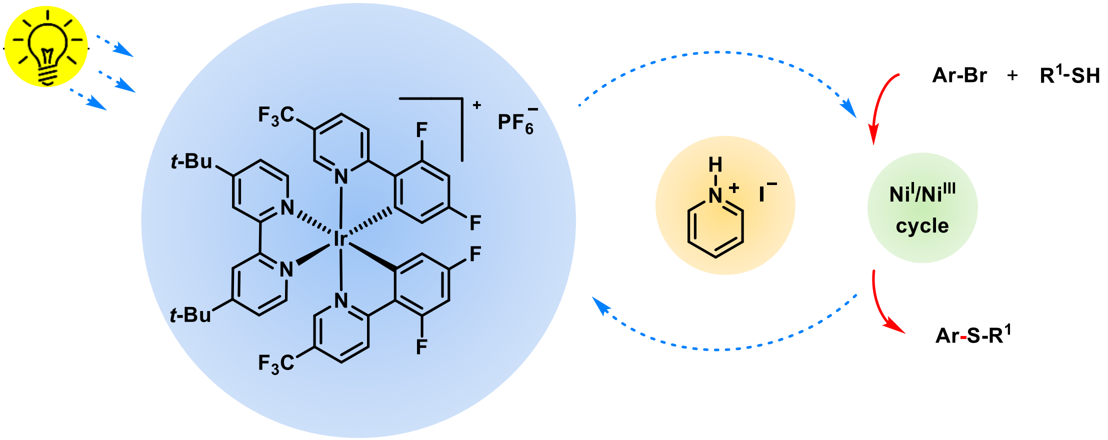

Figure 3-5. Schematic representation of C–S cross-coupling using Ir/Ni/pyHI protocol. The addition of pyHI expand the scope of this reaction to ArBr.

I noticed that, in my protocol, addition of BIPA to the reaction mixture promoted the formation of a highly absorbing Ni-thiolate complex, acting as inner filter (**Figure 3-6**). Considering the abundant amino groups on the surface of **CD2** (9303 µmol/g, **section 6.2 in Chapter 6**), I hypothesized that the reaction could be performed under “base-free” conditions to limit the formation of these highly absorbing species. In absence of the base (BIPA), aryl bromides (and iodides) reacted efficiently using my catalytic system (**Table 3-3**). Spectroscopic investigations also identified dramatic changes in emission and absorbance for **CD2** in the presence of BIPA, indicating a strong interaction between these two components (**Figure 3-7**). No changes in the emission of **CD2** were observed in presence of the starting materials, but the addition of $NiBr_2$ resulted in moderate quenching. This is in agreement with the accepted mechanistic hypothesis that these cross-couplings are initiated by a photocatalytic reduction of Ni^{II} to Ni^{I}.[151-153] No significant changes in the absorption of **CD2** in the presence of the Ni complex implied negligible static interactions (**Figure 6-45** and **Figure 6-48**), but indicated a dynamic type of quenching.

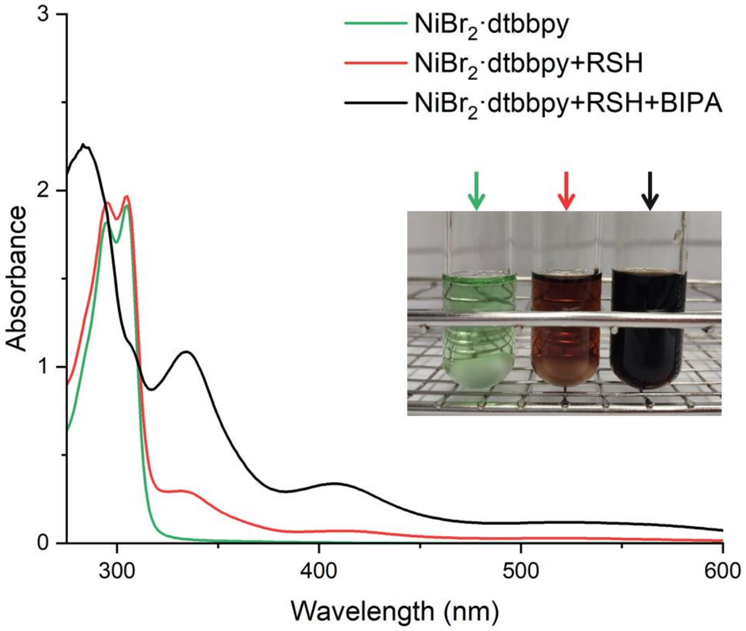

Figure 3-6. Formation of highly absorbing Ni-thiolate species in the presence of BIPA.

Table 3-3. Comparison of the applicability of aryl bromides and aryl iodides in the C–S cross-coupling in the absence of BIPA.

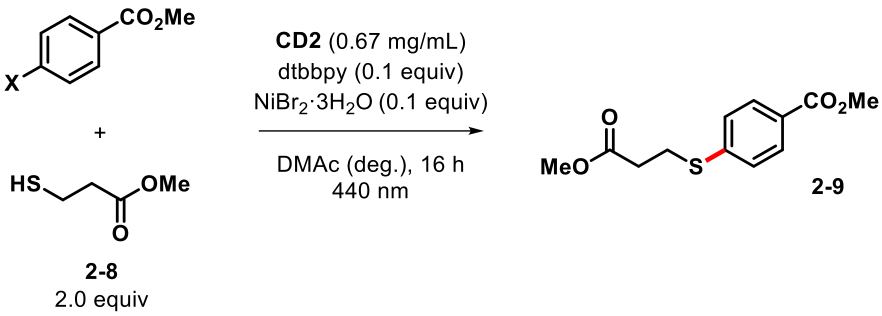

Entry	X	Conditions	2-9 [%]
1	I	As shown	99
2	Br	As shown	95

Reaction conditions: methyl 4-iodobenzoate or methyl 4-bromobenzoate (190.3 µmol), methyl 3-mercaptopropionate (380.5 µmol), **CD2** (2 mg), $NiBr_2 \cdot 3H_2O$ (19.0 µmol) and dtbbpy (19.0 µmol) in DMAc (3 mL), 440 nm LED lamp (100% power), 16 h. NMR yields determined by ^{1}H-NMR using 1,3,5-trimethoxybenzene as internal standard. deg. = degassed.

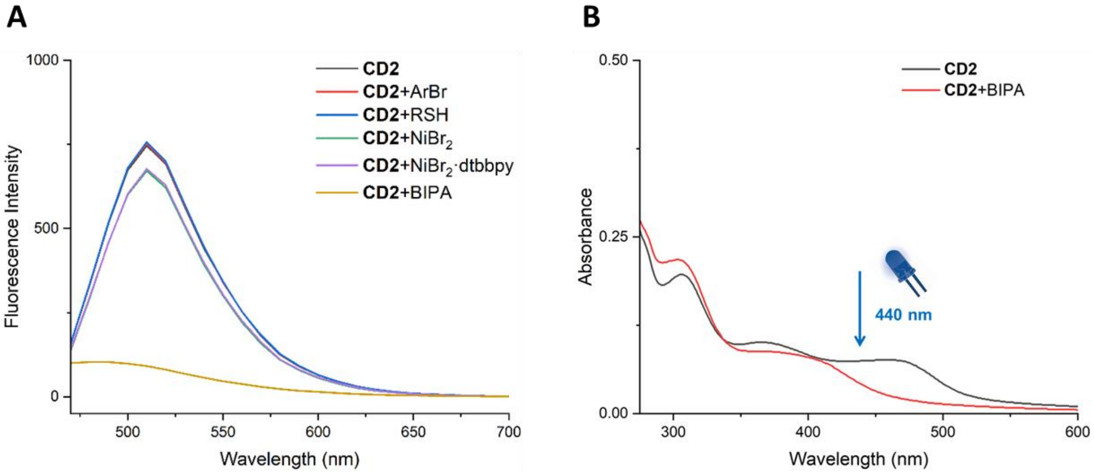

Figure 3-7. Emission (A, λ_{ex} = 440 nm) and UV-Vis absorption (B) spectra of **CD2** in the presence of different reaction components (DMAc, 298 K).

This result was corroborated by a decrease in the excited state lifetime of **CD2** in the presence of the Ni complex in a concentration-dependent manner (**Figure 6-50**). The dynamic Stern-Volmer plot permitted to calculate a bimolecular quenching rate constant (K_q) of 9.18×10^{10} M^{-1} s^{-1} for the Ni complex (**Figure 3-8**). Steady-state quenching rate constant could not be accurately measured due to the broad absorption of Ni(dtbbpy)Br_2 that overlaps with **CD2** (**Figure 6-49**).

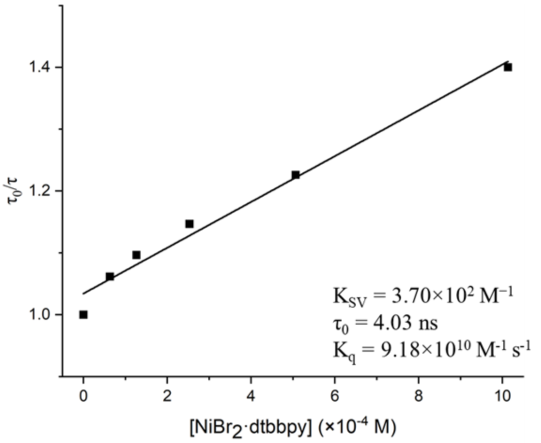

$$\frac{F_0}{F} = \frac{\tau_0}{\tau} = 1 + K_{SV}[Q] = 1 + \tau_0 K_q [Q]$$

F_0: the **CD2** fluorescence intensity without a quencher
F: the **CD2** fluorescence intensity with a quencher
K_{SV}: the Stern–Volmer quenching constant
[Q]: the quencher concentration
τ_0: the **CD2** lifetime in the absence of quencher
τ: the **CD2** lifetime in the presence of quencher
K_q: the bimolecular quenching rate constant

Figure 3-8. Dynamic Stern−Volmer quenching plot of **CD2**.

Next, I sought to clarify if the catalytic performance of **CD2** could be ascribed to surface effects, which eventually promotes dynamic interaction with the Ni catalyst overcoming diffusion/lifetime limitations. A collection of CDs was synthesized using different amino-containing doping agents (**Figure 3-9A**). Within this library, two CDs (**CD2** and **CD14)** have a highly positive zeta potential and show significantly better catalytic performances in a model C–S cross-coupling (**Figure 3-9B** and **Figure 3-10**). However, **CD2** and **CD14** also show a stronger absorption at 440 nm than all other CDs and are the only examples that emit green light. These results suggest that the photocatalytic activity is a synergistic effect of the surface and photophysical properties of the dots.

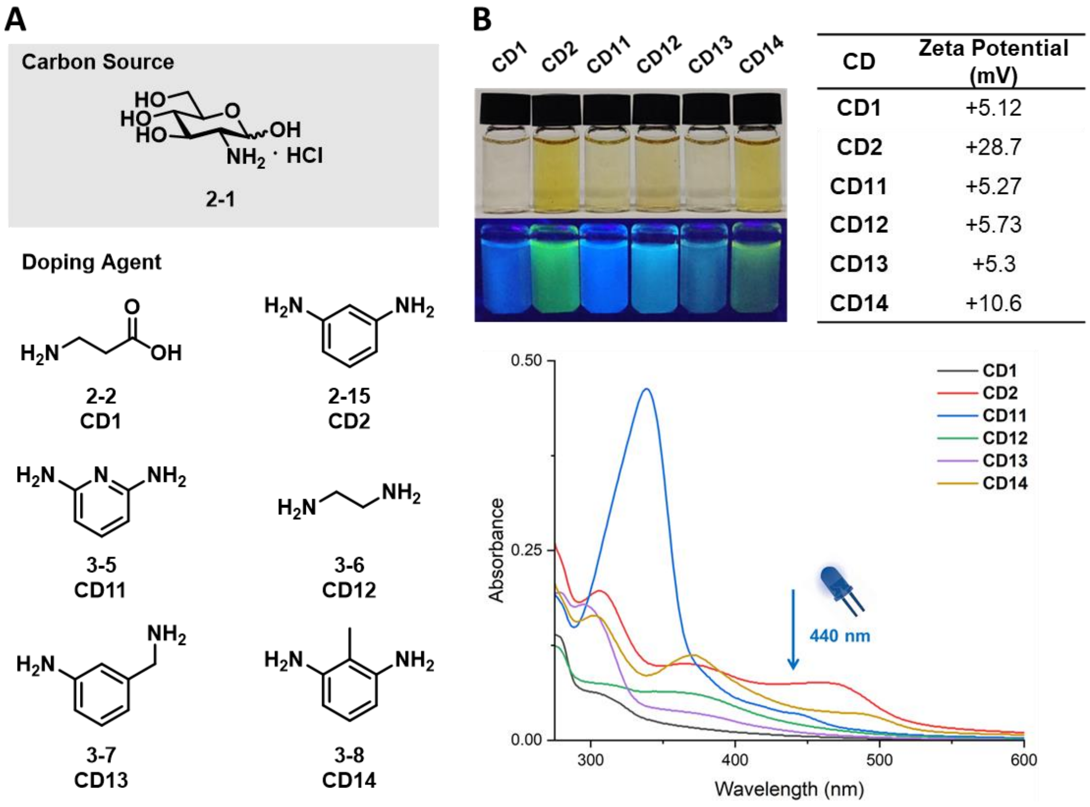

CD	Zeta Potential (mV)
CD1	+5.12
CD2	+28.7
CD11	+5.27
CD12	+5.73
CD13	+5.3
CD14	+10.6

Figure 3-9. Chemical structures of carbon source and doping agents used for CD synthesis (A), characterization of CDs (13.3 µg/mL, DMAc, 298 K, for UV-Vis absorption) (B).

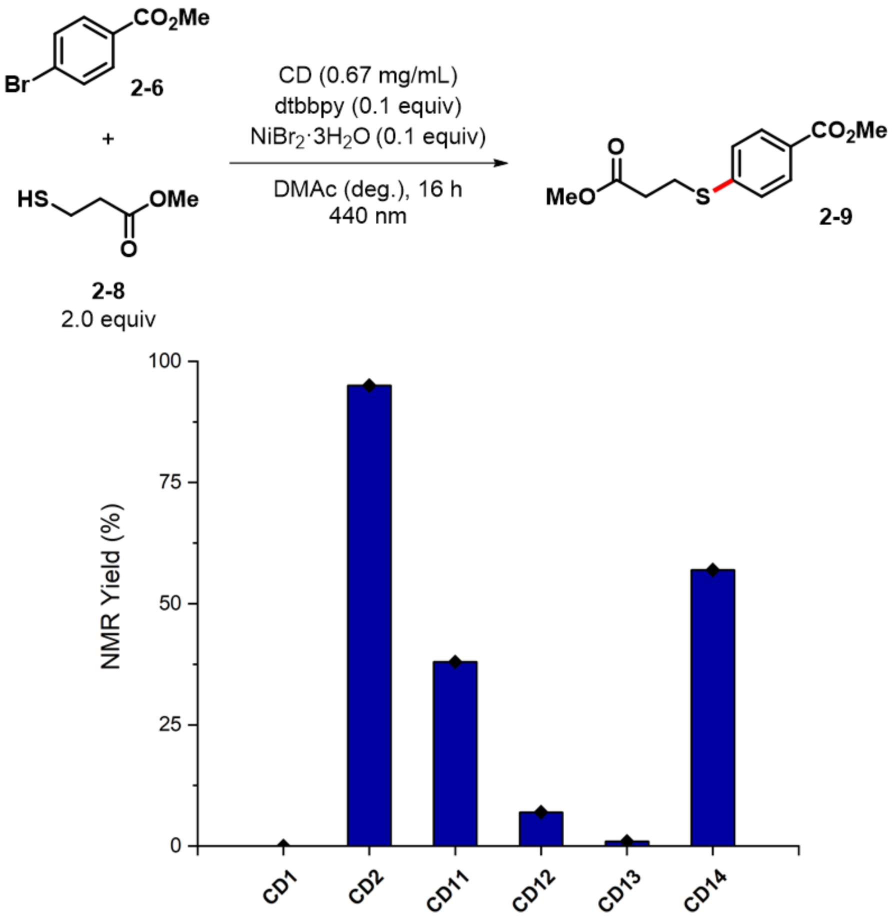

Figure 3-10. Evaluation of different CDs as photocatalysts for C-S cross-coupling.

3.2.3. The role of pyHI in the C-S cross-coupling

I wondered whether the addition of pyHI could increase the rate of the C–S coupling protocol, shortening the long reaction time required for quantitative product formation (16 h, **Figure 3-11** and **Figure 3-12**). Indeed, I observed a significant increase in the reaction rate. In agreement with Nocera and coworkers, I found that pyHI suppressed the formation of the Ni-thiolate complex in a concentration-dependent manner (**Figure 3-13** and **Figure 6-53**). The addition of pyridine (py) as an additive also resulted in an increased reaction rate, albeit less significant, confirming the important role of the base (in form of pyH^+) in connecting the photocatalyst and Ni cycle.[144] UV-Vis spectroscopy confirmed that pyridine had, in contrast to BIPA, little effect on the spectral properties of **CD2** (**Figure 6-46** and **Figure 6-47**).

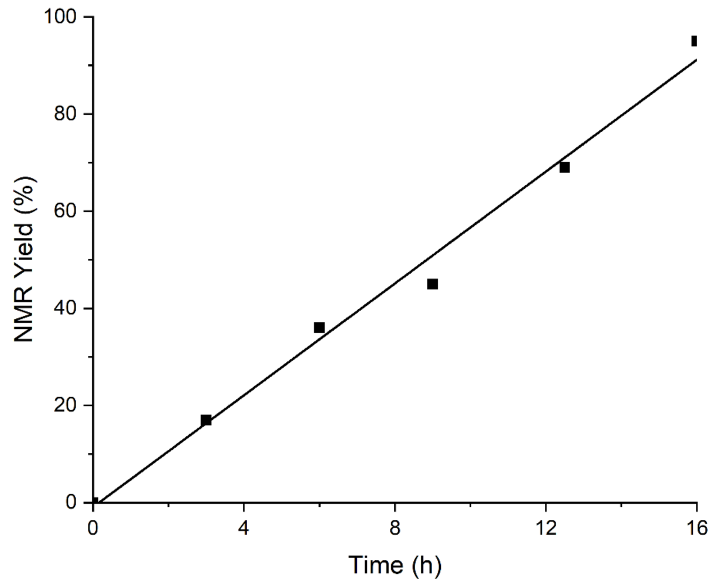

Figure 3-11. Reaction progress for the *S*-arylation using **CD2** as photocatalyst. Each reaction was performed following the optimized conditions (**Table 6-18**, entry 1) and quenched after the selected amount of time.

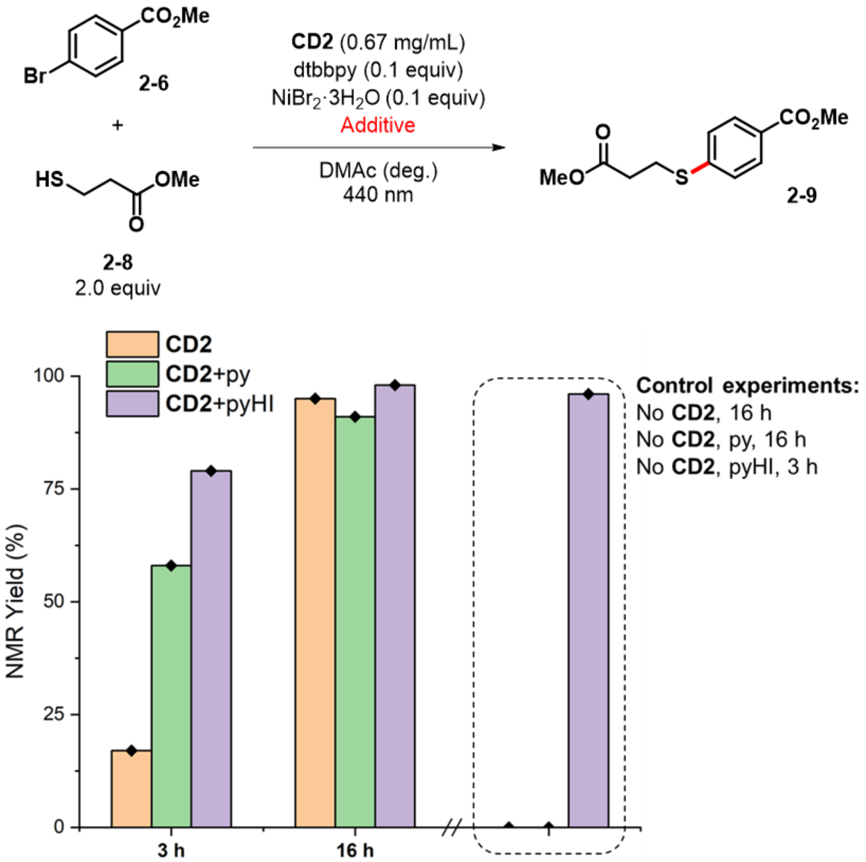

Control experiments:
No **CD2**, 16 h
No **CD2**, py, 16 h
No **CD2**, pyHI, 3 h

Figure 3-12. Conditions optimization and control experiments to accelerate the C-S cross-coupling using additives py or pyHI.

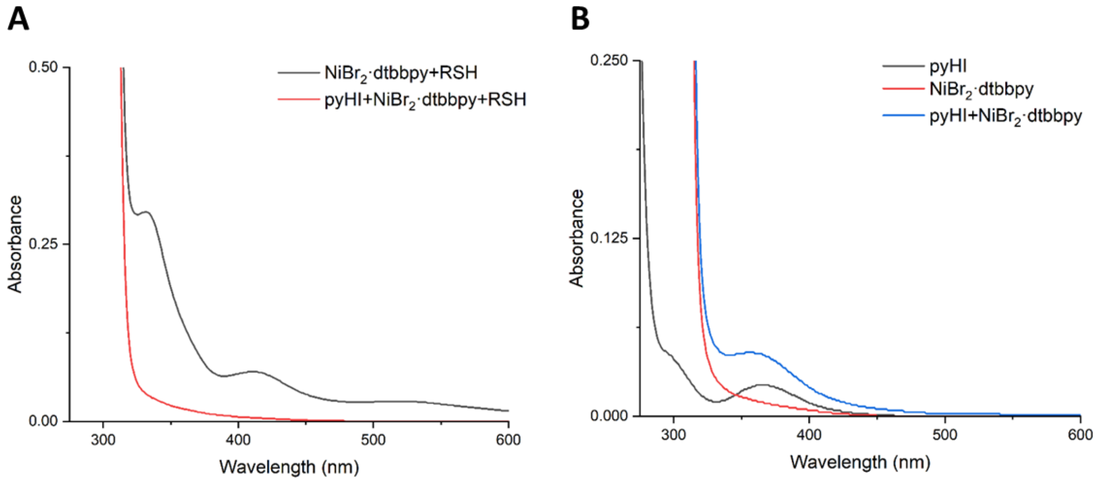

Figure 3-13. Photophysical characterization of pyHI in the C-S cross-coupling (DMAc, 298 K).

To my surprise, control studies showed that the reaction could be performed even in the absence of the photocatalyst, when pyHI was present (**Figure 3-12**). This result might be explained with the formation a visible-light-induced ion pair charge transfer state derived from pyHI that could activate the Ni cycle. Indeed, heteroarenium iodides have been previously shown to act as photocatalysts in photoredox catalysis.[154] The pyHI protocol seemed specific to the C-S cross-coupling; little to no yields were obtained under those conditions for other carbon-heteroatom cross-couplings (**Figure 6-44**). Moreover, longer wavelengths (525 nm) did not enable cross-couplings using pyHI, but excellent yields were obtained using the **CD2** protocol under green light irradiation (**Figure 3-14**), offering an interesting alternative for light-sensitive substrates.

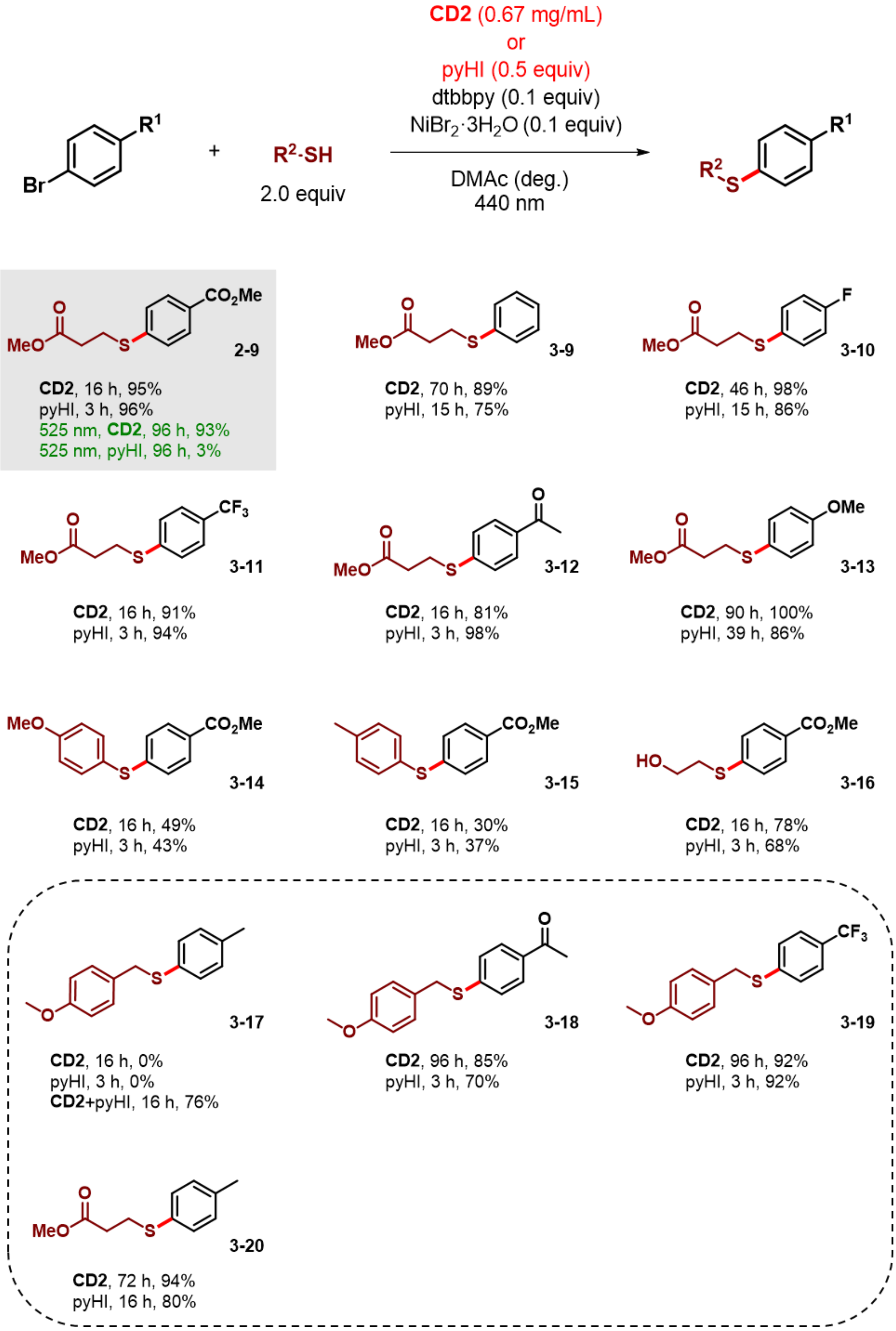

Figure 3-14. Comparison of reaction scope for the **CD2** and pyHI protocols.

The fact that pyHI alone can induce cross-couplings contradicts the findings from Nocera and coworkers, which reported that both, pyHI and a photocatalyst, were required for productive catalysis (**Figure 3-5**).[144] By studying the scope and limitations of the C-S cross-coupling using either **CD2** or pyHI as photocatalysts, I realized that the discrepancy between Nocera's and my findings is connected to the substrates used (**Figure 3-14**). Moderate to excellent yields were achieved for a range of starting material combinations, including primary and aromatic thiols, as well as electron-poor and electron-rich aryl bromides using either the **CD2** or the pyHI protocol. The only exception was the reaction of 4-methoxybenzyl mercaptan with 4-bromotoluene to prepare **3-17** that did not result in any product formation, which is also the model reaction analyzed in the mechanistic study of the Ir/Ni/pyHI protocol by Nocera and coworkers. However, I synthesized compounds **3-18**, **3-19** and **3-20** in good yields, indicating that 4-methoxybenzyl mercaptan and 4-bromotoluene individually are not responsible for this discrepancy. Moreover, a protocol that included both **CD2** and pyHI afforded compound **3-17** in good yield, highlighting the applicability of **CD2** as sustainable alternative for Ir(III) photocatalysts. Although I have no satisfactory explanation for this phenomenon, these results stressed how small variations in the starting materials combination apparently have dramatic effects on the reaction mechanism.

3.3. Conclusion

I demonstrated that CDs are efficient colloidal nano-catalysts for metallaphotocatalytic carbon–heteroatom cross-couplings in combination with a Ni(II) complex. Aryl halides were coupled with a carboxylic acid, a thiol, a sodium sulfonate, a sulfonamide, and an amine, under blue light irradiation. In particular, the synergistic effect of the amino-rich surface and photophysical properties made **CD2** a valuable alternative to precious Ir complexes for C-S cross-coupling reactions. Mild, base-free conditions were applied to couple a wide range of aryl halides and thiols. Mechanistic studies suggested dynamic quenching of the **CD2** excited state by the Ni co-catalyst and identified that pyHI can act as photocatalyst in such transformations. A systematic comparison between the two protocols stressed how small variations in the starting materials combination could have dramatic effects on the reaction mechanism.

4. Carbon dots as photocatalysts for *E*-to-*Z* isomerization

4.1. Introduction

Alkenes are an important class of precursors in organic synthesis. While several methods to access the thermodynamically stable *E*-alkenes have been reported, the preparation of the thermodynamically less stable *Z*-alkenes remains challenging. *E*-to-*Z* isomerization, enabled by energy-transfer catalysis, has proved to be a useful protocol to obtain the thermodynamically unfavoured *Z*-alkenes. This reaction process is generally promoted by the use of expensive transition-metal catalysts leading to cost constraints when considering large-scale applications.[106, 155] The use of non-precious metal photocatalysts offers a suitable alternative strategy in terms of economic cost and environmental issues. Thus, much research has focused on the development of cheap, environmentally friendly visible-light-absorbing photocatalysts that react as efficient senstizers to enable the *E*-to-*Z* isomerization of alkenes *via* energy transfer.

In Chapter 2 and Chapter 3, CDs and their nanocomposites with TiO_2 have proven valuable visible-light-absorbing photocatalysts for a broad range of carbon–heteroatom cross-couplings. Moreover, I showed that the CD surface and photophysical properties could be tuned to improve the photocatalytic efficiency and replace expensive metal catalysts in cross coupling reactions. Inspired by these results, I hypothesized that CDs can also act as ideal alternatives to Ir-based polypyridyl complexes for the visible-light photocatalytic *E*-to-*Z* isomerization.

Compared to the preciously discussed cross coupling reaction (*vida supra*), the isomerization reaction follows an alternative photoactivation mode proceeding *via* energy-transfer catalysis. In this chapter, I explore the use of CDs as well as their nanocomposites with TiO_2 as photocatalysts which enable energy-transfer reactions under blue light irradiation. This approach was demonstrated in a proof of concept *E*-to-*Z* isomerization for several alkenes with varying functionalities and presumably differing triplet energies.

4.2. Results and discussion

4.2.1. Proof of concept

To test the use of CDs as photosensitizers, I conducted a preliminary experiment using **CD1**/TiO_2 and **CD2**/TiO_2 as photocatalysts for the *E*-to-*Z* isomerization of *trans*-stilbene (**4-1**) (**Figure 4-1**, entries 2-3). Pleasingly, under blue light irradiation, a significant amount of isomerization (3:7 *Z*/*E* ratio) was observed suggesting activation of the alkene *via* energy transfer had occurred. Improved results (1:1 *Z*/*E* ratio) were obtained when the reaction was performed with **CD1** and **CD2** as photocatalysts (**Figure 4-1**, entries 4-5). Modest *Z*/*E* isomerization was also achieved in the presence of **CD2** under green light irradiation (34:66 *Z*/*E* ratio) (**Figure 4-1**, entries 7-10). The *Z*/*E* ratio dropped when the solvent was changed from DMSO to MeCN, probably due to the lower solubility of the CDs in MeCN (**Table 6-24**). This entry highlights the prominent role of the CD in enabling *E*-to-*Z* isomerization.

In a control reaction, all four photocatalysts demonstrated that sensitization of the *Z*-isomer is also possible under blue or green light irradiation (**Figure 4-1**, entry 11 and **Table 6-25**). This is not surprising, since the excited state energy levels of *trans*-stilbene (**4-1**) and *cis*-stilbene (**4-2**) are relatively low and both isomers are efficient quenchers of the excited state of our CD photocatalysts. Nevertheless, these preliminary results confirmed the capabilities of CDs to enable efficient sensitization for energy-transfer catalysis.

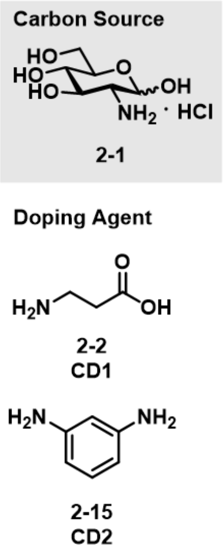

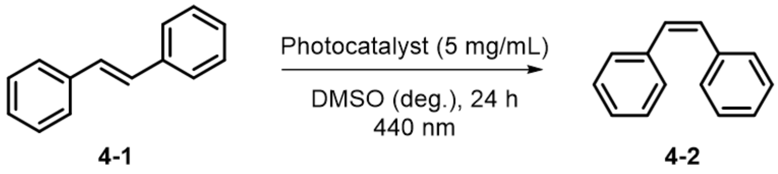

Entry	Conditions	*Z*+*E* [%], *Z*/*E*
1	No photocatalyst	97, 2:98
2	**CD1**/TiO_2	98, 32:68
3	**CD2**/TiO_2	98, 34:66
4	**CD1**	95, 55:45
5	**CD2**	96, 56:44
6	No photocatalyst, 525 nm[a]	98, 0:100
7	**CD1**/TiO_2, 525 nm[a]	99, 4:96
8	**CD2**/TiO_2, 525 nm[a]	quant., 1:99
9	**CD1**, 525 nm[a]	99, 5:95
10	**CD2**, 525 nm[a]	99, 34:66
11	**CD2 (*Z*-to-*E*)**, 525 nm[a]	quant., 47:53

[a] 525 nm LED lamp (200% power). Reaction conditions: *trans*-stilbene (0.19 mmol), DMSO (3 mL), photocatalyst (15 mg), 440 nm LED lamp (50% power), 24 h. NMR yields were determined by ^{1}H-NMR using 1,3,5-trimethoxybenzene as internal standard. deg. = degassed.

Figure 4-1. Screening of photocatalysts for the isomerization of *trans*-stilbene (**4-1**).

4.2.2. Isomerization of ethyl (*E*)-3-(*p*-tolyl)but-2-enoate

Next, I studied the isomerization of ethyl (*E*)-3-(*p*-tolyl)but-2-enoate (**4-3**), an alkene with a larger energy gap between the excited state energy levels of the *E*- and *Z*-isomers.[156] NMR analysis confirmed that **CD1** and **CD2** can effectively photocatalyze the *E*-to-*Z* isomerization reactions under blue light irradiation (**Figure 4-2**, entries 4-5). In agreement with the observed isomerization of stilbene (**Figure 4-1**), higher *Z*/*E* ratios were obtained using CDs as photocatalyst (**Figure 4-2**, entries 2-5). More powerful light, longer reaction times, and optimized CD amount dramatically improved the results (**Figure 4-2**, entry 6, **Table 6-26**). No *Z*-isomer was obtained under green light irradiation (**Table 6-26**).

In previous chapters, I noticed that the CD surface and photophysical properties dramatically affected the photocatalytic efficiency in cross coupling reactions. I therefore performed a preliminary screening of different CDs available from the previous project, to verify if dots with different properties could influence the isomerization results. **CD11** and **CD15**, prepared from GlcN·HCl (**2-1**) and 2,6-diaminopyridine (**3-5**) (with or without the addition of β-Ala (**2-2**), respectively), showed improved selectivity in the isomerization reaction (**Figure 4-2**, entry 7 and entry 9). Excellent selectivity was observed (85:15 *Z*/*E* and 87:13 *Z*/*E* ratio, respectively) after 24 h reaction time. To exclude the presence of small organic dyes generated during the carbonization process and responsible for the isomerization, **CD11** was extensively washed with MeCN prior to the reaction. Excellent yields were obtained even with the washed material**,** confirming the activity of **CD11** (**Figure 4-2**, entry 8). Spectroscopic analysis discarded the possibilities of a possible electron donor-acceptor interaction between **CD11** and compound **4-3**, as no changes in the absorption of **CD11** were detected in the presence of the alkene (**Figure 4-3**). Moreover, the Stern-Volmer plot showed a linear behavior, implying an efficient dynamic type quenching of process.

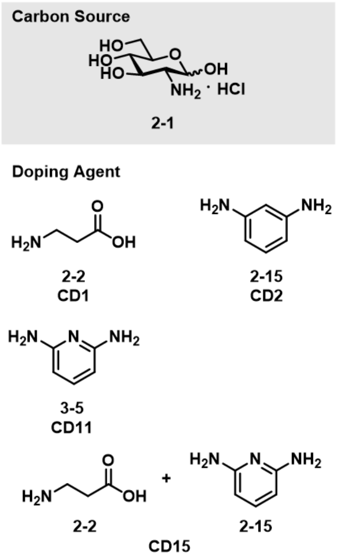

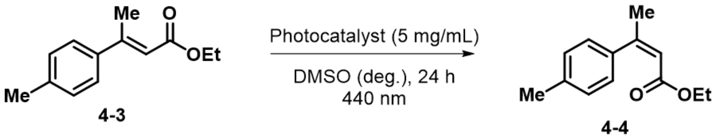

Entry	Conditions	*Z*+*E* [%], *Z*/*E*
1	No photocatalyst	99, 0:100
2	**CD1**/TiO_2	98, 16:84
3	**CD2**/TiO_2	quant., 13:87
4	**CD1**	97, 23:77
5	**CD2**	quant., 25:75
6	**CD1** (1.67 mg/mL)[b], 48 h	93, 68:32
7	**CD11** (1.67 mg/mL)[b]	quant., 85:15
8	**CD11** (1.67 mg/mL)[b] washed by MeCN	96, 86:14
9	**CD15** (1.67 mg/mL)[b]	98, 87:13

[a] 525 nm LED lamp (200% power). [b] 440 nm LED lamp (100% power). Reaction conditions: ethyl (*E*)-3-(*p*-tolyl)but-2-enoate (0.19 mmol), DMSO (3 mL), photocatalyst (15 mg), 440 nm LED lamp (50% power), 24 h. NMR yields were determined by ^{1}H-NMR using 1,2,4,5-tetramethylbenzene as internal standard. deg. = degassed.

Figure 4-2. Screening of photocatalysts and reaction conditions for isomerization of ethyl (*E*)-3-(*p*-tolyl)but-2-enoate (**4-3**).

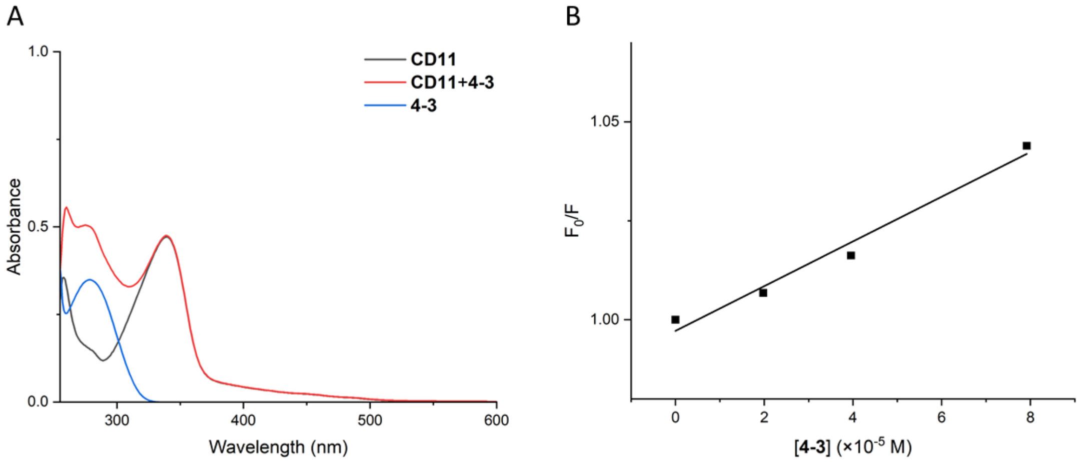

Figure 4-3. UV-Vis absorption spectra of **CD11** alone and in the presence of ethyl (*E*)-3-(*p*-tolyl)but-2-enoate (**4-3**) (DMSO, 298 K) (A). Stern−Volmer quenching plot of **CD11** based on fluorescence (B).

The excellent performance of **CD11** and **CD15** prompted me to explore new CDs based on analogues of 1,3-diaminobenzene (**2-15**) or 2,6-diaminopyridine (**3-5**) as doping agents. All the new synthesized CDs were tested in the photocatalyzed *E*-to-*Z* isomerization of ethyl (*E*)-3-(*p*-tolyl)but-2-enoate (**4-3**) (**Figure 4-4**). Moderate to excellent yields were obtained when the reactions were performed under blue light irradiation for most CDs. Low yields were obtained only for the reaction catalyzed by **CD26** (2:98 *Z*/*E* ratio) and **CD6** (11:89 *Z*/*E* ratio). Still, no obvious correlation between the doping agent, the CD properties, and the isomerization results could be found. Further studies to identify which CD features are required for an efficient isomerization are currently underway.

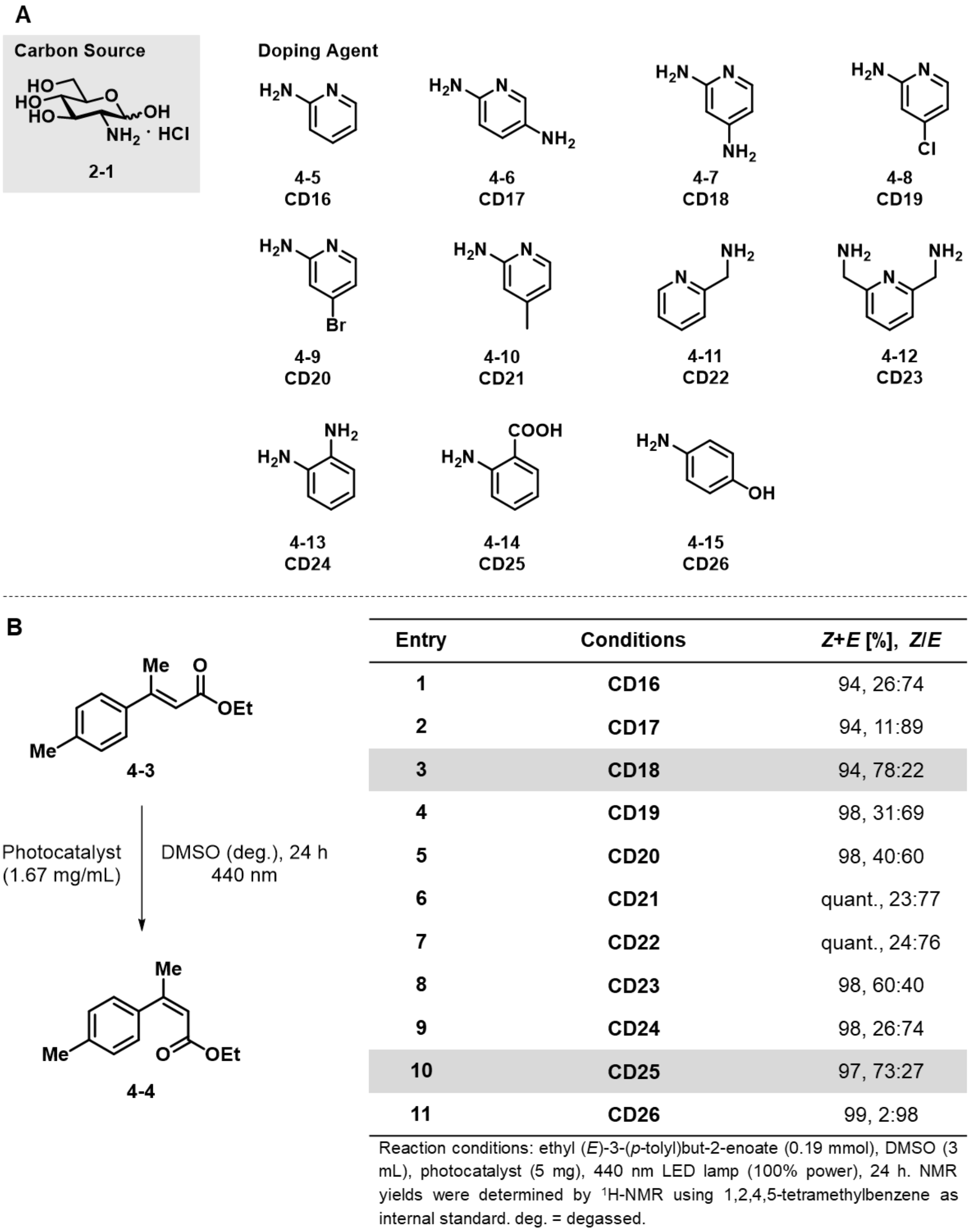

Entry	Conditions	Z+E [%], Z/E
1	**CD16**	94, 26:74
2	**CD17**	94, 11:89
3	**CD18**	94, 78:22
4	**CD19**	98, 31:69
5	**CD20**	98, 40:60
6	**CD21**	quant., 23:77
7	**CD22**	quant., 24:76
8	**CD23**	98, 60:40
9	**CD24**	98, 26:74
10	**CD25**	97, 73:27
11	**CD26**	99, 2:98

Reaction conditions: ethyl (*E*)-3-(*p*-tolyl)but-2-enoate (0.19 mmol), DMSO (3 mL), photocatalyst (5 mg), 440 nm LED lamp (100% power), 24 h. NMR yields were determined by ^{1}H-NMR using 1,2,4,5-tetramethylbenzene as internal standard. deg. = degassed.

Figure 4-4. Screening of different CDs (A) as photocatalyst for isomerization of ethyl (*E*)-3-(*p*-tolyl)but-2-enoate (**4-3**) (B). The best results are highlighted in grey.

4.2.3. Reaction scope

I then tested the applicability of **CD1**, **CD2**, **CD11** and **CD15** in the isomerization of alkenes with different excited state energies. All four CDs exhibited some photocatalytic activity under blue light irradiation (**Figure 4-5**), however, the *Z*/*E* ratio remained quite low. Further screening of conditions showed no improvement for the isomerization of ethyl cinnamate (**4-16**) (**Table 6-27**).

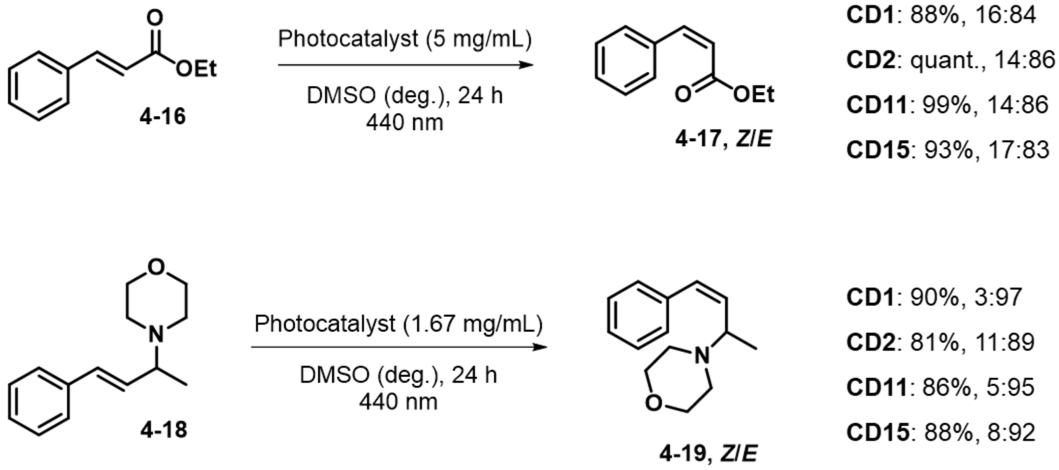

Figure 4-5. Application of **CD1**, **CD2**, **CD11** and **CD15** as photocatalysts for isomerization of ethyl cinnamate (top) and (*E*)-4-(4-phenylbut-3-en-2-yl)morpholine (bottom).

In contrast, the use of more powerful light, longer reaction times, and optimized CD amount resulted in efficient isomerization of (*E*)-4,4,5,5-tetramethyl-2-(2-phenylprop-1-en-1-yl)-1,3,2-dioxaborolane (**4-20**) (**Figure 4-6**, entry 8, **Table 6-29**). This compound is particularly interesting, as boronic esters are valuable linchpins for the synthesis of complex molecules.

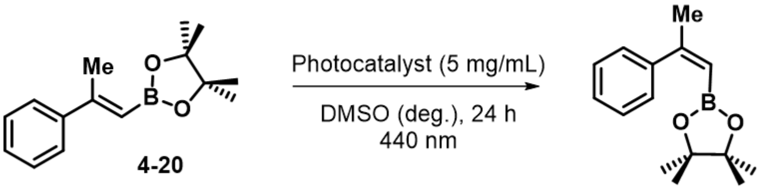

4-20

4-21, ***Z*/*E***

Entry	Conditions	*Z*+*E* [%], *Z*/*E*
1	No photocatalyst	92, 2:98
2	**CD1**	80, 4:96
3	**CD2**	82, 4:96
4	**CD11**	93, 17:83
5	**CD15**	87, 15:85
8	**CD11** (1.67 mg/mL)[a], 96 h	92, 65:35

[a] 440 nm LED lamp (100% power). Reaction conditions: (*E*)-4,4,5,5-tetramethyl-2-(2-phenylprop-1-en-1-yl)-1,3,2-dioxaborolane (0.19 mmol), DMSO (3 mL), photocatalyst (15 mg), 440 nm LED lamp (50% power), 24 h. NMR yields were determined by ^{1}H-NMR using 1,3,5-trimethoxybenzene as internal standard. deg. = degassed.

Figure 4-6. Application of **CD1**, **CD2**, **CD11** and **CD15** as photocatalysts for isomerization of (*E*)-4,4,5,5-tetramethyl-2-(2-phenylprop-1-en-1-yl)-1,3,2-dioxaborolane.

4.3. Conclusion

In conclusion, I successfully verified the hypothesis that CDs can act as photocatalysts in energy-transfer reactions such as *E*-to-*Z* isomerization. The simple isomerization of *trans*-stilbene (**4-1**) indicated that CDs (**CD1** and **CD2**) performed significantly better than their nanocomposites with TiO_2. Efficient isomerization of ethyl (*E*)-3-(*p*-tolyl)but-2-enoate (**4-3**) could be achieved, after a systematic screening of reaction conditions and CD photocatalysts. A collection of CDs was synthesized using analogues of 1,3-diaminobenzene (**2-15**) or 2,6-diaminopyridine (**3-5**) as doping agents. Within this library, most CDs effectively photocatalyzed the *E*-to-*Z* isomerization of ethyl (*E*)-3-(*p*-tolyl)but-2-enoate (**4-3**) under blue light irradiation. Four CDs (**CD1**, **CD2**, **CD11** and **CD15**) were tested for the *E*-to-*Z* isomerization of alternative alkenes, showing moderate catalytic activity. These preliminary results demonstrate the applicability of CDs in energy-transfer reactions. Further optimization and translation to other energy-transfer reactions (e.g. [2+2] cycloadditions) are currently being pursued.

5. Conclusion and outlook

This thesis highlights the use of CDs, a low-cost and easy-to-prepare nanomaterials, to construct heterogeneous or quasi-homogeneous photocatalytic systems for different types of organic synthesis. Previously, CDs have been designed to generate metal-free, visible-light-absorbing nano-catalysts for simple organic transformations, such as water splitting and pollutant degradation. In this thesis, I demonstrated their applicability as photocatalysts for metallaphotocatalytic cross-couplings and isomerization reactions, performed mechanistic studies, and further explored the catalytic effects of a broad library of CDs.

In Chapter 2, I have successfully synthesized CDs from carbohydrates and prepared CD/TiO_2 nanocomposites to overcome the problem of CD short PL lifetime. The obtained heterogeneous nanocomposites could act as visible-light-absorbing photocatalysts for Ni-catalyzed carbon‒heteroatom cross-couplings. High yields were observed under blue light irradiation. Compared to the organic dye fluorescein, CD/TiO_2 nanocomposites exhibited superior photostability and excellent recyclability. Finally, I have synthesized a library of CD photosensitizers from different carbon sources, including waste products, and doping agents and immobilized them on TiO_2. Good to excellent performances were detected for all CDs in the Ni-catalyzed C-O cross-couplings, showing the high flexibility of this catalytic system.

In Chapter 3, I demonstrated the possibility of using CDs as colloidal photocatalysts, for Ni-catalyzed carbon–heteroatom cross-couplings. Compared to heterogeneous CD/TiO_2 nanocomposites, this colloidal system has many advantages: no requirement of pre-immobilization on TiO_2, wider scope of Ni ligands, higher surface area for catalysis, and better light penetration. Colloidal CDs could efficiently photocatalyze the coupling of aryl halides with a carboxylic acid, a thiol, a sodium sulfonate, a sulfonamide, and an amine. Next, I found that **CD2** could serve as a suitable alternative to precious Ir complexes for C-S cross-coupling and further investigated the mechanism of the reaction. A library of CDs using different amino-containing doping agents indicated that the excellent catalytic performance of **CD2** could be ascribed to a combination of its positive surface and photophysical properties. Finally, I identified a new protocol that uses pyHI, a common additive in some photocatalytic reactions, for the photocatalyzed C-S cross-coupling.

These results demonstrated the potential of CD-based photocatalytic system for carbon–heteroatom cross-couplings. Following the work in Chapter 2 and Chapter 3, several follow-up projects could be imagined (**Figure 5**):

1. In Chapter 2, experimental results have demonstrated that the photocatalytic performance of CDs are not significantly affected by carbohydrates sources. Hence, I will use abundant and cheap materials such as industrial waste lactose and naturally sourced polysaccharides chitin to prepare CDs as valuable photocatalysts.
2. The presence of both the photocatalyst and the transition-metal catalyst is essential for metallaphotocatalytic carbon-heteroatom cross-couplings. A one-pot synthesis could be introduced to form CD/Ni complexes. During the process of one-pot synthesis, the Ni catalysts could be fixed on the CD surface, ensuring efficient electronic communication between CD and Ni catalysts.[157]

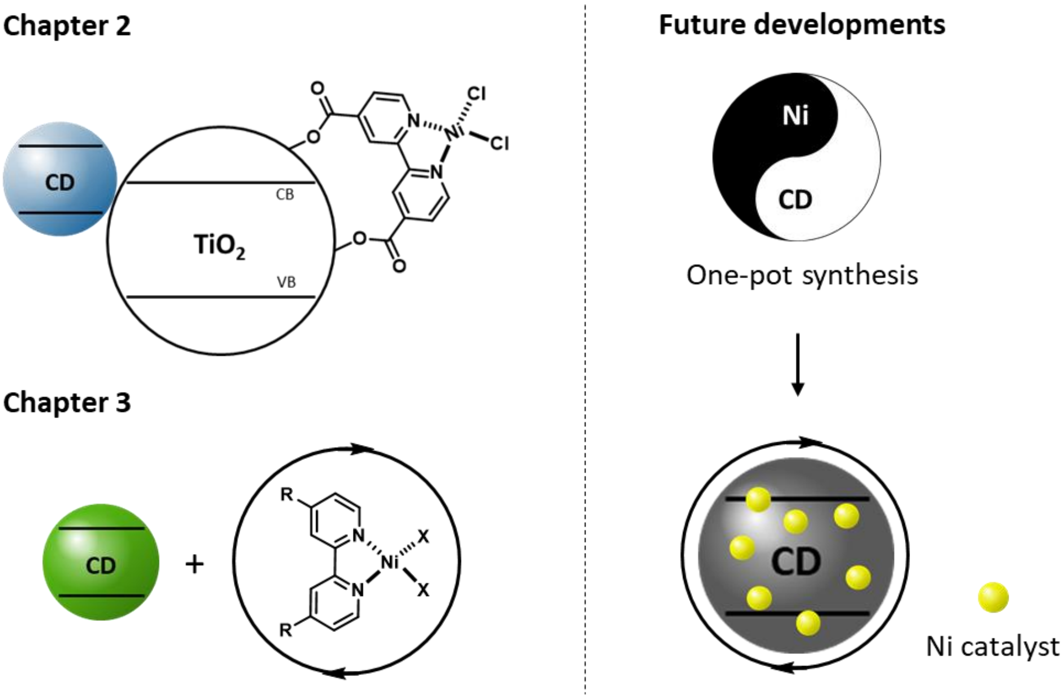

Figure 5. Schematic representation of CDs as metal-free photocatalysts in the thesis and future developments.

In Chapter 4, I reported that CDs are efficient nano-photocatalysts for energy-transfer reactions, such as the isomerization of *E*-alkenes under visible light irradiation. CDs could photocatalyze *E*-to-*Z* isomerization reactions of several different alkenes, and high yields were obtained under optimized reaction conditions for some *E*-alkenes. These are exciting preliminary results expanding the scope of CD in various areas of photocatalysis.

Possible follow-up works are listed below:

1. A broader library of CDs and extensive characterization will be performed to explore the potential factors affecting the catalytic performance.
2. The reaction scope of CDs as photocatalysts will be expanded to other visible-light-mediated energy-transfer catalysis, such as cyclization reactions.

6. Experimental section

6.1. General materials and methods

All substrates, reagents, and solvents were obtained from commercial suppliers and were used without further purification unless otherwise noted. All light-emitting diode (LED) lamps were purchased from Kessil Lighting (https://www.kessil.com/science/index.php). Analytical thin layer chromatography (TLC) was performed on pre-coated TLC-sheets, ALUGRAM Xtra SIL G/UV$_{254}$ sheets (Macherey-Nagel) and visualized with 254 nm light or staining solutions followed by heating. Purification of final compounds was carried out by flash chromatography on the Reveleris X2 Flash Chromatography System from GRACE using prepacked columns with 40 µm silica gel. Silica 60 M (0.04-0.063 mm) silica gel (Sigma Aldrich) was used for dry loading of the crude compounds on the flash chromatography system. CDs were synthesized using a domestic microwave (SEVERIN). Centrifugation of CDs and CD/titanium dioxide (TiO_2 P25) nanocomposites were carried out using an Eppendorf 5810R centrifuge and an Eppendorf 5430 centrifuge, respectively. NMR spectra were recorded on an Ascend^{TM} 400 (400 MHz, Bruker) spectrometer, and are reported in ppm relative to the residual solvent peaks. Peaks are reported as: s = singlet, d = doublet, t = triplet, q = quartet, m = multiplet or unresolved, with coupling constants in Hz. IR spectra were recorded on a Perkin-Elmer FT-IR spectrometer (Spectrum 100). The morphologies of CDs were observed using transmission electron microscopy (TEM, Zeiss EM 912Ω). The prepared CDs were diluted with distilled water to suitable concentrations and then deposited onto carbon-coated copper grids. After drying at room temperature, the samples were imaged. The morphologies and elemental composition of CDs and CD/TiO_2 P25 nanocomposites were measured using SEM-EDX (LEO 1550 system). The CD water solution was sonicated for 10 min and then deposited on the silicon substrate. The freeze-dried CD/TiO_2 P25 nanocomposites were suspended in distilled water and sonicated for 5 min. The resulting suspension was deposited on the silicon substrate. After drying at room temperature, the samples were coated with Au and imaged. Fluorescence spectra of CDs were measured using a microplate reader (SpectraMax M5, Molecular Devices). Absorption spectra of CDs and CD/TiO_2 P25 nanocomposites were collected using a Shimadzu UV-1900 (solutions), or a Shimadzu UV-2600 spectrometer equipped with an integrating sphere (solids). XRD spectra were measured with a Bruker D8 Advanced X-ray diffractometer with Cu Kα radiation. Hydrodynamic size and zeta potential of CDs were measured with a dynamic light scattering instrument (DLS, Zetasizer Nano, Malvern). PL lifetime was measured using the time-correlated single photon counting technique (TCSPC, FluoTime 250, fluorescence lifetime spectrometer). ICP-OES was carried out using a Horiba Ultra 2 instrument equipped with a photomultiplier tube detection system.

Setup for blue light experiments.[70] Two vials were placed in the middle of the stirring plate (4.5 cm away from single lamp). The reaction was irradiated with a single blue LED lamp (Kessil PR160L-440). A fan was used to avoid possible heating of the reaction mixture.

Figure 6-1. Image of the setup using a single blue LED lamp.

Setup for green light experiments.[70] Two vials were placed in the middle of the stirring plate (4.5 cm away from each lamp). The reaction was irradiated with two green LED lamps (Kessil PR160L-525). A fan was used to avoid the possible heating of the reaction mixture.

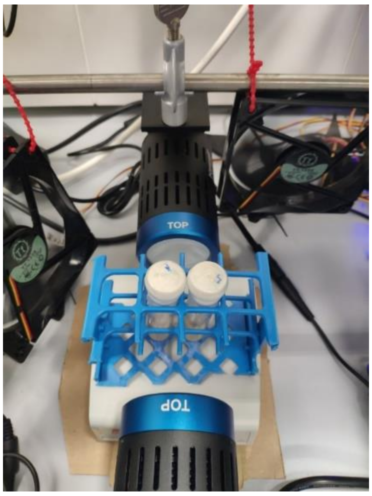

Figure 6-2. Image of the setup using two green LED lamps.

6.2. Synthesis and characterization of CD1 and CD2

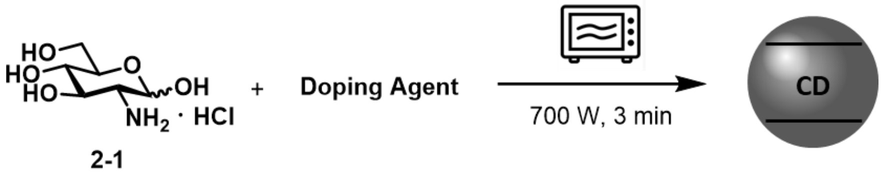

GlcN·HCl (**2-1**) was dissolved in ultrapure H_2O (20 mL) in a conical flask (300 mL). The doping agent was added and the mixture was agitated to yield a homogenous solution. The flask was transferred into a domestic microwave in a fume hood and heated at 700 W for 3 min. The crude mixture was cooled for 10 min before ultrapure H_2O (40 mL) was added. The resulting solution was filtered through a filter paper and centrifuged at 8000 rpm for 0.5 h through Amicon® Ultra-15 centrifugal filter units. The filtrate was lyophilized to yield the desired CDs.

Table 6-1. Summary of the conditions used for the synthesis of the CDs.

Entry	**CD**	**Carbon source (mmol/mL)**	**Doping agent (mmol/mL)**
1	**CD1**	GlcN·HCl (**2-1**) (0.12)	β-Ala (**2-2**) (0.13)
2	**CD2**[a]	GlcN·HCl (**2-1**) (0.15)	1,3-Diaminobenzene (**2-15**) (0.17)

[a] The doping agent was first dissolved in MeOH (10 mL) and then added to the aqueous solution (20 mL) of carbon source.

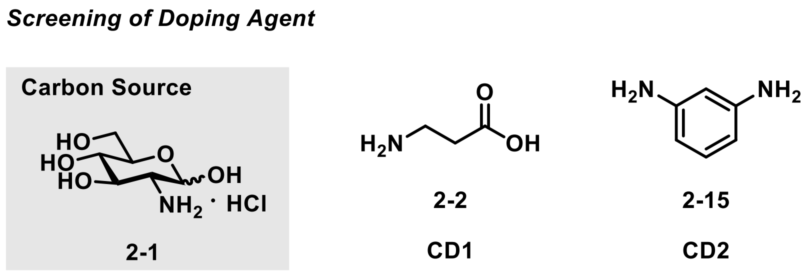

Figure 6-3. Chemical structures of carbon source and doping agents used for CD synthesis.

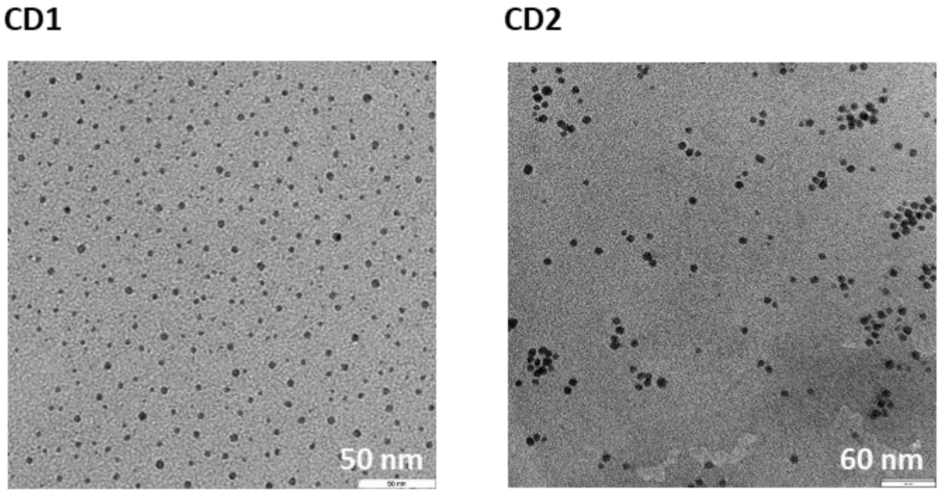

Figure 6-4. TEM images of **CD1** and **CD2**.

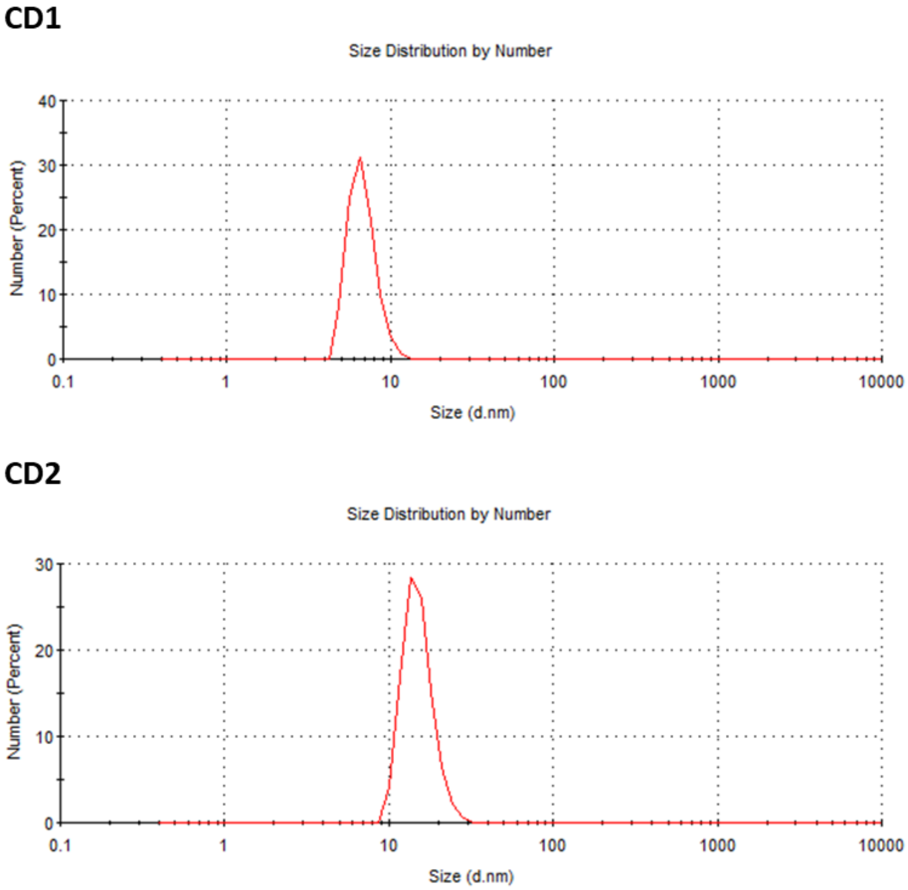

Figure 6-5. DLS profiles of **CD1** and **CD2** (H_2O, 298 K).

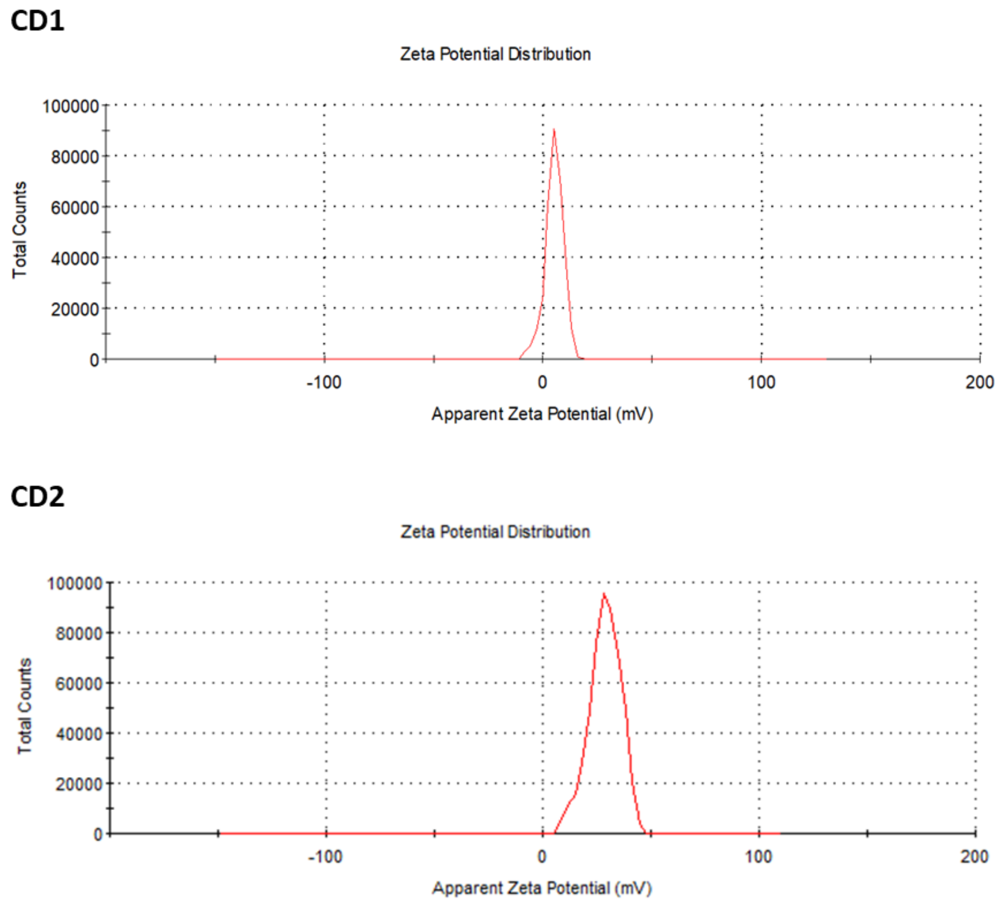

Figure 6-6. Zeta potential of **CD1** and **CD2** (H_2O, 298 K).

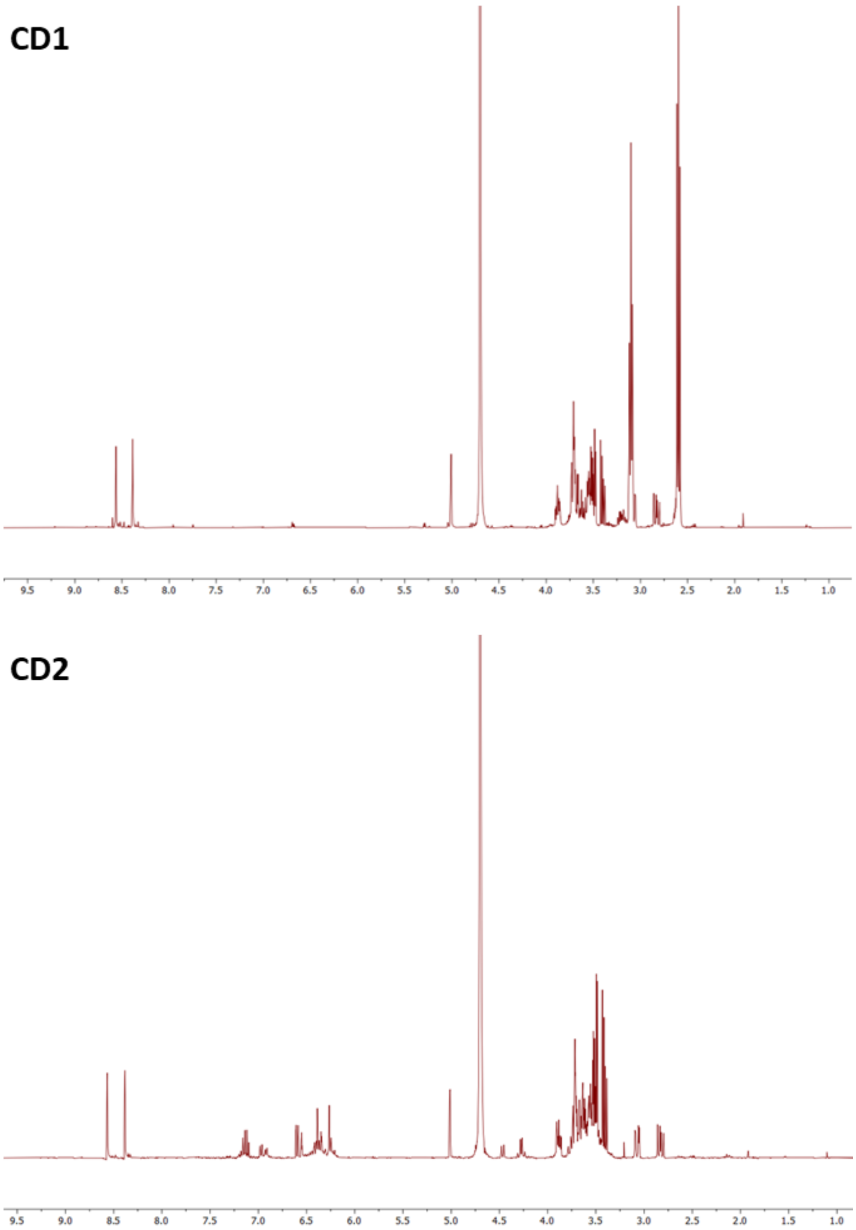

Figure 6-7. ^{1}H NMR spectra of **CD1** and **CD2** in D_2O (400 MHz).

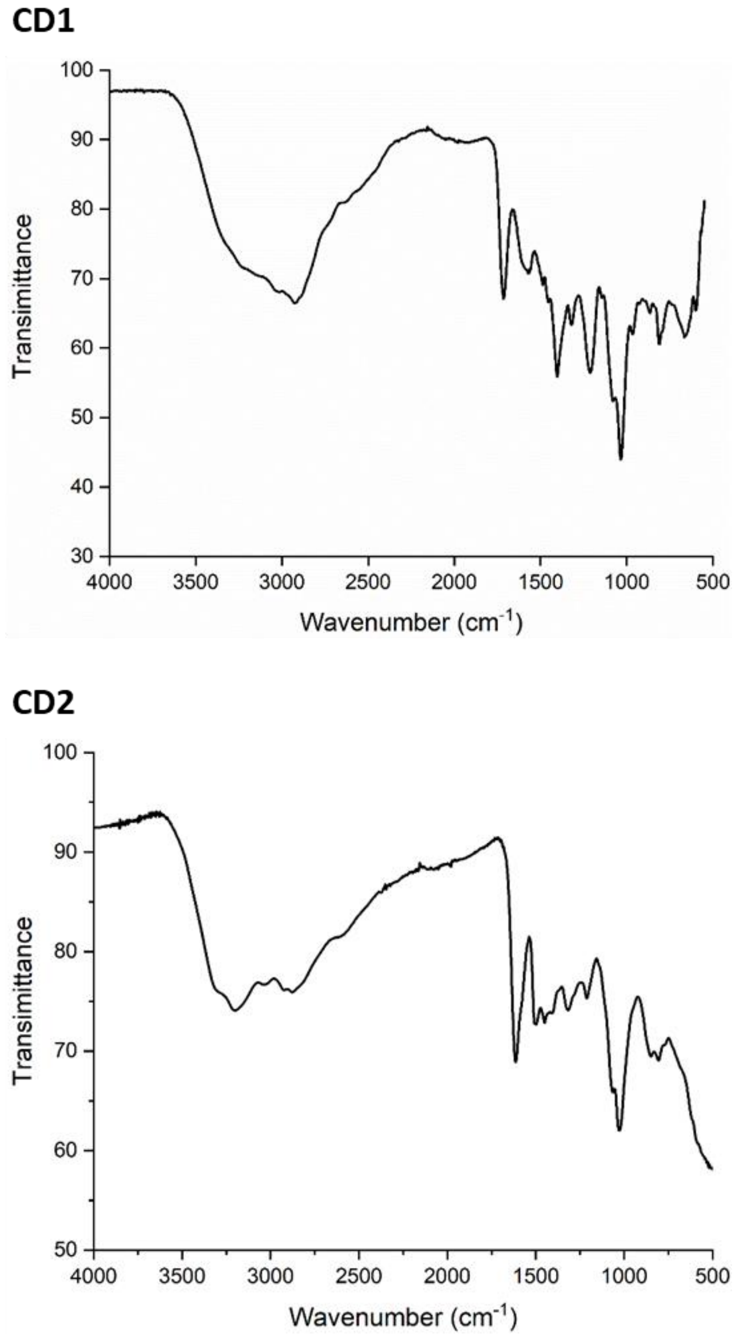

Figure 6-8. IR spectra of **CD1** and **CD2**.

Table 6-2 Elemental composition of **CD1** and **CD2**. All values are given as weight %.

	C	N	O	Cl
CD1	50.33	11.10	31.15	7.42
CD2	53.54	16.71	19.49	10.26

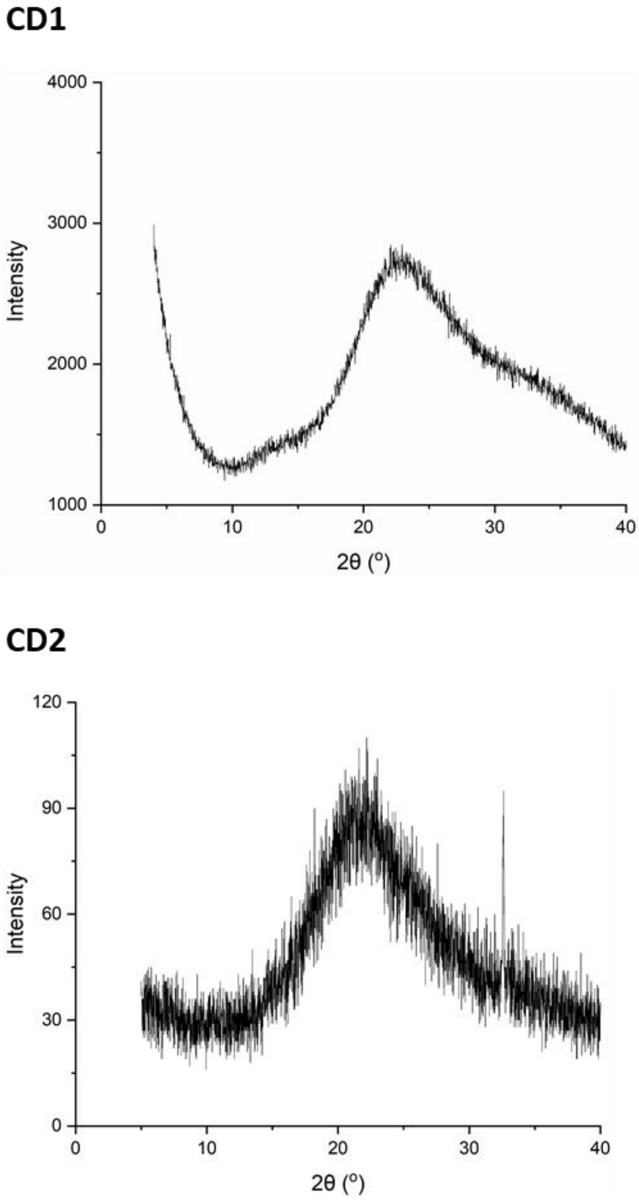

Figure 6-9. Powder XRD profiles of **CD1** and **CD2**.

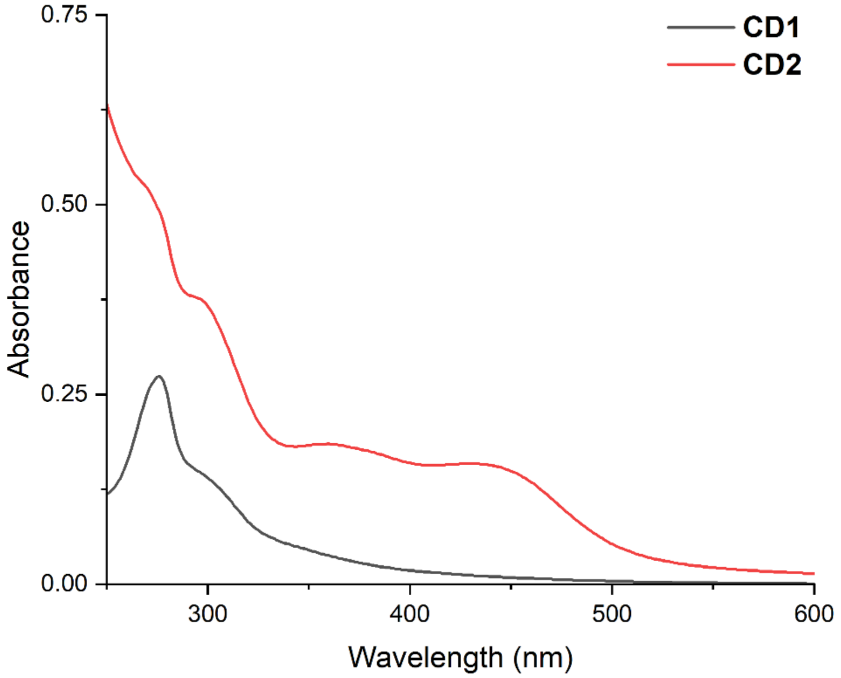

Figure 6-10. Absorption spectra of **CD1** and **CD2** (25 µg/mL, H_2O, 298 K).

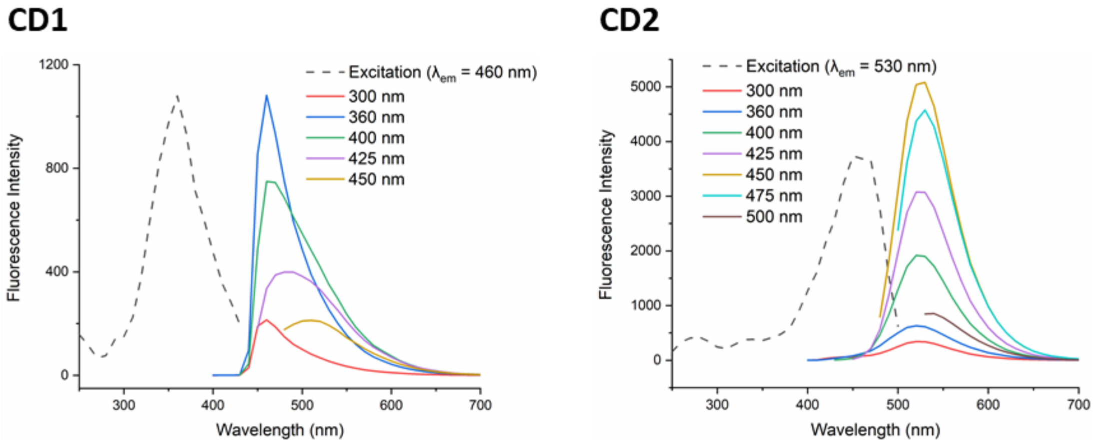

Figure 6-11. Excitation and emission spectra of **CD1** and **CD2** recorded upon excitation with different excitation wavelengths (H_2O, 298 K).

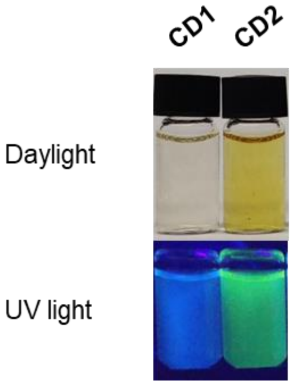

Figure 6-12. Photographs of aqueous solutions of **CD1** and **CD2** in daylight and under UV light irradiation (λ_{ex} = 366 nm).

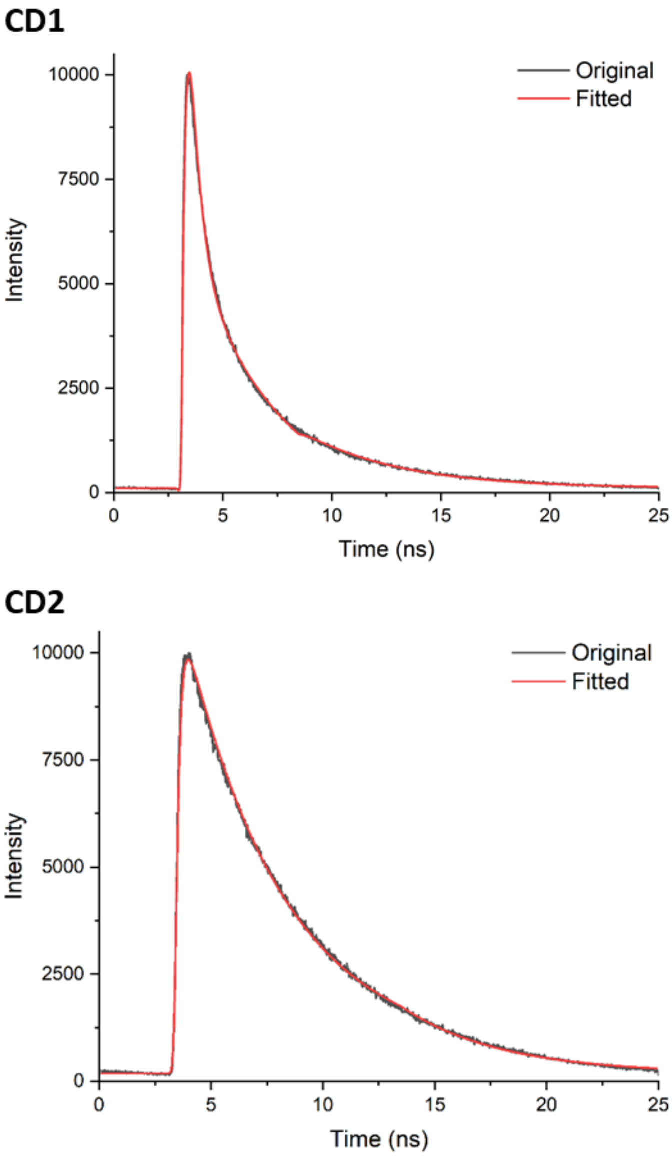

	A_1	A_2	τ_1 (ns)	τ_2 (ns)
CD1	10.49	6.131	0.451	4.454
CD2	11.164		4.399	

Figure 6-13. Photoluminescence lifetime of **CD1** and **CD2** (H_2O, 298 K).

Quantification of primary amines on the CD surface. Primary amines on the CD surface were quantified using the commercially available ninhydrin reagent (Sigma-Aldrich) using a reported protocol (https://www.sigmaaldrich.com/deepweb/assets/sigmaaldrich/product/documents/327/050/n7285pis.pdf). The reference curve was produced using the amino acid β-Ala (**2-2**) containing a primary amine group (**Figure 6-14**). The absorption values of sample solution were obtained to be 0.526 (**CD1**) and 0.952 (**CD2**) at 570 nm. The primary amines on the CD surface were quantified to be 5016 µmol/g (**CD1**) and 9303 µmol/g (**CD2**), respectively.

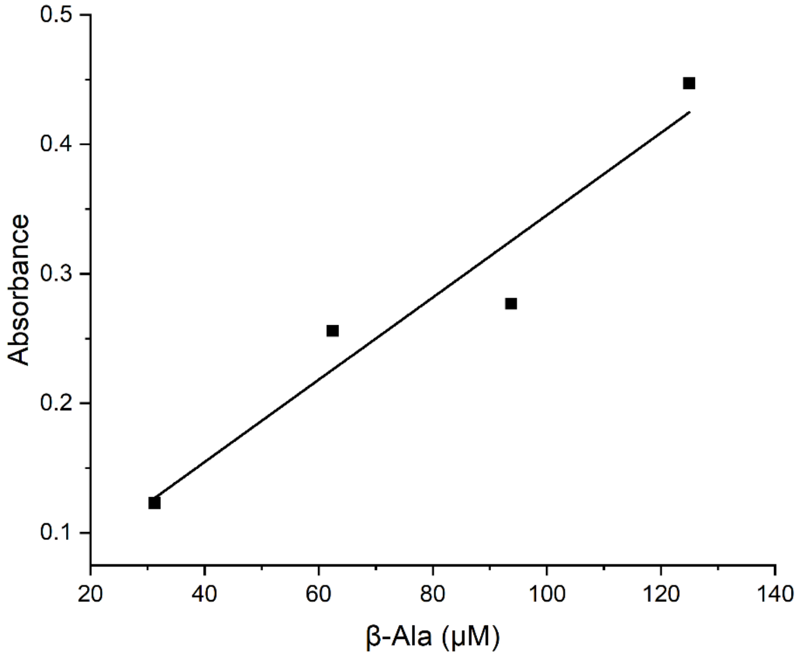

Figure 6-14. Reference plot showing the absorbance (λ = 570 nm) of solutions of β-Ala at different concentrations in the presence of the ninhydrin reagent.

HOMO and LUMO energy levels of CD2. Cyclic voltammetry (CV) as an electrochemical technique can be used to measure the HOMO and LUMO energy levels of **CD2**. The cyclic voltammetries of ferrocene and **CD2** were recorded with a three-electrode cell (a Pt working electrode, a Ag/AgCl reference electrode and a Pt counter electrode) at room temperature. A MeCN solution (10 mL) of 0.1 M tetrabutylammonium hexafluorophosphate was prepared as the supporting electrolyte of ferrocene (1 mg/mL). Meanwhile, a MeCN solution (8 mL) of 0.1 M tetrabutylammonium hexafluorophosphate was prepared as the supporting electrolyte of **CD2** and the aqueous solution (2 mL) of **CD2** (0.6 mg) was added for measurements.

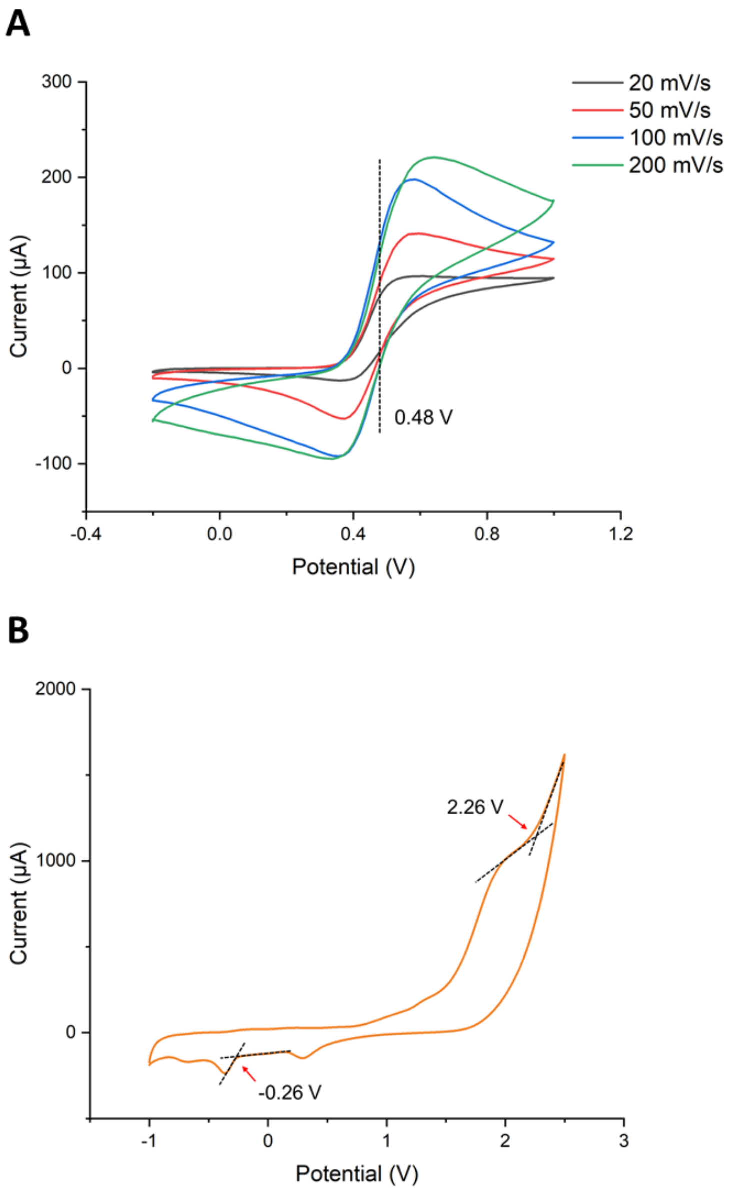

Figure 6-15. Cyclic voltammograms of ferrocene (A, scan rate: 20, 50, 100, 200 mV/s) and **CD2** (B)

As shown in **Figure 6-15A**, the value of the Fc^+/Fc formal potential is 0.48 V versus Ag/AgCl. Owing to a more positive potential of saturated calomel electrode (SCE, +44 mV vs. Ag/AgCl) and the value (-5.1 eV) in the Fermi scale of the Fc^+/Fc formal potential (assuming its value is 0.40 V vs. SCE in MeCN),[158, 159] the value of the Fc^+/Fc formal potential can be -5.06 eV in the Fermi scale assuming its value is 0.40 V vs. Ag/AgCl.

The HOMO and LUMO energy levels of **CD2** can be determined using the following equations:[158]

$$E_{HOMO} = -(E_{onset,ox} - 0.48 + 5.06)eV = -(E_{onset,ox} + 4.58)eV$$

$$E_{LUMO} = -(E_{onset,red} - 0.48 + 5.06)eV = -(E_{onset,red} + 4.58)eV$$

$$E_{gap} = (E_{onset,ox} - E_{onset,red})eV$$

$E_{onset,ox}$ is the onset of oxidation potential; $E_{onset,red}$ is the onset of reduction potential.

As shown in **Figure 6-15B**, the onset of oxidation ($E_{onset,ox}$) and reduction ($E_{onset,red}$) potential are 2.26 V and -0.26 V, respectively. According the above equations, the HOMO and LUMO energy levels of **CD2** were calculated to be -6.84 eV and -4.32 eV, respectively, the electrochemical band gap was calculated to be 2.52 eV.

6.3. Experimental section for Chapter 2

6.3.1. Synthesis and characterization of other CDs

The carbohydrate carbon source was dissolved in ultrapure H_2O (20 mL) in a conical flask (300 mL). The doping agent was added and the mixture was agitated to yield a homogenous solution. The flask was transferred into a domestic microwave in a fume hood and heated at 700 W for the respective time. The crude mixture was cooled for 10 min before ultrapure H_2O (40 mL) was added. The resulting solution was filtered through a filter paper and centrifuged at 8000 rpm for 0.5 h through Amicon® Ultra-15 centrifugal filter units. The filtrate was lyophilized to yield the desired CDs.

Table 6-3 Summary of the conditions used for the synthesis of the CDs.

Entry	**CD**	**Carbon source (mmol/mL)**	**Doping agent (mmol/mL)**	**Time / min**
1	**CD3**	GlcN·HCl (**2-1**) (0.23)	l-Cys (**2-16**) (0.25)	3
2	**CD4**		PEG (**2-17**) (0.25)	9
3	**CD5**		Gly (**2-18**) (0.25)	3
4	**CD6**	Glc (**1-1**) (0.12)	β-Ala (**2-2**) (0.13)	4.5
5	**CD7**	GlcNAc (**2-19**) (0.12)		4.5
6	**CD8**	Gal (**2-20**) (0.12)		4.5
7	**CD9**	Lac (**2-21**) (0.12)		4.5
8	**CD10**	Pullulan (**2-22**) (25 mg/mL)		5

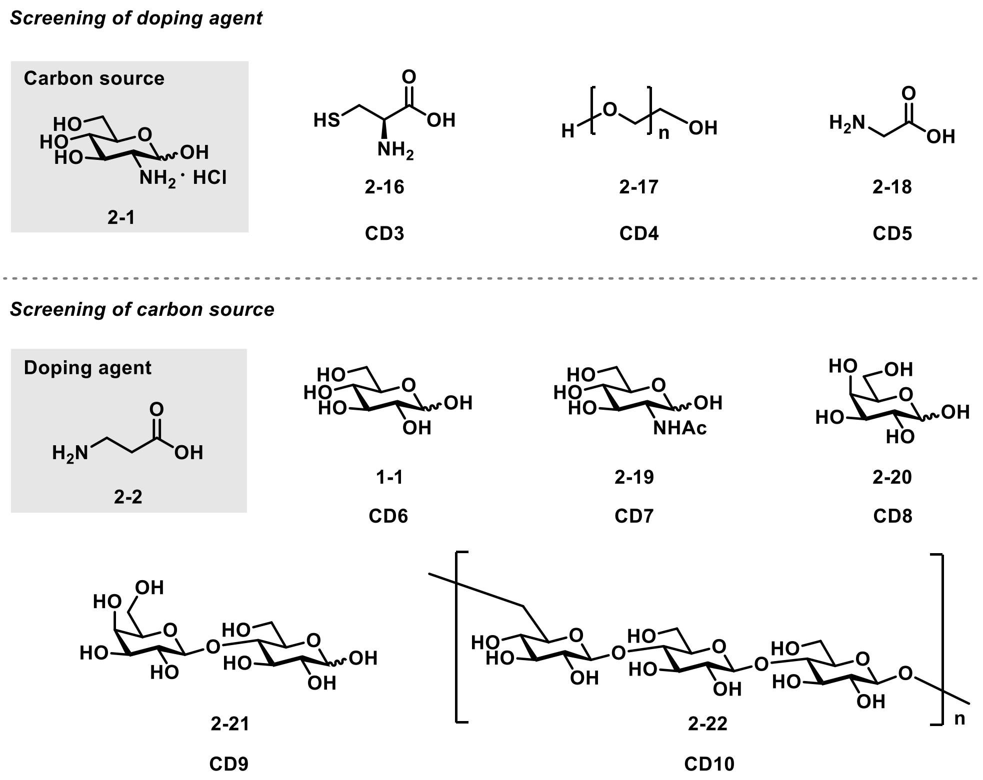

Figure 6-16. Chemical structures of carbon sources and doping agents used for CD synthesis.

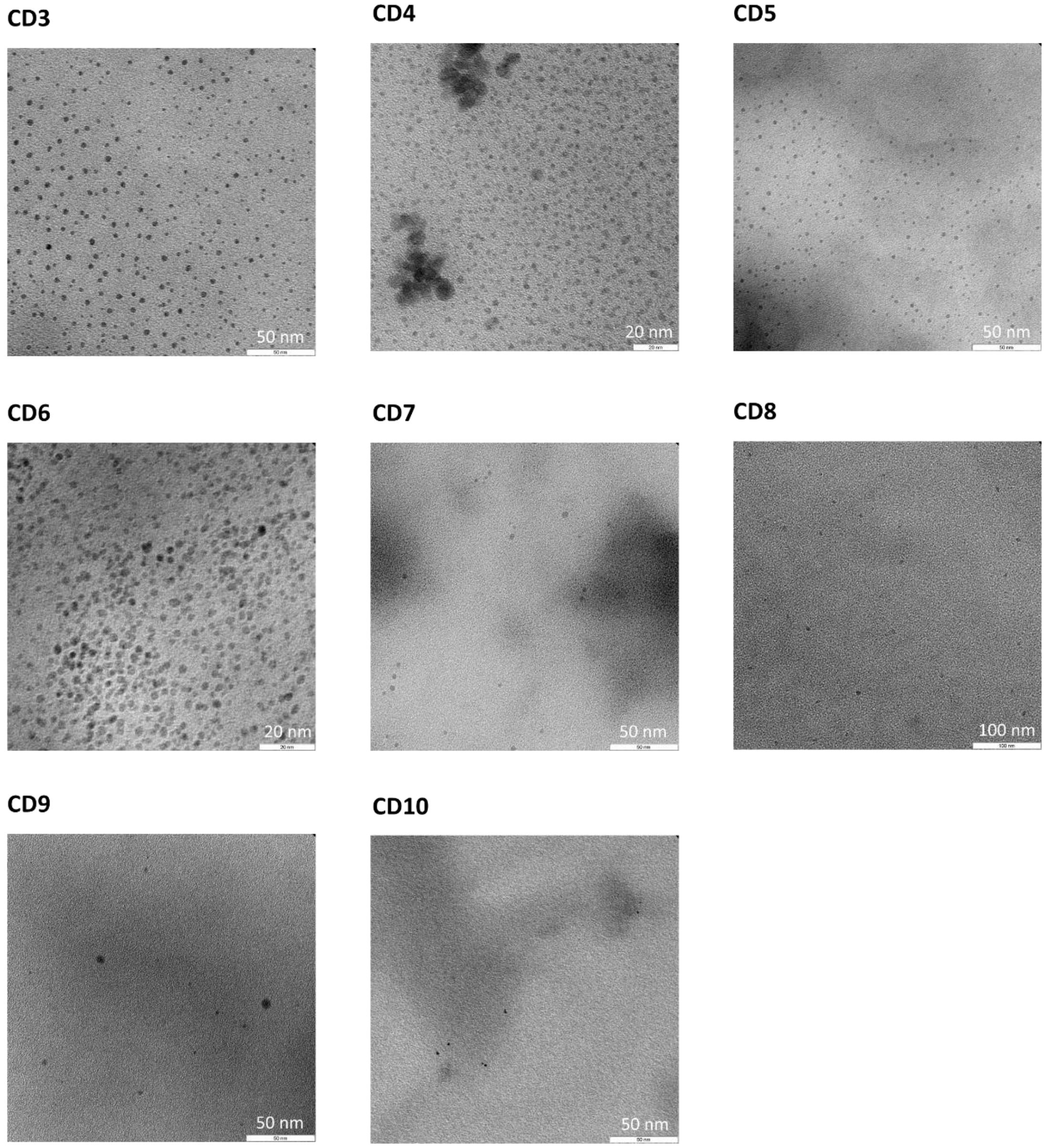

Figure 6-17. TEM images of **CD3**-**CD10**.

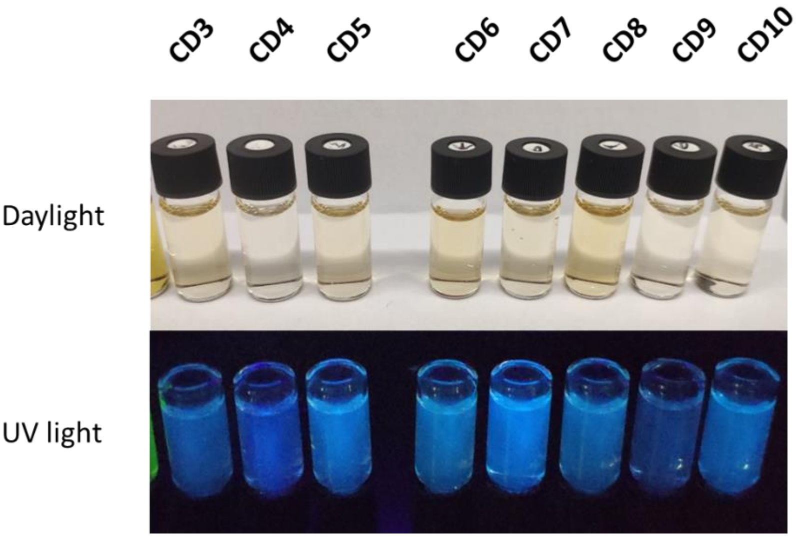

Figure 6-18. Photographs of aqueous solutions of **CD3-CD10** in daylight and under UV light irradiation (λ_{ex} = 366 nm).

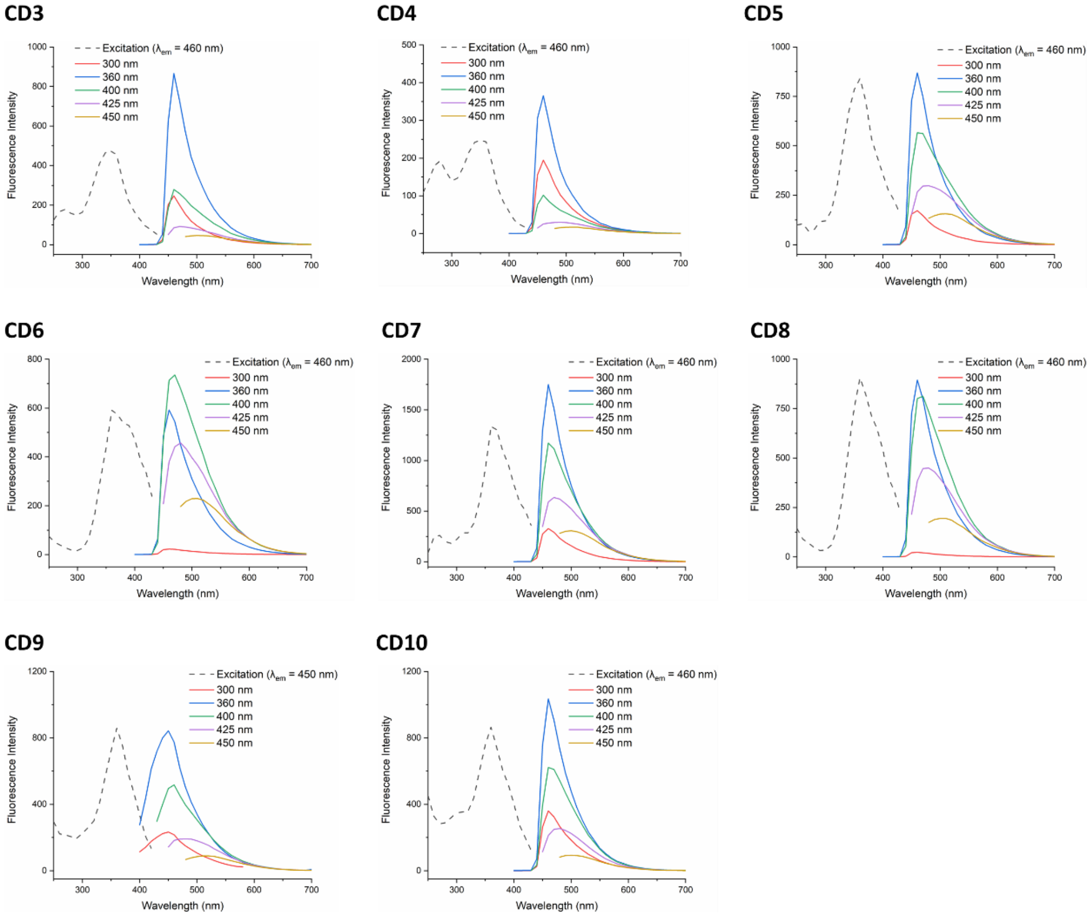

Figure 6-19. Excitation and emission spectra of **CD3-CD10** recorded upon excitation with different excitation wavelengths (H_2O, 298 K).

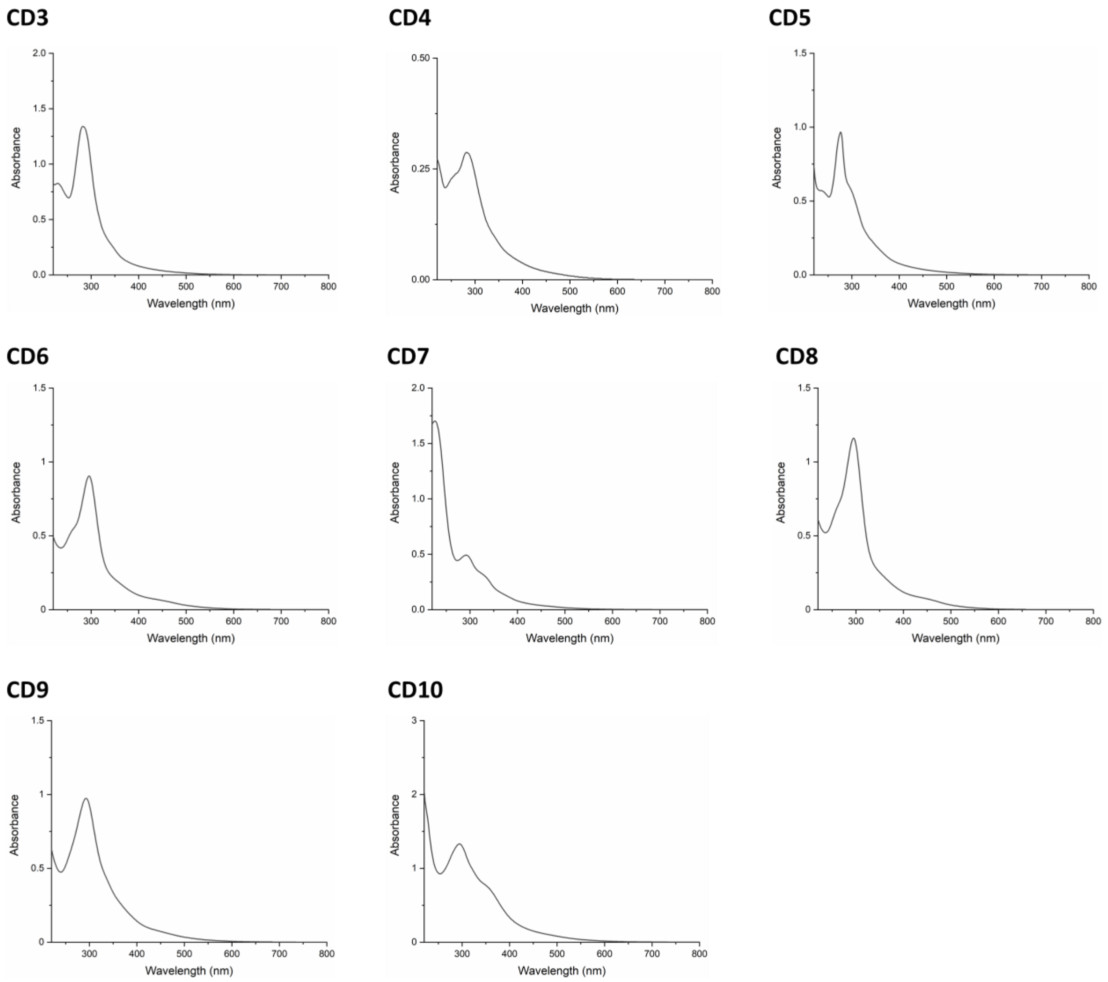

Figure 6-20. Absorption spectra of **CD3**-**CD10** (H_2O, 298 K).

6.3.2. Preparation and characterization of CD/TiO_2 P25 nanocomposites

TiO_2 P25 (120 mg) was dispersed in ultrapure H_2O (80 mL) in a round-bottom flask. The respective amount of CDs was added to prepare nanocomposites with different CD-to-TiO_2 P25 mass ratios. The mixture was shielded from light and stirred for 24 h at room temperature. The resulting CD/TiO_2 nanocomposites were centrifuged at 5000 rpm for 15 min and further washed two times with ultrapure H_2O. The nanocomposites were lyophilized to afford a light brown powder. The amount of CDs immobilized on the TiO_2 P25 surface was determined using UV-Vis absorption spectroscopy.

Table 6-4 Conditions used for the preparation of the CD/TiO_2 nanocomposites.

Entry	CD	CD-to-TiO_2 P25 mass ratio	CD Immobilization (weight % (CD/nanocomposite))
1	**CD1**	1 : 20	1.5
2		1 : 10	1.8
3		1 : 4	2.4
4		1 : 1	5.0
5		4 : 1	8.1
6		1 : 1 (CD-to-SiO_2)	1.6
7	**CD2**	1 : 1	-[a]
8	**CD3**	1 : 1	2.5
9	**CD4**	1 : 1	13.6
10	**CD5**	1 : 1	3.4
11	**CD6**	1 : 1	3.7
12	**CD7**	1 : 1	11.9
13	**CD8**	1 : 1	3.0
14	**CD9**	1 : 1	11.4
15	**CD10**	1 : 1	27.2

[a] Quantification by UV-Vis was not possible due to the formation of side-products in the solution that affected the measurements.

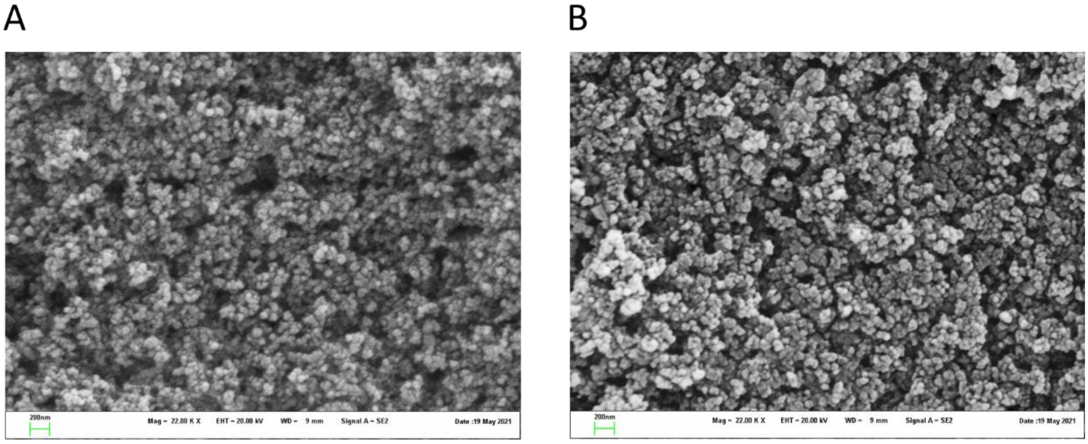

Sample	C	O	Ti	Ni
CD1/TiO$_2$	23.86	59.04	17.15	0
CD1/TiO$_2$ (after)	32.75	60.79	6.26	0.23

Figure 6-21. SEM image and elemental composition of **CD1**/TiO$_2$ P25 nanocomposite (A) and **CD1**/TiO$_2$ P25 nanocomposite after the catalytic reaction (B). All values are given as atomic %.

Table 6-5 ICP-OES measurements of the Ni content of **CD1**/TiO$_2$ P25 nanocomposite and **CD1**/TiO$_2$ P25 nanocomposite after the catalytic reaction.

Sample	Ni (mg/g)
CD1/TiO$_2$	0.016
CD1/TiO$_2$ (after)	24.8

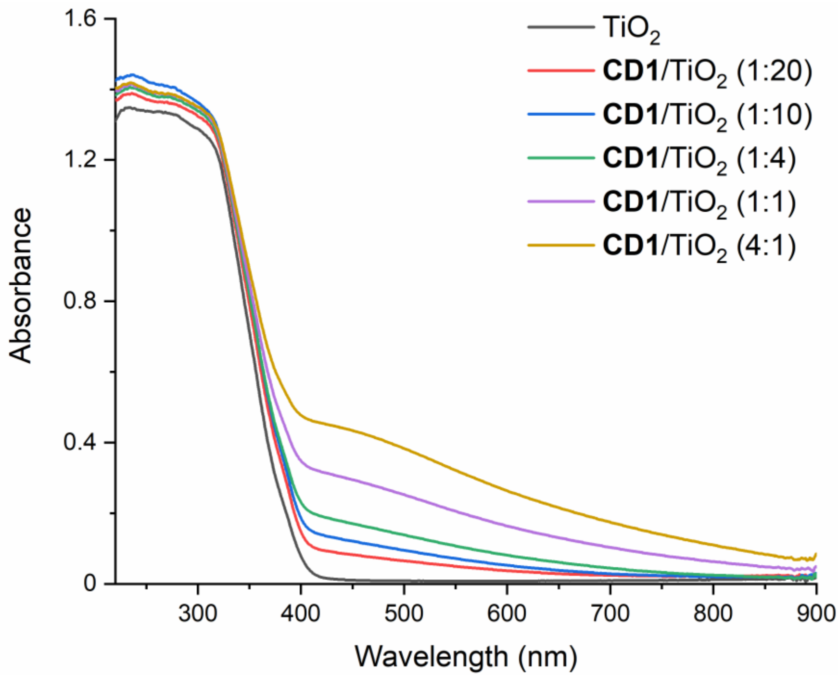

Figure 6-22. Absorption spectra (solid state) of **CD1**/TiO_2 nanocomposites prepared using different **CD1**-to-TiO_2 P25 mass ratios.

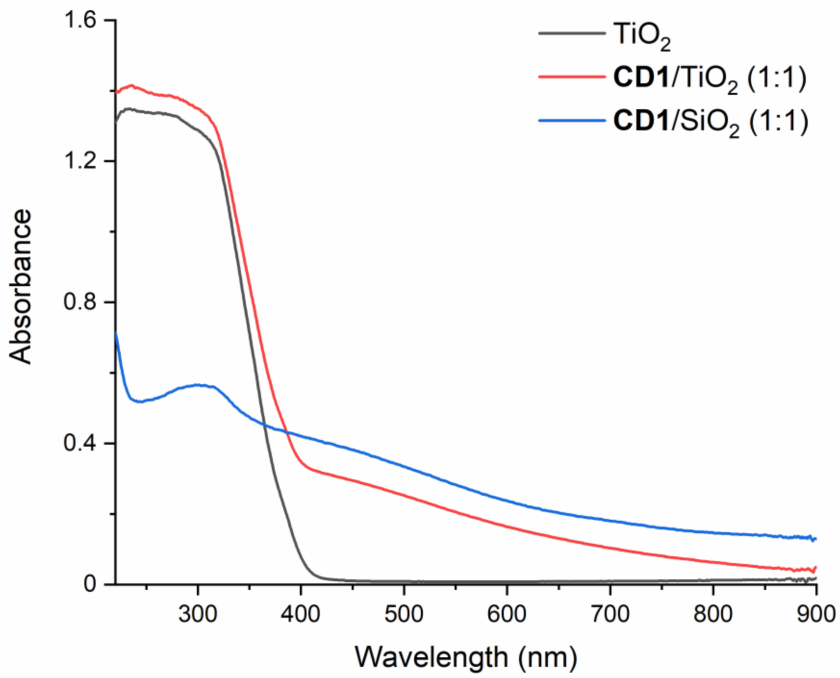

Figure 6-23. Absorption spectra (solid state) of **CD1**/TiO_2 and **CD1**/SiO_2 nanocomposites (mass ratio = 1:1).

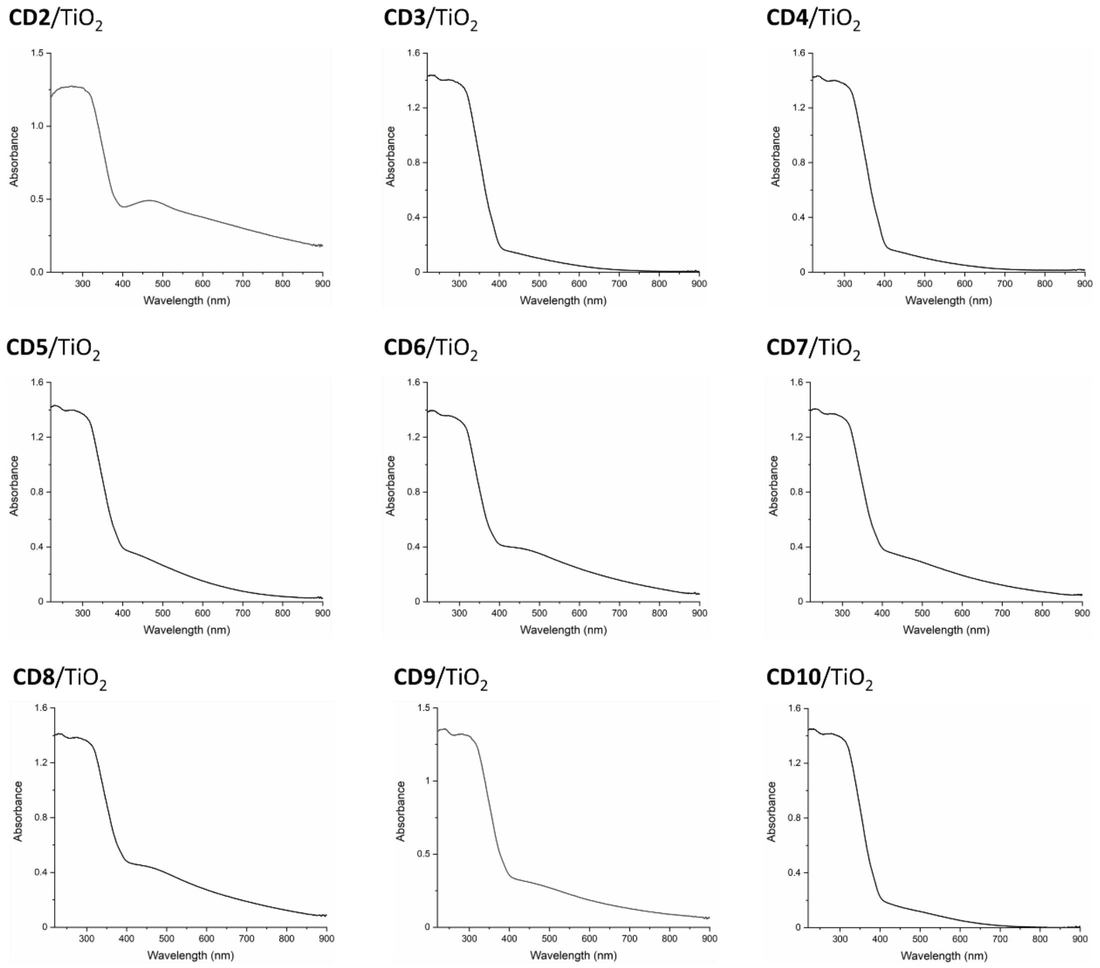

Figure 6-24. Absorption spectra (solid state) of **CD2**/TiO$_2$-**CD10**/TiO$_2$ nanocomposites.

6.3.3. Cross-coupling reaction

6.3.3.1. *O*-arylation of Boc-Pro-OH

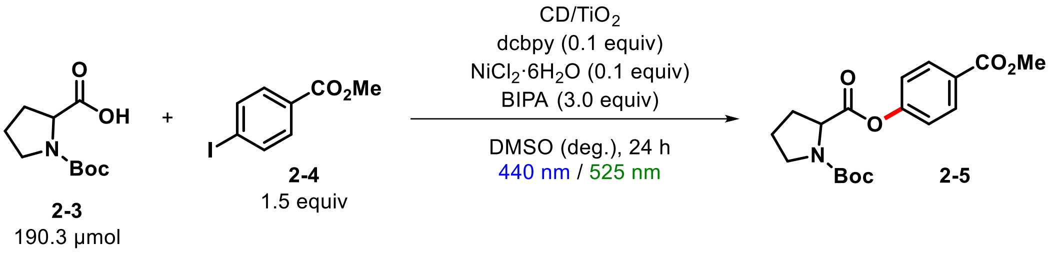

General experimental procedure. Boc-Pro-OH (**2-3**, 41.0 mg, 190.3 µmol), methyl 4-iodobenzoate (**2-4**, 74.8 mg, 285.4 µmol) and the respective CD/TiO$_2$ nanocomposite (**Table 6-6**) were added to an oven-dried glass vial equipped with a stir bar. Subsequently, a DMSO solution (3 mL) of dcbpy (4.7 mg, 19.0 µmol), NiCl$_2$·6H$_2$O (4.5 mg, 19.0 µmol), and BIPA (90.5 µL, 570.8 µmol) were added. The glass vial was sealed with a septum and Parafilm. The reaction mixture was stirred and sonicated for 10 min to obtain a fine dispersion and subsequently degassed with Argon for 10 min. The vial was then irradiated with the respective LED lamps at room temperature for the respective time. 1,3,5-Trimethoxybenzene (32.0 mg, 190.3 µmol) was added as internal standard to determine NMR yields. An aliquot of the resulting mixture (~250 µL) was filtered through a syringe filter, diluted with DMSO-d$_6$ (~250 µL) and subjected to ^{1}H-NMR analysis.

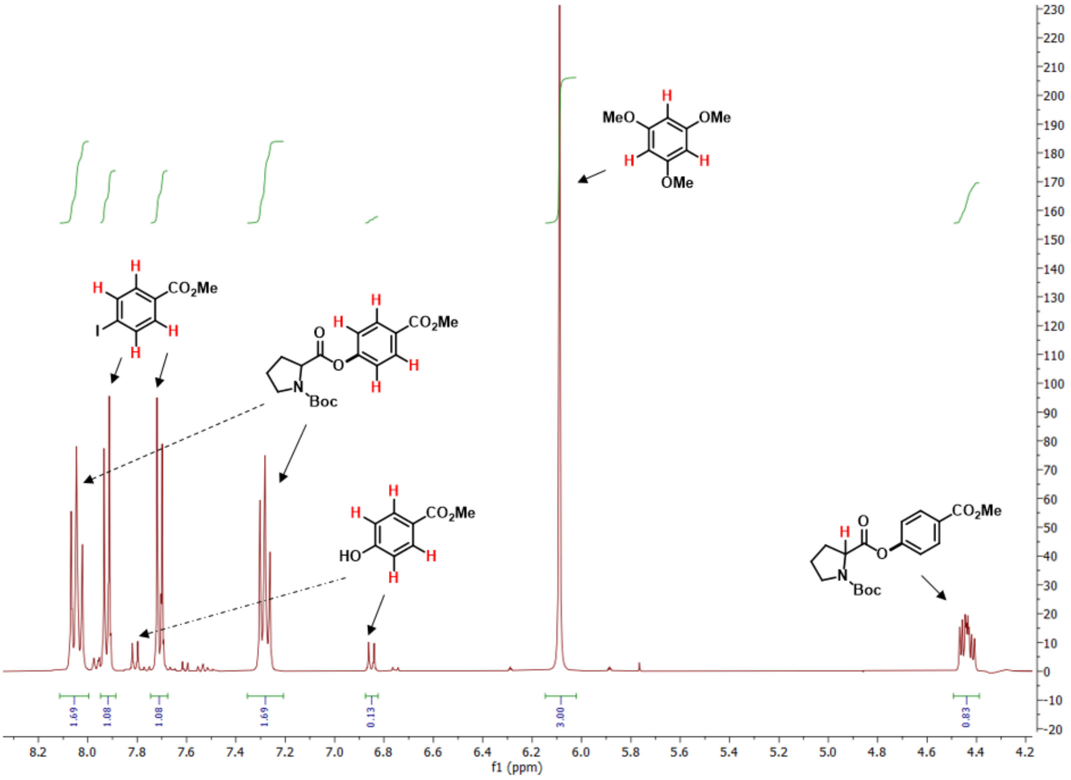

Figure 6-25. Representative ^{1}H-NMR spectrum of the crude reaction mixture to determine yields by ^{1}H-NMR analysis using 1,3,5-trimethoxybenzene as internal standard (DMSO-d_6, 400 MHz).

Table 6-6 Summary of the CD/TiO_2 nanocomposites used in the photocatalyzed C-O cross-coupling of Boc-Pro-OH with methyl 4-iodobenzoate.

Entry	**Nanocomposite**	**Initial CD-to-TiO_2 P25 mass ratio[a]**	**CD Immobilization[b] (weight % (CD/nanocomposite))**	**Amount[c] / mg**
1	TiO_2 P25	-	-	30.0
2	**CD1**	-	-	30.0
3	**CD1**/TiO_2	1 : 20	1.5	30.5
4		1 : 10	1.8	30.5
5		1 : 4	2.4	30.8
6		1 : 1	5.0	31.6
7		4 : 1	8.1	32.6
8		1 : 1 (CD-to-SiO_2)	1.6	30.5
9	**CD2**/TiO_2	1 : 1	-	30.0
10	**CD3**/TiO_2	1 : 1	2.5	30.8
11	**CD4**/TiO_2	1 : 1	13.6	34.7
12	**CD5**/TiO_2	1 : 1	3.4	31.1
13	**CD6**/TiO_2	1 : 1	3.7	31.1
14	**CD7**/TiO_2	1 : 1	11.9	34.1
15	**CD8**/TiO_2	1 : 1	3.0	30.9
16	**CD9**/TiO_2	1 : 1	11.4	33.9
17	**CD10**/TiO_2	1 : 1	27.2	41.2

[a] CD-to-TiO_2 P25 mass ratio used for the preparation of the nanocomposite. [b] Weight % of CD immobilized on TiO_2 as calculated by UV-Vis spectroscopy. [c] Amount of nanocomposite used in the C-O arylation of Boc-Pro-OH.

Procedure to obtain the isolated yield. An oven-dried vial (19 x 100 mm) equipped with a stir bar was charged with **CD1**/TiO_2 (63.2 mg), Boc-Pro-OH (**2-3**, 82 mg, 380.6 µmol, 1.0 equiv), methyl 4-iodobenzoate (**2-4**, 149.6 mg, 571 µmol, 1.5 equiv), $NiCl_2 \cdot 6H_2O$ (9 mg, 38 µmol, 10 mol%) and dcbpy (9.3 mg, 38 µmol, 10 mol%). Subsequently, DMSO (anhydrous, 6 mL) and BIPA (180.9 µL, 1.14 mmol, 3.0 equiv) were added and the vial was sealed with a septum and Parafilm. The reaction mixture was sonicated for 5-10 min followed by stirring for 5 min to obtain a fine dispersion. The mixture was then degassed by bubbling Argon for 10 min. The mixture was irradiated using the 440 nm setup with rapid stirring (1400 rpm). After 40 h, one equivalent of 1,3,5-trimethoxybenzene (internal standard, 64 mg, 380 µmol) was added and the mixture was stirred for 5 min. An aliquot of the reaction mixture (~200 µL) was filtered, diluted with DMSO-d_6 and subjected to ^{1}H-NMR analysis to determine the NMR yield (90%). Thereafter, the NMR sample was combined with the reaction mixture. The reaction mixture was diluted with H_2O (40 mL) and extracted with dichloromethane (3 x 30 mL). The combined organic phases were washed with brine (50 mL), dried over Na_2SO_4 and concentrated. The product was purified by flash column chromatography (SiO_2, Hexane/EtOAc elution gradient of 0-20%) on a Grace Reveleris system using a 12 g cartridge. In some cases, mixed fractions containing small amounts of the phenol byproduct and the desired product were observed. These could be easily purified by a basic extraction (DCM and 0.5 M NaOH), followed by drying the organic phase over Na_2SO_4 and solvent evaporation to maximize the reaction yield. The title compound was isolated as a yellowish solid.

Isolated yield: 84% (111.5 mg, 319 µmol)

1-(tert-butyl) 2-(4-(methoxycarbonyl)phenyl) pyrrolidine-1,2-dicarboxylate 2-5: ^{1}H NMR (400 MHz, $CDCl_3$) rotameric mixture, δ 8.04 (m, 2H), 7.16 (m, 2H), 4.49 (dd, *J* = 8.6, 4.4 Hz, 0.4H), 4.43 (dd, *J* = 8.7, 4.3 Hz, 0.6H), 3.87 (m, 3H), 3.66 – 3.39 (m, 2H), 2.42 – 2.26 (m, 1H), 2.19 – 2.09 (m, 1H), 2.07 – 1.86 (m, 2H), 1.44 (m, 9H). ^{13}C NMR (151 MHz, $CDCl_3$) rotameric mixture, signals for minor rotamer are enclosed in parenthesis δ (171.21) 171.16, (166.37) 166.23, 154.51 (154.23), 153.68, 131.29 (131.15), 127.87 (127.71), (121.57) 121.20, 80.36, (80.16), 59.23 (59.14), 52.28 (52.21), (46.69) 46.50, 31.06 (30.01), 28.45, (24.60) 23.77.

The data are in full agreement with those previously published in the literature.[70]

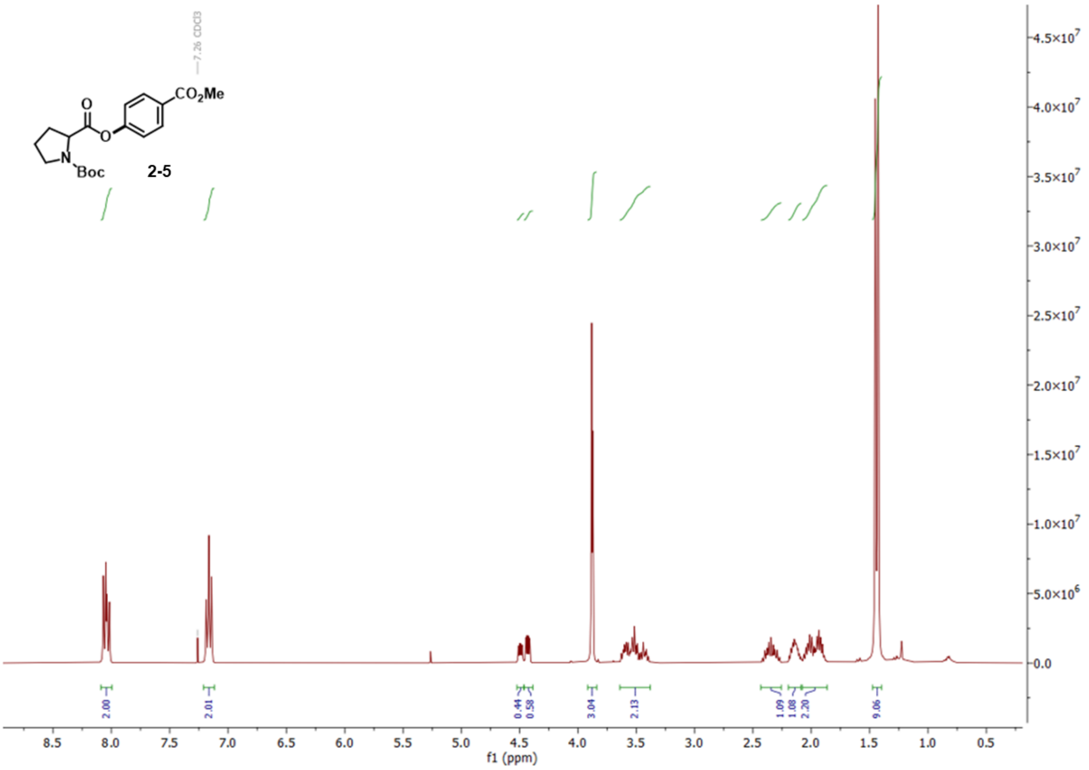

Figure 6-26. ^{1}H-NMR spectrum of compound **2-5** ($CDCl_3$, 400 MHz).

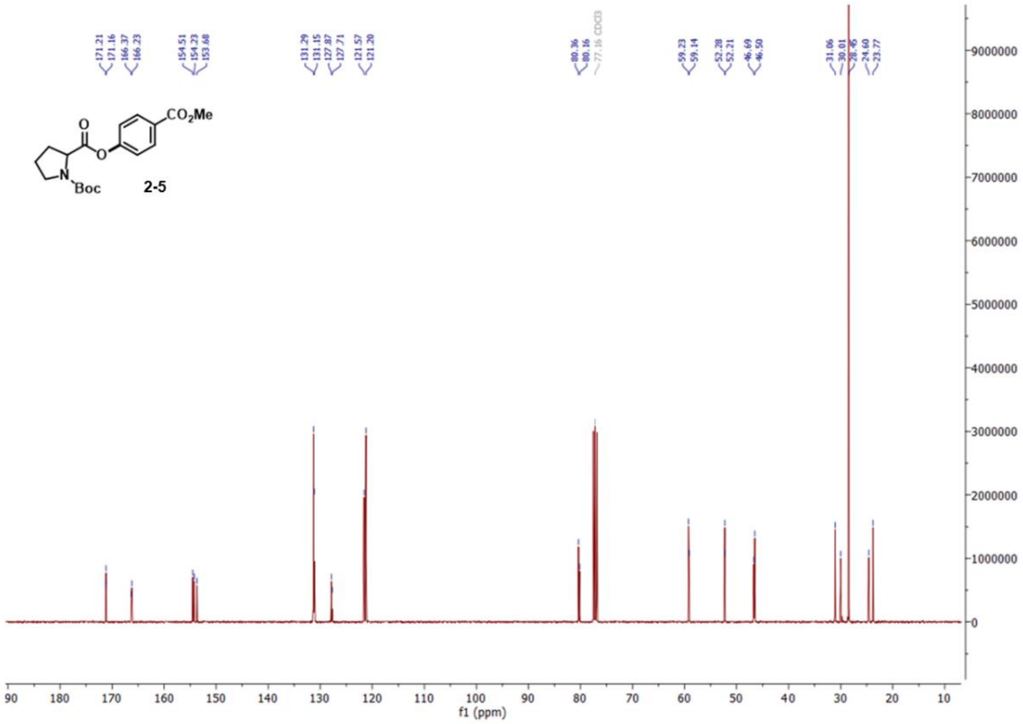

Figure 6-27. ^{13}C-NMR spectrum of compound **2-5** ($CDCl_3$, 151 MHz).

Table 6-7 Screening of **CD1**/TiO_2 nanocomposites prepared using different **CD1**-to-TiO_2 P25 mass ratios for the metallaphotocatalytic *O*-arlyation of Boc-Pro-OH with methyl 4-iodobenzoate.

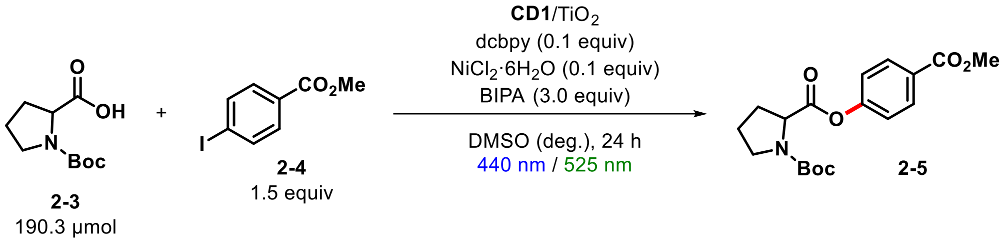

Entry	CD1-to-TiO_2 P25 mass ratio[a]	2-5 [%][b]	2-5 [%][c]
1	1 : 20	52	8
2	1 : 10	64	10
3	1 : 4	80	19
4	**1 : 1**	**83**	**22**
5	**1 : 1**[d]	**84**	-
6	4 : 1	70	14

[a] CD-to-TiO_2 P25 mass ratio used for the preparation of the nanocomposite. Reaction conditions: methyl 4-iodobenzoate (285.4 µmol), Boc-Pro-OH (190.3 µmol), $NiCl_2 \cdot 6H_2O$ (19.0 µmol) and dcbpy (19.0 µmol) in DMSO (anhydrous, 3 mL), BIPA (570.8 µmol), **CD1**/TiO_2, 24 h. NMR yields were determined by ^{1}H-NMR using 1,3,5-trimethoxybenzene as internal standard. [b] 440 nm LED lamp (50% power). [c] 525 nm LED lamp (200% power). [d] **CD1**/TiO_2 stored at room temperature for 26 weeks. deg. = degassed.

Table 6-8 Screening of different amount of **CD1**/TiO_2 nanocomposites for the metallaphotocatalytic *O*-arylation of Boc-Pro-OH with methyl 4-iodobenzoate.

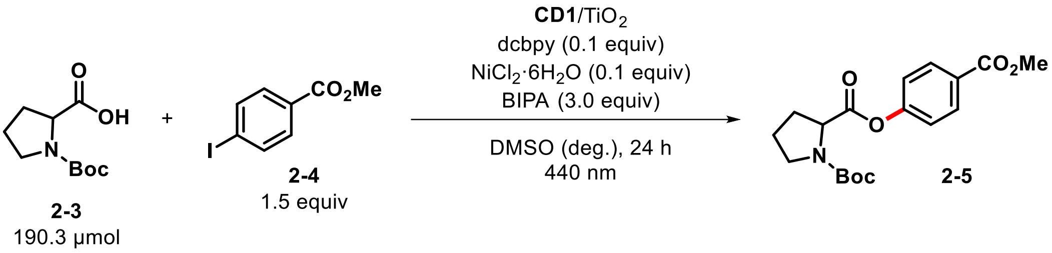

Entry	CD1/TiO_2 / mg	2-5 [%]
1	20	85
2	10	70
3	5	63
4	1	49
5	0	7

Reaction conditions: methyl 4-iodobenzoate (285.4 μmol), Boc-Pro-OH (190.3 μmol), $NiCl_2 \cdot 6H_2O$ (19.0 μmol) and dcbpy (19.0 μmol) in DMSO (anhydrous, 3 mL), BIPA (570.8 μmol), **CD1**/TiO_2, 440 nm LED lamp (50% power), 24 h. NMR yields were determined by ^1H-NMR using 1,3,5-trimethoxybenzene as internal standard. deg. = degassed.

6.3.3.2. *O*-arylation of MeOH

An oven-dried vial (19 x 100 mm) equipped with a stir bar was charged with **CD1**/TiO_2 (15.8 mg), methyl 4-bromobenzoate (**2-6**, 20.47 mg, 95.2 µmol, 1.0 equiv), $NiBr_2 \cdot 3H_2O$ (nickel(II) bromide trihydrate, 2.6 mg, 9.5 µmol, 10 mol%) and mcbpy (4'-methyl-2,2'-bipyridine-4-carboxylic acid, 2.1 mg, 9.5 µmol, 10 mol%). Subsequently, MeOH (anhydrous, 1.5 mL) and BIPA (45 µL, 285.6 µmol, 3.0 equiv) were added and the vial was sealed with a septum and Parafilm. The reaction mixture was sonicated for 5-10 min followed by stirring for 5 min to obtain a fine dispersion. The mixture was then degassed by bubbling Argon for 10 min. The mixture was irradiated using the 440 nm LED setup with rapid stirring (1400 rpm). After 14 h, one equivalent of 1,3,5-trimethoxybenzene (internal standard, 16 mg, 95.2 µmol) was added and the mixture was stirred for 5 min. An aliquot of the reaction mixture (~200 µL) was filtered, diluted with DMSO-d_6 and subjected to ^{1}H-NMR analysis. The product was identified by spiking the crude reaction mixture with a pure sample of the desired product.

The data are in full agreement with those previously published in the literature.[149]

Table 6-9 *O*-arylation of methanol using **CD1**/TiO_2 and the 440 nm LED setup.

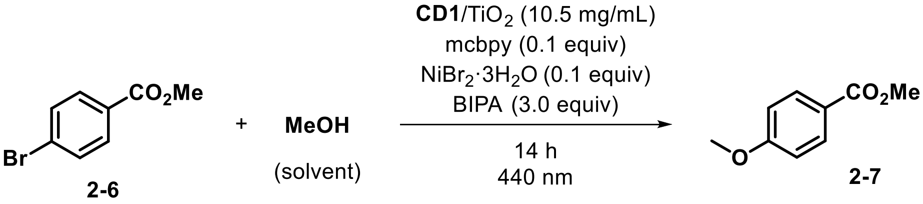

Entry	Conversion [%][a]	2-7 [%]
1	quant.	93

Reaction conditions: methyl 4-bromobenzoate (95.2 µmol), $NiBr_2 \cdot 3H_2O$ (9.5 µmol), mcbpy (9.5 µmol) and BIPA (285.6 µmol) in MeOH (1.5 mL), **CD1**/TiO_2 (15.8 mg), 440 nm LED lamp (100% power), 14 h. NMR yields determined by ^{1}H-NMR using 1,3,5-trimethoxybenzene as internal standard. [a] Conversion of methyl 4-bromobenzoate determined by ^{1}H-NMR using 1,3,5-trimethoxybenzene as internal standard. quant. = quantitative.

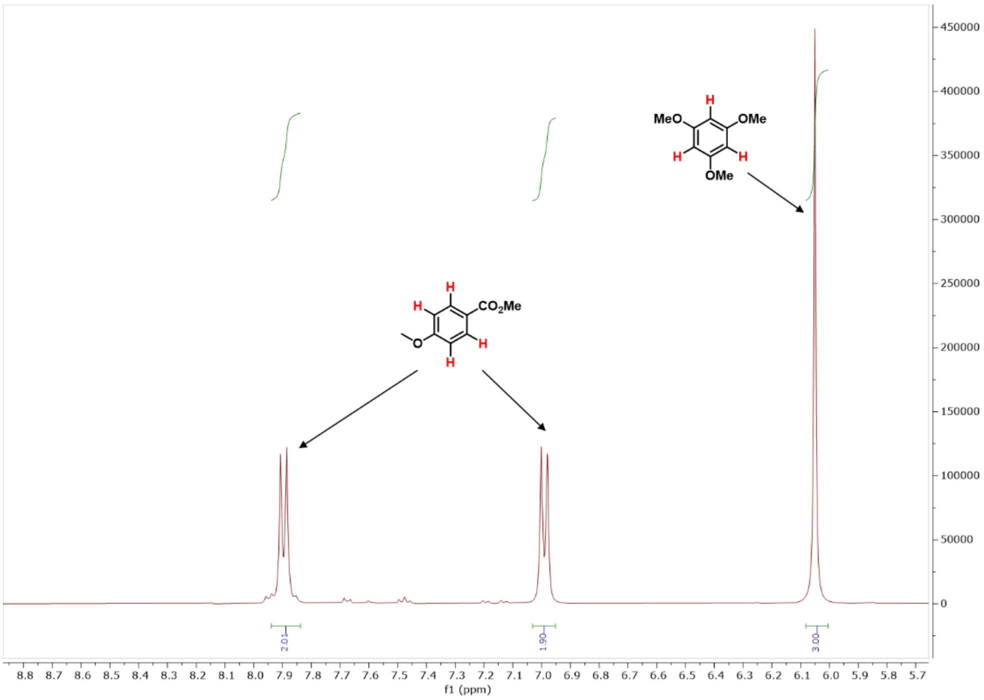

Figure 6-28. Representative ^{1}H-NMR spectrum of a crude reaction mixture for determining NMR yields in the *O*-arylation of methanol (DMSO-d_6, 400 MHz).

6.3.3.3. *S*-arylation of methyl 3-mercaptopropionate

An oven-dried vial (19 x 100 mm) equipped with a stir bar was charged with **CD1**/TiO_2 (31.6 mg), methyl 4-iodobenzoate (**2-4**, 49.87 mg, 190.3 µmol, 1.0 equiv), methyl 3-mercaptopropionate (**2-8**, 45.2 µL, 380.5 µmol, 2.0 equiv), $NiBr_2 \cdot 3H_2O$ (5.2 mg, 19 µmol, 10 mol%) and mcbpy (4.2 mg, 19 µmol, 10 mol%). Subsequently, MeCN (anhydrous, 3 mL) and BIPA (150.8 µL, 951.5 µmol, 5.0 equiv) were added and the vial was sealed with a septum and Parafilm. The reaction mixture was sonicated for 5-10 min followed by stirring for 5 min to obtain a fine dispersion. The mixture was then degassed by bubbling Argon for 10 min. The mixture was irradiated using the 440 nm LED setup with rapid stirring (1400 rpm). After 17 h, one equivalent of 1,3,5-trimethoxybenzene (internal standard, 32 mg, 190.3 µmol) was added and the mixture was stirred for 5 min. An aliquot of the reaction mixture (~200 µL) was filtered, diluted with DMSO-d_6 and subjected to ^{1}H-NMR analysis. The product was identified by spiking the crude reaction mixture with a pure sample of the desired product.

The data are in full agreement with those previously published in the literature.[149]

Table 6-10 *S*-arylation of methyl 3-mercaptopropionate using **CD1**/TiO_2 and the 440 nm LED setup.

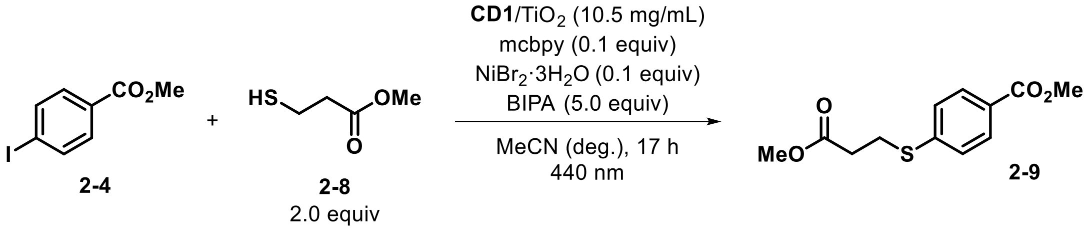

Entry	Conversion [%][a]	2-9 [%]
1	quant.	98

Reaction conditions: methyl 4-iodobenzoate (190.3 µmol), methyl 3-mercaptopropionate (380.5 µmol), $NiBr_2 \cdot 3H_2O$ (19.0 µmol), mcbpy (19.0 µmol) and BIPA (951.5 µmol) in MeCN (3 mL), **CD1**/TiO_2 (31.6 mg), 440 nm LED lamp (50% power), 17 h. NMR yields determined by ^{1}H-NMR using 1,3,5-trimethoxybenzene as internal standard. [a] Conversion of methyl 4-iodobenzoate determined by ^{1}H-NMR using 1,3,5-trimethoxybenzene as internal standard. deg. = degassed. quant. = quantitative.

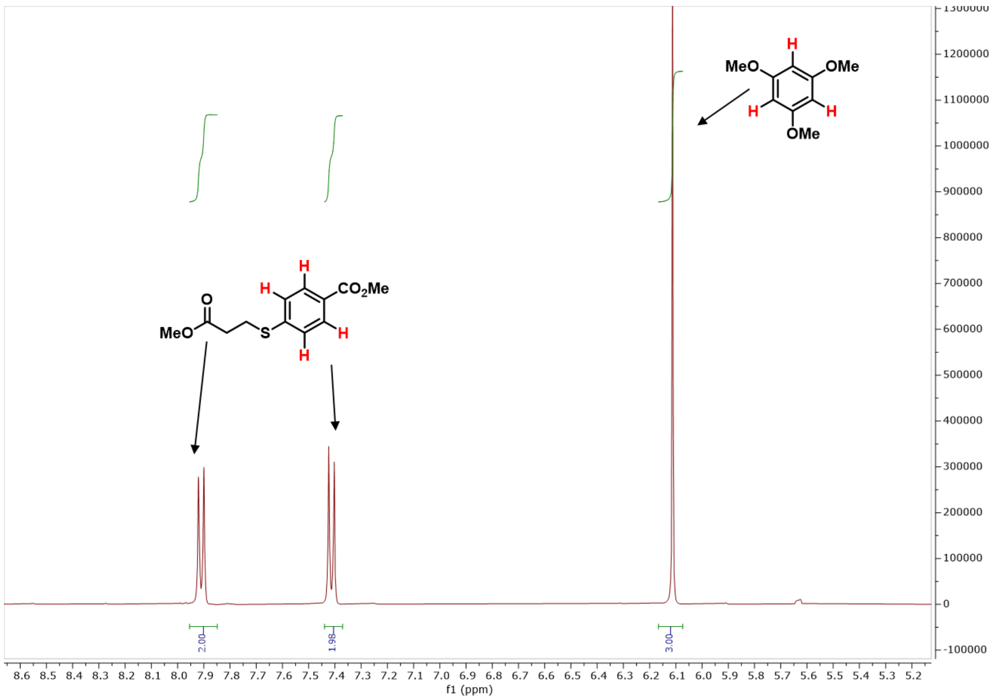

Figure 6-29. Representative ^{1}H-NMR spectrum of a crude reaction mixture for determining NMR yields in the *S*-arylation of methyl 3-mercaptopropionate (DMSO-d$_6$, 400 MHz).

6.3.3.4. *S*-arylation of sodium *p*-toluensulfinate

An oven-dried vial (19 x 100 mm) equipped with a stir bar was charged with **CD1**/TiO_2 (31.6 mg), 4-iodobenzotrifluoride (**2-10**, 14.7 µL, 100 µmol, 1.0 equiv), sodium *p*-toluensulfinate (**2-11**, 38.8 mg, 200 µmol, 2.0 equiv), $NiCl_2$·glyme (nickel(II) chloride ethylene glycol dimethyl ether complex, 2.2 mg, 10 µmol, 10 mol%) and mcbpy (2.1 mg, 10 µmol, 10 mol%). Subsequently, DMAc (anhydrous, 2 mL) was added and the vial was sealed with a septum and Parafilm. The reaction mixture was sonicated for 5-10 min followed by stirring for 5 min to obtain a fine dispersion. The mixture was then degassed by bubbling Argon for 10 min. The mixture was irradiated using the 440 nm LED setup with rapid stirring (1400 rpm). After 72 h, one equivalent of 1,3,5-trimethoxybenzene (internal standard, 16.8 mg, 100 µmol) was added and the mixture was stirred for 5 min. An aliquot of the reaction mixture (~200 µL) was filtered, diluted with DMSO-d_6 and subjected to ^{1}H-NMR analysis. The product was identified by spiking the crude reaction mixture with a pure sample of the desired product.

The data are in full agreement with those previously published in the literature.[160]

Table 6-11 *S*-arylation of sodium *p*-toluensulfinate using **CD1/**TiO_2 and the 440 nm LED setup.

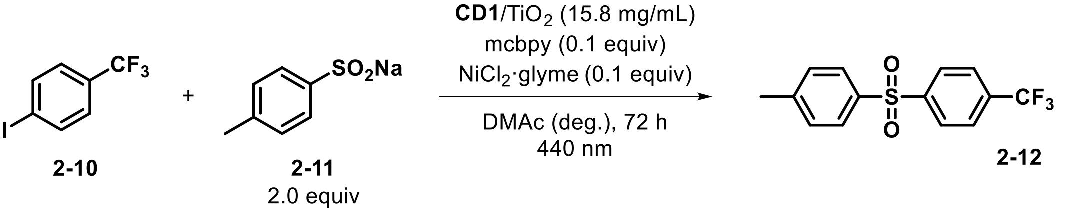

2-10

2-11
2.0 equiv

2-12

Entry	Conversion [%][a]	2-12 [%]
1	quant.	55

Reaction conditions: 4-iodobenzotrifluoride (100 µmol), sodium *p*-toluensulfinate (200 µmol), $NiCl_2$·glyme (10 µmol) and mcbpy (10 µmol) in DMAc (2 mL), **CD1**/TiO_2 (31.6 mg), 440 nm blue LED lamp (100% power), 72 h. NMR yields determined by ^{1}H-NMR using 1,3,5-trimethoxybenzene as internal standard. [a] Conversion of 4-iodobenzotrifluoride determined by ^{1}H-NMR using 1,3,5-trimethoxybenzene as internal standard. deg. = degassed. quant. = quantitative.

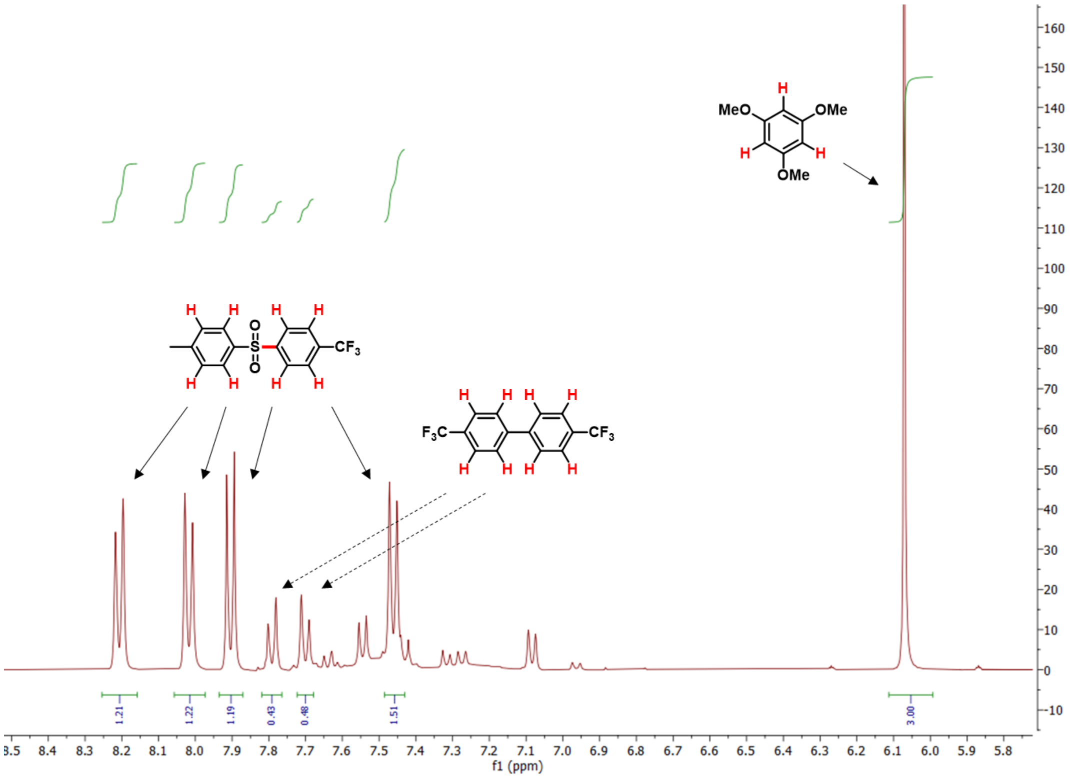

Figure 6-30. Representative ^{1}H-NMR spectrum of a crude reaction mixture for determining NMR yields in the *S*-arylation of sodium *p*-toluensulfinate (DMSO-d_6, 400 MHz).

6.3.3.5. *N*-arylation of *p*-toluensulfonamide

An oven-dried vial (19 x 100 mm) equipped with a stir bar was charged with **CD1**/TiO_2 (31.6 mg), 4-iodobenzotrifluoride (**2-10**, 14.7 µL, 100 µmol, 1.0 equiv), *p*-toluensulfonamide (**2-13**, 34.2 mg, 200 µmol, 2.0 equiv), $NiBr_2{\cdot}3H_2O$ (2.7 mg, 10 µmol, 10 mol%), mcbpy (2.1 mg, 10 µmol, 10 mol%) and DBU (1,8-diazabicyclo[5.4.0]undec-7-en, 22.4 µL, 150 µmol, 1.5 equiv). Subsequently, DMSO (anhydrous, 2 mL) was added and the vial was sealed with a septum and Parafilm. The reaction mixture was sonicated for 5-10 min followed by stirring for 5 min to obtain a fine dispersion. The mixture was then degassed by bubbling Argon for 10 min. The mixture was irradiated using the 440 nm LED setup with rapid stirring (1400 rpm). After 14 h, one equivalent of 1,3,5-trimethoxybenzene (internal standard, 16.8 mg, 100 µmol) was added and the mixture was stirred for 5 min. An aliquot of the reaction mixture (~200 µL) was filtered, diluted with DMSO-d_6 and subjected to ^{1}H-NMR analysis.The product was identified by spiking the crude reaction mixture with a pure sample of the desired product.

The data are in full agreement with those previously published in the literature.[161]

Table 6-12 *N*-arylation of *p*-toluensulfonamide using **CD1**/TiO_2 and the 440 nm LED setup.

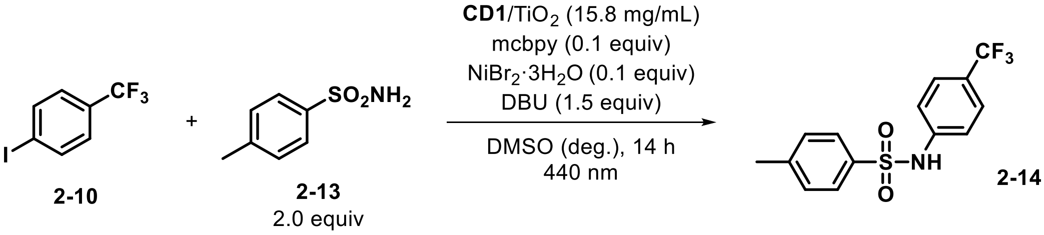

Entry	Conversion [%][a]	2-14 [%]
1	quant.	90

Reaction conditions: 4-iodobenzotrifluoride (100 µmol), *p*-toluensulfonamide (200 µmol), $NiBr_2{\cdot}3H_2O$ (10 µmol), mcbpy (10 µmol) and DBU (150 µmol) in DMSO (2 mL), **CD1**/TiO_2 (31.6 mg), 440 nm blue LED lamp (100% power), 14 h. NMR yields determined by ^{1}H-NMR using 1,3,5-trimethoxybenzene as internal standard. [a] Conversion of 4-iodobenzotrifluoride determined by ^{1}H-NMR using 1,3,5-trimethoxybenzene as internal standard. deg. = degassed. quant. = quantitative.

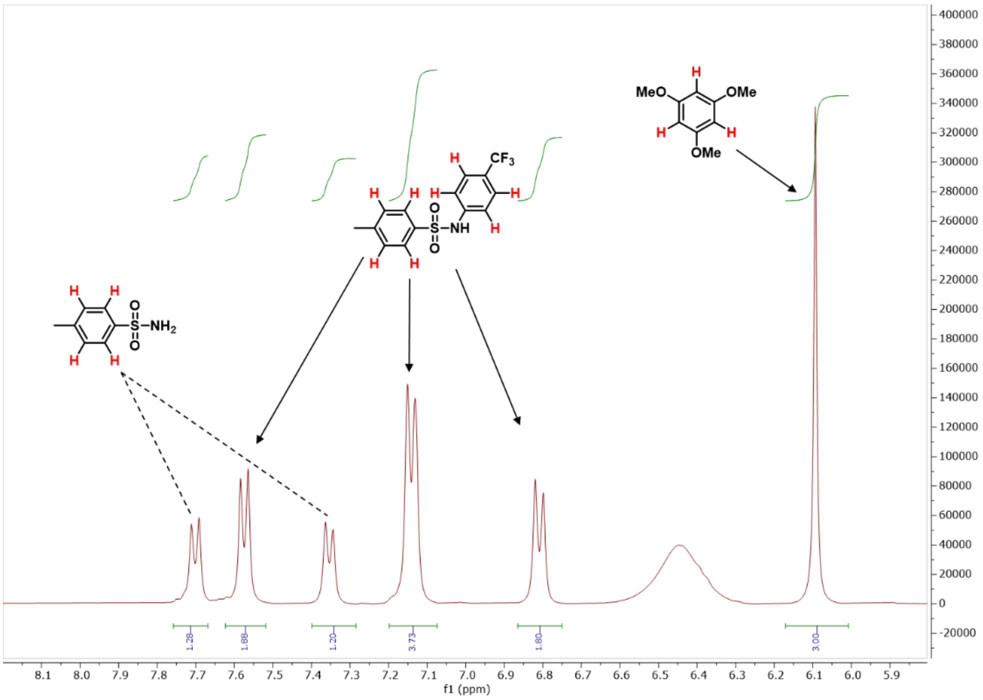

Figure 6-31. Representative ^{1}H-NMR spectrum of a crude reaction mixture for determining NMR yields in the *N*-arylation of *p*-toluensulfonamide (DMSO-d_6, 400 MHz).

6.3.3.6. Photobleaching experiments

The photocatalyst (**CD1**/TiO_2, 31.6 mg; Fluo (fluorescein)/TiO_2, 0.54 mg of Fluo and 30 mg of TiO_2) was added to an oven-dried glass vial equipped with a stir bar. DMSO (1.5 mL) was added and the reaction mixture was stirred and sonicated for 10 min to obtain a fine dispersion. The vial equipped with an air balloon was then transferred into a dark fume hood and irradiated with a blue LED lamp (440 nm LED lamp, 50% power) at room temperature. After the respective time, Boc-Pro-OH (**2-3**, 41.0 mg, 190.3 µmol), methyl 4-iodobenzoate (**2-4**, 74.8 mg, 285.4 µmol), a DMSO solution (1.5 mL) of dcbpy (4.7 mg, 19.0 µmol), $NiCl_2 \cdot 6H_2O$ (4.5 mg, 19.0 µmol), and BIPA (90.5 µL, 570.8 µmol) were added. The glass vial was sealed with a septum and Parafilm. The reaction mixture was stirred and sonicated for 10 min to obtain a fine dispersion and subsequently degassed with Argon for 10 min. The vial was then irradiated with a blue LED lamp (440 nm LED lamp, 50% power) at room temperature for 24 h. 1,3,5-Trimethoxybenzene (32.0 mg, 190.3 µmol) was added as internal standard to determine NMR yields. An aliquot of the resulting mixture (~250 µL) was filtered through a syringe filter, diluted with DMSO-d_6 (~250 µL) and subjected to ^{1}H-NMR analysis.

6.3.3.7. Recycling experiments

Boc-Pro-OH (**2-3**, 41.0 mg, 190.3 µmol), methyl 4-iodobenzoate (**2-4**, 74.8 mg, 285.4 µmol) and **CD1**/TiO_2 nanocomposite (31.6 mg) were added to an oven-dried glass vial equipped with a stir bar. Subsequently, a DMSO solution (3 mL) of dcbpy (4.7 mg, 19.0 µmol), $NiCl_2 \cdot 6H_2O$ (4.5 mg, 19.0 µmol), and BIPA (90.5 µL, 570.8 µmol) were added. The glass vial was sealed with a septum and Parafilm. The reaction mixture was stirred and sonicated for 10 min to obtain a fine dispersion and subsequently degassed with Argon for 10 min. The vial was then irradiated with a blue LED lamp (440 nm LED lamp, 50% power) at room temperature. After 24 h, the reaction mixture was centrifuged and washed twice with DMSO (3 mL). The remaining nanocomposite was lyophilized overnight and reused in the next reaction. For the controlled studies, $NiCl_2 \cdot 6H_2O$ (4.5 mg, 19.0 µmol) or $NiCl_2 \cdot 6H_2O$ (4.5 mg, 19.0 µmol)/dcbpy (4.7 mg, 19.0 µmol) were added to the new reaction mixture.

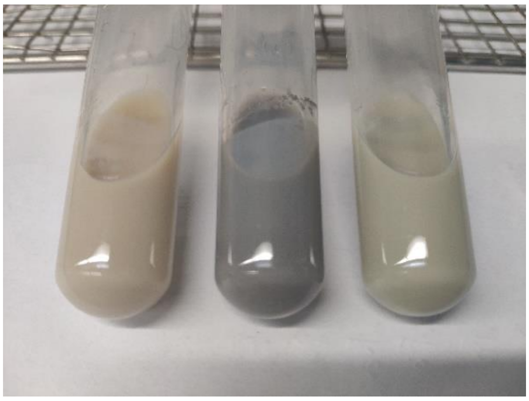

Figure 6-32. Photograph of the reaction mixture (+ none group, left; + $NiCl_2 \cdot 6H_2O$ group, middle; + $NiCl_2 \cdot 6H_2O$/dcbpy, right) after C-O cross-coupling reaction (cycle 4).

6.4. Experimental section for Chapter 3

6.4.1. Synthesis and characterization of other CDs

GlcN·HCl (**2-1**) was dissolved in ultrapure H_2O (20 mL) in a conical flask (300 mL). The doping agent was added and the mixture was agitated to yield a homogenous solution. The flask was transferred into a domestic microwave in a fume hood and heated at 700 W for 3 min. The crude mixture was cooled for 10 min before ultrapure H_2O (40 mL) was added. The resulting solution was filtered through a filter paper and centrifuged at 8000 rpm for 0.5 h through Amicon® Ultra-15 centrifugal filter units. The filtrate was lyophilized to yield the desired CDs.

Table 6-13 Summary of the conditions used for the synthesis of the CDs.

Entry	CD	Carbon source (mmol/mL)	Doping agent (mmol/mL)
1	**CD11**	GlcN·HCl (**2-1**) (0.12)	2,6-Diaminopyridine (**3-5**) (0.13)
2	**CD12**	GlcN·HCl (**2-1**) (0.12)	EDA (**3-6**) (0.13)
3	**CD13**	GlcN·HCl (**2-1**) (0.12)	3-Aminobenzylamine (**3-7**) (0.13)
4	**CD14**	GlcN·HCl (**2-1**) (0.12)	2,6-Diaminotoluene (**3-8**) (0.13)

[a] The doping agent was first dissolved in MeOH (10 mL) and then added to the aqueous solution (20 mL) of carbon source. EDA = ethylenediamine.

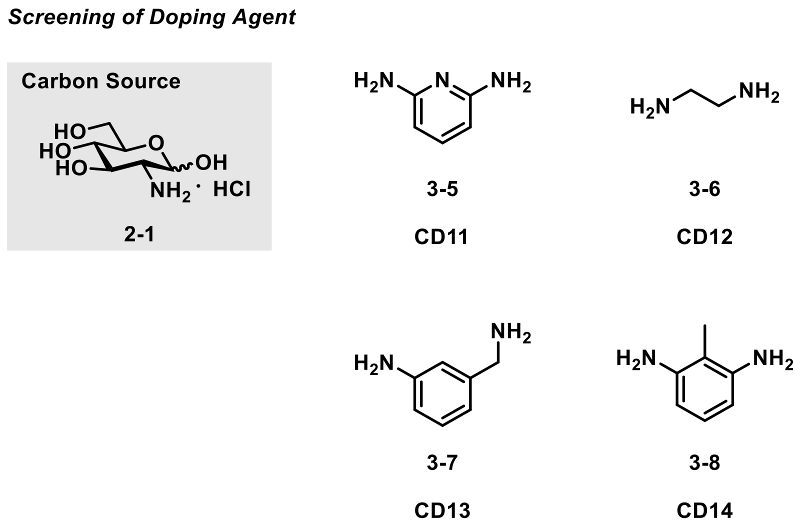

Figure 6-33. Chemical structures of carbon source and doping agents used for CD synthesis.

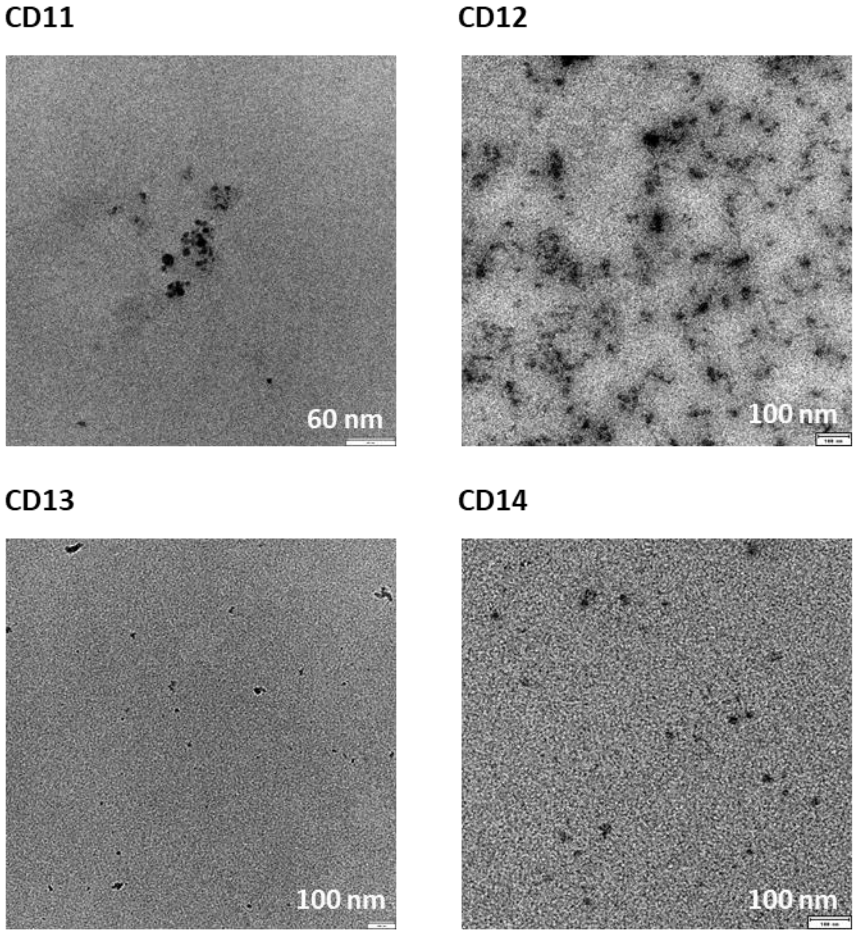

Figure 6-34. TEM images of **CD11**-**CD14**.

CD11

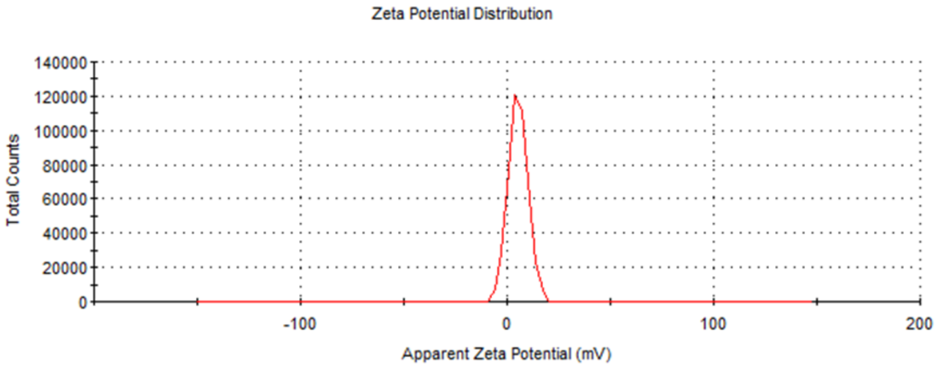

CD12

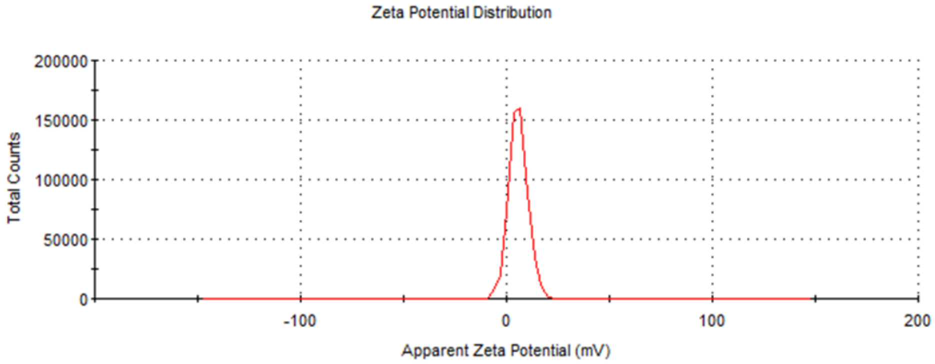

CD13

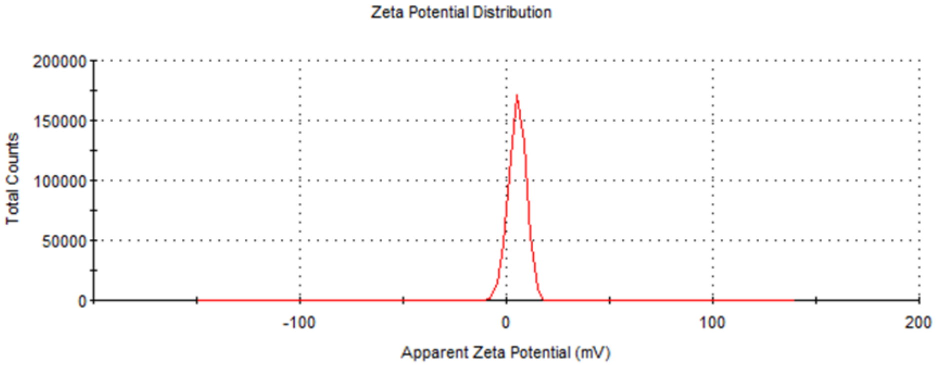

CD14

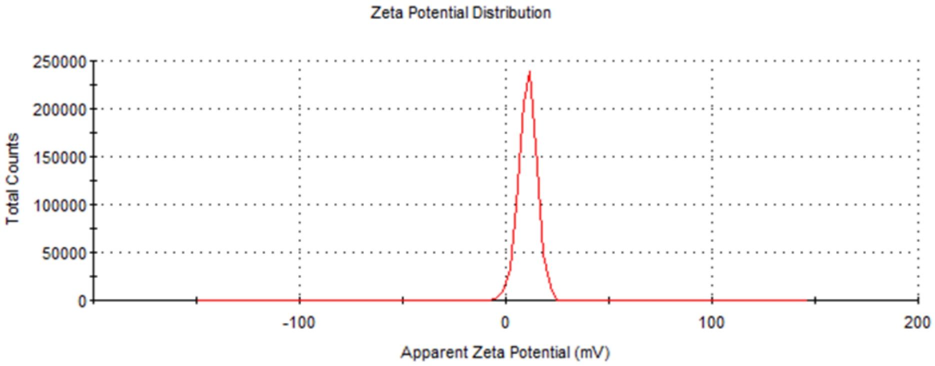

Figure 6-35. Zeta potential of **CD11-CD14** (H_2O, 298 K).

CD11

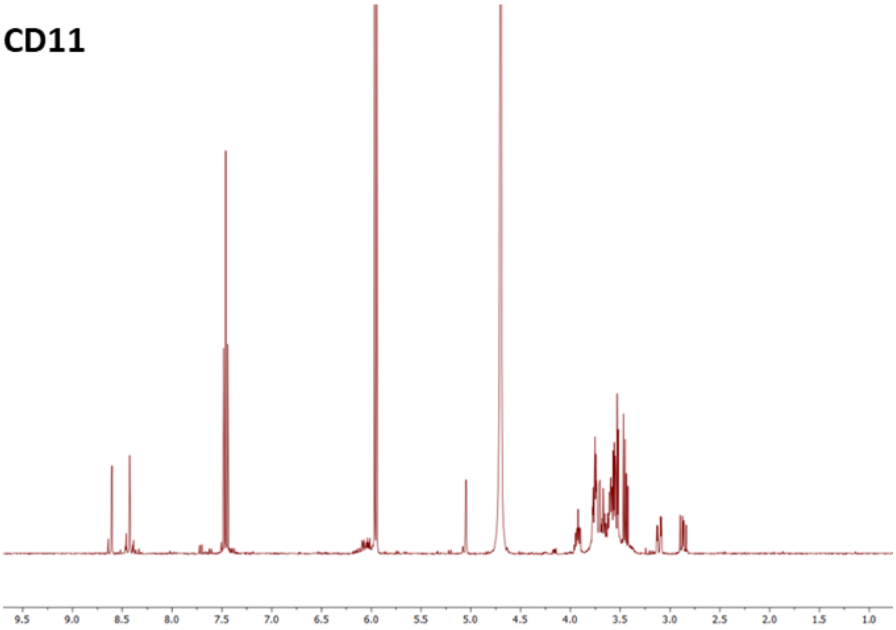
9.5
9.0
8.5
8.0
7.5
7.0
6.5
6.0
5.5
5.0
4.5
4.0
3.5
3.0
2.5
2.0
1.5
1.0

CD12

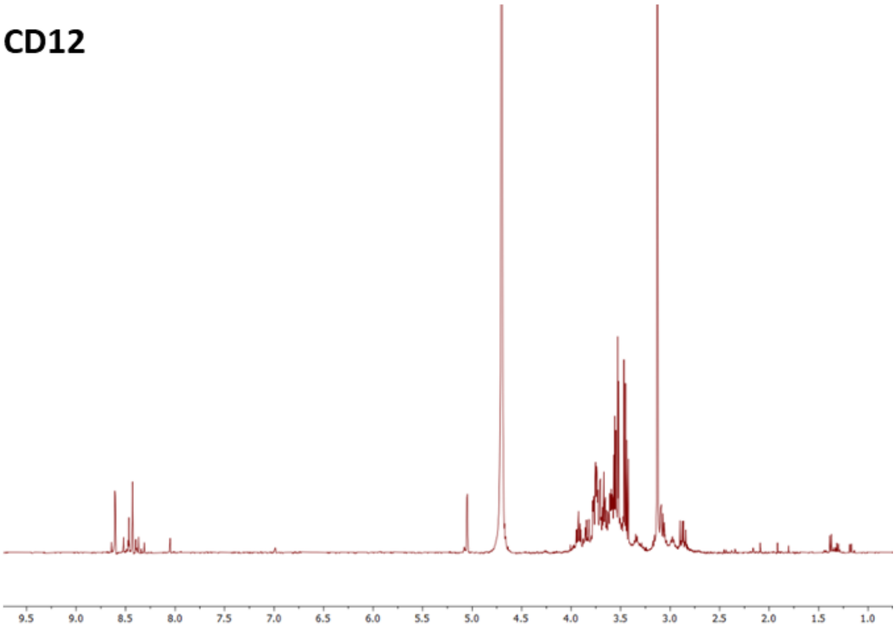
9.5
9.0
8.5
8.0
7.5
7.0
6.5
6.0
5.5
5.0
4.5
4.0
3.5
3.0
2.5
2.0
1.5
1.0

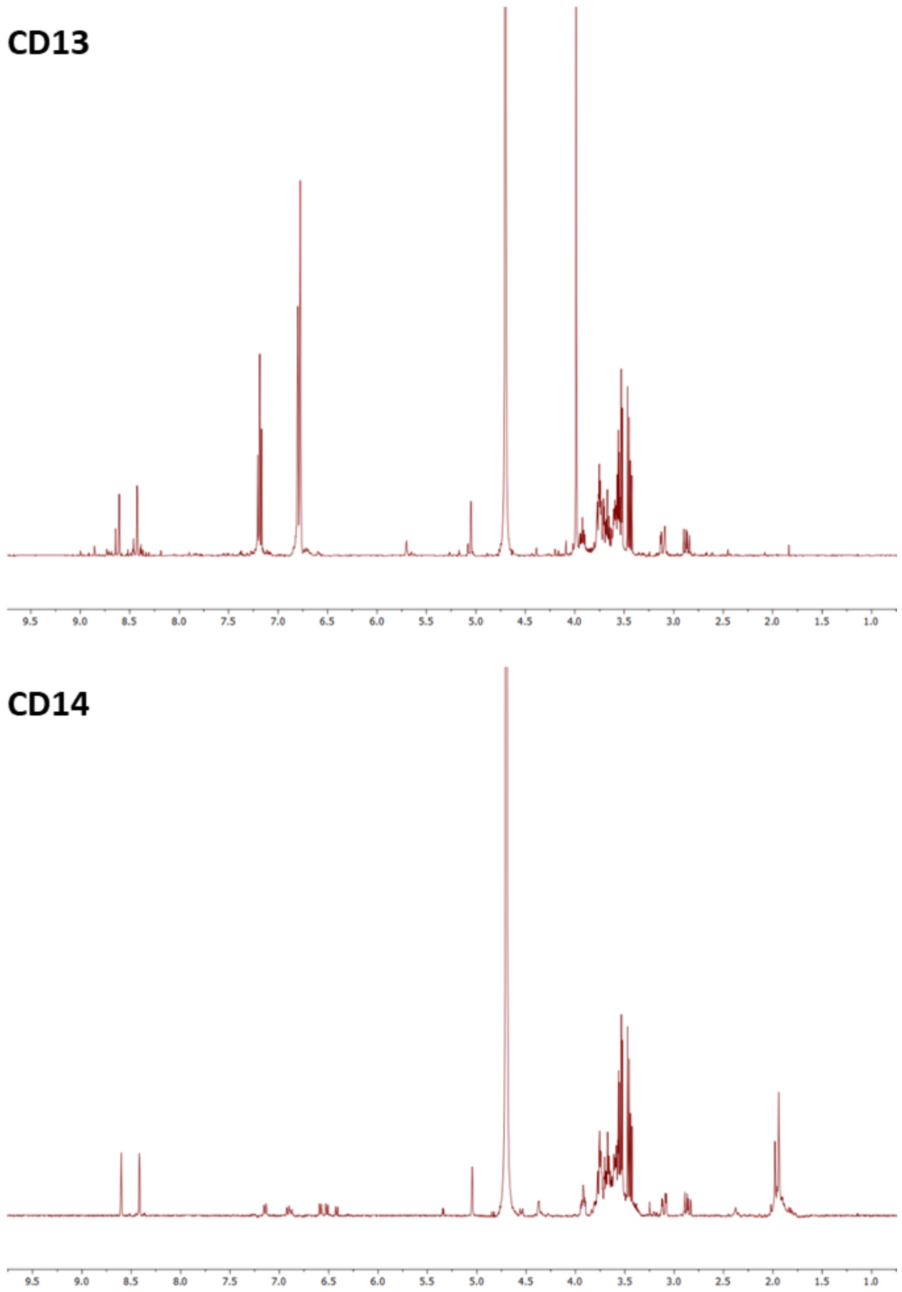

Figure 6-36. ^{1}H NMR spectra of **CD11-CD14** in D_2O (400 MHz).

Table 6-14 Elemental composition of **CD11-CD14**. All values are given as weight %.

	C	N	O	Cl
CD11	48.24	21.68	16.16	13.92
CD12	49.39	20.46	23.77	6.38
CD13	56.50	17.82	18.20	7.48
CD14	48.32	24.16	19.16	8.36

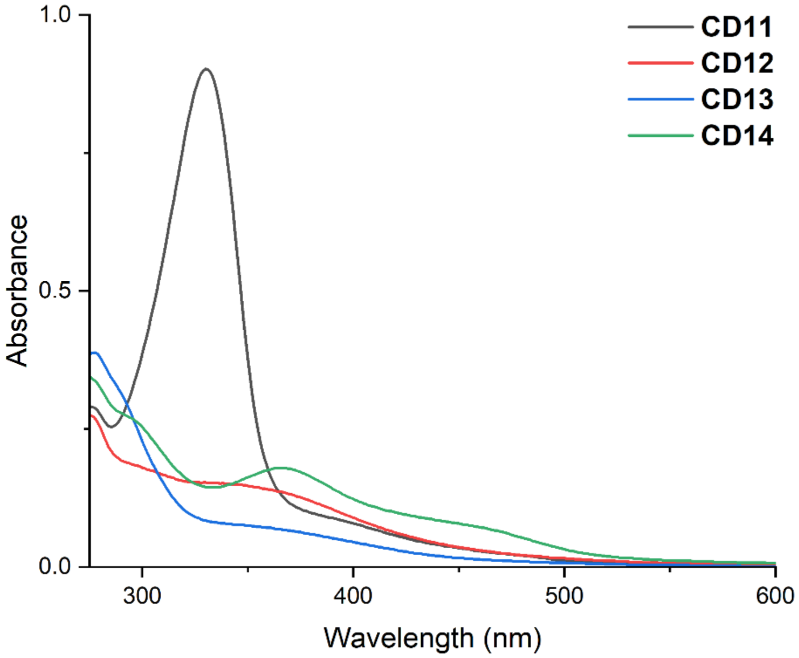

Figure 6-37. Absorption spectra of **CD11-CD14** (25 µg/mL, H_2O, 298 K).

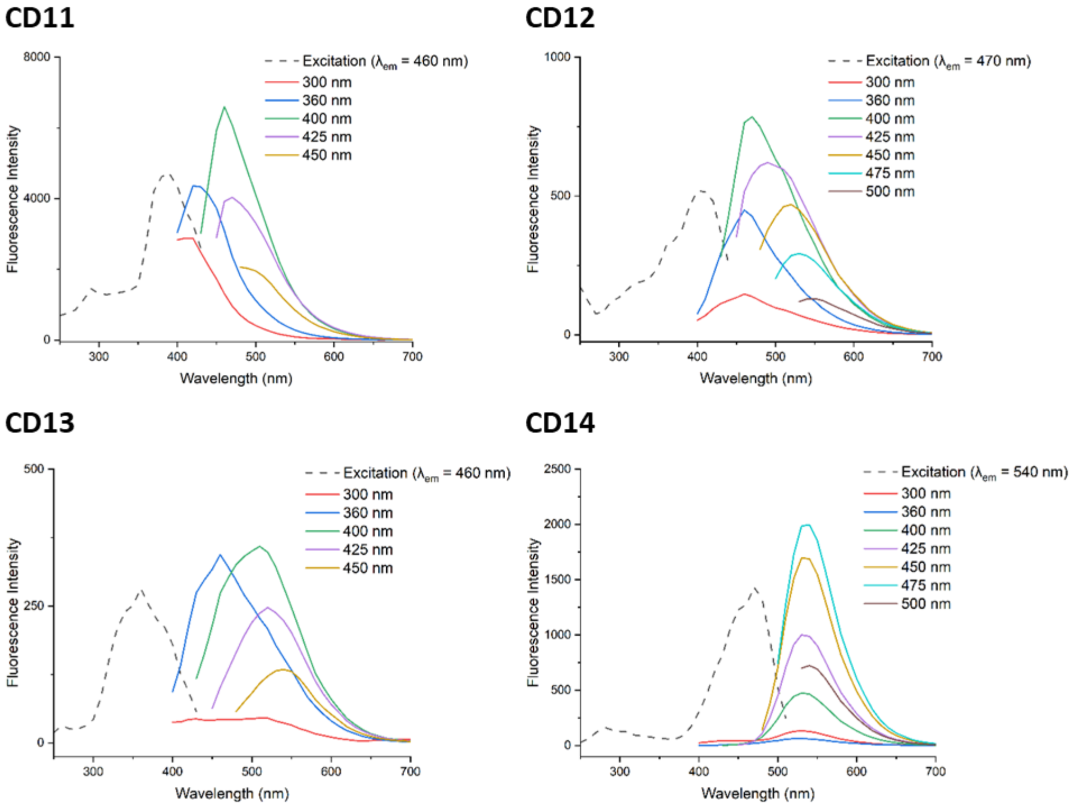

Figure 6-38. Excitation and emission spectra of **CD11-CD14** recorded upon excitation with different excitation wavelengths (H_2O, 298 K).

6.4.2. Cross-coupling reaction

6.4.2.1. *O*-arylation of Boc-Pro-OH

Boc-Pro-OH (**2-3**, 41.0 mg, 190.3 µmol) and methyl 4-iodobenzoate (**2-4**, 74.8 mg, 285.4 µmol) or 4-iodobenzotrifluoride (**2-10**, 41.9 mg, 285.4 µmol) were added to an oven-dried glass vial equipped with a stir bar. Subsequently, a DMSO solution (3 mL) of dtbbpy (5.1 mg, 19.0 µmol), $NiCl_2 \cdot 6H_2O$ (4.5 mg, 19.0 µmol), photocatalyst (CD or CD/TiO_2, 30 mg), and BIPA (90.5 µL, 570.8 µmol) were added. The glass vial was sealed with a septum and Parafilm. The reaction mixture was stirred and sonicated for 10 min and subsequently degassed with Argon for 10 min. The vial was then irradiated with the 440 nm LED lamp at room temperature for 24 h. 1,3,5-Trimethoxybenzene (32.0 mg, 190.3 µmol) was added as internal standard to determine NMR yields. An aliquot of the resulting mixture (~250 µL) was filtered through a syringe filter, diluted with DMSO-d_6 (~250 µL) and subjected to ^{1}H-NMR analysis.

Table 6-15 Conditions optimization and control experiments for the *O*-arylation of Boc-Pro-OH using different photocatalysts.

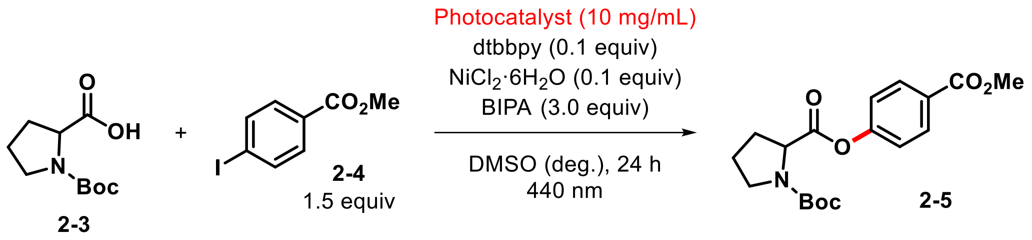

Entry	Conditions	2-5 [%]
1	**CD1**	0
2	**CD1**, no dtbbpy	0
3	**CD1**, dcbpy instead of dtbbpy	0
4	**CD1**/TiO_2	61
5	**CD1**/TiO_2, no dtbbpy	4
6	**CD1**/TiO_2, dcbpy instead of dtbbpy	83
7	**CD2**	35
8	**CD2**, no dtbbpy	0
9	**CD2**, dcbpy instead of dtbbpy	23
10	**CD2**/TiO_2	26
11	**CD2**/TiO_2, no dtbbpy	1
12	**CD2**/TiO_2, dcbpy instead of dtbbpy	34
13	**CD2** (0.67 mg/mL), no light	0
14	**CD2** (10 mg/mL)[a]	36
15	**CD2** (3.33 mg/mL)[a]	70
16	**CD2** (0.67 mg/mL)[a]	80
17	**CD2** (0.17 mg/mL)[a]	82

[a] 440 nm LED lamp (100% power). Reaction conditions: Boc-Pro-OH (190.3 μmol), methyl 4-iodobenzoate (285.4 μmol), photocatalysts (30 mg), $NiCl_2 \cdot 6H_2O$ (19.0 μmol) and dtbbpy (19.0 μmol) in DMSO (3 mL), BIPA (570.8 μmol), 440 nm LED lamp (50% power), 24 h. NMR yields determined by ^{1}H-NMR using 1,3,5-trimethoxybenzene as internal standard. deg. = degassed.

Table 6-16 *O*-arylation of Boc-Pro-OH with optimized conditions.

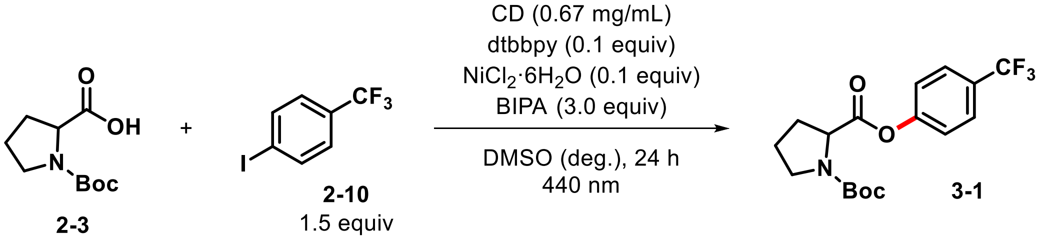

Entry	**CD**	**3-1 [%]**
1	No CD	21
2	**CD1**	46
3	**CD2**	87

Reaction conditions: Boc-Pro-OH (190.3 µmol), 4-iodobenzotrifluoride (285.4 µmol), CD (2 mg), $NiCl_2 \cdot 6H_2O$ (19.0 µmol) and dtbbpy (19.0 µmol) in DMSO (3 mL), BIPA (570.8 µmol), 440 nm LED lamp (100% power), 24 h. NMR yields determined by ^{1}H-NMR using 1,3,5-trimethoxybenzene as internal standard. deg. = degassed.

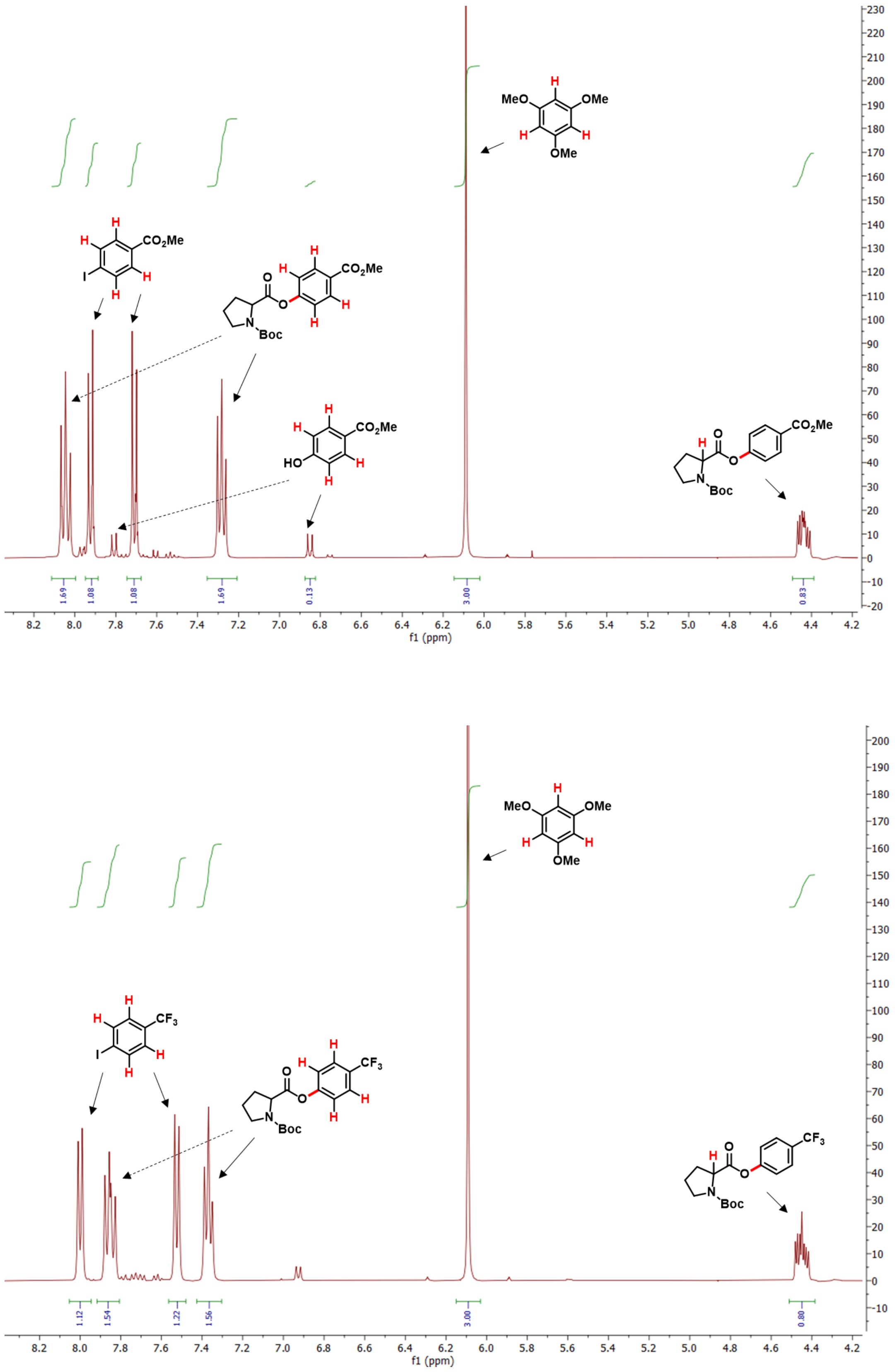

Figure 6-39. Representative ^{1}H-NMR spectra of a crude reaction mixture for determining NMR yields in the *O*-arylation of Boc-Pro-OH (DMSO-d_6, 400 MHz).

6.4.2.2. *S*-arylation of methyl 3-mercaptopropionate

Methyl 4-iodobenzoate (**2-4**, 49.9 mg, 190.3 µmol) or methyl 4-bromobenzoate (**2-6**, 40.9 mg, 190.3 µmol) was added to an oven-dried glass vial equipped with a stir bar. Subsequently, a DMAc solution (3 mL) of dtbbpy (5.1 mg, 19.0 µmol), $NiBr_2 \cdot 3H_2O$ (5.2 mg, 19.0 µmol) and CD (2 mg) were added. Subsequently, methyl 3-mercaptopropionate (**2-8**, 42.1 µL, 380.5 µmol) and BIPA (150.8 µL, 951.5 µmol) were added. The glass vial was sealed with a septum and Parafilm. The reaction mixture was stirred and sonicated for 10 min and subsequently degassed with Argon for 10 min. The vial was then irradiated with the 440 nm LED lamp at room temperature for 16 h. 1,3,5-Trimethoxybenzene (32.0 mg, 190.3 µmol) was added as internal standard to determine NMR yields. An aliquot of the resulting mixture (~250 µL) was filtered through a syringe filter, diluted with DMSO-d_6 (~250 µL) and subjected to ^{1}H-NMR analysis.

Table 6-17 *S*-arylation of methyl 3-mercaptopropionate.

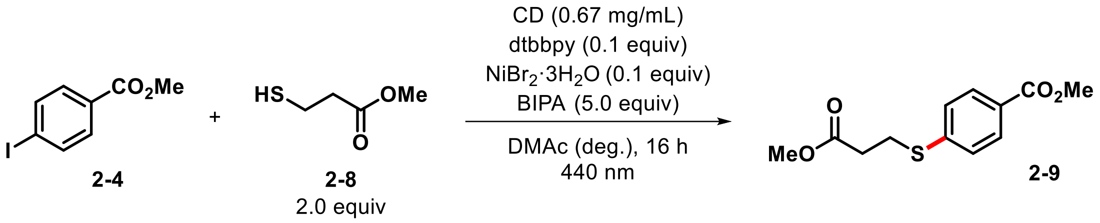

Entry	CD	2-9 [%]
1	No CD	25
2	**CD1**	16
3	**CD2**	95

Reaction conditions: methyl 4-iodobenzoate (190.3 µmol), methyl 3-mercaptopropionate (380.5 µmol), CD (2 mg), $NiBr_2 \cdot 3H_2O$ (19.0 µmol), dtbbpy (19.0 µmol) and BIPA (951.5 µmol) in DMAc (3 mL), 440 nm LED lamp (100% power), 16 h. NMR yields determined by ^{1}H-NMR using 1,3,5-trimethoxybenzene as internal standard. deg. = degassed.

Table 6-18 Conditions optimization and control experiments for the *S*-arylation of methyl 3-mercaptopropionate using **CD2**. The reaction is performed following the above procedure, in the absence of BIPA.

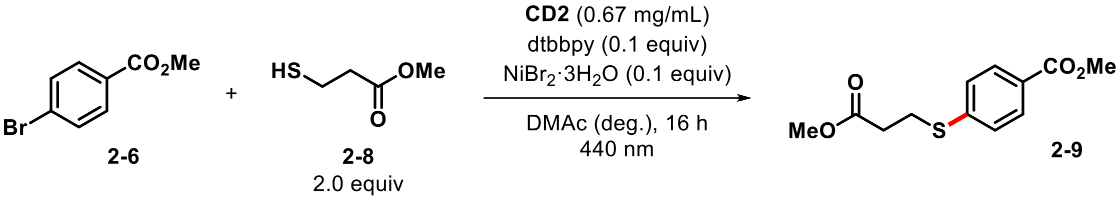

Entry	Conditions	2-9 [%]
1	As shown	95
2	No **CD2**	0
3	No dtbbpy	14
4	No $NiBr_2 \cdot 3H_2O$	0
5	No degassed	31
6	No light	0
7	440 nm[a]	59
8	Methyl 4-chlorobenzoate instead of methyl 4-bromobenzoate	1
9	**CD2** (0.67 mg/mL), washed by MeCN	97
10	**CD2** (0.67 mg/mL)[b], pre-irradiated for 6 h	54
11	**CD2** (0.67 mg/mL)[b], pre-irradiated for 24 h	25
12	**CD2** (3.33 mg/mL), 3 h	10
13	**CD2** (0.67 mg/mL), 3 h	17
14	**CD2** (0.17 mg/mL), 3 h	2
15	No **CD2**, + py (951.5 µmol)	0
16	+ py (951.5 µmol), 3 h	58
17	+ py (951.5 µmol)	91

[a] 440 nm LED lamp (50% power). [b] **CD2** was pre-irradiated with the 440 nm LED lamp (50% power) and then used in the *S*-arylation of methyl 3-mercaptopropionate. Reaction conditions: methyl 4-bromobenzoate (190.3 µmol), methyl 3-mercaptopropionate (380.5 µmol), **CD2** (2 mg), $NiBr_2 \cdot 3H_2O$ (19.0 µmol) and dtbbpy (19.0 µmol) in DMAc (3 mL), 440 nm LED lamp (100% power), 16 h. NMR yields determined by ^{1}H-NMR using 1,3,5-trimethoxybenzene as internal standard. deg. = degassed. py = pyridine.

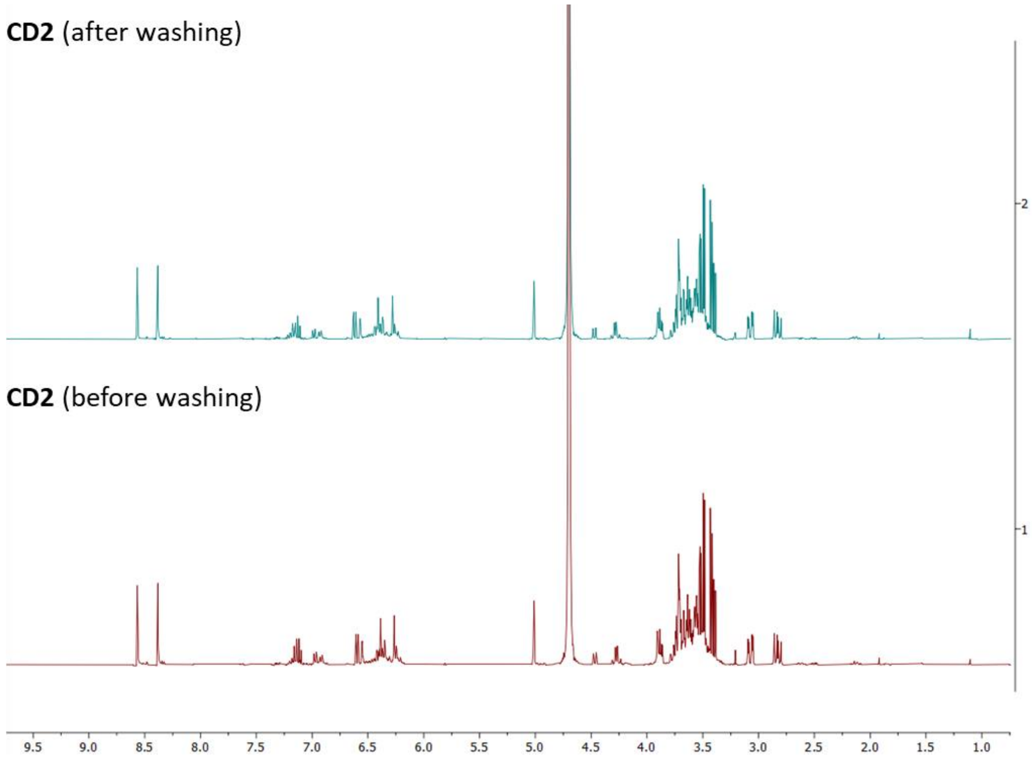

Figure 6-40. ^{1}H NMR spectra of **CD2** before and after MeCN washing (D_2O, 400 MHz).

Table 6-19 Conditions optimization and control experiments for the *S*-arylation of methyl 3-mercaptopropionate using pyHI. The reaction is performed following the above procedure, in the absence of BIPA and using pyHI instead of **CD2**.

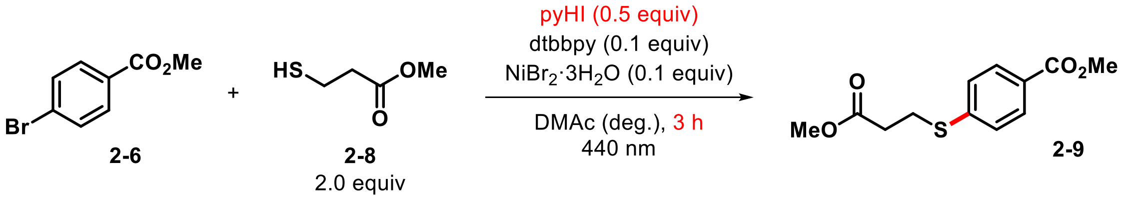

Entry	Conditions	2-9 [%]
1	As shown	96
2	pyHI (0.2 equiv)	65
3	pyHI (0.05 equiv)	0
4	No dtbbpy	60
5	No $NiBr_2 \cdot 3H_2O$	0
6	No degassed	2
7	No light	0

Reaction conditions: methyl 4-bromobenzoate (190.3 µmol), methyl 3-mercaptopropionate (380.5 µmol), pyHI (95.2 µmol), $NiBr_2 \cdot 3H_2O$ (19.0 µmol) and dtbbpy (19.0 µmol) in DMAc (3 mL), 440 nm LED lamp (100% power), 3 h. NMR yields determined by ^{1}H-NMR using 1,3,5-trimethoxybenzene as internal standard. deg. = degassed. pyHI = pyridinium iodide.

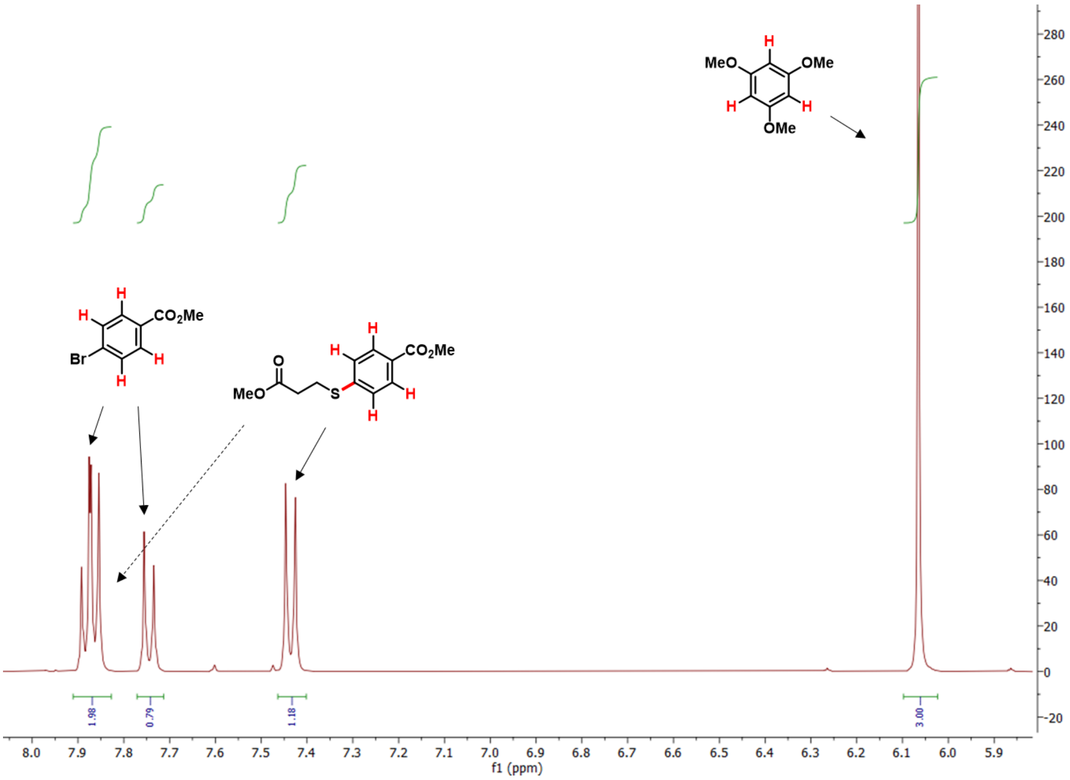

Figure 6-41. Representative ^{1}H-NMR spectrum of a crude reaction mixture for determining NMR yields in the *S*-arylation of methyl 3-mercaptopropionate (DMSO-d$_6$, 400 MHz).

6.4.2.3. *S*-arylation of sodium *p*-toluensulfinate

Sodium *p*-toluensulfinate (**2-11**, 33.9 mg, 190.3 µmol) was added to an oven-dried glass vial equipped with a stir bar. Subsequently, a DMAc solution (2 mL) of dtbbpy (2.5 mg, 9.5 µmol), $NiCl_2$·glyme (2.1 mg, 9.5 µmol), CD (1.3 mg) and 4-iodobenzotrifluoride (**2-10**, 14.0 µL, 95.2 µmol) were added. The glass vial was sealed with a septum and Parafilm. The reaction mixture was stirred and sonicated for 10 min and subsequently degassed with Argon for 10 min. The vial was then irradiated with the 440 nm LED lamp at room temperature for 24 h. 1,3,5-Trimethoxybenzene (16.0 mg, 95.2 µmol) was added as internal standard to determine NMR yields. An aliquot of the resulting mixture (~250 µL) was filtered through a syringe filter, diluted with DMSO-d_6 (~250 µL) and subjected to ^{1}H-NMR analysis.

Table 6-20 *S*-arylation of sodium *p*-toluensulfinate.

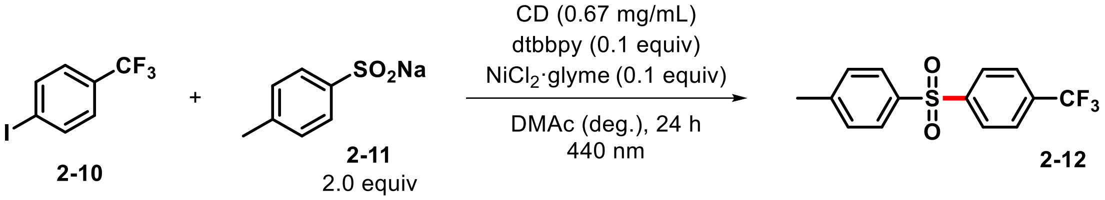

Entry	CD	2-12 [%]
1	No CD	4
2	**CD1**	56
3	**CD2**	60

Reaction conditions: 4-iodobenzotrifluoride (95.2 µmol), sodium *p*-toluensulfinate (190.3 µmol), CD (1.3 mg), $NiCl_2$·glyme (9.5 µmol) and dtbbpy (9.5 µmol) in DMAc (2 mL), 440 nm LED lamp (100% power), 24 h. NMR yields determined by ^{1}H-NMR using 1,3,5-trimethoxybenzene as internal standard. deg. = degassed.

6.4.2.4. *N*-arylation of *p*-toluensulfonamide

Methyl 4-iodobenzoate (**2-4**, 24.9 mg, 95.2 µmol) and *p*-toluensulfonamide (**2-13**, 32.6 mg, 190.3 µmol) were added to an oven-dried glass vial equipped with a stir bar. Subsequently, a DMSO solution (2 mL) of dtbbpy (2.5 mg, 9.5 µmol), $NiBr_2·3H_2O$ (2.6 mg, 9.5 µmol), CD (1.3 mg) and DBU (21.3 µL, 142.8 µmol) were added. The glass vial was sealed with a septum and Parafilm. The reaction mixture was stirred and sonicated for 10 min and subsequently degassed with Argon for 10 min. The vial was then irradiated with the 440 nm LED lamp at room temperature for 16 h. 1,3,5-Trimethoxybenzene (16.0 mg, 95.2 µmol) was added as internal standard to determine NMR yields. An aliquot of the resulting mixture (~250 µL) was filtered through a syringe filter, diluted with DMSO-d_6 (~250 µL) and subjected to ^{1}H-NMR analysis.

Table 6-21 *N*-arylation of *p*-toluensulfonamide.

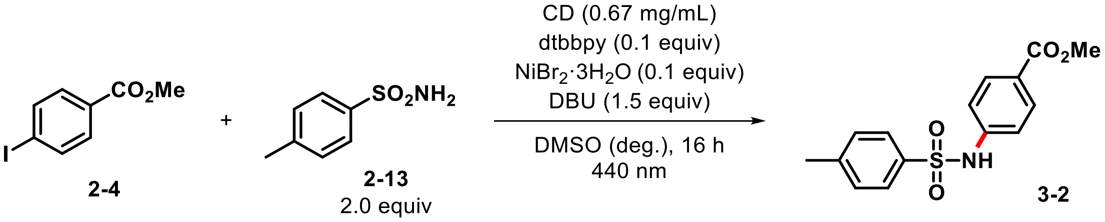

Entry	CD	3-2 [%]
1	No CD	12
2	**CD1**	45
3	**CD2**	55

Reaction conditions: Methyl 4-iodobenzoate (95.2 µmol), *p*-toluensulfonamide (190.3 µmol), CD (1.3 mg), $NiBr_2·3H_2O$ (9.5 µmol) and dtbbpy (9.5 µmol) in DMSO (2 mL), DBU (142.8 µmol), 440 nm LED lamp (100% power), 16 h. NMR yields determined by ^{1}H-NMR using 1,3,5-trimethoxybenzene as internal standard. deg. = degassed.

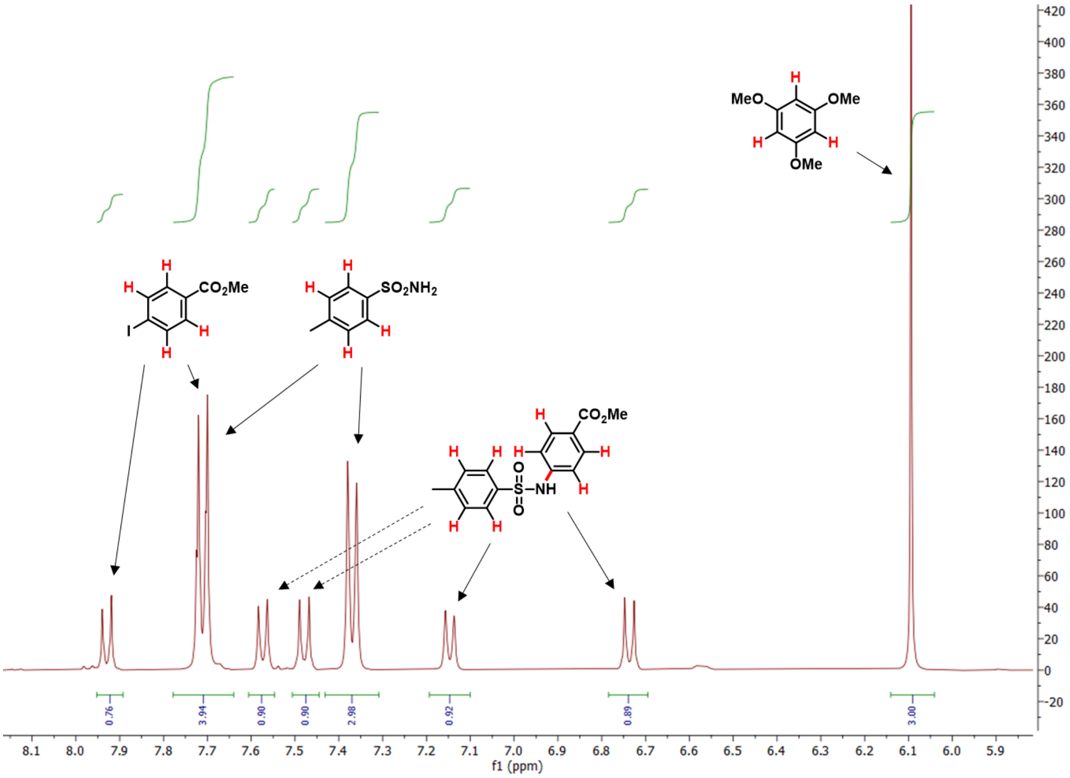

Figure 6-42. Representative ^{1}H-NMR spectrum of a crude reaction mixture for determining NMR yields in the *N*-arylation of *p*-toluensulfonamide (DMSO-d_6, 400 MHz).

6.4.2.5. *N*-arylation of pyrrolidine

Methyl 4-bromobenzoate (**2-6**, 20.5 mg, 95.2 µmol) was added to an oven-dried glass vial equipped with a stir bar. Subsequently, a DMAc solution (2 mL) of $NiBr_2 \cdot 3H_2O$ (2.6 mg, 9.5 µmol), CD (1.3 mg) and pyrrolidine (**3-3**, 23.8 µL, 285.6 µmol) were added. The glass vial was sealed with a septum and Parafilm. The reaction mixture was stirred and sonicated for 10 min and subsequently degassed with Argon for 10 min. The vial was then irradiated with the 440 nm LED lamp at room temperature for 17 h. 1,3,5-Trimethoxybenzene (16.0 mg, 95.2 µmol) was added as internal standard to determine NMR yields. An aliquot of the resulting mixture (~250 µL) was filtered through a syringe filter, diluted with DMSO-d_6 (~250 µL) and subjected to ^{1}H-NMR analysis.

Table 6-22 *N*-arylation of pyrrolidine.

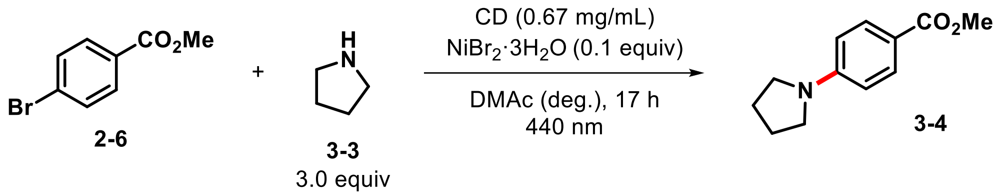

Entry	CD	3-4 [%]
1	No CD	1
2	**CD1**	2
3	**CD2**	61

Reaction conditions: Methyl 4-bromobenzoate (95.2 µmol), pyrrolidine (285.6 µmol), CD (1.3 mg) and $NiBr_2 \cdot 3H_2O$ (9.5 µmol) in DMAc (2 mL), 440 nm LED lamp (100% power), 17 h. NMR yields determined by ^{1}H-NMR using 1,3,5-trimethoxybenzene as internal standard. deg. = degassed.

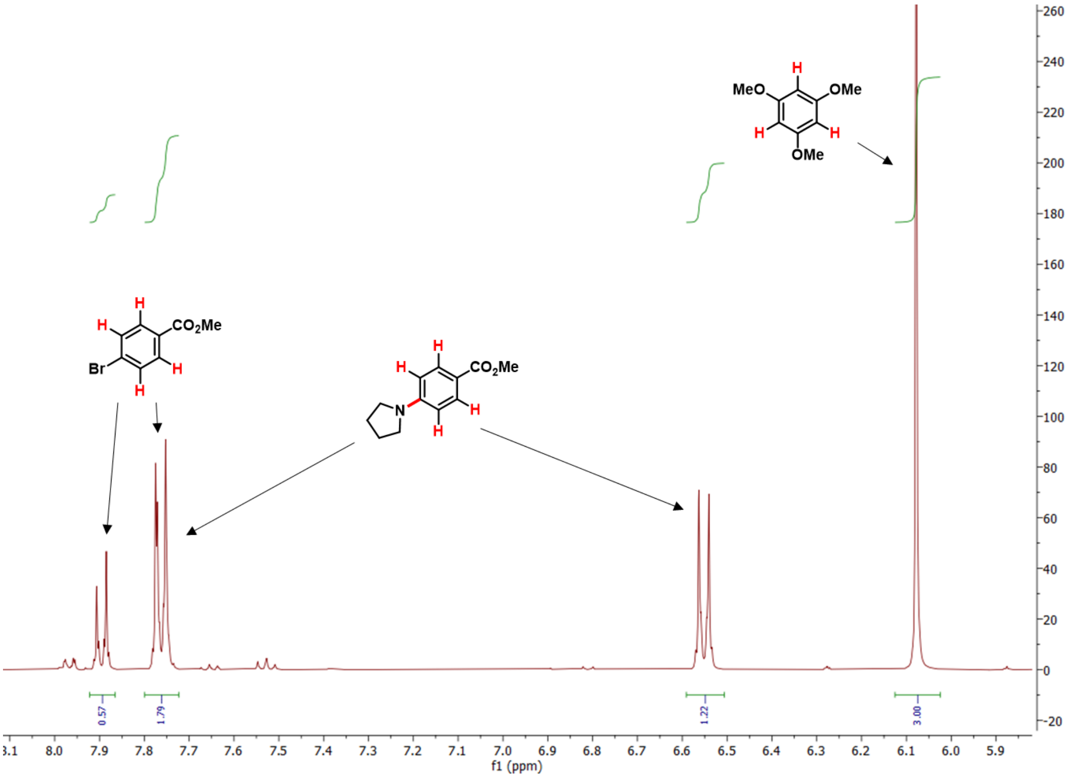

Figure 6-43. Representative ^{1}H-NMR spectrum of a crude reaction mixture for determining NMR yields in the *N*-arylation of pyrrolidine (DMSO-d$_6$, 400 MHz).

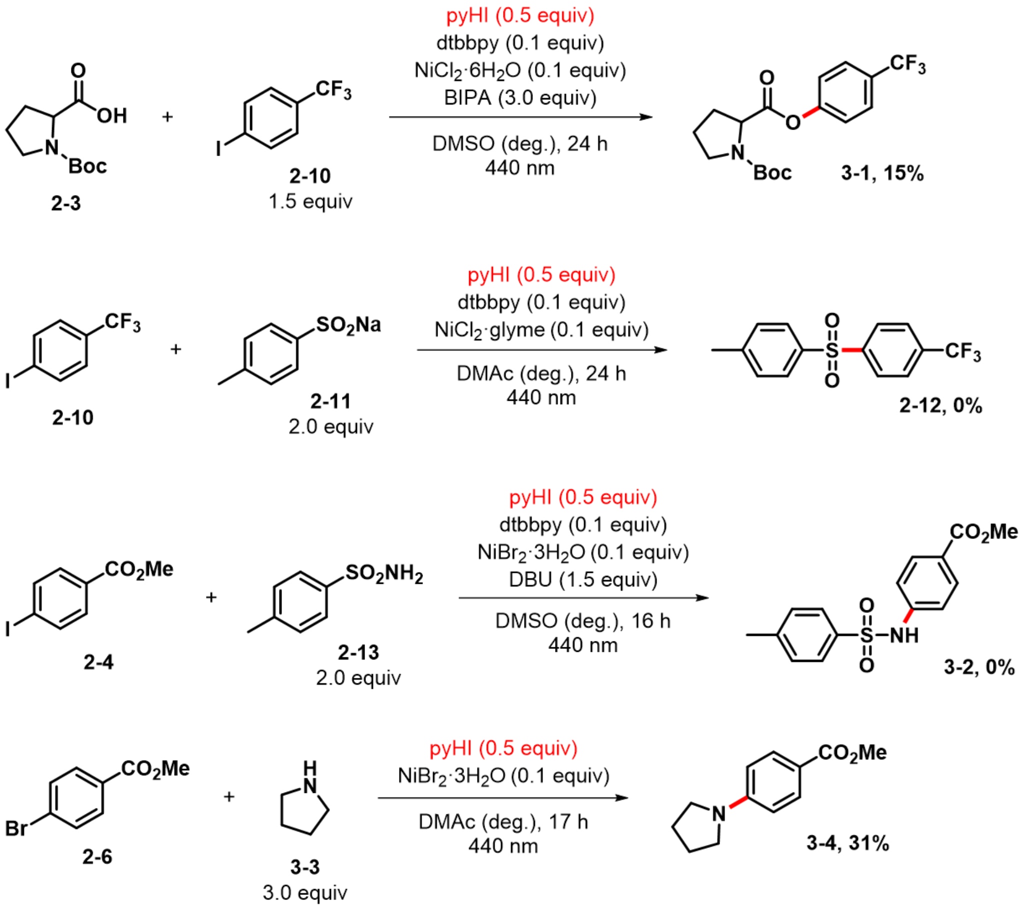

Figure 6-44. Application of pyHI as photocatalyst for C-O, C-S, and C-N cross-couplings. The reactions are performed following the above procedures, using pyHI (0.5 equiv.) instead of **CD2**.

6.4.2.6. Photophysical characterization of *S*-arylation of methyl 3-mercaptopropionate catalyzed by CD

UV-Vis absorption and fluorescence. Different solutions of CD (2 mg) and other reaction components were prepared in DMAc (3 mL) and then diluted with DMAc (50×) for UV-Vis absorption and fluorescence measurements.

Solution	Concentrations
CD	CD (13.3 µg/mL)
CD+ArBr	CD (13.3 µg/mL), methyl 4-bromobenzoate (**2-6**, 1.3 mM)
CD+RSH	CD (13.3 µg/mL), methyl 3-mercaptopropionate (**2-9**, 2.5 mM)
CD+$NiBr_2$	CD (13.3 µg/mL), $NiBr_2·3H_2O$ (126.7 µM)
CD+$NiBr_2$·dtbbpy	CD (13.3 µg/mL), $NiBr_2·3H_2O$ (126.7 µM) and dtbbpy (126.7 µM)
CD+BIPA	CD (13.3 µg/mL), BIPA (6.3 mM)
CD+py	CD (13.3 µg/mL), py (6.3 mM)

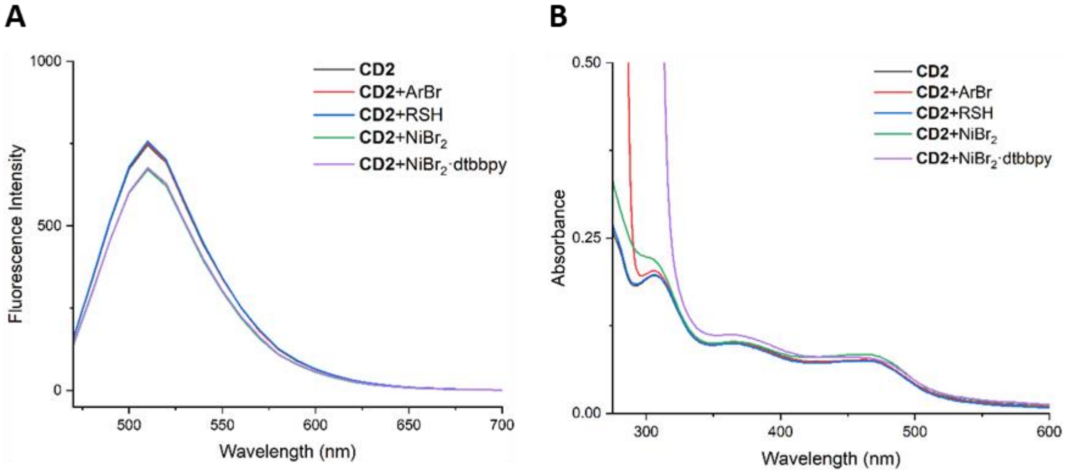

Figure 6-45. Emission (A, λ_{ex} = 440 nm) and UV-Vis absorption (B) spectra of **CD2** in the presence of different reaction components (DMAc, 298 K).

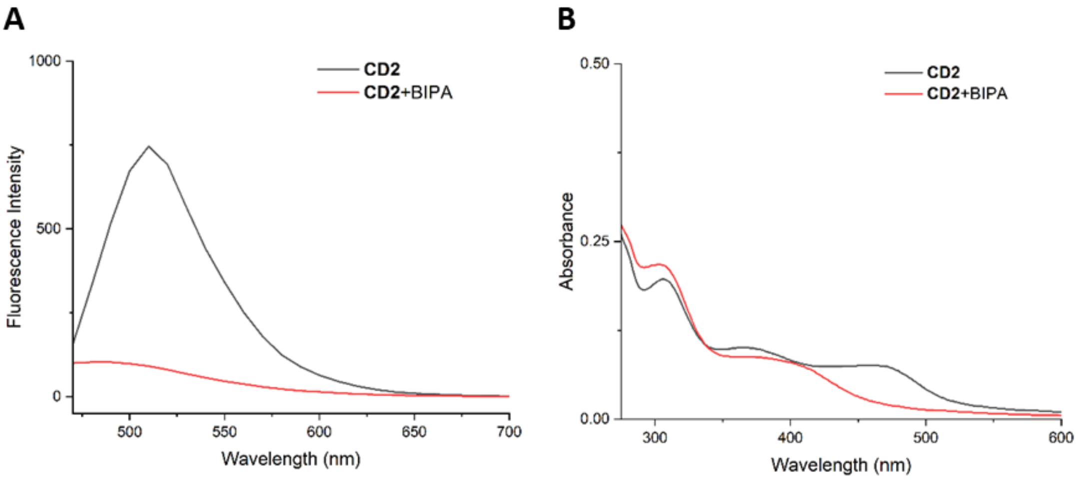

Figure 6-46. Emission (A, λ_{ex} = 440 nm) and UV-Vis absorption (B) spectra of **CD2** in the presence of base BIPA (DMAc, 298 K).

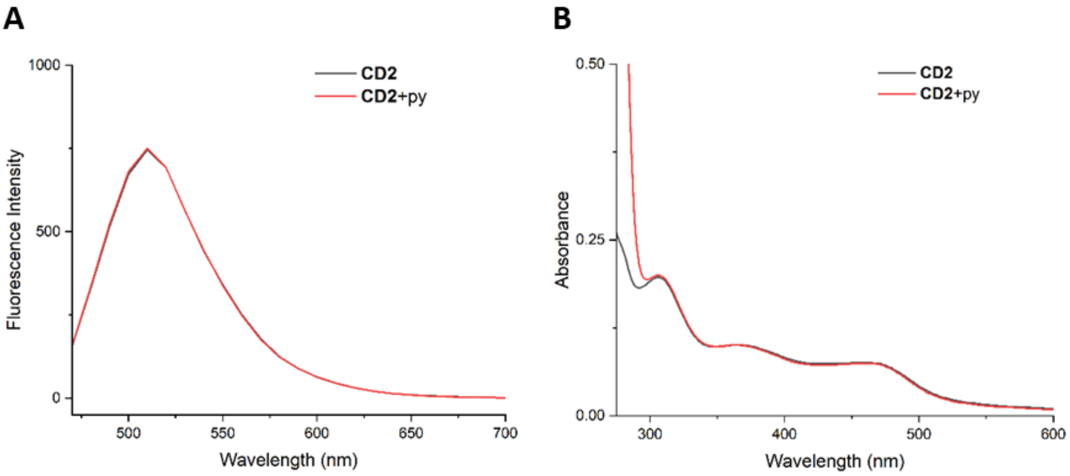

Figure 6-47. Emission (A, λ_{ex} = 440 nm) and UV-Vis absorption (B) spectra of **CD2** in the presence of py (DMAc, 298 K).

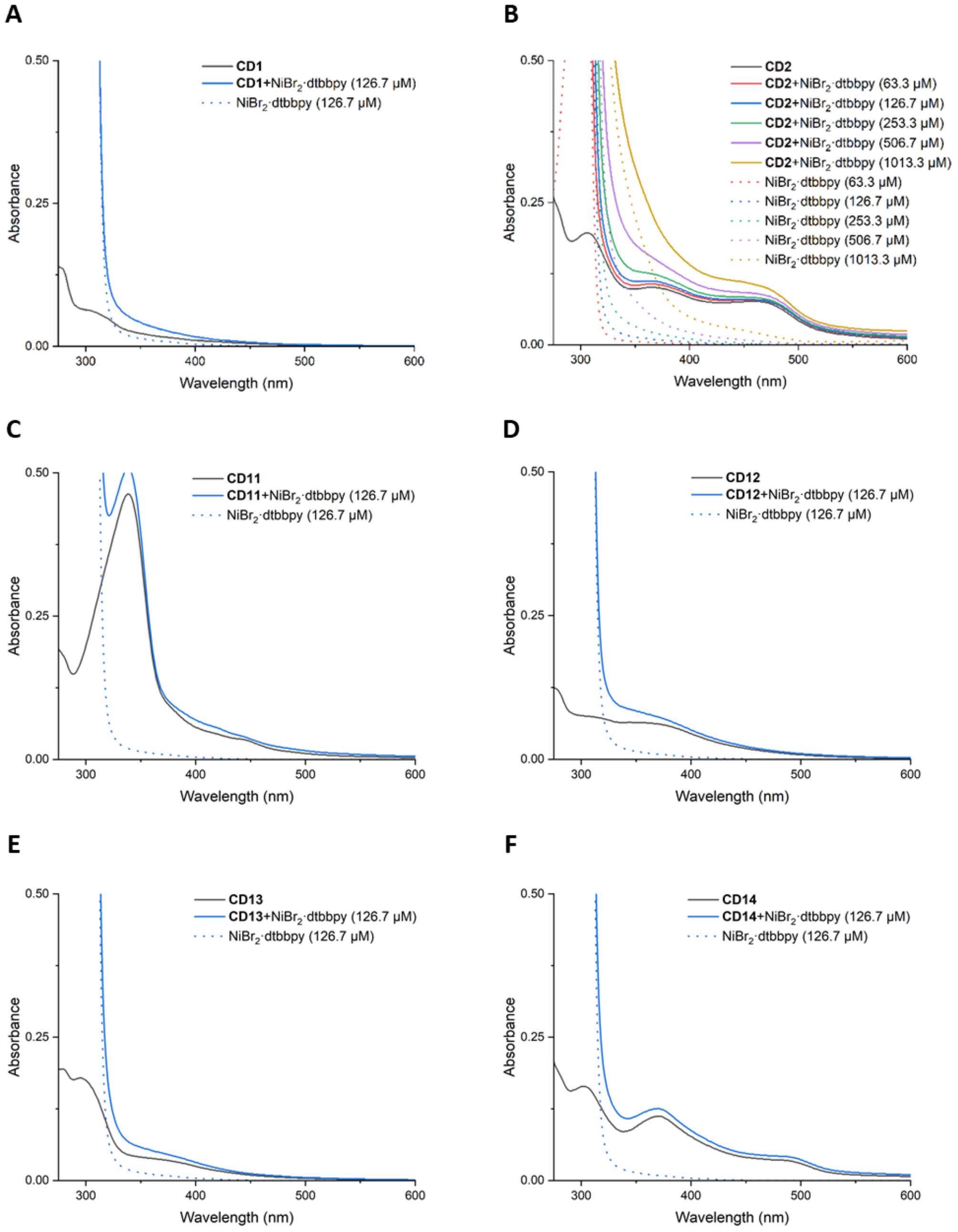

Figure 6-48. UV-Vis absorption spectra of CDs in the presence of NiBr$_2$·dtbbpy (DMAc, 298 K).

Quenching studies. The DMAc solution (3 mL) of **CD2** (2 mg) and different amounts of quencher ($NiBr_2$·dtbbpy) was prepared and then diluted with DMAc (50×) for fluorescence measurements (F, λ_{ex} = 440 nm, λ_{em} = 510 nm). The **CD2** lifetime in the presence of quencher is shown in **Figure 6-50**.

$$\frac{F_0}{F} = \frac{\tau_0}{\tau} = 1 + K_{SV}[Q] = 1 + \tau_0 K_q[Q]$$

F_0 is the **CD2** fluorescence intensity without a quencher; F is the **CD2** fluorescence intensity with a quencher; K_{SV} is the Stern–Volmer quenching constant; [Q] is the quencher concentration; τ_0 is the **CD2** lifetime in the absence of quencher; τ is the **CD2** lifetime in the presence of quencher; K_q is the bimolecular quenching rate constant.

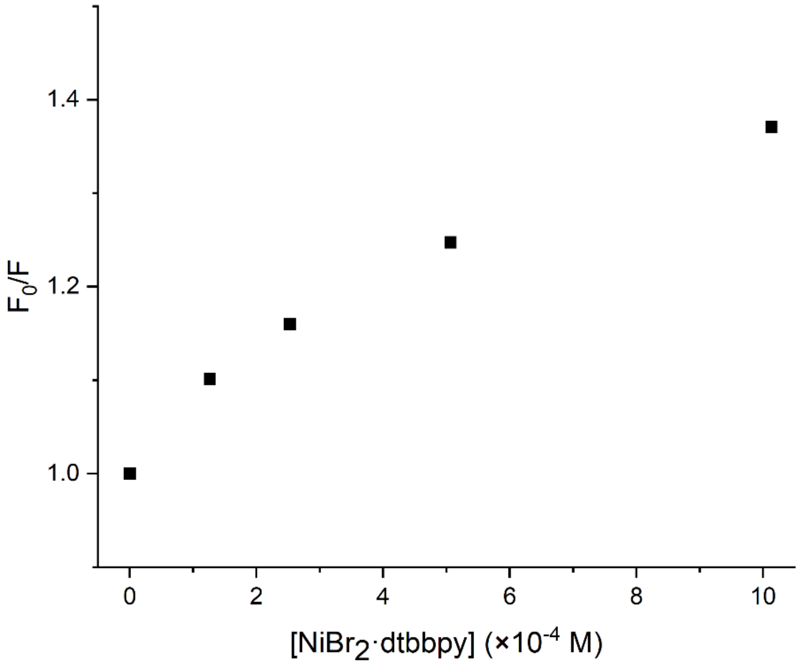

Figure 6-49. Steady-state Stern−Volmer quenching plot of **CD2** based on fluorescence. Steady-state quenching rate constant could not be accurately measured due to the broad absorption of $Ni(dtbbpy)Br_2$ that overlaps with **CD2**.

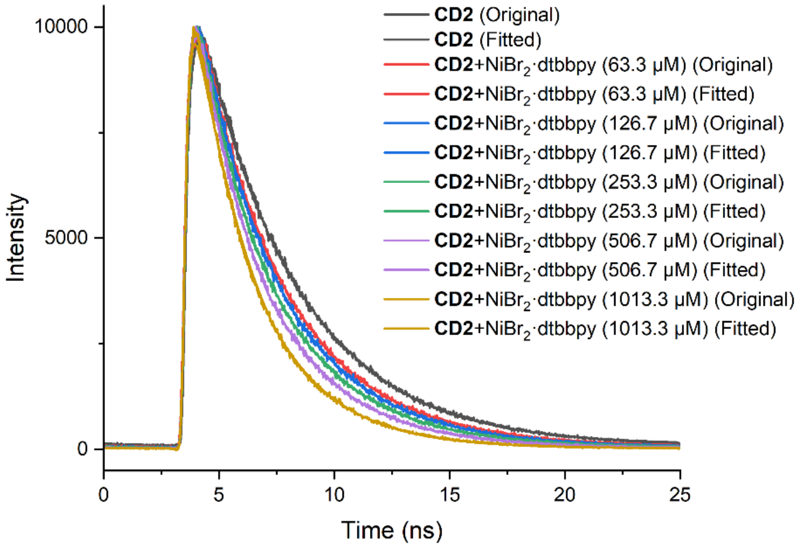

	A_1	**τ_1 (ns)**
CD2	11.705	4.032
+ NiBr$_2$·dtbbpy (63.3 μM**)**	11.774	3.798
+ NiBr$_2$·dtbbpy (126.7 μM)	11.892	3.677
+ NiBr$_2$·dtbbpy (253.3 μM)	11.954	3.516
+ NiBr$_2$·dtbbpy (506.7 μM)	12.044	3.289
+ NiBr$_2$·dtbbpy (1013.3 μM)	11.996	2.880

Figure 6-50. Photoluminescence lifetime of **CD2** in the presence of NiBr$_2$·dtbbpy (DMAc, 298 K, λ_{ex} = 470 nm, λ_{em} = 520 nm).

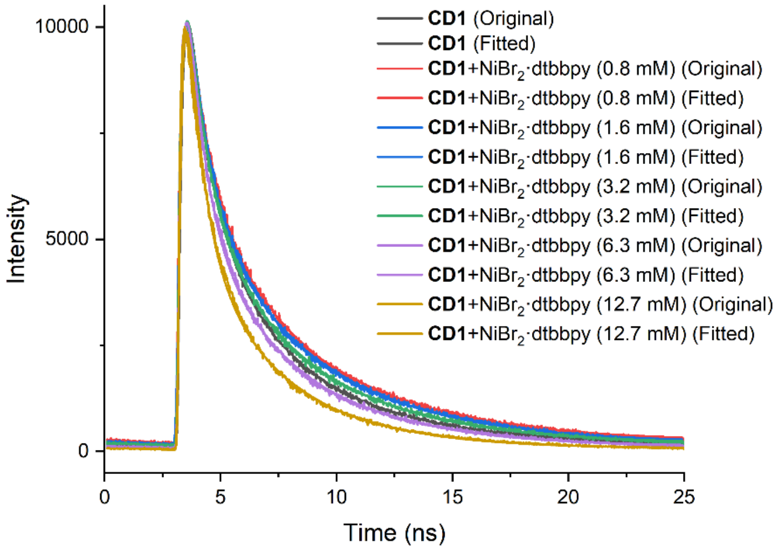

	A_1	**A_2**	**τ_1 (ns)**	**τ_2 (ns)**
CD1 (0.17 mg/mL)	6.136	7.29	4.540	0.966
+ NiBr$_2$·dtbbpy (0.8 mM)	6.790	6.51	5.074	0.870
+ NiBr$_2$·dtbbpy (1.6 mM)	6.573	7.01	4.964	0.860
+ NiBr$_2$·dtbbpy (3.2 mM)	6.400	7.42	4.767	0.826
+ NiBr$_2$·dtbbpy (6.3 mM)	6.004	8.31	4.408	0.755
+ NiBr$_2$·dtbbpy (12.7 mM)	5.50	9.04	3.892	0.692

Figure 6-51. Photoluminescence lifetime of **CD1** in the presence of NiBr$_2$·dtbbpy (DMAc, 298 K, λ_{ex} = 375 nm, λ_{em} = 460 nm).

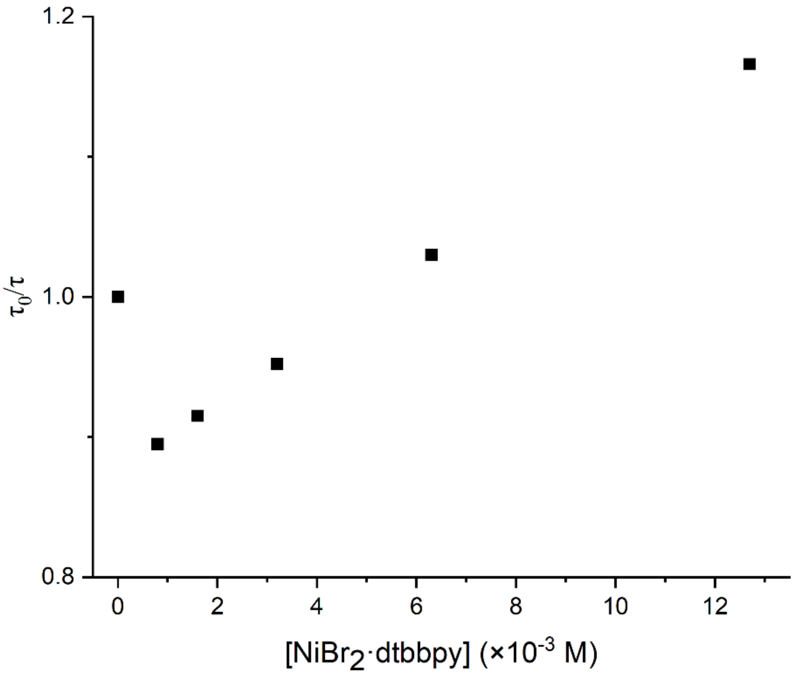

Figure 6-52. Dynamic Stern−Volmer quenching plot of **CD1** showing a drastic increase in lifetime upon addition of quencher, probably due to the formation of some static adducts between **CD1** and NiBr$_2$·dtbbpy.

6.4.2.7. Photophysical characterization of *S*-arylation of methyl 3-mercaptopropionate catalyzed by pyHI

UV-Vis absorption. Different solutions of pyHI (95.2 µmol) and other reaction components were prepared in DMAc (3 mL) and then diluted with DMAc (50×) for UV-Vis absorption measurements.

Solution	Concentrations
pyHI	pyHI (634.7 µM)
pyHI+RSH	pyHI (634.7 µM), methyl 3-mercaptopropionate (**2-9**, 2.5 mM)
pyHI+$NiBr_2$·dtbbpy	pyHI (634.7 µM), $NiBr_2·3H_2O$ (126.7 µM) and dtbbpy (126.7 µM)

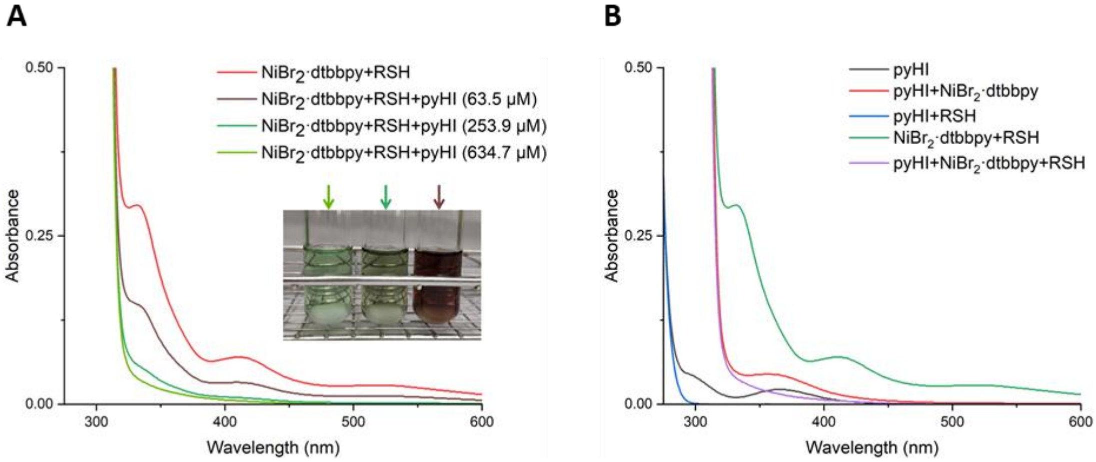

Figure 6-53. UV-Vis absorption spectra of pyHI in the presence of different reaction components (DMAc, 298 K).

6.5. Experimental section for Chapter 4

6.5.1. Synthesis and characterization of other CDs

GlcN·HCl (**2-1**) was dissolved in ultrapure H_2O (20 mL) in a conical flask (300 mL). The doping agent was added and the mixture was agitated to yield a homogenous solution. The flask was transferred into a domestic microwave in a fume hood and heated at 700 W for the respective time. The crude mixture was cooled for 10 min before ultrapure H_2O (40 mL) was added. The resulting solution was filtered through a filter paper and centrifuged at 8000 rpm for 0.5 h through Amicon® Ultra-15 centrifugal filter units. The filtrate was lyophilized to yield the desired CDs.

Table 6-23 Summary of the conditions used for the synthesis of the CDs.

Entry	**CD**	**Carbon source (mmol/mL)**	**Doping agent (mmol/mL)**	**Time / min**
1	**CD15**	GlcN·HCl (**2-1**) (0.12)	β-Ala (**2-2**) (0.06) 2,6-Diaminopyridine (**2-15**) (0.06)	3
2	**CD16**	GlcN·HCl (**2-1**) (0.12)	2-Aminopyridine (**4-5**) (0.13)	3
3	**CD17**[b]	GlcN·HCl (**2-1**) (0.08)	2,5-Diaminopyridine (**4-6**) (0.08)	4.5
4	**CD18**	GlcN·HCl (**2-1**) (0.12)	2,4-Diaminopyridine (**4-7**) (0.13)	3
5	**CD19**[b]	GlcN·HCl (**2-1**) (0.08)	2-Amino-4-chloropyridine (**4-8**) (0.08)	3
6	**CD20**[c]	GlcN·HCl (**2-1**) (0.07)	2-Amino-4-bromopyridine (**4-9**) (0.07)	3
7	**CD21**	GlcN·HCl (**2-1**) (0.12)	2-Amino-4-methylpyridine (**4-10**) (0.13)	3
8	**CD22**	GlcN·HCl (**2-1**) (0.12)	2-Picolylamine (**4-11**) (0.13)	3
9	**CD23**[a]	GlcN·HCl (**2-1**) (0.09)	2,6-Pyridinedimethanamine (**4-12**) (0.10)	4.5
10	**CD24**[a]	GlcN·HCl (**2-1**) (0.09)	1,2-Diaminobenzene (**4-13**) (0.10)	3
11	**CD25**[b]	GlcN·HCl (**2-1**) (0.08)	Anthranilic acid (**4-14**) (0.08)	4.5
12	**CD26**[d]	GlcN·HCl (**2-1**) (0.05)	4-Aminophenol (**4-15**) (0.06)	4.5

[a]The doping agent was first dissolved in MeOH (5 mL) and then added to the aqueous solution (20 mL) of carbon source. [b]The doping agent was first dissolved in MeOH (10 mL) and then added to the aqueous solution (20 mL) of carbon source. [c]The doping agent was first dissolved in MeOH (15 mL) and then added to the aqueous solution (20 mL) of carbon source. [d]The doping agent was first dissolved in MeOH (25 mL) and then added to the aqueous solution (20 mL) of carbon source.

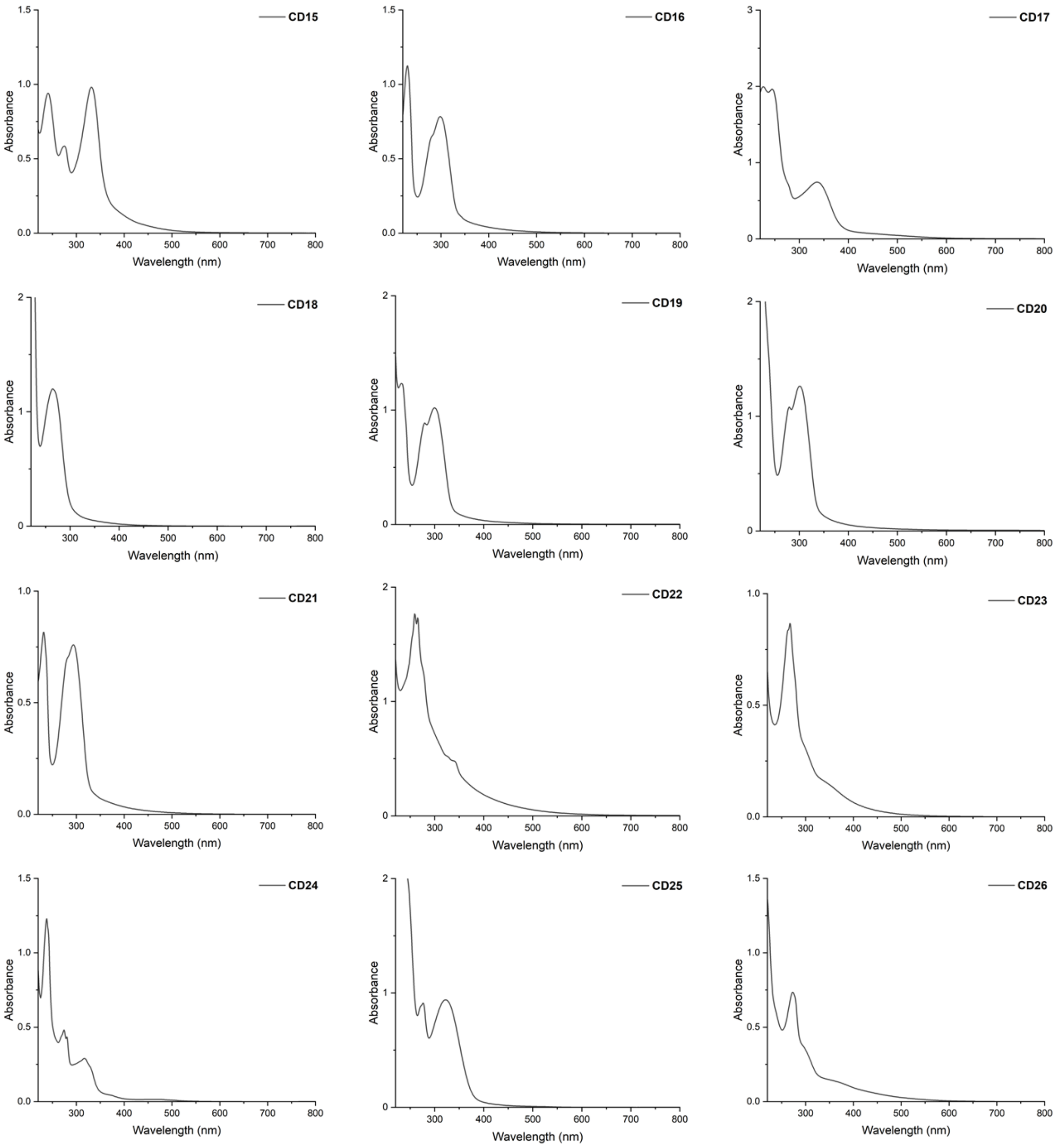

Figure 6-54. Absorption spectra of **CD15-CD26** (H_2O, 298 K).

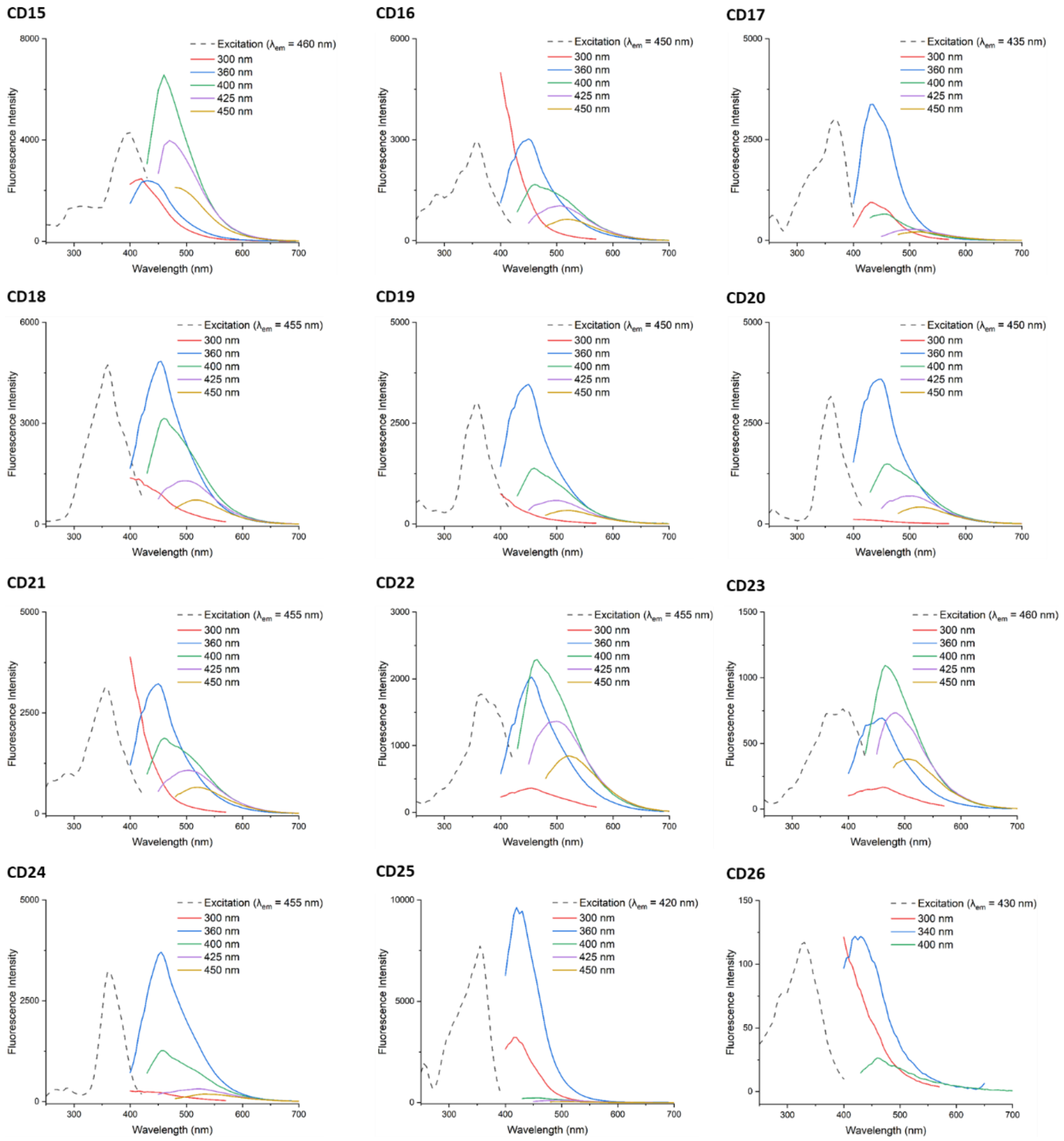

Figure 6-55. Excitation and emission spectra of **CD15-CD26** recorded upon excitation with different excitation wavelengths (H_2O, 298 K).

6.5.2. Isomerization reaction

Compounds **4-3**, **4-18** and **4-20** were kindly provided by Lewis Mcghie and Dr. John J. Molloy.

6.5.2.1. Isomerization of stilbene

Trans-stilbene (**4-1**, 34.2 mg, 0.19 mmol) or *cis*-stilbene (**4-2**, 33.5 µL, 0.19 mmol) was added to an oven-dried glass vial equipped with a stir bar. Subsequently, a DMSO solution (3 mL) of photocatalyst (15 mg) was added. The glass vial was sealed with a septum and Parafilm. The reaction mixture was stirred and sonicated for 10 min and subsequently degassed with Argon for 10 min. The vial was then irradiated with the 440 nm LED lamp at room temperature for 24 h. 1,3,5-Trimethoxybenzene (32.0 mg, 0.19 mmol) was added as internal standard to determine NMR yields. An aliquot of the resulting mixture (~250 µL) was filtered through a syringe filter, diluted with DMSO-d_6 (~250 µL) and subjected to ^{1}H-NMR analysis.

Table 6-24 Screening of photocatalysts and reaction conditions for isomerization of *trans*-stilbene.

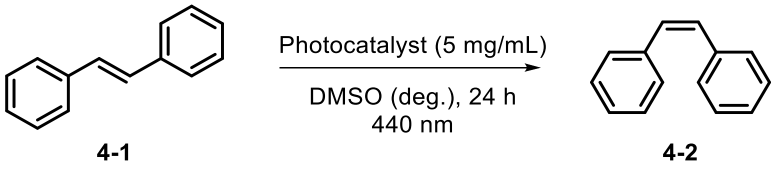

Entry	Conditions	*Z*+*E* [%], *Z*/*E*
1	TiO_2	96, 2:98
2	**CD11**	98, 66:34
3	**CD15**	98, 66:34
4	TiO_2, 525 nm[a]	99, 0:100
5	No photocatalyst, MeCN	99, 1:99
6	**CD1**/TiO_2, MeCN	98, 15:85

[a] 525 nm LED lamp (200% power). Reaction conditions: *trans*-stilbene (0.19 mmol), DMSO (3 mL), photocatalyst (15 mg), 440 nm LED lamp (50% power), 24 h. NMR yields were determined by ^{1}H-NMR using 1,3,5-trimethoxybenzene as internal standard. deg. = degassed.

Table 6-25 Screening of photocatalysts and reaction conditions for isomerization of *cis*-stilbene.

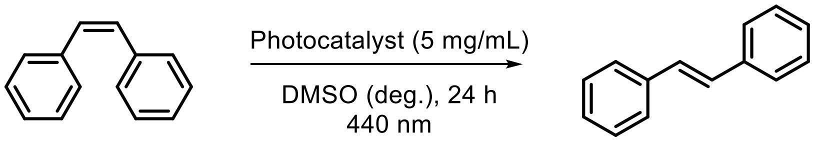

4-2

4-1

Entry	Conditions	*Z*+*E* [%], *Z*/*E*
1	No photocatalyst	quant., 92:8
2	TiO_2	97, 36:64
3	**CD1**/TiO_2 (10 mg/mL)	quant., 25:75
4	**CD2**/TiO_2	quant., 38:62
5	**CD1**	quant., 52:48
6	**CD2**	99, 56:44
7	**CD3**	99, 66:34
8	**CD4**	98, 64:36
9	No photocatalyst, 525 nm[a]	quant., 100:0
10	TiO_2, 525 nm[a]	quant., 96:4
11	**CD1**/TiO_2, 525 nm[a]	99, 30:70
12	**CD2**/TiO_2, 525 nm[a]	quant., 60:40
13	**CD1**, 525 nm[a]	quant., 64:36
14	**CD1**/TiO_2 (10 mg/mL), MeCN	quant., 13:87

[a] 525 nm LED lamp (200% power). Reaction conditions: *cis*-stilbene (0.19 mmol), DMSO (3 mL), photocatalyst (15 mg), 440 nm LED lamp (50% power), 24 h. NMR yields were determined by ^{1}H-NMR using 1,3,5-trimethoxybenzene as internal standard. deg. = degassed.

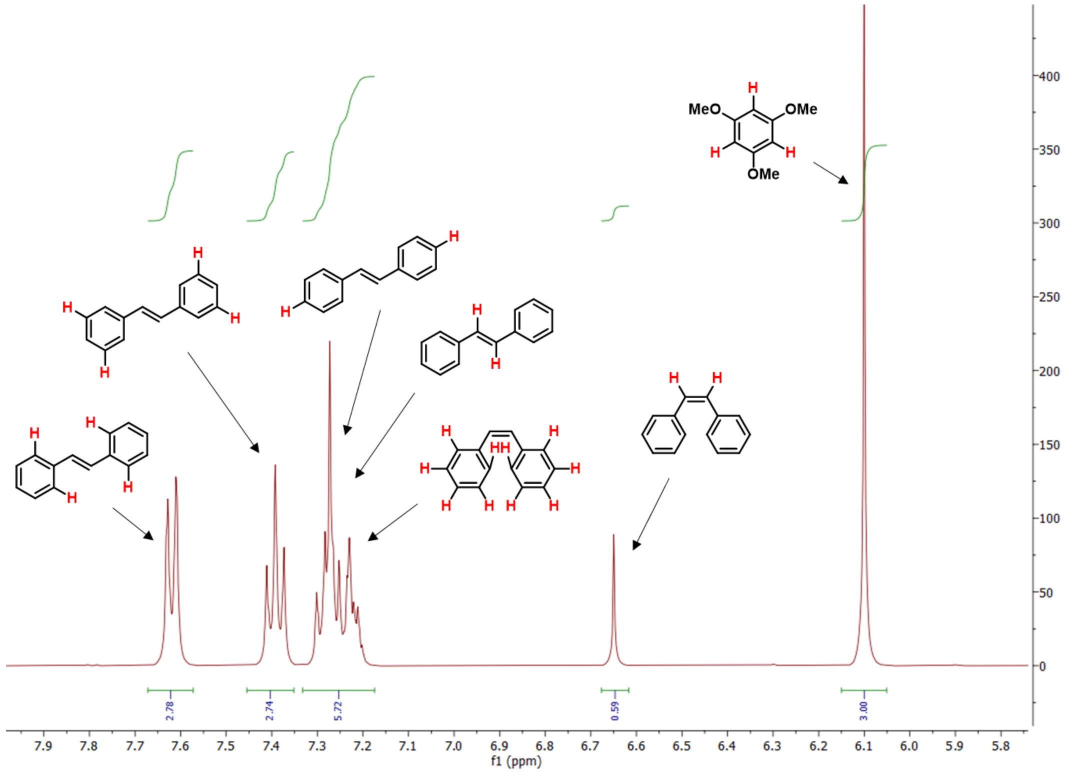

Figure 6-56. Representative ^{1}H-NMR spectrum of a crude reaction mixture for determining *Z*/*E* ratio in the isomerization of stilbene (DMSO-d$_6$, 400 MHz).

6.5.2.2. Isomerization of ethyl (*E*)-3-(*p*-tolyl)but-2-enoate

Ethyl (*E*)-3-(*p*-tolyl)but-2-enoate (**4-3**, 38.8 mg, 0.19 mmol) was added to an oven-dried glass vial equipped with a stir bar. Subsequently, a DMSO solution (3 mL) of photocatalyst (15 mg) was added. The glass vial was sealed with a septum and Parafilm. The reaction mixture was stirred and sonicated for 10 min and subsequently degassed with Argon for 10 min. The vial was then irradiated with the 440 nm LED lamp at room temperature for 24 h. 1,2,4,5-Tetramethylbenzene (25.5 mg, 0.19 mmol) was added as internal standard to determine NMR yields. An aliquot of the resulting mixture (~250 µL) was filtered through a syringe filter, diluted with DMSO-d_6 (~250 µL) and subjected to ^{1}H-NMR analysis.

Table 6-26 Screening of photocatalysts and reaction conditions for isomerization of ethyl (*E*)-3-(*p*-tolyl)but-2-enoate.

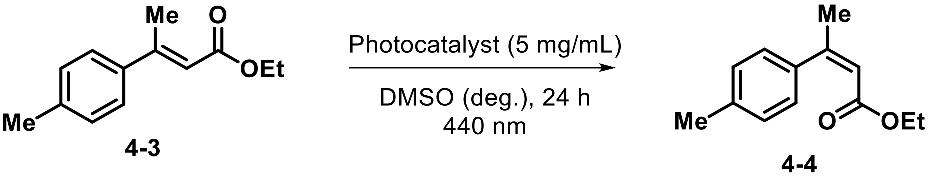

Entry	Conditions	*Z+E* [%], *Z*/*E*
1	No photocatalyst[b]	99, 8:92
2	TiO_2	98, 0:100
3	**CD11**/TiO_2 (1.67 mg/mL)[b]	93, 77:23
4	**CD1**, 120 h	91, 80:20
5	**CD2**, 120 h	95, 74:26
6	**CD1**, 14 days	86, 87:13
7	**CD2**, 14 days	94, 80:20
8	**CD1**, DMSO (1.5 mL)	91, 12:88
9	**CD1** (1.67 mg/mL)	95, 31:69
10	**CD1** (10 mg/mL)	98, 15:85
11	**CD1**[b]	95, 31:69
12	**CD1** (1.67 mg/mL)[b]	93, 38:62
13	1,3-Diaminobenzene (1.67 mg/mL)[b]	98, 15:85
14	2,6-Diaminopyridine (1.67 mg/mL)[b]	99, 25:75
15	2,6-Diaminopyridine (1.67 mg/mL)[b], 4 days	91, 85:15
16	No photocatalyst, 525 nm[a]	99, 0:100
17	TiO_2, 525 nm[a]	quant., 0:100
18	**CD1**/TiO_2, 525 nm[a]	99, 0:100
19	**CD2**/TiO_2, 525 nm[a]	99, 0:100
20	**CD1**, 525 nm[a]	quant., 0:100
21	**CD2**, 525 nm[a]	quant., 0:100

[a] 525 nm LED lamp (200% power). [b] 440 nm LED lamp (100% power). Reaction conditions: ethyl (*E*)-3-(*p*-tolyl)but-2-enoate (0.19 mmol), DMSO (3 mL), photocatalyst (15 mg), 440 nm LED lamp (50% power), 24 h. NMR yields were determined by ^{1}H-NMR using 1,2,4,5-tetramethylbenzene as internal standard. deg. = degassed.

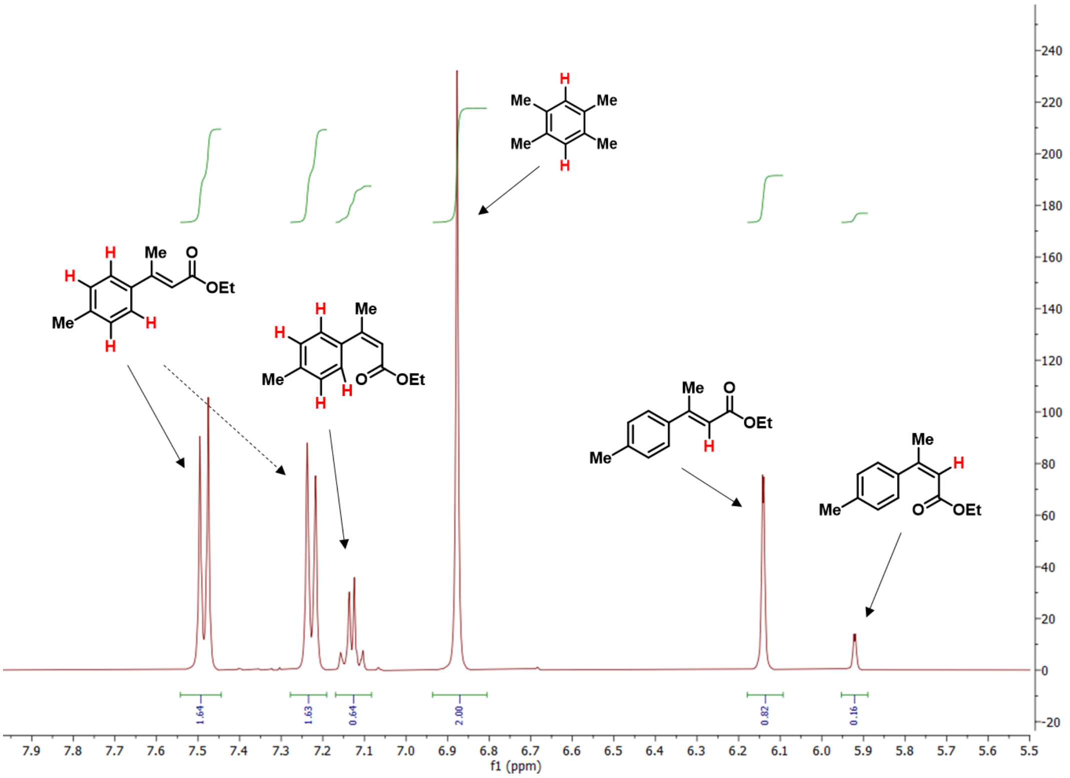

Figure 6-57. Representative ^{1}H-NMR spectrum of a crude reaction mixture for determining *Z*/*E* ratio in the isomerization of ethyl (*E*)-3-(*p*-tolyl)but-2-enoate (DMSO-d$_6$, 400 MHz).

6.5.2.3. Isomerization of ethyl cinnamate

Ethyl cinnamate (**4-16**, 31.9 μL, 0.19 mmol) was added to an oven-dried glass vial equipped with a stir bar. Subsequently, a DMSO solution (3 mL) of photocatalyst (15 mg) was added. The glass vial was sealed with a septum and Parafilm. The reaction mixture was stirred and sonicated for 10 min and subsequently degassed with Argon for 10 min. The vial was then irradiated with the 440 nm LED lamp at room temperature for 24 h. 1,2,4,5-Tetramethylbenzene (25.5 mg, 0.19 mmol) was added as internal standard to determine NMR yields. An aliquot of the resulting mixture (~250 μL) was filtered through a syringe filter, diluted with DMSO-d_6 (~250 μL) and subjected to ^{1}H-NMR analysis.

Table 6-27 Screening of photocatalysts and reaction conditions for isomerization of ethyl cinnamate.

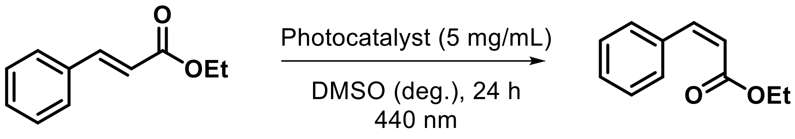

4-16 **4-17**

Entry	Conditions	*Z+E* [%], *Z*/*E*
1	No photocatalyst	quant., 0:100
2	**CD1**	96, 13:87
3	**CD2**	quant., 16:84
4	**CD1**, 7 days	77, 11:89
5	**CD2**, 7 days	97, 10:90
6	**CD1**[b]	88, 16:84
7	**CD2**[b]	quant., 14:86
8	**CD11**[b]	99, 14:86
9	**CD15**[b]	93, 17:83
10	**CD11** (1.67 mg/mL)[b]	98, 13:87
11	**CD15** (1.67 mg/mL)[b]	quant., 17:83
12	No photocatalyst, 525 nm[a]	99, 0:100
13	**CD1**, 525 nm[a]	quant., 0:100
14	**CD2**, 525 nm[a]	quant., 0:100

[a] 525 nm LED lamp (200% power). [b] 440 nm LED lamp (100% power). Reaction conditions: ethyl cinnamate (0.19 mmol), DMSO (3 mL), photocatalyst (15 mg), 440 nm LED lamp (50% power), 24 h. NMR yields were determined by ^{1}H-NMR using 1,2,4,5-tetramethylbenzene as internal standard. deg. = degassed.

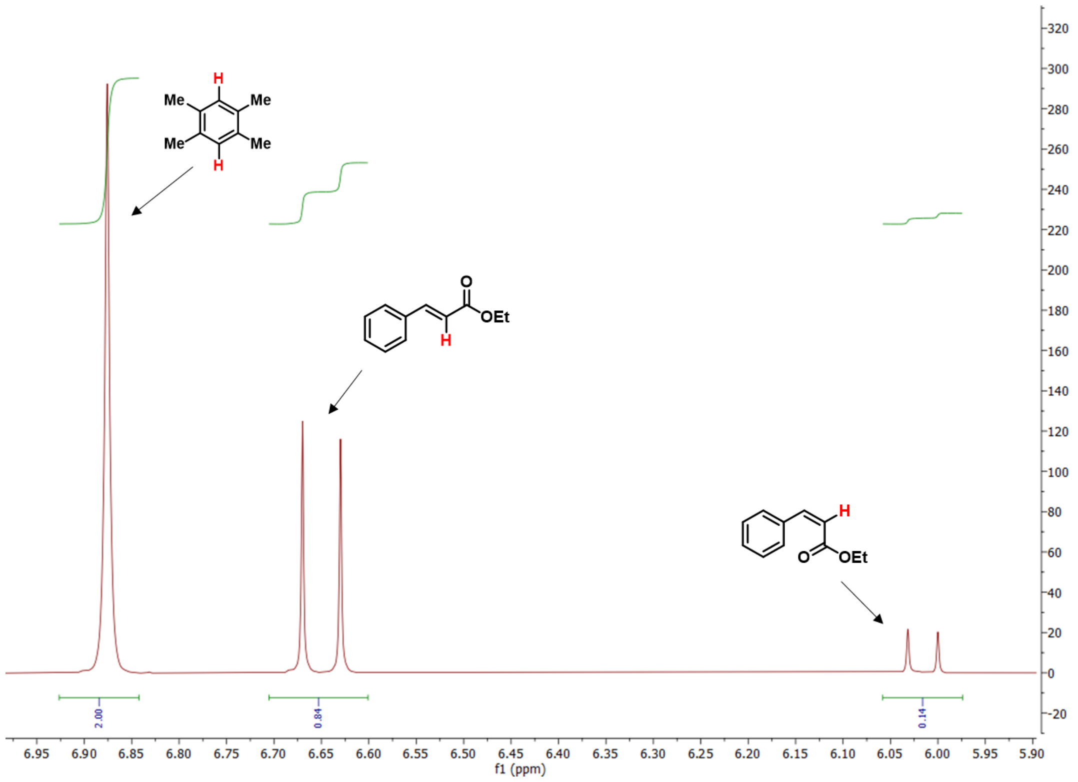

Figure 6-58. Representative ^{1}H-NMR spectrum of a crude reaction mixture for determining *Z*/*E* ratio in the isomerization of ethyl cinnamate (DMSO-d_6, 400 MHz).

6.5.2.4. Isomerization of (*E*)-4-(4-phenylbut-3-en-2-yl)morpholine

(*E*)-4-(4-phenylbut-3-en-2-yl)morpholine (**4-18**, 41.2 mg, 0.19 mmol) was added to an oven-dried glass vial equipped with a stir bar. Subsequently, a DMSO solution (3 mL) of photocatalyst (5 mg) was added. The glass vial was sealed with a septum and Parafilm. The reaction mixture was stirred and sonicated for 10 min and subsequently degassed with Argon for 10 min. The vial was then irradiated with the 440 nm LED lamp at room temperature for 24 h. 1,2,4,5-Tetramethylbenzene (25.5 mg, 0.19 mmol) was added as internal standard to determine NMR yields. An aliquot of the resulting mixture (~250 µL) was filtered through a syringe filter, diluted with DMSO-d_6 (~250 µL) and subjected to ^{1}H-NMR analysis.

Table 6-28 Screening of photocatalysts and reaction conditions for isomerization of (*E*)-4-(4-phenylbut-3-en-2-yl)morpholine.

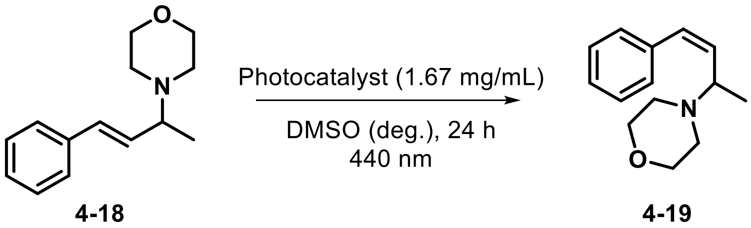

Entry	Conditions	*Z*+*E* [%], *Z*/*E*
1	No photocatalyst	93, 1:99
2	**CD1**	90, 3:97
3	**CD2**	81, 11:89
4	**CD11**	86, 5:95
5	**CD15**	88, 8:92

Reaction conditions: (*E*)-4-(4-phenylbut-3-en-2-yl)morpholine (0.19 mmol), DMSO (3 mL), photocatalyst (5 mg), 440 nm LED lamp (100% power), 24 h. NMR yields were determined by ^{1}H-NMR using 1,2,4,5-tetramethylbenzene as internal standard. deg. = degassed.

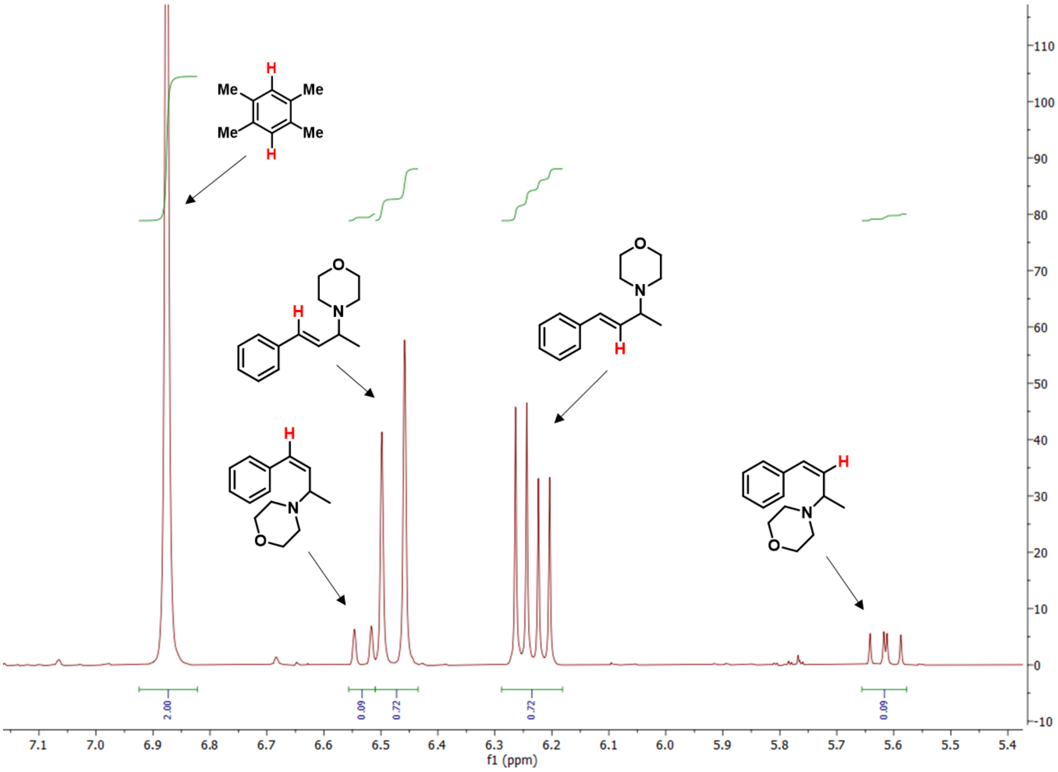

Figure 6-59. Representative ^{1}H-NMR spectrum of a crude reaction mixture for determining *Z*/*E* ratio in the isomerization of (*E*)-4-(4-phenylbut-3-en-2-yl)morpholine (DMSO-d$_6$, 400 MHz).

6.5.2.5. Isomerization of (*E*)-4,4,5,5-tetramethyl-2-(2-phenylprop-1-en-1-yl)-1,3,2-dioxaborolane

(*E*)-4,4,5,5-tetramethyl-2-(2-phenylprop-1-en-1-yl)-1,3,2-dioxaborolane (**4-20**, 46.4 mg, 0.19 mmol) was added to an oven-dried glass vial equipped with a stir bar. Subsequently, a DMSO solution (3 mL) of photocatalyst (15 mg) was added. The glass vial was sealed with a septum and Parafilm. The reaction mixture was stirred and sonicated for 10 min and subsequently degassed with Argon for 10 min. The vial was then irradiated with the 440 nm LED lamp at room temperature for 24 h. 1,3,5-Trimethoxybenzene (32.0 mg, 0.19 mmol) was added as internal standard to determine NMR yields. An aliquot of the resulting mixture (~250 µL) was filtered through a syringe filter, diluted with DMSO-d_6 (~250 µL) and subjected to ^{1}H-NMR analysis.

Table 6-29 Screening of photocatalysts and reaction conditions for isomerization of (*E*)-4,4,5,5-tetramethyl-2-(2-phenylprop-1-en-1-yl)-1,3,2-dioxaborolane.

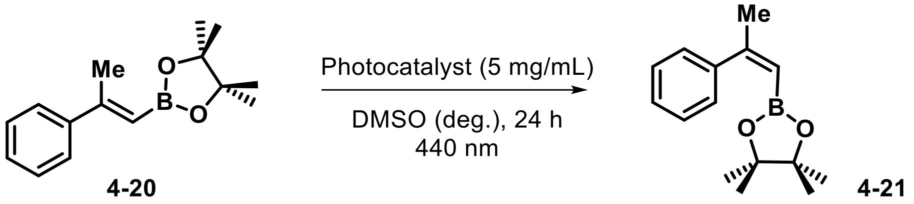

Entry	Conditions	*Z*+*E* [%], *Z*/*E*
1	**CD11** (20 mg/mL)[a]	73, 19:81
2	**CD11** (10 mg/mL)[a]	83, 29:71
3	**CD11** (5 mg/mL)[a]	90, 44:56
4	**CD11** (0.67 mg/mL)[a]	97, 26:74
5	**CD11** (0.17 mg/mL)[a]	98, 12:88
6	**CD11** (1.67 mg/mL)[a]	96, 32:68
7	**CD15** (1.67 mg/mL)[a]	92, 26:74
8	**CD11** (1.67 mg/mL)[a], 72 h	93, 58:42
9	**CD15** (1.67 mg/mL)[a], 72 h	86, 41:59
10	**CD15** (1.67 mg/mL)[a], 96 h	85, 52:48
11	**CD11** (1.67 mg/mL)[a], 12 days	78, 63:37
12	**CD15** (1.67 mg/mL)[a], 12 days	73, 75:25

[a] 440 nm LED lamp (100% power). Reaction conditions: (*E*)-4,4,5,5-tetramethyl-2-(2-phenylprop-1-en-1-yl)-1,3,2-dioxaborolane (0.19 mmol), DMSO (3 mL), photocatalyst (15 mg), 440 nm LED lamp (50% power), 24 h. NMR yields were determined by ^{1}H-NMR using 1,3,5-trimethoxybenzene as internal standard. deg. = degassed.

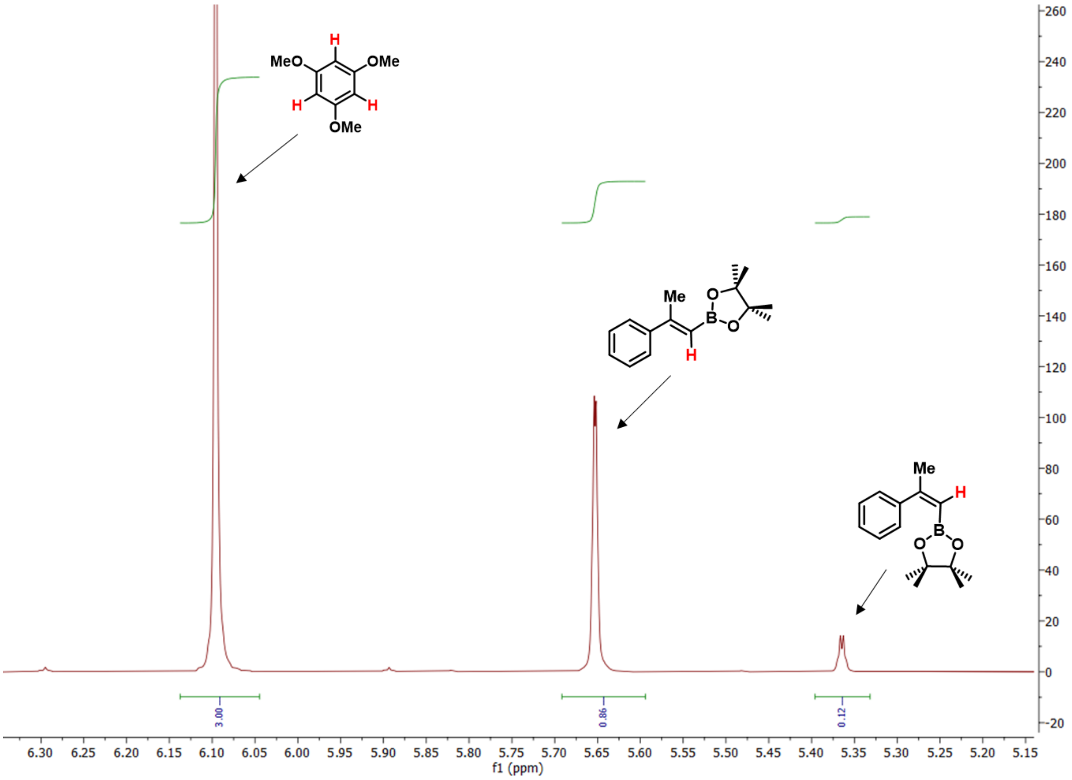

Figure 6-60. Representative ^{1}H-NMR spectrum of a crude reaction mixture for determining *Z*/*E* ratio in the isomerization of (*E*)-4,4,5,5-tetramethyl-2-(2-phenylprop-1-en-1-yl)-1,3,2-dioxaborolane (DMSO-d_6, 400 MHz).

6.5.2.6. Photophysical characterization of the isomerization of ethyl (*E*)-3-(*p*-tolyl)but-2-enoate catalyzed by CD11

UV-Vis absorption and fluorescence. Different solutions of **CD11** (2 mg) and ethyl (*E*)-3-(*p*-tolyl)but-2-enoate (3.0 µmol) were prepared in DMSO (3 mL) and then diluted with DMSO (50×) for UV-Vis absorption and fluorescence measurements.

Solution	Concentrations
CD11	**CD11** (13.3 µg/mL)
CD11+**4-3**	**CD11** (13.3 µg/mL), ethyl (E)-3-(p-tolyl)but-2-enoate (**4-3**, 19.8 µM)

7. References

(1) Hong, G.; Diao, S.; Antaris, A. L.; Dai, H. Carbon Nanomaterials for Biological Imaging and Nanomedicinal Therapy. *Chem. Rev.* **2015**, *115*, 10816-10906.

(2) Wang, X.; Liu, X.; Chen, J.; Han, H.; Yuan, Z. Evaluation and mechanism of antifungal effects of carbon nanomaterials in controlling plant fungal pathogen. *Carbon* **2014**, *68*, 798-806.

(3) Battigelli, A.; Menard-Moyon, C.; Bianco, A. Carbon nanomaterials as new tools for immunotherapeutic applications. *J. Mater. Chem. B* **2014**, *2*, 6144-6156.

(4) Xu, X.; Ray, R.; Gu, Y.; Ploehn, H. J.; Gearheart, L.; Raker, K.; Scrivens, W. A. Electrophoretic Analysis and Purification of Fluorescent Single-Walled Carbon Nanotube Fragments. *J. Am. Chem. Soc.* **2004**, *126*, 12736-12737.

(5) Lim, S. Y.; Shen, W.; Gao, Z. Carbon quantum dots and their applications. *Chem. Soc. Rev.* **2015**, *44*, 362-381.

(6) Hutton, G. A. M.; Martindale, B. C. M.; Reisner, E. Carbon dots as photosensitisers for solar-driven catalysis. *Chem. Soc. Rev.* **2017**, *46*, 6111-6123.

(7) Wu, Z. L.; Liu, Z. X.; Yuan, Y. H. Carbon dots: materials, synthesis, properties and approaches to long-wavelength and multicolor emission. *J. Mater. Chem. B* **2017**, *5*, 3794-3809.

(8) Hu, S.-L.; Niu, K.-Y.; Sun, J.; Yang, J.; Zhao, N.-Q.; Du, X.-W. One-step synthesis of fluorescent carbon nanoparticles by laser irradiation. *J. Mater. Chem.* **2009**, *19*, 484-488.

(9) Tian, L.; Ghosh, D.; Chen, W.; Pradhan, S.; Chang, X.; Chen, S. Nanosized Carbon Particles From Natural Gas Soot. *Chem. Mater.* **2009**, *21*, 2803-2809.

(10) Wang, Q.; Zheng, H.; Long, Y.; Zhang, L.; Gao, M.; Bai, W. Microwave–hydrothermal synthesis of fluorescent carbon dots from graphite oxide. *Carbon* **2011**, *49*, 3134-3140.

(11) Zhou, Y.; Mintz, K. J.; Sharma, S. K.; Leblanc, R. M. Carbon Dots: Diverse Preparation, Application, and Perspective in Surface Chemistry. *Langmuir* **2019**, *35*, 9115-9132.

(12) Yang, Y.; Cui, J.; Zheng, M.; Hu, C.; Tan, S.; Xiao, Y.; Yang, Q.; Liu, Y. One-step synthesis of amino-functionalized fluorescent carbon nanoparticles by hydrothermal carbonization of chitosan. *Chem. Commun.* **2012**, *48*, 380-382.

(13) Zhai, X.; Zhang, P.; Liu, C.; Bai, T.; Li, W.; Dai, L.; Liu, W. Highly luminescent carbon nanodots by microwave-assisted pyrolysis. *Chem. Commun.* **2012**, *48*, 7955-7957.

(14) Zong, J.; Zhu, Y.; Yang, X.; Shen, J.; Li, C. Synthesis of photoluminescent carbogenic dots using mesoporous silica spheres as nanoreactors. *Chem. Commun.* **2011**, *47*, 764-766.

(15) Hill, S. A.; Benito-Alifonso, D.; Davis, S. A.; Morgan, D. J.; Berry, M.; Galan, M. C. Practical Three-Minute Synthesis of Acid-Coated Fluorescent Carbon Dots with Tuneable Core Structure. *Sci. Rep.* **2018**, *8*, 12234.

(16) Wang, F.; Hao, Q.; Zhang, Y.; Xu, Y.; Lei, W. Fluorescence quenchometric method for determination of ferric ion using boron-doped carbon dots. *Microchim. Acta* **2015**, *183*, 273-279.

(17) Hill, S.; Galan, M. C. Fluorescent carbon dots from mono- and polysaccharides: synthesis, properties and applications. *Beilstein J. Org. Chem.* **2017**, *13*, 675-693.

(18) Gong, X.; Zhang, Q.; Gao, Y.; Shuang, S.; Choi, M. M.; Dong, C. Phosphorus and Nitrogen Dual-Doped Hollow Carbon Dot as a Nanocarrier for Doxorubicin Delivery and Biological Imaging. *ACS Appl. Mater. Interfaces* **2016**, *8*, 11288-11297.

(19) Yang, C.; Thomsen, R. P.; Ogaki, R.; Kjems, J.; Teo, B. M. Ultrastable green fluorescence carbon dots with a high quantum yield for bioimaging and use as theranostic carriers. *J. Mater. Chem. B* **2015**, *3*, 4577-4584.

(20) Gogoi, N.; Chowdhury, D. Novel carbon dot coated alginate beads with superior stability, swelling and pH responsive drug delivery. *J. Mater. Chem. B* **2014**, *2*, 4089-4099.

(21) Liu, S.; Zhao, N.; Cheng, Z.; Liu, H. Amino-functionalized green fluorescent carbon dots as surface energy transfer biosensors for hyaluronidase. *Nanoscale* **2015**, *7*, 6836-6842.

(22) Shen, P.; Gao, J.; Cong, J.; Liu, Z.; Li, C.; Yao, J. Synthesis of Cellulose-Based Carbon Dots for Bioimaging. *ChemistrySelect* **2016**, *1*, 1314-1317.

(23) Zhu, H.; Wang, X.; Li, Y.; Wang, Z.; Yang, F.; Yang, X. Microwave synthesis of fluorescent carbon nanoparticles with electrochemiluminescence properties. *Chem. Commun.* **2009**, 5118-5120.

(24) Gude, V.; Das, A.; Chatterjee, T.; Mandal, P. K. Molecular origin of photoluminescence of carbon dots: aggregation-induced orange-red emission. *Phys. Chem. Chem. Phys.* **2016**, *18*, 28274-28280.

(25) Chandra, S.; Pathan, S. H.; Mitra, S.; Modha, B. H.; Goswami, A.; Pramanik, P. Tuning of photoluminescence on different surface functionalized carbon quantum dots. *RSC Adv.* **2012**, *2*, 3602-3606.

(26) Sun, Y.; Shen, C.; Wang, J.; Lu, Y. Facile synthesis of biocompatible N, S-doped carbon dots for cell imaging and ion detecting. *RSC Adv.* **2015**, *5*, 16368-16375.

(27) Roy, P.; Chen, P.-C.; Periasamy, A. P.; Chen, Y.-N.; Chang, H.-T. Photoluminescent carbon nanodots: synthesis, physicochemical properties and analytical applications. *Mater. Today* **2015**, *18*, 447-458.

(28) Liu, R.; Wu, D.; Feng, X.; Mullen, K. Bottom-up fabrication of photoluminescent graphene quantum dots with uniform morphology. *J. Am. Chem. Soc.* **2011**, *133*, 15221-15223.

(29) Zhou, Y.; Desserre, A.; Sharma, S. K.; Li, S.; Marksberry, M. H.; Chusuei, C. C.; Blackwelder, P. L.; Leblanc, R. M. Gel-like Carbon Dots: Characterization and their Potential Applications. *ChemPhysChem* **2017**, *18*, 890-897.

(30) Zhou, Y.; Liyanage, P. Y.; Geleroff, D. L.; Peng, Z.; Mintz, K. J.; Hettiarachchi, S. D.; Pandey, R. R.; Chusuei, C. C.; Blackwelder, P. L.; Leblanc, R. M. Photoluminescent Carbon Dots: A Mixture of Heterogeneous Fractions. *ChemPhysChem* **2018**, *19*, 2589-2597.

(31) Cayuela, A.; Soriano, M. L.; Carrillo-Carrion, C.; Valcarcel, M. Semiconductor and carbon-based fluorescent nanodots: the need for consistency. *Chem. Commun.* **2016**, *52*, 1311-1326.

(32) Yuan, Y. H.; Liu, Z. X.; Li, R. S.; Zou, H. Y.; Lin, M.; Liu, H.; Huang, C. Z. Synthesis of nitrogen-doping carbon dots with different photoluminescence properties by controlling the surface states. *Nanoscale* **2016**, *8*, 6770-6776.

(33) Shen, L.; Zhang, L.; Chen, M.; Chen, X.; Wang, J. The production of pH-sensitive photoluminescent carbon nanoparticles by the carbonization of polyethylenimine and their use for bioimaging. *Carbon* **2013**, *55*, 343-349.

(34) Wu, Z. L.; Gao, M. X.; Wang, T. T.; Wan, X. Y.; Zheng, L. L.; Huang, C. Z. A general quantitative pH sensor developed with dicyandiamide N-doped high quantum yield graphene quantum dots. *Nanoscale* **2014**, *6*, 3868-3874.

(35) Li, L.; Dong, T. Photoluminescence tuning in carbon dots: surface passivation or/and functionalization, heteroatom doping. *J. Mater. Chem. C* **2018**, *6*, 7944-7970.

(36) Sun, Y.-P.; Zhou B.; Lin, Y.; Wang, W.; Fernando, K. A. S.; Pathak, P.; Meziani, M. J.; Harruff. B. A.; Wang, X.; Wang, H.; Luo, P. G.; Yang, H.; Kose, M. E.; Chen, B.; Veca L. M.; Xie, S.-Y. Quantum-Sized Carbon Dots for Bright and Colorful Photoluminescence. *J. Am. Chem. Soc.* **2006**, *128*, 7756-7757.

(37) Guo, Y.; Wang, Z.; Shao, H.; Jiang, X. Hydrothermal synthesis of highly fluorescent carbon nanoparticles from sodium citrate and their use for the detection of mercury ions. *Carbon* **2013**, *52*, 583-589.

(38) Yan, F.; Zou, Y.; Wang, M.; Mu, X.; Yang, N.; Chen, L. Highly photoluminescent carbon dots-based fluorescent chemosensors for sensitive and selective detection of mercury ions and application of imaging in living cells. *Sens. Actuators B Chem.* **2014**, *192*, 488-495.

(39) Qu, K.; Wang, J.; Ren, J.; Qu, X. Carbon dots prepared by hydrothermal treatment of dopamine as an effective fluorescent sensing platform for the label-free detection of iron(III) ions and dopamine. *Chem. Eur. J.* **2013**, *19*, 7243-7249.

(40) Bandi, R.; Dadigala, R.; Gangapuram, B. R.; Guttena, V. Green synthesis of highly fluorescent nitrogen - Doped carbon dots from Lantana camara berries for effective detection of lead(II) and bioimaging. *J. Photochem. Photobiol. B* **2018**, *178*, 330-338.

(41) Jiang, K.; Sun, S.; Zhang, L.; Lu, Y.; Wu, A.; Cai, C.; Lin, H. Red, green, and blue luminescence by carbon dots: full-color emission tuning and multicolor cellular imaging. *Angew. Chem. Int. Ed.* **2015**, *54*, 5360-5363.

(42) Liang, Y. C.; Cao, Q.; Liu, K. K.; Peng, X. Y.; Sui, L. Z.; Wang, S. P.; Song, S. Y.; Wu, X. Y.; Zhao, W. B.; Deng, Y.; et al. Phosphorescent Carbon-Nanodots-Assisted Forster Resonant Energy Transfer for Achieving Red Afterglow in an Aqueous Solution. *ACS nano* **2021**, *15*, 16242-16254.

(43) Jaleel, J. A.; Pramod, K. Artful and multifaceted applications of carbon dot in biomedicine. *J Control. Release* **2018**, *269*, 302-321.

(44) Mewada, A.; Pandey, S.; Thakur, M.; Jadhav, D.; Sharon, M. Swarming carbon dots for folic acid mediated delivery of doxorubicin and biological imaging. *J. Mater. Chem. B* **2014**, *2*, 698-705.

(45) Chen, S.; Sun, T.; Zheng, M.; Xie, Z. Carbon Dots Based Nanoscale Covalent Organic Frameworks for Photodynamic Therapy. *Adv. Funct. Mater.* **2020**, *30*, 2004680.

(46) Rosso, C.; Filippini, G.; Prato, M. Carbon Dots as Nano-Organocatalysts for Synthetic Applications. *ACS Catal.* **2020**, *10*, 8090-8105.

(47) Ethordevic, L.; Arcudi, F.; Cacioppo, M.; Prato, M. A multifunctional chemical toolbox to engineer carbon dots for biomedical and energy applications. *Nat. Nanotechnol.* **2022**, *17*, 112-130.

(48) Seayad, J.; List, B. Asymmetric organocatalysis. *Org. Biomol. Chem.* **2005**, *3*, 719-724.

(49) Min, C.; Seidel, D. Asymmetric Bronsted acid catalysis with chiral carboxylic acids. *Chem. Soc. Rev.* **2017**, *46*, 5889-5902.

(50) Majumdar, B.; Mandani, S.; Bhattacharya, T.; Sarma, D.; Sarma, T. K. Probing Carbocatalytic Activity of Carbon Nanodots for the Synthesis of Biologically Active Dihydro/Spiro/Glyco Quinazolinones and Aza-Michael Adducts. *J. Org. Chem.* **2017**, *82*, 2097-2106.

(51) Taylor, M. S.; Jacobsen, E. N. Asymmetric catalysis by chiral hydrogen-bond donors. *Angew. Chem. Int. Ed.* **2006**, *45*, 1520-1543.

(52) McGilvra, J. D.; Unni, A. K.; Modi, K.; Rawal, V. H. Highly diastereo- and enantioselective Mukaiyama aldol reactions catalyzed by hydrogen bonding. *Angew Chem Int. Ed.* **2006**, *45*, 6130-6133.

(53) Knowles, R. R.; Jacobsen, E. N. Attractive noncovalent interactions in asymmetric catalysis: links between enzymes and small molecule catalysts. *Proc. Natl. Acad. Sci. U. S. A.* **2010**, *107*, 20678-20685.

(54) Mayank; Singh, A.; Kaur, N.; Singh, N.; Jang, D. O. A carbon quantum dot-encapsulated micellar reactor for the synthesis of chromene derivatives in water. *Mol. Catal.* **2017**, *439*, 100-107.

(55) Melchiorre, P.; Marigo, M.; Carlone, A.; Bartoli, G. Asymmetric aminocatalysis--gold rush in organic chemistry. *Angew. Chem. Int. Ed.* **2008**, *47*, 6138-6171.

(56) Zhang, L.; Fu, N.; Luo, S. Pushing the limits of aminocatalysis: enantioselective transformations of alpha-branched beta-ketocarbonyls and vinyl ketones by chiral primary amines. *Acc. Chem. Res.* **2015**, *48*, 986-997.

(57) Pei, X.; Xiong, D.; Wang, H.; Gao, S.; Zhang, X.; Zhang, S.; Wang, J. Reversible Phase Transfer of Carbon Dots between an Organic Phase and Aqueous Solution Triggered by CO_2. *Angew. Chem. Int. Ed.* **2018**, *57*, 3687-3691.

(58) König, B. Photocatalysis in Organic Synthesis - Past, Present, and Future. *Eur. J. Org. Chem.* **2017**, 1979-1981.

(59) Liu, Q.; Wu, L.-Z. Recent advances in visible-light-driven organic reactions. *Natl. Sci. Rev.* **2017**, *4*, 359-380.

(60) Candish, L.; Collins, K. D.; Cook, G. C.; Douglas, J. J.; Gomez-Suarez, A.; Jolit, A.; Keess, S. Photocatalysis in the Life Science Industry. *Chem. Rev.* **2022**, *122*, 2907-2980.

(61) Strieth-Kalthoff, F.; James, M. J.; Teders, M.; Pitzer, L.; Glorius, F. Energy transfer catalysis mediated by visible light: principles, applications, directions. *Chem. Soc. Rev.* **2018**, *47*, 7190-7202.

(62) Gualandi, A.; Anselmi, M.; Calogero, F.; Potenti, S.; Bassan, E.; Ceroni, P.; Cozzi, P. G. Metallaphotoredox catalysis with organic dyes. *Org. Biomol. Chem.* **2021**, *19*, 3527-3550.

(63) Cavedon, C.; Seeberger, P. H.; Pieber, B. Photochemical Strategies for Carbon–Heteroatom Bond Formation. *Eur. J. Org. Chem.* **2019**, 1379-1392.

(64) Schultz, D. M.; Yoon, T. P. Solar synthesis: prospects in visible light photocatalysis. *Science* **2014**, *343*, 1239176.

(65) Prier, C. K.; Rankic, D. A.; MacMillan, D. W. Visible light photoredox catalysis with transition metal complexes: applications in organic synthesis. *Chem. Rev.* **2013**, *113*, 5322-5363.

(66) Nicewicz, D. A.; Nguyen, T. M. Recent Applications of Organic Dyes as Photoredox Catalysts in Organic Synthesis. *ACS Catal.* **2013**, *4*, 355-360.

(67) Speckmeier, E.; Fischer, T. G.; Zeitler, K. A Toolbox Approach To Construct Broadly Applicable Metal-Free Catalysts for Photoredox Chemistry: Deliberate Tuning of Redox Potentials and Importance of Halogens in Donor-Acceptor Cyanoarenes. *J. Am. Chem. Soc.* **2018**, *140*, 15353-15365.

(68) Shang, T. Y.; Lu, L. H.; Cao, Z.; Liu, Y.; He, W. M.; Yu, B. Recent advances of 1,2,3,5-tetrakis(carbazol-9-yl)-4,6-dicyanobenzene (4CzIPN) in photocatalytic transformations. *Chem. Commun.* **2019**, *55*, 5408-5419.

(69) Neumann, M.; Fuldner, S.; Konig, B.; Zeitler, K. Metal-free, cooperative asymmetric organophotoredox catalysis with visible light. *Angew. Chem. Int. Ed.* **2011**, *50*, 951-954.

(70) Reischauer, S.; Strauss, V.; Pieber, B. Modular, Self-Assembling Metallaphotocatalyst for Cross-Couplings Using the Full Visible-Light Spectrum. *ACS Catal.* **2020**, *10*, 13269-13274.

(71) Gisbertz, S.; Pieber, B. Heterogeneous Photocatalysis in Organic Synthesis. *ChemPhotoChem* **2020**, *4*, 456-475.

(72) Schneider, J.; Matsuoka, M.; Takeuchi, M.; Zhang, J.; Horiuchi, Y.; Anpo, M.; Bahnemann, D. W. Understanding TiO_2 Photocatalysis: Mechanisms and Materials. *Chem. Rev.* **2014**, *114*, 9919-9986.

(73) Cheng, H.; Xu, W. Recent advances in modified TiO_2 for photo-induced organic synthesis. *Org. Biomol. Chem.* **2019**, *17*, 9977-9989.

(74) Nauth, A. M.; Schechtel, E.; Doren, R.; Tremel, W.; Opatz, T. TiO_2 Nanoparticles Functionalized with Non-innocent Ligands Allow Oxidative Photocyanation of Amines with Visible/Near-Infrared Photons. *J. Am. Chem. Soc.* **2018**, *140*, 14169-14177.

(75) Wang, X.; Blechert, S.; Antonietti, M. Polymeric Graphitic Carbon Nitride for Heterogeneous Photocatalysis. *ACS Catal.* **2012**, *2*, 1596-1606.

(76) Cao, S.; Low, J.; Yu, J.; Jaroniec, M. Polymeric photocatalysts based on graphitic carbon nitride. *Adv. Mater.* **2015**, *27*, 2150-2176.

(77) Su, F.; Mathew, S. C.; Lipner, G.; Fu, X.; Antonietti, M.; Blechert, S.; Wang, X. mpg-C_3N_4-Catalyzed Selective Oxidation of Alcohols Using O_2 and Visible Light. *J. Am. Chem. Soc.* **2010**, *132*, 16299-16301.

(78) Pieber, B.; Shalom, M.; Antonietti, M.; Seeberger, P. H.; Gilmore, K. Continuous Heterogeneous Photocatalysis in Serial Micro-Batch Reactors. *Angew. Chem. Int. Ed.* **2018**, *57*, 9976-9979.

(79) Mehta, A.; D, P.; Thakur, A.; Basu, S. Enhanced photocatalytic water splitting by gold carbon dot core shell nanocatalyst under visible/sunlight. *New J. Chem.* **2017**, *41*, 4573-4581.

(80) Hu, S.; Tian, R.; Wu, L.; Zhao, Q.; Yang, J.; Liu, J.; Cao, S. Chemical regulation of carbon quantum dots from synthesis to photocatalytic activity. *Chem. Asian J.* **2013**, *8*, 1035-1041.

(81) Li, H.; He, X.; Kang, Z.; Huang, H.; Liu, Y.; Liu, J.; Lian, S.; Tsang, C. H.; Yang, X.; Lee, S. T. Water-soluble fluorescent carbon quantum dots and photocatalyst design. *Angew. Chem. Int. Ed.* **2010**, *49*, 4430-4434.

(82) Han, Y.; Huang, H.; Zhang, H.; Liu, Y.; Han, X.; Liu, R.; Li, H.; Kang, Z. Carbon Quantum Dots with Photoenhanced Hydrogen-Bond Catalytic Activity in Aldol Condensations. *ACS Catal.* **2014**, *4*, 781-787.

(83) Sarma, D.; Majumdar, B.; Sarma, T. K. Visible-light induced enhancement in the multi-catalytic activity of sulfated carbon dots for aerobic carbon–carbon bond formation. *Green Chem.* **2019**, *21*, 6717-6726.

(84) Manjupriya, R.; Roopan, S. M. Carbon dots-based catalyst for various organic transformations. *J. Mater. Sci.* **2021**, *56*, 17369-17410.

(85) Shi, R.; Li, Z.; Yu, H.; Shang, L.; Zhou, C.; Waterhouse, G. I. N.; Wu, L. Z.; Zhang, T. Effect of Nitrogen Doping Level on the Performance of N-Doped Carbon Quantum Dot/TiO_2 Composites for Photocatalytic Hydrogen Evolution. *ChemSusChem* **2017**, *10*, 4650-4656.

(86) Li, M.; Wang, M.; Zhu, L.; Li, Y.; Yan, Z.; Shen, Z.; Cao, X. Facile microwave assisted synthesis of N-rich carbon quantum dots/dual-phase TiO_2 heterostructured nanocomposites with high activity in CO_2 photoreduction. *Appl. Catal. B* **2018**, *231*, 269-276.

(87) Yang, Z.; Xu, M.; Liu, Y.; He, F.; Gao, F.; Su, Y.; Wei, H.; Zhang, Y. Nitrogen-doped, carbon-rich, highly photoluminescent carbon dots from ammonium citrate. *Nanoscale* **2014**, *6*, 1890-1895.

(88) Reckmeier, C. J.; Schneider, J.; Xiong, Y.; Häusler, J.; Kasák, P.; Schnick, W.; Rogach, A. L. Aggregated Molecular Fluorophores in the Ammonothermal Synthesis of Carbon Dots. *Chem. Mater.* **2017**, *29*, 10352-10361.

(89) Magano, J.; Dunetz, J. R. Large-scale applications of transition metal-catalyzed couplings for the synthesis of pharmaceuticals. *Chem. Rev.* **2011**, *111*, 2177-2250.

(90) Johansson Seechurn, C. C.; Kitching, M. O.; Colacot, T. J.; Snieckus, V. Palladium-catalyzed cross-coupling: a historical contextual perspective to the 2010 Nobel Prize. *Angew. Chem. Int. Ed.* **2012**, *51*, 5062-5085.

(91) Karen E. Torraca, X. H., Cynthia A. Parrish, and Stephen L. Buchwald. An Efficient Intermolecular Palladium-Catalyzed Synthesis of Aryl Ethers. *J. Am. Chem. Soc.* **2001**, *123*, 10770-10771.

(92) Jepsen, T. H.; Larsen, M.; Jørgensen, M.; Solanko, K. A.; Bond, A. D.; Kadziola, A.; Nielsen, M. B. Synthesis of Functionalized Dibenzothiophenes - An Efficient Three-

Step Approach Based on Pd-Catalyzed C-C and C-S Bond Formations. *Eur. J. Org. Chem.* **2011**, 53-57.

(93) Diccianni, J.; Lin, Q.; Diao, T. Mechanisms of Nickel-Catalyzed Coupling Reactions and Applications in Alkene Functionalization. *Acc. Chem. Res.* **2020**, *53*, 906-919.

(94) Wolfe J. P.; Buchwald, S. L. Nickel-Catalyzed Amination of Aryl Chlorides. *J. Am. Chem. Soc.* **1997**, *119*, 6054-6058.

(95) Urgaonkar, S.; Xu, J.-H.; Verkade, J. G. Application of a New Bicyclic Triaminophosphine Ligand in Pd-Catalyzed Buchwald-Hartwig Amination Reactions of Aryl Chlorides, Bromides, and Iodides. *J. Org. Chem.* **2003**, *68*, 8416-8423.

(96) Fitzner, M.; Wuitschik, G.; Koller, R. J.; Adam, J. M.; Schindler, T.; Reymond, J. L. What can reaction databases teach us about Buchwald-Hartwig cross-couplings? *Chem. Sci.* **2020**, *11*, 13085-13093.

(97) Zuo, Z.; Ahneman, D. T.; Chu, L.; Terrett, J. A.; Doyle, A. G.; MacMillan, D. W. C. Merging photoredox with nickel catalysis: Coupling of α-carboxyl sp^3-carbons with aryl halides. *Science* **2014**, *345*, 437-440.

(98) Milligan, J. A.; Phelan, J. P.; Badir, S. O.; Molander, G. A. Alkyl Carbon-Carbon Bond Formation by Nickel/Photoredox Cross-Coupling. *Angew. Chem. Int. Ed.* **2019**, *58*, 6152-6163.

(99) Pieber, B.; Malik, J. A.; Cavedon, C.; Gisbertz, S.; Savateev, A.; Cruz, D.; Heil, T.; Zhang, G.; Seeberger, P. H. Semi-heterogeneous Dual Nickel/Photocatalysis using Carbon Nitrides: Esterification of Carboxylic Acids with Aryl Halides. *Angew. Chem. Int. Ed.* **2019**, *58*, 9575-9580.

(100) Ghosh, I.; Khamrai, J.; Savateev, A.; Shlapakov, N.; Antonietti, M.; König, B. Organic semiconductor photocatalyst can bifunctionalize arenes and heteroarenes. *Science* **2019**, *365*, 360-366.

(101) Vara, B. A.; Li, X.; Berritt, S.; Walters, C. R.; Petersson, E. J.; Molander, G. A. Scalable thioarylation of unprotected peptides and biomolecules under Ni/photoredox catalysis. *Chem. Sci.* **2018**, *9*, 336-344.

(102) Oderinde, M. S.; Jones, N. H.; Juneau, A.; Frenette, M.; Aquila, B.; Tentarelli, S.; Robbins, D. W.; Johannes, J. W. Highly Chemoselective Iridium Photoredox and Nickel Catalysis for the Cross-Coupling of Primary Aryl Amines with Aryl Halides. *Angew. Chem. Int. Ed.* **2016**, *55*, 13219-13223.

(103) Luo, J.; Zhang, J. Donor–Acceptor Fluorophores for Visible-Light-Promoted Organic Synthesis: Photoredox/Ni Dual Catalytic $C(sp^3)$–$C(sp^2)$ Cross-Coupling. *ACS Catal.* **2016**, *6*, 873-877.

(104) Singh, K.; Staig, S. J.; Weaver, J. D. Facile synthesis of Z-alkenes via uphill catalysis. *J. Am. Chem. Soc.* **2014**, *136*, 5275-5278.

(105) Fabry, D. C.; Ronge, M. A.; Rueping, M. Immobilization and continuous recycling of photoredox catalysts in ionic liquids for applications in batch reactions and flow systems: catalytic alkene isomerization by using visible light. *Chem. Eur. J.* **2015**, *21*, 5350-5354.

(106) Cai, W.; Fan, H.; Ding, D.; Zhang, Y.; Wang, W. Synthesis of Z-alkenes via visible light promoted photocatalytic E --> Z isomerization under metal-free conditions. *Chem. Commun.* **2017**, *53*, 12918-12921.

(107) Bhadra, M.; Kandambeth, S.; Sahoo, M. K.; Addicoat, M.; Balaraman, E.; Banerjee, R. Triazine Functionalized Porous Covalent Organic Framework for Photo-organocatalytic E-Z Isomerization of Olefins. *J. Am. Chem. Soc.* **2019**, *141*, 6152-6156.

(108) Nevesely, T.; Wienhold, M.; Molloy, J. J.; Gilmour, R. Advances in the E --> Z Isomerization of Alkenes Using Small Molecule Photocatalysts. *Chem. Rev.* **2022**, *122*, 2650-2694.

(109) Metternich, J. B.; Artiukhin, D. G.; Holland, M. C.; von Bremen-Kuhne, M.; Neugebauer, J.; Gilmour, R. Photocatalytic E --> Z Isomerization of Polarized Alkenes Inspired by the Visual Cycle: Mechanistic Dichotomy and Origin of Selectivity. *J. Org. Chem.* **2017**, *82*, 9955-9977.

(110) Zhan, J.; Geng, B.; Wu, K.; Xu, G.; Wang, L.; Guo, R.; Lei, B.; Zheng, F.; Pan, D.; Wu, M. A solvent-engineered molecule fusion strategy for rational synthesis of carbon quantum dots with multicolor bandgap fluorescence. *Carbon* **2018**, *130*, 153-163.

(111) Vallan, L.; Urriolabeitia, E. P.; Ruiperez, F.; Matxain, J. M.; Canton-Vitoria, R.; Tagmatarchis, N.; Benito, A. M.; Maser, W. K. Supramolecular-Enhanced Charge Transfer within Entangled Polyamide Chains as the Origin of the Universal Blue Fluorescence of Polymer Carbon Dots. *J. Am. Chem. Soc.* **2018**, *140*, 12862-12869.

(112) Shen, Z.; Zhang, C.; Yu, X.; Li, J.; Wang, Z.; Zhang, Z.; Liu, B. Microwave-assisted synthesis of cyclen functional carbon dots to construct a ratiometric fluorescent probe for tetracycline detection. *J. Mater. Chem. C* **2018**, *6*, 9636-9641.

(113) Zhi, B.; Cui, Y.; Wang, S.; Frank, B. P.; Williams, D. N.; Brown, R. P.; Melby, E. S.; Hamers, R. J.; Rosenzweig, Z.; Fairbrother, D. H.; et al. Malic Acid Carbon Dots: From Super-resolution Live-Cell Imaging to Highly Efficient Separation. *ACS Nano* **2018**, *12*, 5741-5752.

(114) Sri, S.; Kumar, R.; Panda, A. K.; Solanki, P. R. Highly Biocompatible, Fluorescence, and Zwitterionic Carbon Dots as a Novel Approach for Bioimaging Applications in Cancerous Cells. *ACS Appl. Mater. Interfaces* **2018**, *10*, 37835-37845.

(115) Zhao, H.; Duan, J.; Xiao, Y.; Tang, G.; Wu, C.; Zhang, Y.; Liu, Z.; Xue, W. Microenvironment-Driven Cascaded Responsive Hybrid Carbon Dots as a

Multifunctional Theranostic Nanoplatform for Imaging-Traceable Gene Precise Delivery. *Chem. Mater.* **2018**, *30*, 3438-3453.

(116) Yang, P.; Zhao, J.; Wang, J.; Cui, H.; Li, L.; Zhu, Z. Multifunctional Nitrogen-Doped Carbon Nanodots for Photoluminescence, Sensor, and Visible-Light-Induced H_2 Production. *ChemPhysChem* **2015**, *16*, 3058-3063.

(117) Wu, J.; Ma, S.; Sun, J.; Gold, J. I.; Tiwary, C.; Kim, B.; Zhu, L.; Chopra, N.; Odeh, I. N.; Vajtai, R.; et al. A metal-free electrocatalyst for carbon dioxide reduction to multi-carbon hydrocarbons and oxygenates. *Nat. Commun.* **2016**, *7*, 13869.

(118) Cao, L.; Sahu, S.; Anilkumar, P.; Bunker, C. E.; Xu, J.; Fernando, K. A.; Wang, P.; Guliants, E. A.; Tackett, K. N., 2nd; Sun, Y. P. Carbon nanoparticles as visible-light photocatalysts for efficient CO_2 conversion and beyond. *J. Am. Chem. Soc.* **2011**, *133*, 4754-4757.

(119) Martindale, B. C.; Hutton, G. A.; Caputo, C. A.; Reisner, E. Solar hydrogen production using carbon quantum dots and a molecular nickel catalyst. *J. Am. Chem. Soc.* **2015**, *137*, 6018-6025.

(120) Liu, Y.; Zhao, Y.; Wu, Q.; Wang, X.; Nie, H.; Zhou, Y.; Huang, H.; Shao, M.; Liu, Y.; Kang, Z. Charge storage of carbon dot enhances photo-production of H_2 and H_2O_2 over Ni_2P/carbon dot catalyst under normal pressure. *Chem. Eng. J.* **2021**, *409*, 128184.

(121) Zhou, Z.; Tian, P.; Liu, X.; Mei, S.; Zhou, D.; Li, D.; Jing, P.; Zhang, W.; Guo, R.; Qu, S.; Rogach, A. L. Hydrogen Peroxide-Treated Carbon Dot Phosphor with a Bathochromic-Shifted, Aggregation-Enhanced Emission for Light-Emitting Devices and Visible Light Communication. *Adv. Sci.* **2018**, *5*, 1800369.

(122) Li, S.; Ji, K.; Zhang, M.; He, C.; Wang, J.; Li, Z. Boosting the photocatalytic CO_2 reduction of metal-organic frameworks by encapsulating carbon dots. *Nanoscale* **2020**, *12*, 9533-9540.

(123) Filippini, G.; Amato, F.; Rosso, C.; Ragazzon, G.; Vega-Peñaloza, A.; Companyó, X.; Dell'Amico, L.; Bonchio, M.; Prato, M. Mapping the Surface Groups of Amine-Rich Carbon Dots Enables Covalent Catalysis in Aqueous Media. *Chem* **2020**, *6*, 3022-3037.

(124) Weng, Y.-X.; Li, L.; Liu, Y.; Wang, L.; Yang, G.-Z. Surface-Binding Forms of Carboxylic Groups on Nanoparticulate TiO_2 Surface Studied by the Interface-Sensitive Transient Triplet-State Molecular Probe. *J. Phys. Chem. B* **2003**, *107*, 4356-4363.

(125) Agrawal, S.; English, N. J.; Thampi, K. R.; MacElroy, J. M. Perspectives on ab initio molecular simulation of excited-state properties of organic dye molecules in dye-sensitised solar cells. *Phys. Chem. Chem. Phys.* **2012**, *14*, 12044-12056.

(126) Xu, L.; Bai, X.; Guo, L.; Yang, S.; Jin, P.; Yang, L. Facial fabrication of carbon quantum dots (CDs)-modified N-TiO_{2-x} nanocomposite for the efficient photoreduction of Cr(VI) under visible light. *Chem. Eng. J.* **2019**, *357*, 473-486.

(127) Zhang, J.; Zhang, X.; Dong, S.; Zhou, X.; Dong, S. N-doped carbon quantum dots/TiO_2 hybrid composites with enhanced visible light driven photocatalytic activity toward dye wastewater degradation and mechanism insight. *J. Photochem. Photobiol. A* **2016**, *325*, 104-110.

(128) Li, M.; Wang, M.; Zhu, L.; Li, Y.; Yan, Z.; Shen, Z.; Cao, X. Facile microwave assisted synthesis of N-rich carbon quantum dots/dualphase TiO_2 heterostructured nanocomposites with high activity in CO_2 photoreduction. *Appl. Catal. B* **2018**, *231*, 269-276.

(129) Zhu, C.; Yue, H.; Jia, J.; Rueping, M. Nickel-Catalyzed C-Heteroatom Cross-Coupling Reactions under Mild Conditions *via* Facilitated Reductive Elimination. *Angew. Chem. Int. Ed.* **2021**, *60*, 17810-17831.

(130) Lan, G.; Quan, Y.; Wang, M.; Nash, G. T.; You, E.; Song, Y.; Veroneau, S. S.; Jiang, X.; Lin, W. Metal–Organic Layers as Multifunctional Two-Dimensional Nanomaterials for Enhanced Photoredox Catalysis. *J. Am. Chem. Soc.* **2019**, *141*, 15767-15772.

(131) Zhu, Y.-Y.; Lan, G.; Fan, Y.; Veroneau, S. S.; Song, Y.; Micheroni, D.; Lin, W. Merging Photoredox and Organometallic Catalysts in a Metal–Organic Framework Significantly Boosts Photocatalytic Activities. *Angew. Chem. Int. Ed.* **2018**, *57*, 14090-14094.

(132) Pan, Y.; Zhang, N.; Liu, C.-H.; Fan, S.; Guo, S.; Zhang, Z.-M.; Zhu, Y.-Y. Boosting Photocatalytic Activities for Organic Transformations through Merging Photocatalyst and Transition-Metal Catalyst in Flexible Polymers. *ACS Catal.* **2020**, *10*, 11758-11767.

(133) Franchi, D.; Amara, Z. Applications of Sensitized Semiconductors as Heterogeneous Visible-Light Photocatalysts in Organic Synthesis. *ACS Sustain. Chem. Eng.* **2020**, *8*, 15405-15429.

(134) Hill, S. A.; Benito-Alifonso, D.; Morgan, D. J.; Davis, S. A.; Berry, M.; Galan, M. C. Three-minute synthesis of sp^3 nanocrystalline carbon dots as non-toxic fluorescent platforms for intracellular delivery. *Nanoscale* **2016**, *8*, 18630-18634.

(135) Memming, R.; Kriiger, U. Formation and Reactions of Long Lived Xanthene Dye Radicals. I. Photochemical Studies on Reactions of Semireduced Fluoresceïn. *Ber. Bunsenges. Phys. Chem.* **1974**, *78*, 670-678.

(136) Zheng, Q.; Lavis, L. D. Development of photostable fluorophores for molecular imaging. *Curr. Opin. Chem. Biol.* **2017**, *39*, 32-38.

(137) Gisbertz, S.; Reischauer, S.; Pieber, B. Overcoming limitations in dual photoredox/nickel-catalysed C–N cross-couplings due to catalyst deactivation. *Nat. Catal.* **2020**, *3*, 611-620.

(138) Hill, S. A.; Sheikh, S.; Zhang, Q.; Sueiro Ballesteros, L.; Herman, A.; Davis, S. A.; Morgan, D. J.; Berry, M.; Benito-Alifonso, D.; Galan, M. C. Selective photothermal

killing of cancer cells using LED-activated nucleus targeting fluorescent carbon dots. *Nanoscale Adv.* **2019**, *1*, 2840-2846.

(139) Zhao, Z.; Reischauer, S.; Pieber, B.; Delbianco, M. Carbon dot/TiO_2 nanocomposites as photocatalysts for metallaphotocatalytic carbon–heteroatom cross-couplings. *Green Chem.* **2021**, *23*, 4524-4530.

(140) Reischauer, S.; Pieber, B. Recyclable, Bifunctional Metallaphotocatalysts for C−S Cross-Coupling Reactions. *ChemPhotoChem* **2021**, *5*, 716-720.

(141) Zeininger, L.; Portilla, L.; Halik, M.; Hirsch, A. Quantitative Determination and Comparison of the Surface Binding of Phosphonic Acid, Carboxylic Acid, and Catechol Ligands on TiO_2 Nanoparticles. *Chem. Eur. J.* **2016**, *22*, 13506-13512.

(142) Polshettiwar, V.; Varma, R. S. Green chemistry by nano-catalysis. *Green Chem.* **2010**, *12*, 743-754.

(143) Hasani, M.; Kalhor, H. R. Enzyme-Inspired Lysine-Modified Carbon Quantum Dots Performing Carbonylation Using Urea and a Cascade Reaction for Synthesizing 2-Benzoxazolinone. *ACS Catal.* **2021**, *11*, 10778-10788.

(144) Qin, Y.; Sun, R.; Gianoulis, N. P.; Nocera, D. G. Photoredox Nickel-Catalyzed C-S Cross-Coupling: Mechanism, Kinetics, and Generalization. *J. Am. Chem. Soc.* **2021**, *143*, 2005-2015.

(145) Zhang, J. S.; Zhang, W. D. Nickel complex co-catalyst confined by chitosan onto graphitic carbon nitride for efficient H_2 evolution. *J. Colloid Interface Sci.* **2020**, *560*, 11-20.

(146) Badiani, V. M.; Casadevall, C.; Miller, M.; Cobb, S. J.; Manuel, R. R.; Pereira, I. A. C.; Reisner, E. Engineering Electro- and Photocatalytic Carbon Materials for CO_2 Reduction by Formate Dehydrogenase. *J. Am. Chem. Soc.* **2022**, *144*, 14207-14216.

(147) Corti, V.; Bartolomei, B.; Mamone, M.; Gentile, G.; Prato, M.; Filippini, G. Amine-Rich Carbon Dots as Novel Nano-Aminocatalytic Platforms in Organic Synthesis. *Eur. J. Org. Chem.* **2022**, e202200879.

(148) Du, Y.; Pearson, R. M.; Lim, C. H.; Sartor, S. M.; Ryan, M. D.; Yang, H.; Damrauer, N. H.; Miyake, G. M. Strongly Reducing, Visible-Light Organic Photoredox Catalysts as Sustainable Alternatives to Precious Metals. *Chem. Eur. J.* **2017**, *23*, 10962-10968.

(149) Cavedon, C.; Madani, A.; Seeberger, P. H.; Pieber, B. Semiheterogeneous Dual Nickel/Photocatalytic (Thio)etherification Using Carbon Nitrides. *Org. Lett.* **2019**, *21*, 5331-5334.

(150) Oderinde, M. S.; Frenette, M.; Robbins, D. W.; Aquila, B.; Johannes, J. W. Photoredox Mediated Nickel Catalyzed Cross-Coupling of Thiols With Aryl and Heteroaryl Iodides via Thiyl Radicals. *J. Am. Chem. Soc.* **2016**, *138*, 1760-1763.

(151) Sun, R.; Qin, Y.; Ruccolo, S.; Schnedermann, C.; Costentin, C.; Daniel, G. N. Elucidation of a Redox-Mediated Reaction Cycle for Nickel-Catalyzed Cross Coupling. *J. Am. Chem. Soc.* **2019**, *141*, 89-93.

(152) Till, N. A.; Tian, L.; Dong, Z.; Scholes, G. D.; MacMillan, D. W. C. Mechanistic Analysis of Metallaphotoredox C-N Coupling: Photocatalysis Initiates and Perpetuates Ni(I)/Ni(III) Coupling Activity. *J. Am. Chem. Soc.* **2020**, *142*, 15830-15841.

(153) Till, N. A.; Oh, S.; MacMillan, D. W. C.; Bird, M. J. The Application of Pulse Radiolysis to the Study of Ni(I) Intermediates in Ni-Catalyzed Cross-Coupling Reactions. *J. Am. Chem. Soc.* **2021**, *143*, 9332-9337.

(154) Sun, R.; Yang, X.; Ge, Y.; Song, J.; Zheng, X.; Yuan, M.; Li, R.; Chen, H.; Fu, H. Visible-Light-Induced Oxazoline Formations from N-Vinyl Amides Catalyzed by an Ion-Pair Charge-Transfer Complex. *ACS Catal.* **2021**, *11*, 11762-11773.

(155) Chen, C.; Dugan, T. R.; Brennessel, W. W.; Weix, D. J.; Holland, P. L. Z-selective alkene isomerization by high-spin cobalt(II) complexes. *J. Am. Chem. Soc.* **2014**, *136*, 945-955.

(156) Metternich, J. B.; Gilmour, R. A Bio-Inspired, Catalytic E --> Z Isomerization of Activated Olefins. *J. Am. Chem. Soc.* **2015**, *137*, 11254-11257.

(157) Vijeta, A.; Casadevall, C.; Roy, S.; Reisner, E. Visible-Light Promoted C-O Bond Formation with an Integrated Carbon Nitride-Nickel Heterogeneous Photocatalyst. *Angew. Chem. Int. Ed.* **2021**, *60*, 8494-8499.

(158) Zeng, Z.; Zhang, W.; Arvapalli, D. M.; Bloom, B.; Sheardy, A.; Mabe, T.; Liu, Y.; Ji, Z.; Chevva, H.; Waldeck, D. H.; Wei, J. A fluorescence-electrochemical study of carbon nanodots (CNDs) in bio- and photoelectronic applications and energy gap investigation. *Phys. Chem. Chem. Phys.* **2017**, *19*, 20101-20109.

(159) Cardona, C. M.; Li, W.; Kaifer, A. E.; Stockdale, D.; Bazan, G. C. Electrochemical considerations for determining absolute frontier orbital energy levels of conjugated polymers for solar cell applications. *Adv. Mater.* **2011**, *23*, 2367-2371.

(160) Yue, H.; Zhu, C.; Rueping, M. Cross-Coupling of Sodium Sulfinates with Aryl, Heteroaryl, and Vinyl Halides by Nickel/Photoredox Dual Catalysis. *Angew. Chem. Int. Ed.* **2018**, *57*, 1371-1375.

(161) Ye, F.; Berger, F.; Jia, H.; Ford, J.; Wortman, A.; Börgel, J.; Genicot, C.; Ritter, T. Aryl Sulfonium Salts for Site-Selective Late-Stage Trifluoromethylation. *Angew. Chem. Int. Ed.* **2019**, *58*, 14615-14619.